Elastic Photon Scatter for Tissue Analysis

Gary John Royle

Thesis for the degree of Doctor of Philosophy

University College London
University of London

October 1992

Abstract

This thesis presents a new technique in which x-ray diffraction has been adapted to the clinical environment in order to quantify the osteoporotic state of bone tissue. The constraints of a clinical system demand diffraction apparatus with short wavelengths, a low photon flux and a short measurement time. Of the two forms of measurement for recording diffraction patterns the fixed detector, energy dispersive technique was found to be better suited to clinical work than the scanning detector, angular distributive approach. Various procedures to remove unwanted effects in the data are presented, along with a Monte Carlo simulation designed to investigate the effect of variation in patient thickness and bone volume on the relative proportion of elastic scatter.

Diffraction peaks due to bone and marrow tissue were identified in the scatter pattern of trabecular bone. The relative intensities of the two peaks within the pattern are shown to quantify the relative proportions of the two components, and so the bone-to-marrow peak ratio was proposed as a parameter to assess the osteoporotic state of trabecular tissue. Results from anthropomorphic phantoms demonstrate a significant correlation between this method and the established bone density measurement techniques of quantitative computerised tomography and Compton scatter densitometry.

The inherent uniqueness of the diffraction pattern was also applied to tissue characterisation, in particular to the identification of gallstones. Gallstones can be classified into three main categories according to their crystalline constituents, each type requiring different patient treatment. A clear distinction between the three stone types is demonstrated with this method.

The principal advantages of this technique are its ability to focus on a small volume within the object, such as the trabecular region within bone, the capability of *in-vivo* measurement and the ability to isolate the responses from the bone and marrow.

Contents

List of figures

List of tables

Errata

p.26	line 2	for ‘higher’ read ‘lower’
p.35	line 22	replace with; Coherent (or Rayleigh) scatter is the elastic scatter of photons by electrons with the subsequent interference effects considered.
p.36	lines 8 - 11	replace with the following; $x = \sin(\theta/2) / \lambda$, the momentum transfer (2.3) and $r_e = e^2 / (4\pi\varepsilon_0 m_e c^2)$, the classical electron radius (2.4) e is the electron charge, ε_0 the permittivity of a vacuum, m_e the electron mass and c the velocity of light. Thomson scattering describes the classical elastic scatter of a photon by a single electron from a consideration of the electrostatic force, no interference effects are considered.
p.45	line 23	for ‘mass for energy’ read ‘energy for mass’
p.76	equation 3.5	for $\left(\frac{L}{2}\right)$ read $\left(\frac{L}{2}\right)^2$
p.85	line 9	for ‘form’ read ‘from’
p.90	line 14	for ‘is satisfied’ read ‘is not satisfied’
p.95	line 1	for ‘are’ read ‘is’
p.103	line 16-18	should read ‘$\Phi(f)$ is close to unity where the noise is negligible and close to zero where noise dominates.’
p.113	lines 1, 5	for ‘1 to 4’ read ‘a to d’
p.114	line 8	for ‘sane’ read ‘same’
p.119	line 1 missing	should read ‘very similar to that of water at each angle. An amorphous scattering object produces less’
p.125	figure 6.13	for ‘%’ read ‘fractional’
p.128	line 1 missing	should read ‘The scatter pattern of fresh trabecular bone is seen to result from a combination of the scatter’
p.147	line 17	for ‘does produce’ read ‘does not produce’
p.167	table 3.1A	The effective atomic numbers quoted are for photoelectric interactions, the mean effective atomic numbers for coherent interactions are as follows; muscle (6.94), adipose(5.45), inner bone (7.66), cortical bone (9.69), yellow marrow (5.36), red marrow (6.51).

- 1 -

Pathology and diagnosis of osteoporosis

This opening chapter serves to provide information on bone tissue and the diagnosis of osteoporosis. It describes the physiology of bone tissue, the effect of the more common diseased states, with particular attention paid to osteoporosis, and reviews the current methods of diagnosis. Finally the proposed measurement technique of elastic photon scattering is introduced. Previous work in this field is presented together with a discussion on the application of this technique to diagnosing the diseases considered.

1.1 Bone physiology

1.1.1 The role of the skeleton

The skeleton provides both a calcium reservoir for the body and a structural framework for body form, support, protection, and movement. The skeletal system is also important in the synthesis of both red and white blood cells within the red bone marrow.

The bones are essential in maintaining homeostatic levels of plasma calcium ions. The crystalline structure of the bone is a dynamic reservoir of calcium storage. Ninety nine percent of total body calcium resides in the skeleton, which amounts to approximately 1.5kg of elemental calcium in the average, adult man. However, despite this large amount of calcium very little (<1%) is miscible with extra cellular fluid. Approximately 0.5g of calcium per day are transferred between bone and extra cellular fluid. Active resorption of bone mineral is required to mobilise significant amounts of calcium. Calcium ions are removed from the bone when plasma levels fall below the optimum. In order to maintain homeostatic levels of calcium, any ions removed from the bone must be replaced from the dietary intake. The blood stream acts as the means for transporting the calcium ions through the body.

1.1.2 The structure and composition of bone tissue

In the bone, calcium carbonate and calcium phosphate form calcium hydroxyapatite crystals, which provide about 25 percent of the weight of the bone and give it its characteristic hardness and crystalline structure. The most abundant elements in bone tissue are carbon, oxygen, phosphorous and calcium (Woodard and White 1986). The hydroxyapatite crystals are laid down in an orderly fashion along a protein framework synthesised by the bone cells.

Bone tissue falls into one of two categories depending upon its internal structure. One type is cortical (or *hard* or *compact*) bone; a dense tissue which forms a hard shell always found on the exterior of the bone. The other type is trabecular (or *inner* or *cancellous*) bone, a less dense, fibrous tissue always found on the bone's interior; a cross-section of the trabecular bone displays thin walls of bone tissue (called trabeculae) typically 100-200μm thick enclosing spaces of 600-1000μm across (Whitehouse and Dyson 1974). In three dimensions this forms a honeycomb-like structure of bone fibres surrounding cavities filled with red or yellow bone marrow. A photograph of the arrangement of the bony lamellae in trabecular bone is shown in figure 1.1.

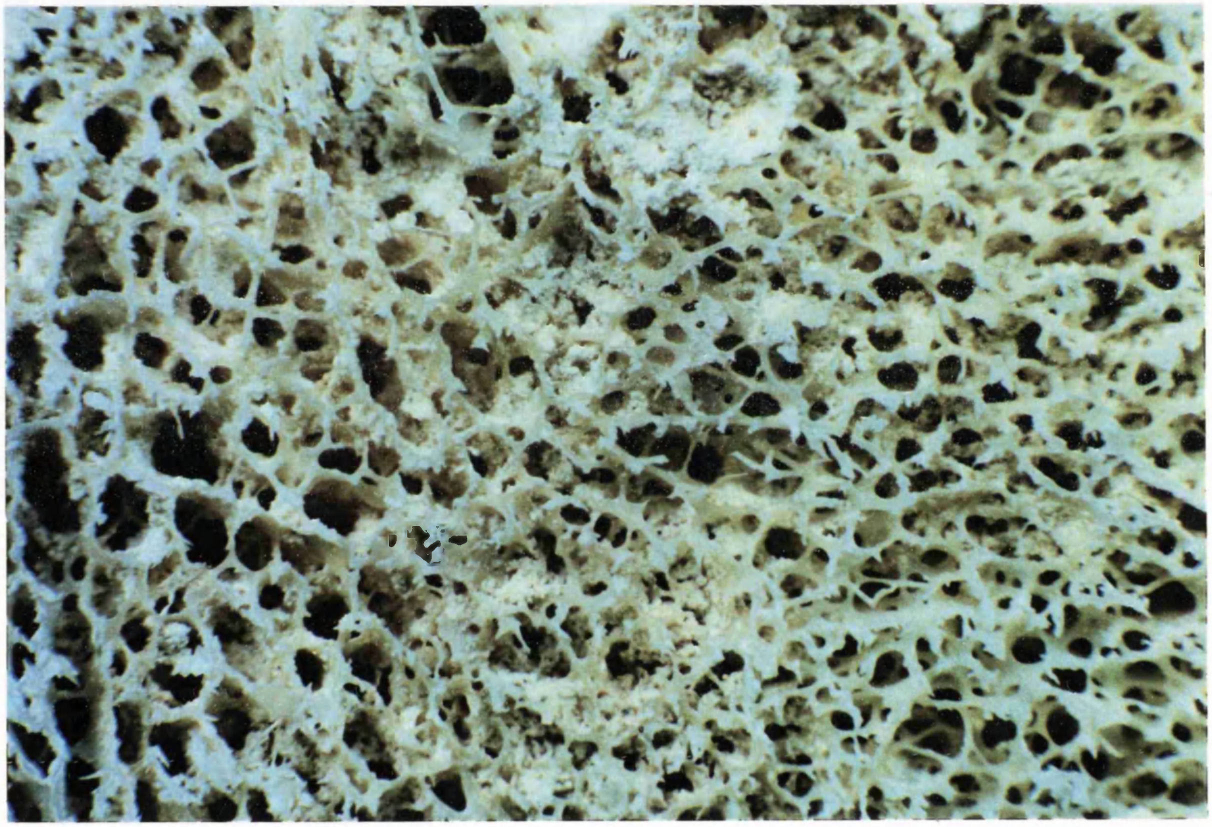

Figure 1.1 A close-up photograph of a section through dry bone, showing the trabecular structure. In living bone tissue the spaces would be filled with bone marrow, a fat-like substance.

The relative quantities of these two types of bone tissue vary between different bones and between different regions within the same bone depending upon the skeletal requirements for strength or lightness at that region. The two types of marrow tissue also differ in properties and location; yellow (*fatty*) marrow is composed almost entirely of fat (96%) and is found in the shafts of long bones and within the trabecular cavities of many bones. Red (*haematopoietic*) marrow is a slightly denser tissue containing a large percentage of water (75%) and very little fat. It is found within the trabecular cavities in the vertebrae and in the articular ends of the long bones. Figure 1.2 shows a diagram of a typical long bone (the femur); a thick shell of cortical bone encases the yellow marrow

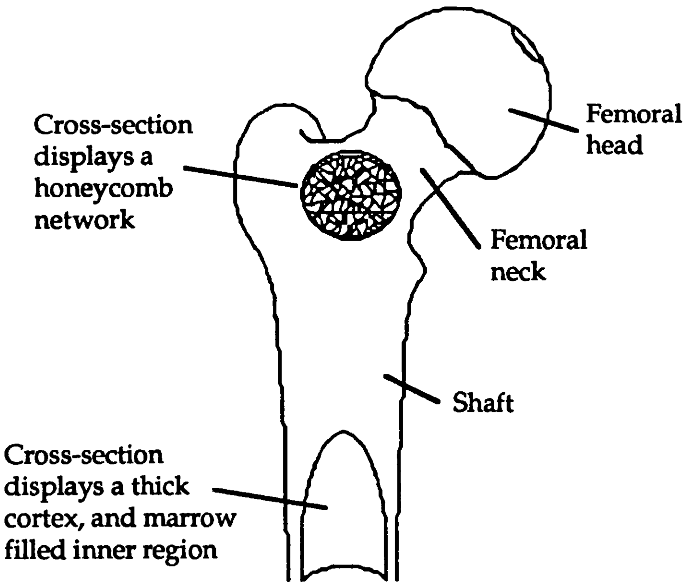

Figure 1.2 A diagram of the femur, detailing the various parts.

filled medullary cavity in the middle section of the bone; towards the ends of the bone the inner section displays a structural arrangement of bone plates surrounded by a thin cortical layer. Shorter bones, such as the vertebrae, are filled throughout with trabeculae; no medullary cavity is present.

1.2 Age related changes in healthy bone

Although bone is a living tissue constantly interacting with the blood stream in a non-diseased state it remains relatively stable. The composition of healthy cortical and trabecular bone experiences only a 2% increase in mineral and a 2% decrease in water in ageing from young, adult bone to elderly bone (Woodard 1964, Dequeker 1973).

Age related changes which commonly occur in bone are a gradual reduction in the quantity of cortical and trabecular bone present in the skeleton, caused by the rate of formation of osseous tissue falling below the rate of resorption, and the conversion, within the trabecular cavities, of red marrow to yellow marrow. The marrow conversion occurs at an early age in the appendicular skeleton (the limbs) so that by the age of 20 the red marrow is restricted to the axial skeleton (the trunk) and the proximal end of the femurs. The increase in the percentage volume of the yellow marrow in these regions then continues at a rate of approximately 0.5% per year reducing to 0.2% per year beyond the age of 40 (Dunnil *et al* 1967).

1.3 The effects of bone disease

A wide variety of skeletal disorders exist, each producing different effects on the individual, however, most cause much discomfort and pain. Those disorders which involve inflammation of the joints are collectively termed arthritis. *Rheumatoid arthritis*, the most common, is characterised by inflammation and swelling of the synovial membrane (a tissue lining the moving parts in a joint, which provides lubrication) and subsequent stiffening and loss of use of the joint. *Osteoarthritis* usually affects the weight bearing joints and is characterised by the formation of lumps of new osseous tissue on the ends of the exposed bone, decreasing the mobility of the joint.

Disruption of the body's metabolism can alter the physiology of bone tissue, as well as that of many other tissues, and generally causes a change in the percentage composition of the bone tissue. A deficiency of vitamin D, for example, results in softer, more pliable bones due to decreased calcification, which is the case in some forms of rickets and osteomalacia. Such effects are generally termed metabolic bone diseases. Another example of this is primary (or secondary) hyperparathyroidism, a disease caused by a disturbance in the production of the parathyroid hormone. This hormone, produced by the thyroid gland, increases the concentration of plasma calcium, and is thought to be the most important factor in maintaining calcium homeostasis in extra cellular fluid. The effect it has is to cause a general increase in bone remodelling, augmenting both formation and resorption. The net bone mass reflects the balance between the two. A section through bone suffering from the disease shows excessive bone loss, disorderly bone formation and incomplete calcification.

Chronic renal failure disrupts the mineral metabolism because of a marked impairment in the intestinal absorption of calcium, an inability to adapt to variations in dietary calcium, and an increase in the level of the parathyroid hormone. This results in renal osteodystrophy, a metabolic bone disease characterised by bone loss, fracture, displaced calcification and secondary hyperparathyroidism. It is identified on radiographs by subperiosteal resorption in the small bones of the hands and feet, resorption of the distal ends of the clavicles, or a mottled appearance of the skull. Large cystic-like tumours can also appear on the long bones, ribs or metacarpals.

Renal disease can frequently result in osteosclerosis. This is a disease, affecting mainly the axial skeleton, which causes an increase in bone density but does not result in fractures, visible deformation or pain. Radiographs of the spine show distinctive horizontal bands of increased bone density alternating with relatively less dense bands of bone. A general coarsening of the trabecular pattern is also seen.

Paget's disease is generally termed a metabolic bone disease but it is not strictly in this category as much of the skeleton remains unaffected. It is commonly found in the middle aged or elderly, the incidence rising with age. The pathology of Paget's disease is divided into three stages: first there is intense resorption of existing bone, this is soon accompanied by accelerated deposition of spicules of lamellar bone (the inner region of bone in which the trabeculae have a layered appearance) in a disorganised manner, and thirdly there is excessive formation of bone culminating in a mosaic pattern of lamellar bone. The resultant effect of this bone remodelling is a thickening of the cortical region and densely packed, coarsely thickened trabeculae. This is seen in the patient as marked deformation of the skeleton. For example, cortical thickening in the skull can increase the circumference by as much as 15cm, and enlargement within the long bones of the legs will cause them to bow forward quite noticeably.

1.4 Osteoporosis

The most common disease of the skeleton is osteoporosis. It affects a considerable number of people in the western world and is a cause of vast expense to the health service in many countries. Osteoporosis is a metabolic bone disease which can be described as a gradual decrease in the quantity of bone tissue at particular regions of the skeleton which reduces the strength of the bone. Continual loss of bone tissue will weaken the bone to such an extent that it is likely to fracture from relatively low trauma. The disease is commonly identified by vertebral crush fractures in the lumbar region of the spine, which has been known to cause a loss in height of several inches, or by fracture of the femoral neck or of the distal radius.

The population at most risk from osteoporosis are thin, white, postmenopausal women. A poor, calcium-deficient diet and lack of exercise also contribute significantly (Simkin *et al* 1987).

1.4.1 Cause and pathology of the disease

Two forms of osteoporosis have been identified (Nordin *et al* 1981, Riggs *et al* 1982);-

(i) *senile osteoporosis*: caused by the normal age-related decrease in cortical and trabecular bone over many years increasing the likelihood of fracture. This involves the majority of elderly women and many elderly men.

(ii) *postmenopausal osteoporosis*: this affects a subset of about 20% of early postmenopausal women (within 10-15 years of menopause) and is seen as an accelerated rate of bone loss in addition to the normal rate of bone loss.

The main determinant of bone loss is unclear; Nordin *et al* (1981) reported an increase in bone resorption to be responsible for senile osteoporosis, and in postmenopausal osteoporosis the rate of resorption is further increased. Darby and Meunier (1981), however, suggest that decreased bone formation is the major cause.

The actual biological mechanism which causes the increased resorption (or decreased formation) of the bone tissue is also unclear and the focus of much attention. The following briefly describes the most common theories:-

Riggs *et al* (1981) suggest that the mechanism for senile osteoporosis is ageing of the bone cells. A differing mechanism exists in the postmenopausal variety; Thomsen *et al* (1986) reported that bone loss in postmenopausal women is not simply an age-related phenomenon, an additional factor exists. This factor is generally thought (Richelson *et al* 1984) to be a decline following menopause in the production of oestrogen, a sex steroid known to be important in bone calcification as well as organic matrix formation in bone, and consequent increased sensitivity of the bone to bone resorbing agents.

Loss of osseous tissue in the cortical bone is seen as a decrease in the thickness of the cortical bone (Barnett and Nordin 1960) and a slight increase in porosity (Dickenson *et al* 1981).

Atrophy in the trabecular bone is seen principally as a reduction in the number of trabeculae, causing an increase in the spacing of the remaining trabeculae (suggested by Weinstein and Hutson (1987) to account for two-thirds of the bone loss), while a much smaller contribution results from a decrease in the width of the trabecular profiles (Parfitt *et al* 1983, Mellish *et al* 1986, Weinstein and Hutson 1987). This is demonstrated in figure 1.3.

Some workers have suggested that as the number of trabeculae is reduced, the remaining trabecular network undergoes thickening to compensate for the loss of bone (Merz and Schenk 1970, Parfitt *et al* 1983). However, other evidence (Lips *et al* 1978) discounts this theory.

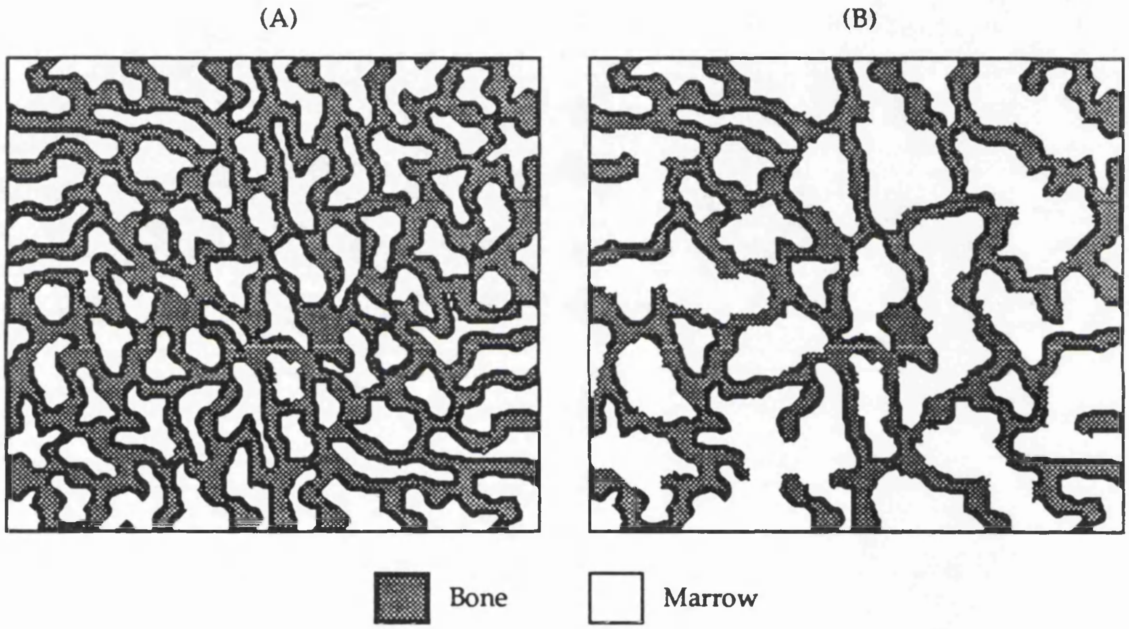

Figure 1.3 Young, healthy bone (A) shows small marrow spaces surrounded by numerous trabeculae. During osteoporosis bone is lost causing adjacent marrow spaces to join up. As a result, in osteoporotic bone (B) there is less bone and the marrow spaces are much larger. Hence, the bone becomes weaker.

The rate of loss of cortical bone in a healthy, adult woman has been reported (Mazess 1982) to start at the age 35-40 with an approximate loss in bone mass of 0.3% per year accelerating to a rate of ~0.9% per year after the age 45-50. The trabecular bone loss rate in healthy women has been reported (Cann *et al* 1985a, Pacifici *et al* 1987, Krølner and Pors Nielsen 1980) to commence around age 30 and to proceed at a rate of 1-1.2% per year.

1.4.2 Skeletal sites affected by osteoporosis

The large network of fibres in trabecular bone present a much larger surface area, on which chemical agents can act, than the area of the cortical bone. This makes trabecular bone metabolically eight times more active than cortical bone. Hence, bone resorbing agents erode the trabecular bone at a faster rate than the cortical bone. This means that the skeletal sites at greatest risk from osteoporotic fracture are those with a high trabecular content; namely, the lumbar vertebrae (~65%), the femoral neck (~50%), and the distal radius (~35%). Other skeletal regions with high trabecular content are not at load-bearing regions and so have a low fracture risk.

1.5 The diagnosis of osteoporosis

For the past 30 years a great deal of work has been focused on the development of a technique for the diagnosis of osteoporosis, and many different methods have been suggested. The essential requirement of any such technique is that the measured result has some dependence upon the degree of osteoporosis. The osteoporotic degree can be assessed in several ways. The most common is a measure of the quantity of bone mineral in a given volume; this is generally expressed as the bone density or the bone mineral content. Other less popular techniques have studied the rate of cortical thinning, the quantity of calcium within the skeleton, or the structural arrangement of the trabeculae.

An important factor in determining the usefulness of the bone measurement is the skeletal region measured.

1.5.1 Correlation between measurement sites

The status of the skeleton, in terms of structure and strength, is fairly regional as the requirements of the body on each section differ. Frequent movement and stressing of a bone causes the body to respond by strengthening that bone (Simkin *et al* 1987), so, for example, in an elderly patient great differences in bone strength will arise between an inactive femur and a frequently used skeletal site, such as the jaw. Furthermore, trends of bone loss have been found to differ at each site; loss of bone in the lumbar spine occurs mainly during the time of menopause, whereas a linear decrease occurs in the femoral neck from young adulthood to old age (Schaadt and Bohr 1988, Aloia *et al* 1990).

Correlation between skeletal sites has important implications for clinical methods which aim to diagnose osteoporosis. Such methods generally measure a small region of the skeleton, and so differences in the diseased state between skeletal regions makes the choice of measurement site crucial. The skeletal sites generally measured are those most at risk from fracture, that is, the lumbar vertebrae, the femoral neck or the distal radius. Also studies have shown (Riggs *et al* 1981, Ruegsegger *et al* 1984, Leichter *et al* 1987) that trabecular bone is a better indicator of the presence of osteoporosis than cortical or total bone, giving greater discrimination between healthy and osteoporotic groups.

Little correlation has been observed between peripheral and axial skeletal sites, Seldin *et al* (1988), for example, observed that useful predictions of the quantity of bone mineral could be obtained only for sites in close proximity. This suggests that wrist or tibia or metacarpal measurements cannot adequately predict the likelihood of vertebral or femoral neck fracture, and consequently, information on risk of fracture can only be of significant use if the status of the bone likely to fracture (i.e. lumbar spine or femoral neck) is studied (Mazess *et al* 1988a, Seldin *et al* 1988, Wilson 1977).

Whether the lumbar spine or the femoral neck is the optimal site for bone measurement is still the cause of much discussion. Measuring both could be a solution but at the cost of increasing measurement time, cost and radiation dose. Some recent reports, however, (Mazess *et al* 1988a, Meltzer *et al* 1989) have found femoral densities to show the highest diagnostic sensitivity for both spine and femur fracture, above that of spinal measurements which did not fully reflect femoral osteoporosis, and that of radius measurements which showed least sensitivity. These findings indicate that the femoral neck could be the optimum site for a single measurement.

The remainder of this section considers each of the measurement techniques proposed. They are classified in terms of the physical parameter measured.

1.5.2 Techniques for measuring the quantity of bone tissue

A full description of each of the techniques which aim to measure the quantity of bone tissue in a skeletal region is presented in a review article, to which I contributed, entitled 'Instrumentation and techniques for bone density measurement' (Speller, Royle and Horrocks 1989). Tabulations comparing the aspects of the various methods which are relevant to this thesis are presented in the following sub-sections.

1.5.2.1 Bone density measurement

The mechanical strength of a bone at a particular region is highly correlated to the quantity of bone tissue present in that region and so a loss of bone increases the susceptibility to fracture (Dalen *et al* 1976). Patients with vertebral fractures, for example, have been found to have less trabecular bone than healthy subjects of the same age (Coupron *et al* 1976). Parameters employed to define the quantity of bone tissue include the bone mass, bone density or bone mineral content (BMC). The bone density indicates the mass of bone within a given volume, whereas the BMC is a measure of the amount of the mineral calcium hydroxyapatite present in a given volume. This mineral is a constant proportion of the bone's mass, so a decrease of the mineral shows an equivalent decrease of the bone mass. Table 1.1 lists the methods currently available for measuring bone density.

Technique	Skeletal site	Radiation dose	Precision	Accuracy
Single photon absorptiometry	Radius and ulna	50µSv	1 - 2% [1-4]	2 - 4% [1-4]
Dual photon absorptiometry	Femoral neck or lumbar spine	0.15mSv	1.3 - 1.5% [5-7]	1 - 2.5% [8]
Quantitative computerised tomography	Femoral neck or lumbar spine	10mSv	1% [9-10]	6 - 9% [10-12]
Compton or Compton to coherent scatter	Femoral neck or lumbar spine	7.5mSv [13]	1 - 3% [14-15]	3% [16]

Table 1.1 Comparison of techniques for bone density measurement. The superscript numerals represent the following references; (1) Cameron *et al* (1968), (2) Christiansen *et al* (1975), (3) Christiansen and Rodbrø (1977), (4) Ringe (1982), (5) Dunn *et al* (1980), (6) Krølner and Pors Nielsen (1980), (7) Tothill *et al* (1983), (8) Peppler and Mazess (1981), (9) Hosie and Smith (1986), (10) Cann (1988), (11) Laval-Jeantet *et al* (1984), (12) Kalender *et al* (1987), (13) Mooney (1992), (14) Webber and Kennett (1976), (15) Koligliatis (1990), (16) Huddleston and Bhaduri (1978).

Photon absorptiometry is probably the most widely employed technique for bone mineral measurement. It provides a measurement of the total amount of bone mineral in the path of a photon beam. Single photon absorptiometry (SPA) (Cameron and Sorenson 1963) uses a single energy photon beam, which means that no account can be made of variation in soft tissue thickness, and so immersion of the limb in a water bath is necessary. This limits the measurement sites to the appendicular skeleton, normally the wrist. Dual photon absorptiometry (DPA) (Krølner and Pors Nielsen 1980, Peppler and Mazess 1981) was introduced to eliminate the requirement of the constant tissue thickness. The use of two separate photon energies produces two transmission equations and so allows the analysis of a two component system (i.e. bone and soft tissue). This makes it possible to study the more clinically relevant areas such as the femur and the lumbar vertebrae.

Quantitative computerised tomography (QCT) and Compton scatter densitometry have the ability to isolate the response of purely trabecular bone, as opposed to a measurement of total bone. Eliminating the cortical bone from the region that is analysed increases the sensitivity of the technique to changes in bone density.

A main cause of error in serial QCT measurements is the conversion of red marrow to the less dense, yellow marrow within the trabecular spaces, which can produce an artificially low estimate of the quantity of bone mineral within the trabecular region (Mazess 1983). Dual energy QCT (Genant and Boyd 1977) can potentially resolve this problem; the use of two x-ray beams of different kV_ps enables two parameters to be evaluated such that the quantity of marrow fat as well as that of trabecular bone can be determined. This technique can achieve accuracy of 3 - 6% (Cann 1988) but at the expense of almost twice the radiation dose.

The main disadvantages of QCT are the huge cost of purchasing the machine and a radiation dose to the patient of ~10mSv. The use of isotope sources, such as Iodine-125 (Ruegsegger *et al* 1981, Hosie *et al* 1985) and Gadolinium-153 (Boyd *et al* 1982), rather than x-rays can reduce the radiation dose to the patient due to the lower photon flux, but the lower flux also restricts examinations to small volumes such as the radius and ulna.

1.5.3 Other techniques for measuring bone mass

Table 1.2 summarises other methods which have been proposed for determining the quantity of bone tissue at a skeletal site.

Technique	Parameter	Skeletal site	Radiation dose	Precision	Accuracy
Radiogrammetry	Thinning of cortical bone	Metacarpals	~0.4mSv	~5% [1-2]	1.5% [3]
In-vivo neutron activation analysis	Total or part body calcium content	All or part of skeleton	6.4 - 20mSv [4-6]	1 - 3% [6-8]	5% [9]
Broadband ultrasonic attenuation	Ultrasonic attenuation vs. frequency is material dependent	Os calcis (heel)	N/A	1.4% [10]	Not reported

Table 1.2 Comparison of bone measurement techniques. References cited are the following; (1) Virtama and Helela (1969), (2) Andresen and Nielsen (1986), (3) Horsman and Simpson (1975), (4) Cohn *et al* (1970), (5) Nelp *et al* (1970), (6) Cohn *et al* (1972), (7) Kennedy *et al* (1982), (8) Nicoll *et al* (1987), Nelp *et al* (1972), (10) Langton *et al* (1984).

Radiogrammetry provides an indication of the bone status by measuring the decrease in thickness of the cortical bone from radiographs (Barnett and Nordin 1960, Virtama and Mahonen 1960). The advantages of this technique are that it is a simple, cheap, widely available technique which gives only a low radiation dose to the patient's hand. Its' usefulness is limited by its inability to quantify any change in trabecular bone. There is also little evidence as to how cortical thinning in the metacarpal correlates with bone loss in the more clinically relevant areas of the skeleton.

Neutron activation analysis is a technique for determining the absolute quantity of a particular element within the body, which in the case of bone measurements is calcium. The neutron flux required for activation is provided by either a neutron generator, a cyclotron or an array of ^{238}Pu, Be sources, all of which are expensive and not widely available. The biggest disadvantage, however, is the high radiation dose received by the patient during a measurement.

The technique of broadband ultrasonic attenuation works on the principal that the degree of attenuation is tissue dependent. This means that rarefied bone tissue will lead to a different response when compared with normal, healthy bone tissue. The requirement of a bone with approximately parallel faces restricts measurement to the os calcis. The main advantage of this technique compared to other methods is the fact that the patient is not exposed to ionising radiation.

1.5.4 Techniques for quantifying trabecular structure

Resistance to fracture depends upon the spatial arrangement and form of each structural element (Merz and Schenk 1970, Parfitt *et al* 1983, Haddaway *et al* 1988) as well as on the quantity of bone tissue present. Kleerekoper *et al* (1985) observed that an equivalent amount of bone distributed as widely spaced, disconnected, thick trabeculae is biomechanically less competent than when distributed as numerous, connected, thin plates. Hence, biomechanically competent trabecular bone forms a stable framework in which the size, shape, quantity, orientation, distribution, and connectivity of the structural elements (the trabeculae) meet the strain demands, with the force being exerted axially on each crossbar (Pugh *et al* 1974).

Various workers have tried to develop techniques for assessing and quantifying the spatial distribution and microstructure present in trabecular bone. This has principally been for research purposes in order to improve the understanding of the cellular mechanisms of bone disease, and also to assess whether detailed structural information can improve the accuracy in the diagnosis of osteoporosis over that of bone density measurements.

This section considers the techniques which have been devised. They primarily consist of two basic divisions; those which are performed *in-vitro* on bone obtained from biopsy, and non-invasive methods.

1.5.4.1 Microscopic analysis of bone biopsy specimens

Quantification of a complex, three-dimensional microstructure, such as trabecular bone, is a difficult problem. This has been simplified, however, by optimising the information available in two-dimensional sections and employing the principles of stereology, which require only that perimeter and area measurements are made on the structures in a two-dimensional section with a calibrated measuring device (Merz and Schenk 1970, Parfitt *et al* 1983).

Parfitt *et al* (1983) described a technique for studying transiliac bone biopsies. The bone samples were sectioned into thin (5μm) slices and stained to improve contrast. Trabecular bone area as a fraction of total trabecular tissue area (marrow and bone) and the perimeter of marrow-bone interface were measured in the same microscopic field either by counting point hits and line intercepts with an eyepiece graticule or by a digitising system in which the image of the bone is projected onto a digitiser tablet allowing the outline of the trabeculae to be traced with a cursor. All measurements were made at a total magnification of x25.

Several three dimensional quantities were obtained from the primary two dimensional area and perimeter length measurements. The most useful parameters were the mean trabecular plate thickness (MTPT) and the mean trabecular plate density (MTPD). Trabecular bone consists mainly of interconnecting plates so to assist visualisation the trabecular bone volume (TBV) is partitioned into an index of the thickness of individual plates (MTPT) and an index of the number of plates (MTPD), as follows

$$\mathrm{TBV} = \mathrm{MTPD} \times \mathrm{MTPT} / 10$$

MTPD is defined as the reciprocal of the mean distance between structural bone elements.

The results obtained gave useful information on the structural changes in bone. For example, a small increase in trabeculae separation was observed with ageing in normal subjects compared with a larger increase in separation together with a small reduction in plate thickness observed in the subjects with non-traumatic vertebral compressions and hip fractures.

An improvement to this method was made by Weinstein and Hutson (1987). An image analysis computer and digitiser tablet were used to simultaneously determine the trabecular area and perimeter of the iliac biopsy specimens. Computer software identified the trabecular boundaries and then calculated the relevant parameters. The software operations of a computer based image analysis system such as this are described in detail by Browne *et al* (1987).

A major disadvantage of this technique is its inability to make any measurements *in-vivo*. Only *in-vitro* studies are possible. This reason also limits the areas which can be investigated to the iliac crest, a site of little clinical relevance.

1.5.4.2 Non-invasive techniques for measuring trabecular structure

Feldkamp *et al* (1983) used high resolution computed tomography to investigate the three dimensional structure of transiliac bone biopsy cores. A microfocus x-ray source was employed. Direct reconstruction from a series of two-dimensional projections enables a three-dimensional density profile to be generated, from which the usual structural parameters can be extracted. Durand and Ruegsegger (1991) developed this technique to perform structural measurements *in-vivo* on the radius and tibia.

The use of magnetic resonance to investigate trabecular structure has been reported (Ford and Wehrli 1991, Wehrli *et al* 1991). Direct detection of bone mineral by NMR has been unsuccessful because of the low proton density of bone and the very short proton relaxation times in a solid. The technique proposed employs the fact that the two physical phases (bone and marrow) cause a magnetic field distribution across the imaging voxel. This results in a spread of resonance frequencies from which a measurement of the decay rate of the signal intensity can be obtained. The time constant for the decay has been found to increase slightly with age in healthy subjects. For osteoporotic subjects, however, the decay times are prolonged. This is thought to arise from an increase in the inter-trabecular spacing.

1.6 Clinical diagnosis: the 'fracture threshold'

In theory osteoporosis could be diagnosed in a patient if the rate of bone loss is significantly lower than the average rate for an age-matched healthy subject. It was proposed (Nordin 1987, Ross *et al* 1987) that for a patient of a particular age a 'fracture threshold' could be set, that is, a level of bone mass below which fracture will occur. However, in reality, regional differences among bones and wide diversity among different subjects produces a wide range of values for bone mass which prevents a fracture threshold from being uniquely defined (Mazess 1987).

Hence, the discrepancy exists in bone density measurements in that subjects can have equal bone mass yet some are osteoporotic and some are not (Riggs *et al* 1982, Cann *et al* 1985b). In some cases healthy subjects have been found to have significantly lower bone density than age-matched osteoporotics. No clear discrimination between healthy and osteoporotic subjects exists within the measurements. This presents a lot of doubt as to when a person can be classified as having osteoporosis. If a postmenopausal woman has a rate of bone loss significantly above the average for normal women of the same age then it is probable, but not definite, that she has osteoporosis. It can be said, however, that the greater the rate of bone loss above the average rate, the greater the probability of osteoporosis being present. Conversely, if the rate is below average then there is less chance of osteoporosis, but it is still possible. Thus early diagnosis becomes rather more probabilistic than definite.

A variety of contributory factors cause the lack of discrimination between healthy and osteoporotic subjects, such as regional differences among different parts of the skeleton, the wide-ranging diversity among individuals, an increase in the porosity of cortical bone with ageing (Dickenson *et al* 1981) and an accumulation of microfractures with ageing, particularly in the middle third of vertebrae (Vernon-Roberts and Pirie 1973). The main contributing factor, however, is thought to be the spatial arrangement and orientation of the trabeculae within trabecular bone (Weinstein and Hutson 1987).

1.7 Conclusions on bone measurements: requirements of a technique

A study of the literature presented on the techniques previously proposed has highlighted several points;

(i) Precision : At present the only technique in general use for diagnosing osteoporosis is the identification of a vertebral crush fracture or fracture of the femoral neck or distal radius from radiographs. By this time the patient is in considerable discomfort and surgery is required. Various workers have reported that bone loss can be prevented, or at least greatly reduced by hormone replacement therapy. For example, calcitonin, a hormone produced by the thyroid gland, exerts a direct action on bone resorption, causing the levels of plasma calcium to be lowered. Reports have also indicated that lost bone can be replaced by the use of agents stimulating bone formation, such as sodium fluoride or anabolic steroids (Chesnut 1988). However it has been suggested that this restorative therapy will only act to increase the thickness of existing trabeculae, without replacing the trabeculae which had been resorbed and so will not greatly increase the mechanical strength of the bone.

These reports lead to the conclusion that for therapy to be successful in fracture prevention early diagnosis is essential. As seen previously the average loss rate of trabecular bone in normal women is 1-1.2% per year, and only 0.9% per year in cortical bone. Current methods for measuring bone mass determine the rate of loss in a patient from several successive measurements of bone mass at regular intervals (often ~6 months). Hence, the average decrease in bone mass over many measurements gives an indication of the loss rate. Then, a decision can be made over whether the loss rate is greater than normal indicating whether or not the patient is osteoporotic.

The precision of a technique can be defined as the reproducibility of its results. A value for the precision is found by the variation in the results of repeat measurements. It is generally expressed as the percentage the variation forms of the mean value. The measurement technique needs to be sufficiently precise to resolve the small changes in bone that occur between successive serial measurements. So for a technique to measure a loss in bone of only 0.6% (i.e. the average decrease in bone mass over a 6 month interval) with any degree of certainty it needs to have a percentage precision better than this value.

Techniques which can focus on the trabecular region for measurement have less of a limitation on their precision requirements than those which measure the total bone (such as DPA). This is because the rate of trabecular bone loss is greater than that of the total bone and so bigger differences will be seen in the former between serial measurements.

(ii) Measurement site: Bone measurements which can usefully predict the presence of osteoporosis must be made at sites of clinical relevance to the disease. Furthermore, lack of correlation of peripheral sites with the condition of the rest of the skeleton prevents areas such as the radius from predicting fracture at other skeletal sites. Therefore, the optimum sites are the lumbar spine or the femoral neck. No conclusive decision has, as yet, been reached as to which provides the best indication. The site chosen for measurement in this project is the femoral neck. The reasons being that;

(a) it generally has less surrounding soft tissue to attenuate the beam,

(b) the trabecular body of the spine is surrounded by thick cortical regions which form a hard, protective arch around the spinal cord. The shapes of these articular lobes are irregular and so could prove problematic in correcting for beam attenuation.

(c) The leg is a less radiosensitive part of the body than the abdomen.

(ii) Trabecular measurement : Trabecular bone, due to its higher metabolic rate, is a better indicator as to the presence of osteoporosis than either cortical bone or total bone, giving greater discrimination between healthy and osteoporotic groups.

(iii) Cost : To successfully reduce and possibly eliminate the threat of osteoporosis it would be desirable to screen the entire population of postmenopausal women. Hence, the cost of producing the measurement apparatus and the cost of operating it on such a large scale will probably ultimately decide which technique is to be employed.

(iv) Patient safety : Many of the techniques that have been suggested to diagnose osteoporosis employ ionising radiation. Thus, the level of radiation dose imparted to the patient is an important factor, particularly if the region irradiated is especially radiosensitive (such as parts of the lower abdomen).

A new technique has been developed which has proved over the course of this project to be capable of providing information on the osteoporotic degree of trabecular bone. This technique will be the focus of attention for the remainder of this thesis. The following sections of this chapter will introduce the technique, discuss its application to the tissues and diseases mentioned previously and review related investigations in this field. The succeeding chapters provide a theoretical description of this technique, describe in detail the method employed, and finally present and discuss the results obtained. Particular emphasis is given in the discussion to the usefulness of the technique in clinical applications.

1.8 Elastic photon scattering

The main aim of this project was to determine whether information could be obtained on the osteoporotic state of bone tissue from the photons elastically (or coherently) scattered from the bone in an extension of the x-ray diffraction technique. At diagnostic x-ray energies elastic scatter occurs to small angles; the probability of coherent scatter to angles greater than ~12° is very small. Measurements of scattered photons commonly concentrate on the inelastic Compton scatter due to the probability of its occurrence being much greater than that of coherent scatter. Experiments to measure transmitted photons generally go to great lengths to prevent scattered photons in the forward direction (i.e. coherent) from being recorded, for example, by the use of anti-scatter grids, fine collimation, etc. Hence, in most radiological measurements, coherently scattered photons are either ignored or discarded.

The technique of elastic photon scattering focuses a finely collimated beam from a diagnostic x-ray tube on the region of interest. Coherent interactions occur within the object, scattering photons in the forward direction. A finely collimated, energy-dispersive photon detector, either positioned at a given, small (<10°) fixed angle to the incident beam or scanning from 0 to 10°, records the scatter (diffraction) pattern. At small angles, interference effects cause peaks at certain momentum transfer values; the fact that the values are dependent upon atomic and molecular spacings means that the scattered pattern is unique for a particular material.

The general physical principles behind this technique are those of x-ray diffraction. Differences occur between this technique and standard x-ray diffraction because of the constraints of *in-vivo* clinical measurement. These constraints will be discussed in detail in § 3.1, but basically the important differences are the wavelengths of the incident x-ray beam and the size of the measured object. Very short wavelengths are required in clinical work due to the thickness of tissue the x-rays need to penetrate, these wavelengths are in general several times smaller than typical x-ray diffraction wavelengths. Such short wavelengths compress the diffraction pattern into the small angle range (≤10°). The diameter of a patient is considerably greater than the very small samples in conventional diffraction, this leads to problems such as overlap of information, beam hardening and multiple scatter; the effects of which need to be assessed and, if necessary, resolved.

1.9 X-ray diffraction

X-ray diffraction occurs due to the interference of elastically scattered photons (a full description is given in chapter 2). The information provided by this effect has proved invaluable over the years and has a great number of applications. Crystallography, for example, utilises the information present following the diffraction of an x-ray beam by a crystal to determine the structural arrangement and orientation of the atoms and molecules within a material. It is used to study the structure of crystalline substances in which the structural elements are of a similar order of magnitude to the wavelengths of the incident x-rays. The most common crystallographic techniques use the monochromatic copper k_α line at 1.542Å.

The following briefly reviews some of the applications of x-ray diffraction most relevant to this project.

1.9.1 Small angle x-ray scattering

Small angle x-ray scattering (SAXS) is a technique developed from conventional x-ray diffraction in an attempt to study structural features of much greater dimension (see Glatter and Kratky 1982). SAXS is capable of measuring features between tens and several thousand Angstroms in size. This is very large in comparison with the x-ray wavelength. Therefore, as the scattering process is characterised by an inverse relationship between particle size and scattering angle (see Bragg's law in § 2.1), this compresses the observable diffraction pattern to small angles. In this respect SAXS is similar to the technique employed in this thesis. However, the main difference is that the elastic photon scattering technique of this thesis is not used to investigate the internal structural arrangement of the tissues, but determines the components present and their relative proportions.

The apparatus for SAXS experiments is generally the Kratky camera (Kratky 1982), shown in figure 1.4. This consists of a finely collimated, monochromatic x-ray beam (usually the Cu k_α line at 1.542Å, equivalent to 8.04keV) focusing on the object. The intensity of the scattered photons are recorded by a photon detector (either solid state or a gas filled proportional counter). During a measurement, the detector rotates very slowly around the object from zero to a few degrees. A single measurement can take several hours in order to obtain a high photon count and, hence, a very small statistical error.

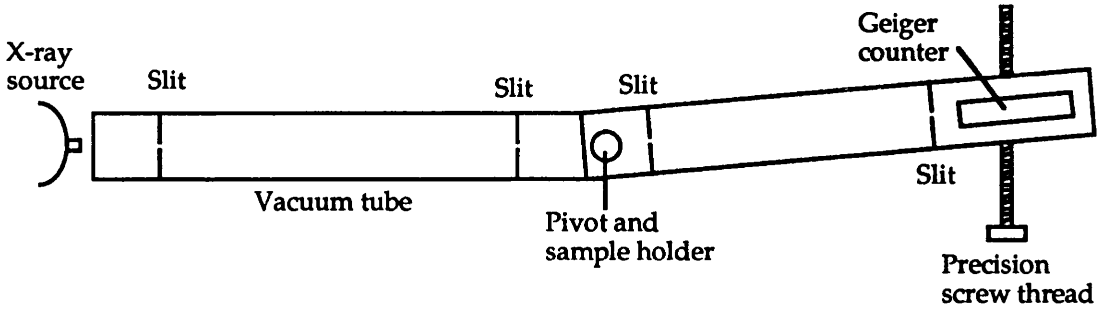

Figure 1.4 Apparatus for small angle x-ray scattering experiments. The x-ray beam enters a mica end window and is collimated by tantalum slits. The apparatus is enclosed in air tight cylinders and operated under vacuum.

The distances from source to object and object to detector are generally several metres in length. This, together with very fine collimation, leads to great accuracy in the angular resolution. The very narrow collimation focuses on a very small region within the object to avoid loss of information from structural differences at different regions. This technique achieves an extremely precise measurement of a small angle diffraction pattern. Figure 1.5 shows the general shape of a small angle diffraction pattern. The position and intensity of the maxima and the slope of the tail give information on the internal structure of the substances it is studying.

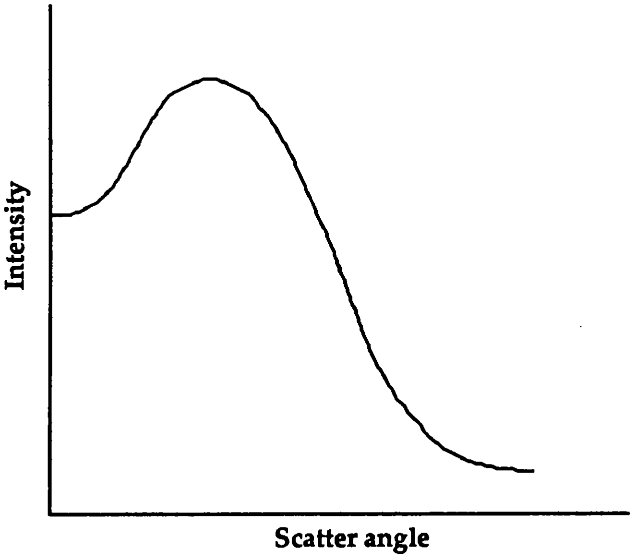

Figure 1.5 A typical small angle diffraction pattern.

SAXS is generally used to perform micro studies on samples, for example, investigating the size and structure of large proteins and other biological molecules of similar magnitude, looking at the effect of stress and strain on the structural arrangement of synthetic polymers, studying irregularities and stress fractures in metal, etc.

1.9.2 Quantitative diffraction analysis

X-ray diffraction has proved very useful for the identification of unknown substances in a sample. Generally a diffraction pattern is obtained by irradiating a small, powdered sample of the substance with the monochromatic output from a copper x-ray tube. A rotating detector records the photon intensity as a function of angle. In order to determine the substances present a peak search is performed on the measured pattern and then a database of x-ray diffraction patterns of known substances is scanned in order to determine which materials cause the peaks. The relative heights of the diffraction peaks are related to the proportion of the substance within the material to which the peaks correspond. Hence, quantitative analysis can be performed to determine the percentage composition of a material. Further details of this are given in § 2.9.

1.10 Review of biological applications for coherent scatter measurement

The use of coherent scatter in radiological studies of biological tissues has primarily been restricted to the measurement of the Compton to coherent scattering ratio for the purpose of bone density measurement. In this case the ratio of the intensities of the two peaks is utilised in order to eliminate the surrounding soft tissue effects.

A review of other applications of coherent scatter, mainly for the purpose of material characterisation, is presented in the following:

Muntz *et al* (1983) obtained x-ray diffraction patterns of the tissue substitute materials Lucite, polyethylene and water. A collimated 45kV$_p$ x-ray beam from a tungsten tube was incident on a slab of the phantom. A collimated high purity Germanium detector, connected to a pulse height analysis system, was swung in an arc around the phantom to generate data at various angles (see figure 1.6).

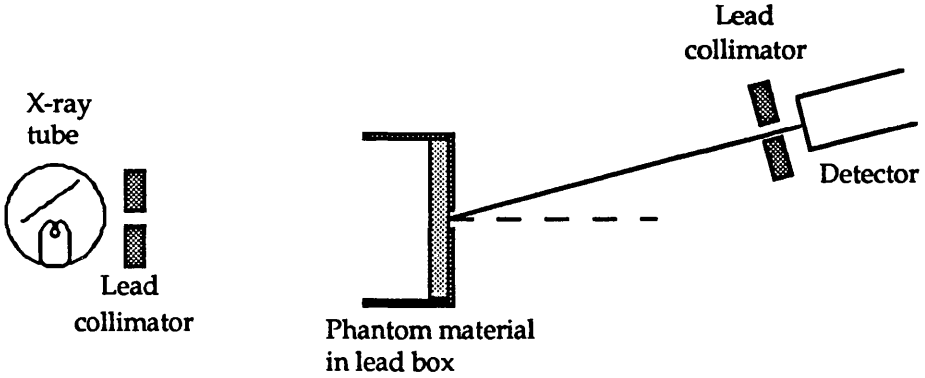

Figure 1.6 Experimental set-up of Muntz *et al* (1983). 5mm circular apertures in lead formed the collimators. The source to object distance was 105.5cm, and the object to detector distance was 44.5cm.

Curves were plotted of the normalised intensities versus scattering angle for each material. Figure 1.7 shows a plot of normalised intensities versus angle for three materials measured for this thesis using a similar technique to that of Muntz and co-workers. Two of the materials are different but this graph is very similar to the result obtained by Muntz and demonstrates the sort of results that are obtained with this technique. The greatest differences between the various materials are the positions and the widths of the peaks. These parameters were employed to characterise the materials.

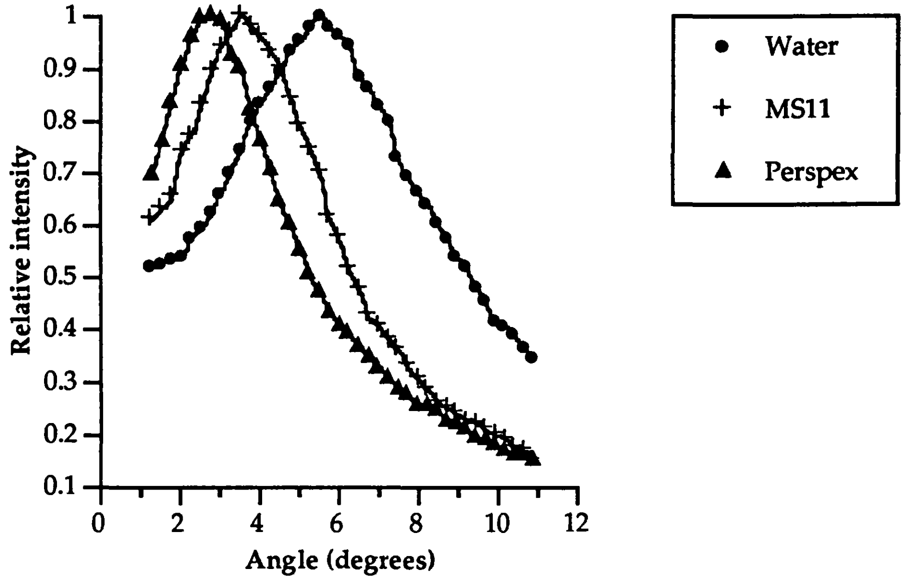

Figure 1.7 Plot of normalised intensity vs. scattering angle for three materials; water, perspex and MS11 (an epoxy resin based muscle tissue substitute). This graph was obtained using the apparatus described in chapter 3 and the method of Muntz *et al* (1983).

A similar study was performed by Bradley *et al* (1988) this time using a monoenergetic source. The total differential scattering cross section was measured for an incident photon energy of 59.5keV (^{241}Am isotope source) and at 1° intervals in the angular range 2 - 10°. The photon beam before the target was defined using an annular collimator and the scattered photon field was limited by a further annular collimator. The target materials were water, nylon and Lucite. The results obtained were similar to those of Muntz *et al* (1983) and the authors reported them to clearly demonstrate the contribution of intermolecular effects to the scattering process.

Evans *et al* (1991) used a similar technique for the study of breast tissue. The photon intensities scattered to the 2 - 12° angular range were measured. Detection was performed using a position sensitive multiwire proportional counter, see figure 1.8. A copper anode x-ray tube provided the photon source, filtration was employed to reduce the energy spread of the incident beam.

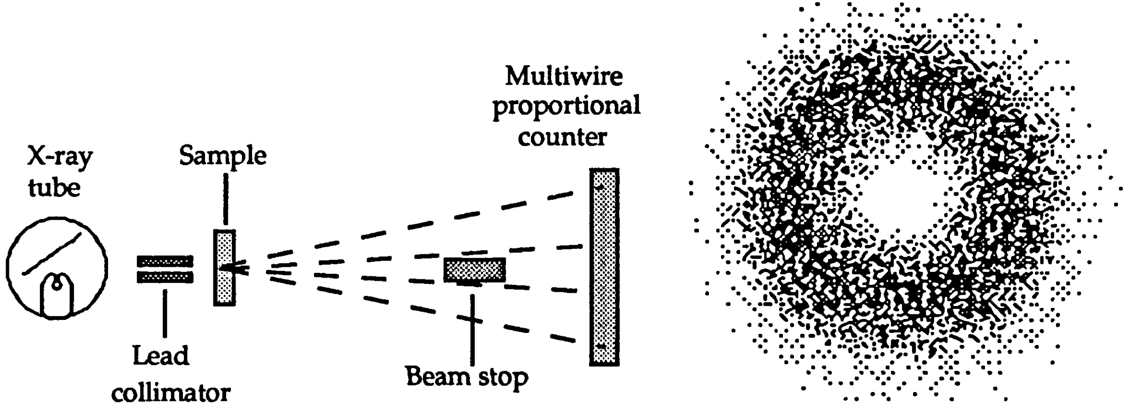

Figure 1.8 Diagram of the apparatus of Evans *et al* (1991) and a typical result showing a halo-like photon intensity distribution. Source to object distance was 20cm and object to detector distance was 28cm.

Water, adipose and breast tissues were measured in small diameter samples. All produced a halo-like photon intensity distribution (which when plotted as a function of angle were similar in shape to those in figure 1.7), yet the positions and widths of the distributions showed some variation.

Newton *et al* (1992) used x-ray scattering to study bone composition. Copper k_α rays (energy 8keV) were focused on a slab of the specimen. The scattered intensity distribution was recorded on x-ray film and the optical density along a diameter of the scattering pattern measured. The results indicated that x-ray scattering measurements are correlated with the ratio of adipose tissue to mineral in bone.

Harding *et al* (1987) employed x-ray diffraction for the purpose of tissue discrimination and material characterisation. The technique used was termed x-ray diffraction computed tomography, a method similar to conventional CT. A single pencil beam CT scanner was used with an array of 61 scintillation detectors arranged beneath the object to spatially resolve the scattered photons. This allowed small angle coherent scatter to be measured in addition to the transmitted radiation, such that a diffraction pattern could be constructed. Various projections are taken, as in CT, and algebraic reconstruction techniques are applied to form an image. The diffraction properties of a stack of 2-D object sections may be imaged. The diffraction patterns of some biological tissues, such as fat, muscle, bone, liver, etc., were obtained (Kosanetzky *et al* 1987). The patterns showed a variety of maxima of different widths and intensities (the same as a standard x-ray diffraction pattern). The shapes of the patterns were different for each material, thus allowing tissue discrimination. Harding *et al* (1990) reported a variation on their tomographic imaging technique system which employed a fixed angle of scatter (3.6°) and energy dispersive solid state detectors. A feasibility study performed on simple phantoms demonstrated this approach to be equally valid to their multiple angle technique.

All of these techniques are potentially capable of tissue characterisation but they have been performed under conditions that are unlikely to be suitable for clinical operation. This is either due to the energy of the x-ray source being too low, which would lead to heavy attenuation of the beam on traversing the patient, or a scanning detector system, which requires a long x-ray exposure thus giving a large dose and evoking the problem of patient movement.

1.11 Outline of the thesis

Chapter 1 has given all of the relevant clinical information concerning osteoporosis. A review of previous work for the diagnosis of the disease has been presented such that all the necessary requirements for a diagnosing technique can be determined. At the end of the chapter the technique proposed in this thesis for diagnosis was introduced.

Chapter 2 serves to provide a theoretical explanation of the way in which the information in the results relates to the material studied. Methods for quantitatively analysing the scatter patterns produced are also described.

Chapters 3, 4 and 5 are concerned with obtaining the scatter pattern results. Chapter 3 describes the relevant technical information for measuring the patterns, while chapters 4 and 5 consider the factors which degrade the patterns and discuss the correction procedures.

The results obtained, particularly those concerning the tissues and diagnosis, are presented and discussed in chapter 6.

Chapter 7 presents some work on the application of this technique to the characterisation of gallstones. Finally the conclusions are discussed in chapter 8.

- 2 -

The theory of elastic photon scattering

For many years x-ray diffraction has proved an invaluable tool in the determination of the internal microstructure of solid materials. In 1912 Laue, attempting to demonstrate the wave motion of x-rays, demonstrated that crystals would diffract x-rays. A clear interpretation of these results was presented in the following few years by the Braggs which led to the development of x-ray diffraction as a means for studying the internal structure of crystals. Since then a great many workers have refined and developed this technique, applying it to a large range of substances, not just a regular crystal lattice, for structural investigation. This chapter provides a theoretical description of the principles of x-ray scatter and diffraction relevant to the project.

2.1 Coherent scatter

If an x-ray photon enters a material it can either pass through undeviated, be absorbed and deposit all of its energy, or be scattered to a new direction. The scatter can be either inelastic, in which a fraction of the photons energy is imparted to the scattering site, or elastic, in which no energy transfer occurs. Photon interactions in the diagnostic energy range (<150keV) are dominated by three processes; coherent scatter, Compton scatter and the photoelectric effect. Firstly a mathematical description of coherent scatter, the process which can lead to diffraction, is given. A description of Compton scatter and photoelectric absorption, together with a discussion of photon attenuation is given in appendix 1.

Coherent (or Rayleigh) scatter is the elastic scatter of a photon by an electron. The diffraction effects under investigation are caused by the interference of elastically (or coherently) scattered waves, hence this process is of great importance in this project. For an elastic collision to occur the electron must be bound to the atom such that the photon momentum can be taken up by the whole atom (which has relatively large mass). Due to the increase in electric charge the electrons appear more bound as the atomic number increases, and so enhances the degree of coherent scatter. Also the incident photon wavelength must be greater than the electron spacing, hence, the probability of coherent scatter is greater at low energies.

The incident photon causes excitation of the bound electron, which then emits a photon of equivalent wavelength, thus returning the electron to its original state. The permissible coherent scattering angles are always small because the recoil imparted to the atom must not produce atomic excitation or ionisation.

The differential cross-section per unit solid angle for coherent scatter is given by

$$d\sigma_{coh}(\theta,\alpha,z) / d\Omega \;=\; [\,F_{coh}(x, z)\,]^2 .\; d\sigma_T(\theta) / d\Omega \qquad (2.1)$$

and

$$d\sigma_T(\theta) / d\Omega \;=\; 1/2\; r_e^2\,(1 + \cos^2\theta\,) \qquad (2.2)$$

that is the differential Thomson cross section per electron for elastic scattering of an unpolarised beam, where

$r_e \;=\; e^2 / (4\pi\varepsilon_0\, m_e c^2)$, the classical electron radius (2.3)

and $x \;=\; \sin(\theta/2) / \lambda$, the momentum transfer (2.4)

where the constant k has a value 29.1445 and $\alpha = h\nu_0 / mc^2$, $h\nu_0$ is the incident photon energy.

The factor $F_{coh}(x, z)$ is the coherent atomic form factor used to correct the Thomson distribution. The square of this quantity is the probability that the z electrons of the atom take up the recoil momentum without absorbing any photon energy. The form factor accounts for the wave interference between scatterings from different electrons.

The form factor is of great importance for this thesis as it quantifies the wave interference occurring within the material.

2.2 Coherent scatter form factors

When the angle between the incident radiation and the direction of scatter is zero in a free atom there will be no phase difference between the waves and the resulting wave will have the maximum possible amplitude (see figure 2.1). As the scattering angle increases the waves from the outer electrons will gradually get out of phase. The contributions of these waves then start to interfere destructively causing a diminution of the amplitude of the resultant wave. Hence, the diffracted intensity of an element peaks at zero degrees and falls off as the scattering angle increases. A mathematical description of this effect is provided by equation

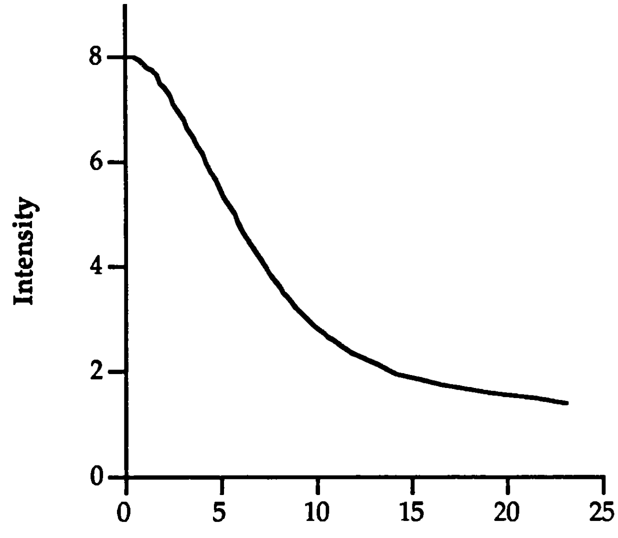

Figure 2.1 The variation of diffracted intensity with scattering angle for a free oxygen atom.

(2.1), the product of the differential Thomson scattering cross-section and the square of the coherent form factor.

Thomson scattering is described as the scattering of x-rays without change of wavelength. The Thomson cross-section for one "free" electron, given by

$$\sigma_T = e^4 /(6\pi\varepsilon_0 m_e{}^2 c^4)$$

represents the target area for removal of energy from the electromagnetic wave by one electron. It is calculated from a consideration of the electrostatic field of the electron. The cross-section for an atom is simply Z times the one electron cross-section. The differential cross-section for a free electron, given by $(1+\cos^2\theta).r_e{}^2 / 2$, decreases continuously from 0 to 90° (see figure 2.2).

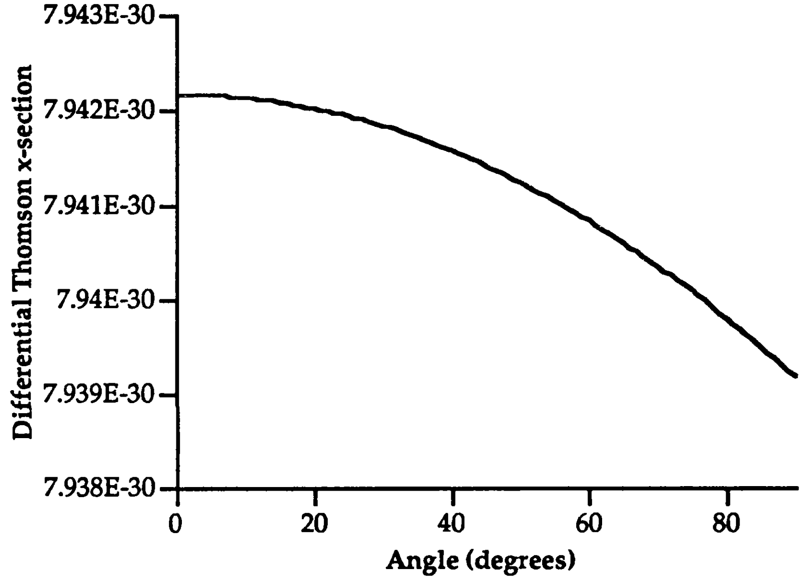

Figure 2.2 The differential Thomson scattering cross-section.

The atomic form factor F(x) describes the deviation of the elastic scattering process for a given atom from the free electron case. It accounts for the wave interference between scatterings from different electrons and is, therefore, dependent upon the spatial distribution of the electrons within the irradiated volume. The free atom form factors for each of the elements over a wide range of momentum transfer values are tabulated in Hubbel *et al* (1977). The data were calculated from a theoretical description of the atom based on a Hartree-Fock model.

The data provide a close approximation to experiment for elements in the free atom case. Previously form factor data for molecules has been calculated by combining the free atom data weighted according to the elemental composition of the molecule, however, recent evidence (Johns and Yaffe 1983, Morin and Berroir 1983) has shown that the data obtained in this way do not provide good approximation in the molecular case. A significant difference exists at small scattering angles between the differential cross section data for molecules calculated from the theoretically evaluated form factors (of Hubbel *et al* 1977) and that determined experimentally. The theoretical form factors calculated for molecules indicate that coherent scatter is forward peaked with a maximum seen at zero scattering angle, whereas experimentally measured data shows the coherent scattering probability to have a maximum at a non-zero scattering angle (i.e. a few degrees). At zero degrees there is almost complete destructive interference. The diffraction effects are more complex for molecules than for the free atom case due to the large number of different scattering sites in close proximity.

Figure 2.3 shows a comparison of form factors for water calculated using the theoretically evaluated form factors of Hubbel *et al* (1977) and those determined experimentally (Morin 1982). The theoretical set were calculated using the mixture rule;- $2[F_{coh}(H)] + [F_{coh}(O)]$, where F_{coh} is the coherent form factor. The square of this value is used in the calculation for differential cross section. The data of Morin (1982) presents tabulations of molecular form factors for water at various temperatures, they were calculated from experimentally measured x-ray diffraction data of Narten and Levy (1971).

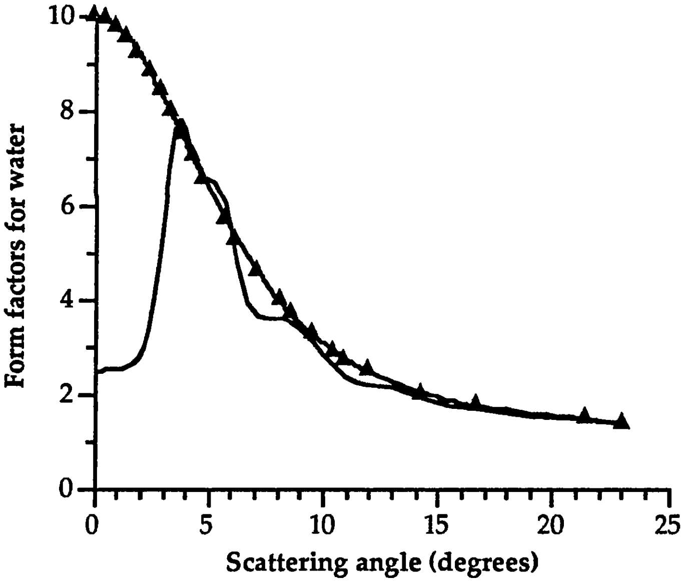

Figure 2.3 Comparison of experimentally measured form factor data (the smooth line) and data calculated from the theoretically obtained form factors (marked by the triangular points).

From this we can see that above ~12° the theoretical data provides a good simulation of the experimental data, but below this great differences exist. The reason for the discrepancy is that the coherent scattering process gives rise to interference effects which are not accounted for in the theoretical model.

The form factor term can be divided into an atomic form factor for isolated atoms, f(x) (the data of Hubbel *et al* (1977)), and an interference function for interatomic effects, s(x), where x is the momentum transfer;

$$F(x) = f(x) . [s(x)]^{1/2}$$

The interference function s(x) strongly correlates with the degree of order within the molecular structure. A dilute gas, for example, approximates the free atom case, so there is no interference and s(x)=1. Whereas a perfect crystal, possessing a highly ordered structure, shows a number of sharp peaks for s(x). As x increases the amplitude of the oscillations greatly decreases and F(x) is closely approximated by the free atom case f(x). This is clearly demonstrated by the comparison of the experimental and the theoretical values (figure 2.3) in which theory approximates the experiment at larger angles.

Johns and Yaffe (1983), and also Morin and Berroir (1983), demonstrated that for a given material the form factor can be evaluated at three levels of complexity, depending on the extent of the inter-electron interference considered:-

(i) consider only the interference between scattering from electrons in the same atom,

(ii) include also the interference between electrons of different atoms belonging to the same molecule,

(iii) take into account the additional effects of interference between molecules.

The third level of complexity involves the more rigorous calculations and provides the closest approximation to the true case. The form factors in this case can, in theory, be calculated from an electron distribution which is the convolution of the distribution of electrons within individual molecules with the distribution of the position and orientation of the molecules relative to one another. This requires knowing certain properties of the molecule, such as the intermolecular distances and the shape of the molecule. The calculations are greatly simplified by the molecule being spherical, or approximately spherical, because orientation of the molecule then causes little variation. Such calculations have been performed by Blum *et al* (1971) to determine the form factors for fluids with nearly spherical molecules, such as water. However, this project is concerned with body tissues, the molecular structures of which are very complex and do not approximate a sphere. Hence, this eliminates the possibility of theoretically calculating form factors for body tissues.

To conclude, this clearly indicates that in order to achieve a mathematical model of coherent scatter within a molecular or crystalline substance that would have accuracy at small scattering angles, at which coherent scatter is most likely, it is essential to use form factors calculated from experimentally measured x-ray diffraction data. Otherwise the contribution of coherent scatter is greatly overestimated in the forward direction.

2.3 X-ray diffraction

2.3.1 The Bragg construction

The most familiar description of x-ray diffraction is that given by the Bragg construction (see for example James 1948). It is used in crystallography to determine the separations of crystal planes which produce x-ray diffraction lines or spots observed at certain angles. Consider the crystal as a lattice of discrete atoms. A beam of x-rays incident on the crystal will cause the scattering centres to resonate with the frequency of the x-rays and emit secondary waves in phase with the incident waves (elastic scatter), other forms of interaction will also occur. Each atom becomes the source of a scattered wave. Figure 2.4 shows waves scattered from atoms on adjacent planes within the crystal lattice.

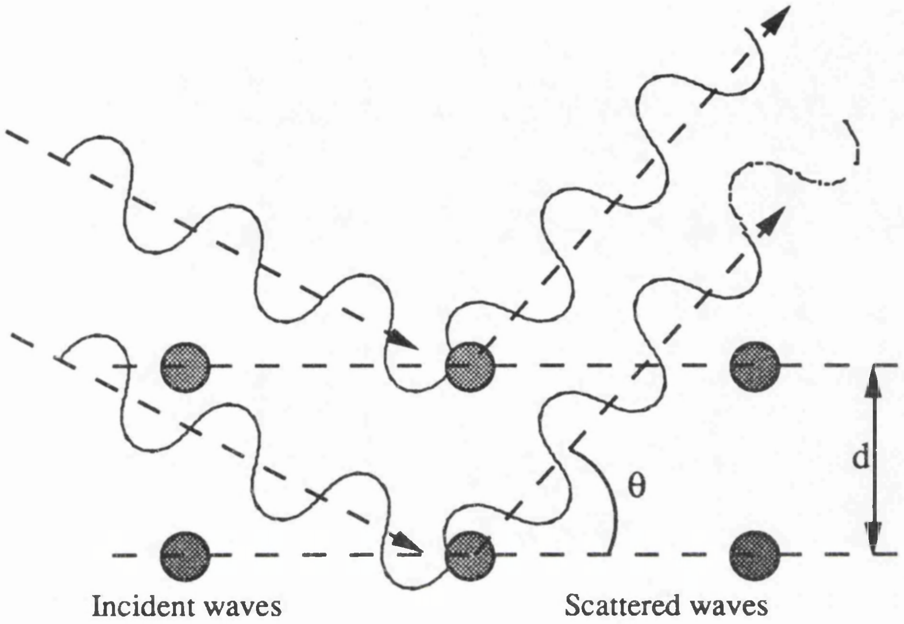

Figure 2.4 Incident waves are scattered to angle θ by atoms in adjacent planes with separation d. The scattered waves are exactly in phase.

The amplitude of the beam in any direction is then obtained by summing the contributions in that direction from each atom, taking into account the phase difference between them (Huygens principle of superposition). For a given plane separation d certain scatter angles θ will occur at which the waves in that direction are exactly in phase, therefore, superposition of the waves will occur to increase the wave amplitude; termed *constructive interference*. Scatter angles at which the waves are not in phase *destructive interference* is said to occur. A simple geometric consideration of figure 2.4 will show that for constructive interference to occur the following condition must hold

$$2\,d\sin\theta = n\lambda \qquad \textbf{Bragg's law} \qquad (2.5)$$

where n is an integer called the order of the diffraction and λ is the wavelength.

This is the minimum condition for efficient diffraction by a crystal of a collimated, monochromatic beam of radiation. If equation 2.5 cannot be satisfied for any type of plane in the crystal then diffraction cannot occur. A monochromatic x-ray beam incident on a crystal at an arbitrary angle will in general not be diffracted; either θ or λ must be varied until combinations of the two occur for which Bragg's law is satisfied.

2.3.2 Explanation of the shape of a scatter pattern

Consider the simplest case, that of the diffraction of a monoenergetic x-ray beam by a regular lattice array of atoms of a single element in a large, perfect crystal (figure 2.5).

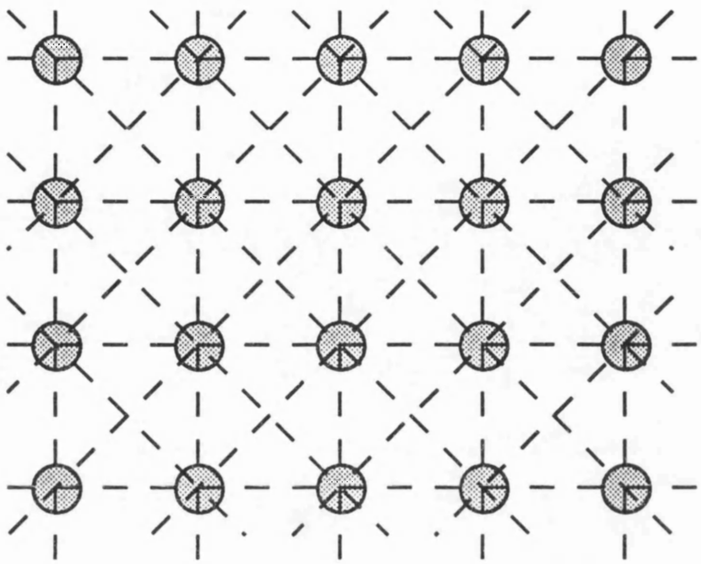

Figure 2.5 Two-dimensional arrangement of a simple crystal lattice of atoms of the same element. The dotted lines show the planes of atoms. The separations of adjacent parallel planes determine the angle and wavelength necessary for diffraction to occur.

Constructive interference will only be met at a few angles (those which satisfy the Bragg conditions), at all other scattering angles the waves will interfere destructively and the amplitude will be zero. An example of the diffraction pattern produced is seen in figure 2.6.

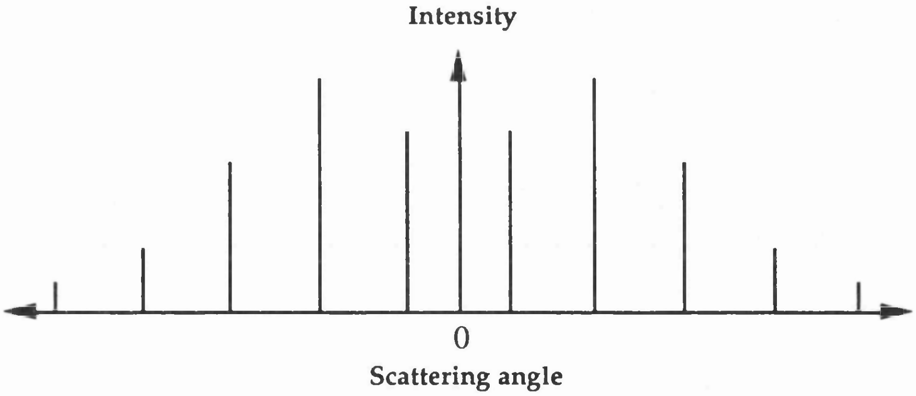

Figure 2.6 A typical diffraction pattern from a simple crystal. The intensity decreases at larger angles due to the decrease in the probability of elastic scatter.

The perfect, crystal, however, does not exist. Deformities occur; slight misalignment of the lattice, lines of stress through the crystal, displaced atoms, etc., cause the separation of the lattice planes to vary slightly throughout the crystal, this results in a broadening of the diffraction peaks or a noisy pattern. A complex crystal involving a few different elements will contain more peaks in the diffraction pattern because the crystal microstructure contains several planes of atoms at various orientations and various distances of separation. Furthermore, the diffraction pattern observed will have been recorded with imperfect measurement apparatus. The detector response, collimator blurring effects, statistical noise, etc., can be minimised but not fully eliminated, and so will all contribute to a less than perfect diffraction pattern. Such irregularities in the crystal structure means that the destructive interference at non-Bragg angles will not be complete. The displaced atoms in the irregularity will lead to a non-zero amplitude even in directions which do not precisely satisfy the Bragg conditions.

The Bragg construction is, thus, a simplified description which does not fully account for the diffraction process. In the following section the theory is expanded to a generalised description that can be applied to any atomic arrangement.

2.3.3 A mathematical description of interference

The following mathematical description is reported in greater detail by Porod (1982). The solution of the wave equation is

$$A \exp \{ i (\omega t - \mathbf{k} . \mathbf{r}) \} \qquad (2.6)$$

where A is the maximum amplitude of the wave, t is the time, **r** is a vector describing the position of a point in space with reference to an arbitrary origin O, and **k** is the wave vector. **k** is defined as $2\pi / \lambda$ and is a vector along the path of the wave propagation. This term is more convenient to use than λ as it can be directly resolved along two or more directions.

The description of Bragg diffraction showed that wave interference is dependent purely on the phase of the scattered waves, hence, in order to consider the effect of interference on the intensity and so describe the shape of the resulting diffraction pattern the constant A is not required. If the absolute amplitude or intensity are required then A must be calculated and included. The representation of the wave can be further simplified, for convenience, by considering the interaction to occur at time t=0, thus removing the ωt term. So, for the purpose of studying the diffraction of the wave by electrons at various positions, the wave can be represented by the form

$$\exp (-i \, \mathbf{k} . \mathbf{r}) \qquad (2.7)$$

The phase of the wave, **k** . **r**, depends upon the spatial position of the scattering site, the electron, and is equal to $2\pi / \lambda$ times the optical path difference between the scattering site and some arbitrary reference point.

Consider waves scattered by two points. Set the position of one point to be the origin O, then the position of the second point is described by the vector **r**.

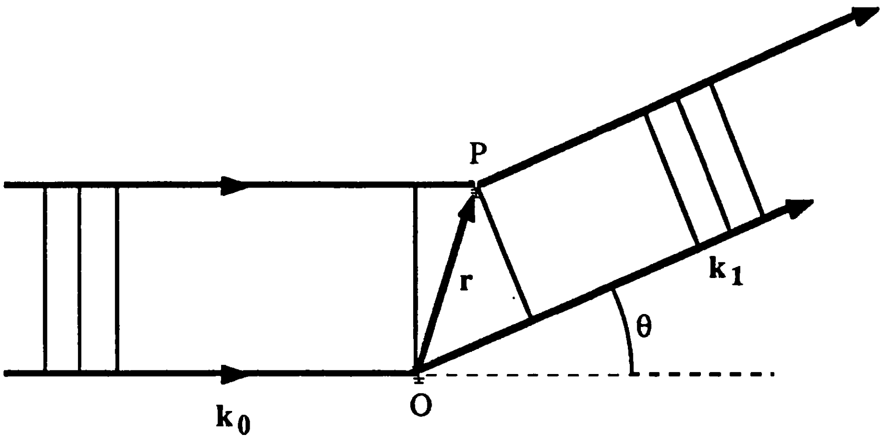

Figure 2.7 The scattering of an incident wave, k_0, by two point centres, O and P. The separation of the two points, described by r, produces a path difference between the scattered waves.

The difference in phase of the incident wave $\mathbf{k_0}$ between points O and P is given by $\mathbf{k_0.r}$. For the diffracted wave the difference in phase between these two points is given by $\mathbf{-k_1.r}$. Therefore, the total phase difference is $\mathbf{(k_0 - k_1).r}$.

The change in wave-vector $\mathbf{(k_0 - k_1)}$ is called the scattering vector, termed **h**. Hence, the scattered wave is represented by the complex form

$$\exp(-i\,\mathbf{h}\,.\,\mathbf{r}) \qquad (2.8)$$

A schematic representation of the scattering vector is given in figure 2.8.

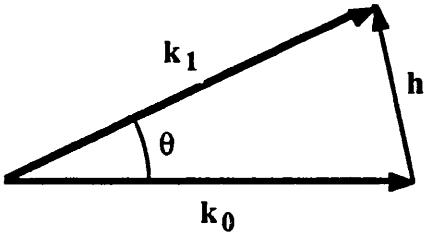

Figure 2.8 The scattering vector is defined as $k_0 + h = k_1$. h lies symmetrically with respect to the incident and scattered waves. In elastic scattering the magnitudes satisfy $k_0 = k_1$.

This shows that the magnitude of **h** is given by

$$h = (k_0 + k_1) \sin(\theta / 2) \qquad (2.9)$$

Substituting for $k_0 = k_1$ (the condition of elastic scatter) and $k_0 = 2\pi / \lambda$ into equation (2.9) gives

$$h = (4\pi / \lambda) . \sin(\theta / 2) \qquad (2.10)$$

The amplitude of the scattered wave resulting from an incident x-ray beam scattered by a large number of points at various positions is proportional to the summation of all secondary waves, each represented by exp(-ih.r); that is

$$\text{Total scattering amplitude} = \sum \exp(-i\mathbf{h}.\mathbf{r}) \qquad (2.11)$$

However, even a relatively small object contains an enormous number of electrons thus making summation impractical, furthermore the exact location of an electron cannot be known. To simplify the summation the scattering site is divided into a set of volume elements dV such that a number of electrons are grouped together. The number of electrons at point **r** can be represented by the electron density at that point $\rho(\mathbf{r})$, defined as the number of electrons per unit volume. Therefore, a volume element dV at position **r** will contain $\rho(\mathbf{r})$ dV electrons. Then summation becomes simply a matter of integrating over the volume V irradiated by the incident beam,

$$\text{Total scattering amplitude } F(\mathbf{h}) = \int_V \rho(\mathbf{r}) \,.\, \exp(-i\mathbf{h}.\mathbf{r}) \,.\, dV \qquad (2.12)$$

This equation is in the standard form of a Fourier transform, showing that the amplitude of the diffracted beam is the Fourier transform of the electron density distribution within the object.

The intensity of the diffracted beam at a particular angle, I(**h**), is the absolute square of the amplitude. This can be obtained by multiplying F by its complex conjugate F*,

$$I(\mathbf{h}) = FF^* = \int_{V_1}\int_{V_2} \rho(\mathbf{r_1})\,\rho(\mathbf{r_2}) \,.\, \exp(-i\mathbf{h}.(\mathbf{r_1}-\mathbf{r_2})) \,.\, dV_1 \,.\, dV_2 \qquad (2.13)$$

This equation shows that the intensity as a function of **h** (which has both wavelength and angular dependence) is determined by the relative distance ($\mathbf{r_1} - \mathbf{r_2}$) between the scattering centres. The equation incorporates Bragg's law but is more generalised as it applies over all values of wavelength and scattering angle and, hence, to all scattering objects, whereas Bragg's law applies to only a few special angles.

The diffracted intensity (equation (2.13)) is expressed as a function of **h**. Equation (2.10) showed the vector **h** to have magnitude $h = (4\pi / \lambda) \,.\, \sin(\theta / 2)$, where λ is wavelength and θ the scattering angle. Diffraction data is commonly plotted as a function of a parameter dependent upon both angle and wavelength. The scatter patterns in this thesis are plotted as a function of momentum transfer, which is described by $x = (1/\lambda) \,.\, \sin(\theta / 2)$.

Calculating the intensity at various scatter angles using equation (2.13) will give the shape of the diffraction pattern, i.e. position of maxima, minima, etc. Various procedures exist for putting this equation into a less complicated format, the format required depends upon the application and the information sought.

However, it is sufficient for the purpose of this project to know that the diffracted intensity is determined by the nature of the chemicals (e.g. elements, molecules, etc.)

within the scattering object (shown by $\rho(\mathbf{r}_1)$ and $\rho(\mathbf{r}_2)$ in equation (2.13)) and by the relative distances between the scattering centres (given by $(\mathbf{r}_1 - \mathbf{r}_2)$), so further simplification of the equation is not necessary.

2.4 Energy dispersive and angular distributed techniques for the observation of scatter patterns

The discussion so far has concentrated on the diffraction of a monoenergetic beam to a range of scattering angles. However, the vector **h** has both wavelength and angular dependence and so the same diffraction pattern is produced regardless of whether the range of h values that are observed are due to the diffraction of either a single wavelength to a range of angles or a range of wavelengths to a single angle. The single wavelength - angular range approach for the observation of diffraction patterns is the one commonly employed in diffraction studies, such as crystallography, optical diffraction, etc. The energy dispersive technique which observes a polychromatic beam scattered to a single angle where it is recorded with energy sensitive detection apparatus is less commonly used but is equally valid. The same theory applies, the only difference being that the intensity is now a function of wavelength.

It is more common to consider x-rays in the diagnostic range in terms of energy, rather than wavelength. The two are equated in the following way;-

The de Broglie hypothesis for wave-particle duality is expressed as

$$\lambda = h / mc \qquad (2.14)$$

where h is the Planck constant (=6.62620 x 10^{-34} Js), m the photon mass and c the photon velocity.

Substituting the mass for energy, using the relativistic energy equation $E = mc^2$, gives

$$\lambda = hc / E \qquad (2.15)$$

thus showing the relationship between energy (in Joules) and wavelength (in metres).

Expressing the energy in terms of electron-volts, the common unit for the x-ray energy, requires inclusion of the electron charge e, such that

$$\lambda = hc / Ee \qquad (2.16)$$

2.5 Diffraction from substances without a regular lattice structure

The diffraction effect does not only result from the separations of atomic planes within a crystal, it occurs due to any appropriate separation of the electrons, which are the scattering sites (demonstrated by equation 2.13). This can be electrons within the same atom, or within adjacent atoms, or adjacent molecules. The actual separation which will lead to diffraction is dependent upon the magnitude of the incident wavelength (demonstrated in simple form by Bragg's law (equation 2.5) and in more detailed form by the presence of h in equation 2.13).

In 1915 Debye showed that a regular crystalline arrangement is not essential for the production of diffraction effects, the collection of electrons into groups to form atoms must give rise to diffraction phenomena, even in the case of a monatomic gas. Diffraction effects are, however, more pronounced in crystalline substances than amorphous substances. Hence this description of diffraction can be widened to include all substances, for example elements, molecules, compounds, mixtures, etc., in which the distances between scattering centres is of the correct order of magnitude.

For the case of a crystal the orientation is very important. Diffraction will only occur if the incident x-ray beam lies at a particular angle to the crystal planes. Hence, the crystal needs to be rotated during measurement to ensure that the correct angles of incidence are encountered. An alternative approach is to crush the crystal into a fine powder, the random orientation of the powder particles will mean that the incident beam must be at the correct diffraction angles for some of the particles. This is the case for the tissues and materials measured in this thesis. Microscopic analysis of bone, for example, reveals a random orientation of minute calcium hydroxyapatite crystals. So for diffraction purposes bone simulates a powder; for any orientation of the bone some of the crystals will be at the appropriate angle. Diffraction peaks will then occur at values of h (or momentum transfer) corresponding to particular separations of atoms/molecules.

2.6 Information content in the measured scatter patterns

The techniques employed for obtaining the scatter patterns are fully described in the following chapter, prior to this, whilst continuing the theoretical description, it would be useful to consider the information contained within the scatter patterns obtained and to discuss the physical mechanisms which lead to the formation of such patterns.

2.6.1 Evidence of interference

The scatter patterns are produced by irradiating the object with a finely collimated x-ray beam and recording either the energy spectrum of the photons scattered to a fixed angle using energy dispersive detection apparatus (termed energy dispersive diffraction) or the angular distribution of the photon intensity (angular distributive diffraction), (for further details see chapter 3). The incident beam was produced by a tungsten anode x-ray tube operating at 70kV. Figure 2.9 shows a comparison of the energy distribution of the incident spectrum and a typical scattered spectrum. The measured scattered spectrum consists predominantly of elastically scattered photons. If no interference effects were taking place then the elastic scattered spectrum should be the same shape as the incident spectrum as there is no transfer of energy. However the scattered spectrum actually recorded has an entirely different shape with some distinguishing features, thus indicating the presence of interference.

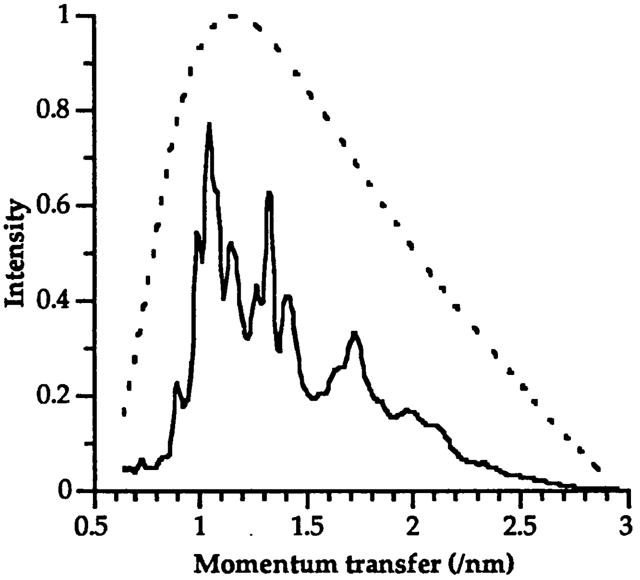

Figure 2.9 The smooth, dotted line shows the shape of a 70kV x-ray spectrum emitted from a tungsten tube (calculated from the data of Birch *et al* 1979). The continuous line shows the energy dispersive scatter pattern of white, granulated sugar. The energy spectrum at a scattering angle of 6 degrees was recorded. A very structured pattern results from more crystalline materials. A smoother pattern with less peaks results from more amorphous substances. The relative heights of the two spectra have been adjusted to compare the shapes of the patterns.

2.6.2 Microstructure 'seen' by a diagnostic x-ray beam

Bragg's law shows that for a particular object the scattering angles at which diffraction occurs are dependent upon the wavelength of the incident x-rays. As the wavelength becomes shorter the diffraction pattern becomes compressed into a smaller angular range. At the very short wavelengths of the diagnostic x-rays used in this project the diffraction pattern is compressed into small angles generally lower than 10°. Diffraction studies in this project, therefore, are restricted to this range.

Table 2.1 shows the wavelength of a few energies within the diagnostic range and gives the corresponding dimensions which will be observed at various scattering angles. The shaded area shows the dimensions studied in this thesis. These separations were determined by first calculating the wavelength to which the energy corresponds, using $\lambda=hc/Ee$ (equation 2.16), and then finding the separation d from Bragg's law, $n\lambda=2d\sin\theta$. The dimensions observed in this thesis correspond to inter-atomic and inter-molecular separations. For example, the O-H bond in the water molecule has a bond length of 0.0958nm and the single carbon bond, C-C, has a length of 0.153nm (Maclwyn-Hughes 1964). Diffraction from dimensions in the range ~0.09 - 0.2nm will generally be from inter-atomic distances, whereas diffraction from dimensions in the shaded region larger than this will generally be from separations between atomic groups within the molecule and between molecules.

Energy (keV)	Wavelength (nm)	Separations of scattering sites (nm)		
		1°	6°	10°
5	0.2480	7.105	1.186	0.714
15	0.0827	2.368	0.395	0.238
40	0.0310	0.888	0.148	0.0893
70	0.0177	0.507	0.0847	0.0510
120	0.0103	0.296	0.0494	0.0298

Table 2.1 Wavelengths of x-ray energies within the diagnostic range, and the dimensions they see.

In order to see larger scale structure within the tissues it will be necessary to use much larger wavelengths and/or much smaller angles. For example, trabeculae within trabecular bone are typically 100 - 200μm thick. Diffraction from objects of this size will result from incident wavelengths of a similar magnitude, such wavelengths are in the infra-red region and therefore do not have the penetrating power for these measurements. Alternatively, to be suitable for clinical work x-rays of ~40keV (0.031nm) are required, with these wavelengths trabeculae dimensions will produce interference effects at scattering angles of approximately 10^{-5}°. X-rays scattered to such small angles would be extremely difficult to measure in practice, a very long object to detector distance with extremely fine collimation would be necessary in order to separate the scattered beam from the primary beam. Such an arrangement would require high photon intensities and long measurement times, thus making it unrealistic for clinical work.

2.7 Interpretation of the patterns

Data on the internal structure, obtained by crystallographic means, has been tabulated for a large number of organic and inorganic molecules (JCPDS: Powder diffraction file 1961). The information given consists of the interatomic and intermolecular separations within the substance together with their relative occurrence. This data was used to interpret the cause of the peaks in the scatter patterns measured in this thesis. For example, the dimensions of the separations tabulated for the calcium carbonate molecule were converted to their respective momentum transfer values at a scattering angle of 6° (the angle at which the energy dispersive scattering measurements were performed). This calculation was done by first using Bragg's law, $n\lambda = 2d.\sin\theta$, where $\theta=6°$ and $n=1$ for first order diffraction, in order to find λ from the tabulated values of d. Then knowing θ and λ the momentum transfer can be calculated from the equation $x = (1/\lambda).\sin(\theta/2)$. The relative intensities of the scattering at each of these momentum transfer values are plotted in figure 2.10. The energy dispersive scatter pattern measured in this thesis for calcium carbonate is plotted on the same axis.

The positions of the line data agree with the positions of the peaks in the measured pattern. This shows that the measurement technique works correctly and it also identifies the dimensions being observed with this technique within the calcium carbonate molecule.

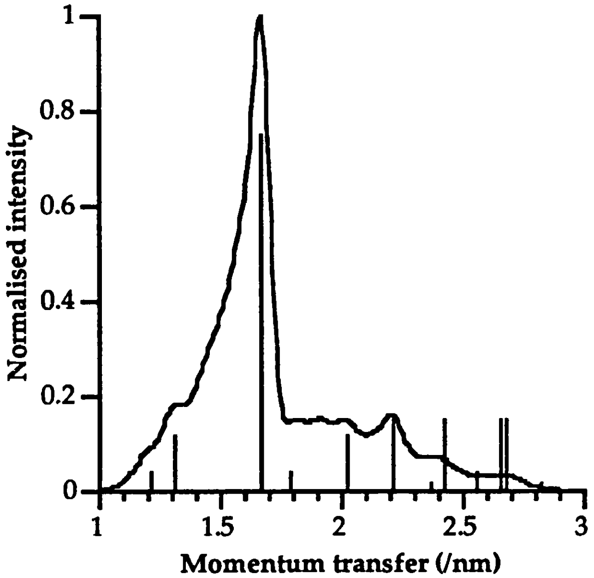

Figure 2.10 Relating the measured scatter pattern of calcium carbonate (continuous curve) with structural data (lines) from crystallography. The respective heights of the two plots are not significant, this graph is to demonstrate the positioning of the peaks.

It is important to note that the shape of the incident spectrum causes the measured pattern to be relatively less intense than the line data at the edges of the pattern. If the intensity of the incident spectrum was constant at each wavelength, rather than peaking at the centre, then this effect would not occur. An attempt was made to produce the measured scattering pattern from the line spectrum of the structure data by applying the effects of the measurement apparatus, as follows;

(1) The intensities of each of the lines were multiplied by the relative intensity of the incident spectrum at the respective photon energy, see figure 2.11, in order to account for the variation of the incident intensity at different energies. The incident spectrum was normalised to peak at 1.

(2) The x-ray beam is attenuated as it passes through the sample of calcium carbonate. The photons will be attenuated both before and after scattering and so the attenuating thickness will be the thickness of the sample. The linear attenuation coefficient was found for each energy over the range (the data of Storm and Israel (1970) was used), and the exponential law of attenuation (given in appendix 1) was used to attenuate the line data by the required amount.

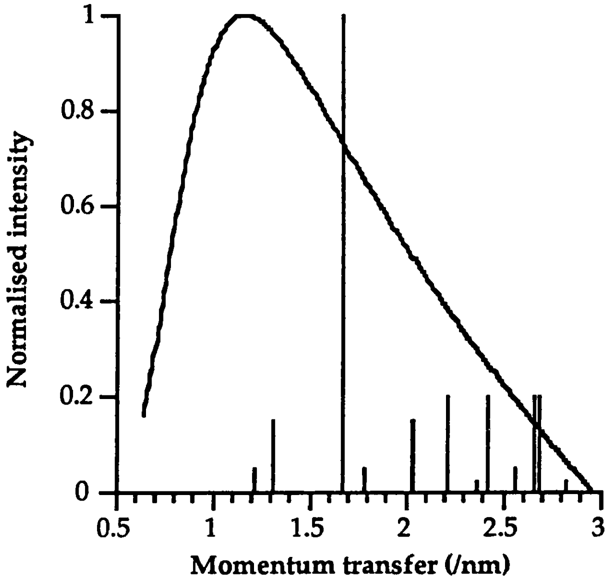

Figure 2.11 Overlying the incident spectrum with the line spectrum. The product of the plots was calculated at each energy.

(4) The spectrum obtained by measurement has broader peaks than the actual spectrum it is observing. This occurs due to the measurement apparatus being imperfect. Peak broadening is caused by the photons detected not having all been scattered by precisely the same angle. A slight difference in the scattering angle causes a small shift in the position of the peak (see § 3.2.3). The collimation of the apparatus has finite width and so will allow through photons at a small range of angles. The quality of the collimation is determined by the way it limits this angular range. This angular range results in a broad measured peak. The degree of broadening is related to the intensity profile of the collimators; this is discussed further and a value estimated in § 3.3.1.

The peak broadening effect can be simulated in the line data by convolution with the collimator response function, the collimator response was measured and is shown later in figure 3.5. The function can be modelled by a gaussian. The FWHM for the gaussian is energy dependent, the function describing it is derived in § 3.3.1. Convolution is performed by multiplying the spectral data by the collimator response function in Fourier space. The result is obtained by inverse Fourier transform of the product, (see Appendix 4 for details on the Fourier transform). A FORTRAN program for the PC, based on algorithms by Press *et al* (1986), was written to perform convolution.

Figure 2.12 compares the measured spectrum with the modified, true spectrum. The patterns are basically the same, however differences clearly occur between the two patterns. The prominent peak in the two patterns match on the higher energy side but differ on the low energy side. This difference is thought to be due to Compton scatter of photons at the energy of the peak. Other differences, such as that over the 1.8 - 2nm^{-1} range, are thought to occur due to impurities in the calcium carbonate sample.

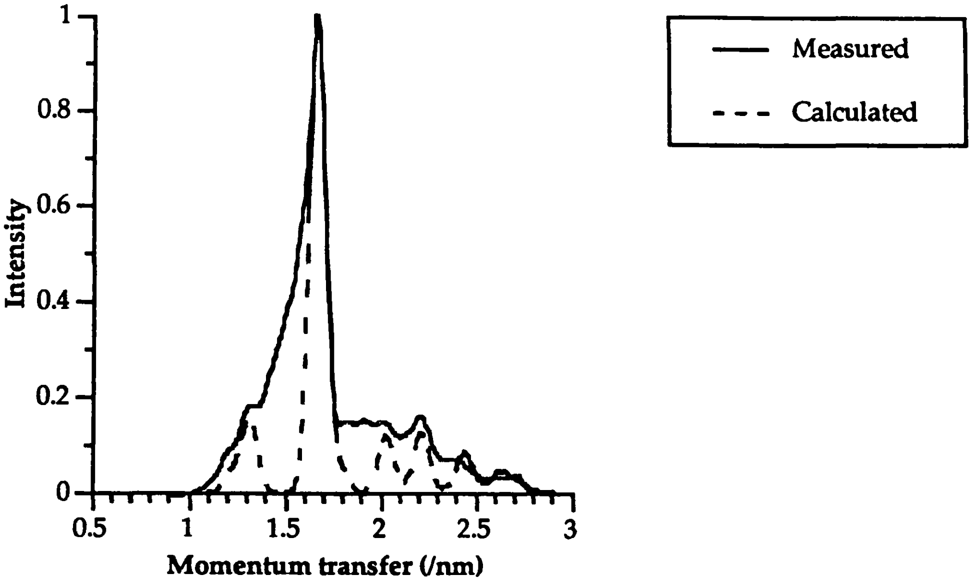

Figure 2.12 A comparison of the experimentally measured scatter pattern of calcium carbonate and the theoretical pattern with the response of the apparatus applied.

A comparison of the measured energy dispersive scatter pattern for bone tissue with line data calculated from the internal spacings within the calcium hydroxyapatite molecule is shown in figure 2.13. The peaks in the measured bone pattern occur at the same positions as the peaks in the line data. This demonstrates that the peaks in the measured scatter pattern are due to the calcium hydroxyapatite crystals in the bone tissue.

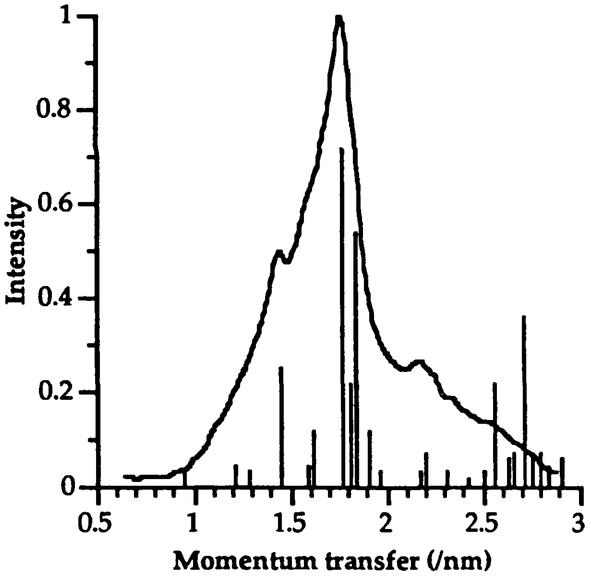

Figure 2.13 Relating the measured scatter pattern of bone tissue (continuous curve) with crystallographic structural data for calcium hydroxyapatite (lines).

Figure 2.14 shows the effect of modifying the line spectrum of calcium hydroxyapatite using the procedure outlined earlier in this section. The differences between the measured pattern and the actual pattern are due principally to the presence of a number of molecules other than calcium hydroxyapatite within the protein matrix of the bone tissue. However the important point to note is that the large peak in the scatter pattern of bone tissue is due to the calcium hydroxyapatite molecule.

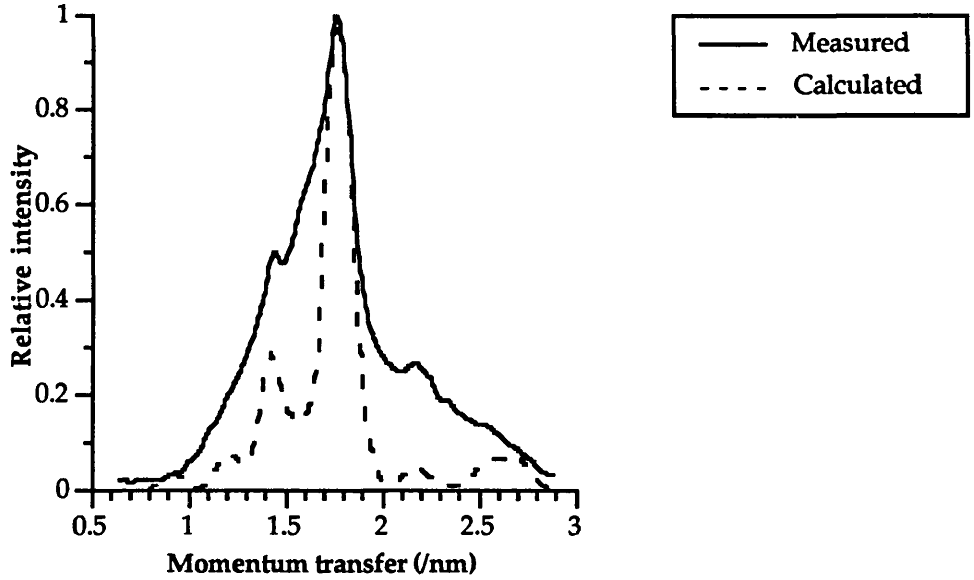

Figure 2.14 A comparison of the experimentally measured scatter pattern of bone tissue with the theoretical pattern with the apparatus response applied.

2.8 Scatter patterns of mixtures

The scatter pattern of a substance which contains two or more components is a combination of each of the scatter patterns of the individual components. The relative heights of the peaks due to each component are dependent upon the proportions of each of the components within the mixture. To demonstrate this effect figure 2.15 shows the individual scatter patterns of calcium carbonate and polyethylene as well as the scatter patterns of mixtures of these powders in various ratios. In each of the patterns of the mixed samples the diffraction peaks of both components are observed. The relative height of the $CaCO_3$ peak can be seen to increase with the percentage of $CaCO_3$ within the mixtures.

Due to the size of the incident wavelengths the diffraction effects observed in these patterns have occurred between adjacent atoms. Molecules from the different components are too far removed for there to be any cross-talk or interference between the different components (i.e. between the $CaCO_3$ and polyethylene molecules). Hence, the pattern of a mixture results purely from a combination of the individual patterns of each of the components.

The relative heights of the peaks from each component are determined by several factors;

(1) The relative concentrations of each of the components: An increase in the concentration of a molecule increases the effective scattering volume, that is, the number of scattering centres. This will necessarily increase the probability of interaction with that molecule and so increase the intensity of the scatter pattern.

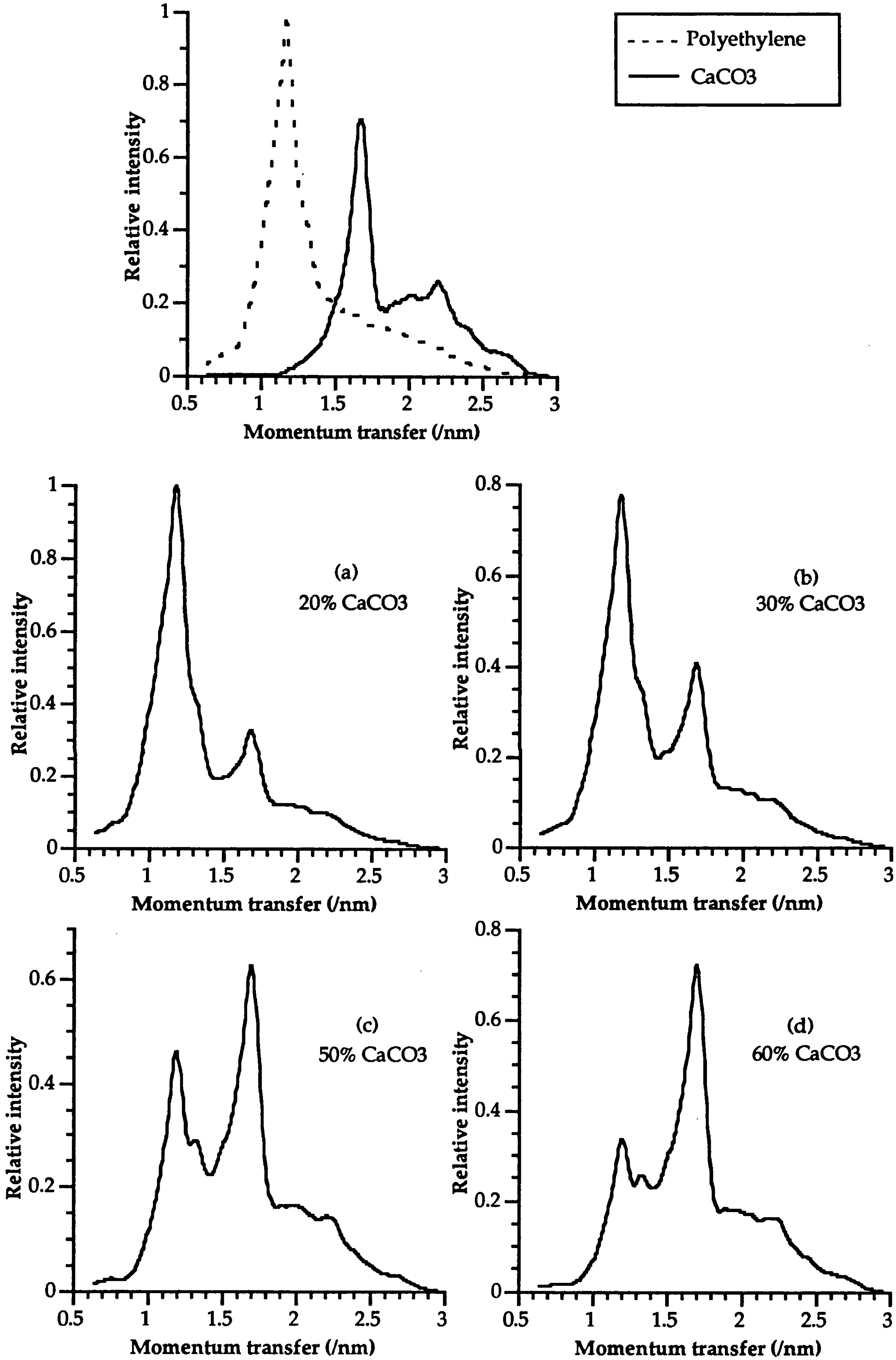

Figure 2.15 Energy dispersive scatter patterns at 6° of calcium carbonate and polyethylene powder together with various mixtures of the two. The mixtures are all thoroughly mixed and in

(2) The probabilities for coherent interaction in each of the components: Equal concentrations of two different substances could produce vastly different amounts of coherent scatter. This factor is determined by the effective atomic numbers of the substances.

(3) The coherent form factors of each of the components: The shape of the scatter pattern produced by a particular substance, in terms of the positions and relative intensities of the diffraction peaks within the pattern, depends upon the interference effects which occur within that substance. These effects are described mathematically by the coherent form factors.

(4) The attenuating properties of each of the components: Consider a small volume of a substance within the scatter object. Photons scattered by this volume will be attenuated by the material they pass through on exiting the object. The degree of attenuation depends upon the energy of the scattered photons and the thickness and stopping power of the surrounding material.

A further description and interpretation of the patterns obtained, together with many examples of the patterns, are given in chapter 6 - the results section.

2.9 Quantitative analysis of two-component mixtures

The ability of x-ray diffraction to identify the constituents of a substance led to its development as a tool for quantitative work. As the relative height of the peak of a particular constituent of the object is related to the relative proportion of that constituent in the object, then if the mathematical relationship is known, the percentage quantity of the constituent can be determined.

This analytical tool has clinical application in the study of osteoporosis. The bone and marrow components of trabecular bone will each produce individual diffraction patterns. Quantitative analysis to determine the relative quantities of bone and marrow tissue within the scattering volume will provide information on the osteoporotic state of the bone in that region.

The mathematical relationships for the case of diffraction from the surface of a flat powder specimen were published by Alexander and Klug (1948). This differs from the situation in this experiment, which is diffraction from within a cylindrical or elliptical object. In the following the description has been adapted to be pertinent to the case of study.

2.9.1 Intensity diffracted by one component of a mixture

Consider a cylindrical sample consisting of two components and irradiated by an

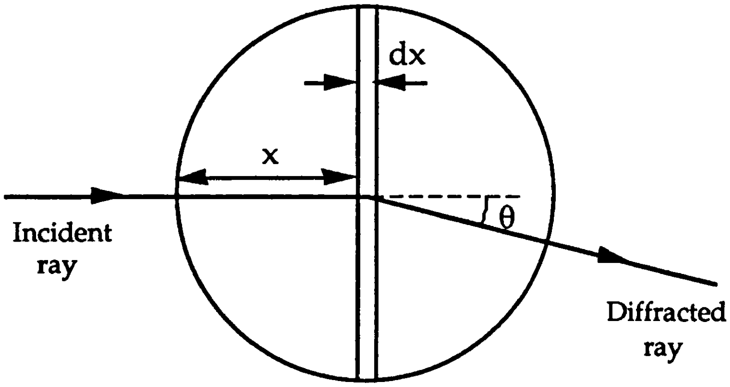

Figure 2.16 Diffraction from a layer at depth x.

incident x-ray beam of cross-sectional area A. Following diffraction the beam leaves the sample at an angle θ relative to the incident beam.

Consider the diffraction taking place from a layer of thickness dx at depth x. The volume of this layer is given by (2.17)

$$dV = A\,dx \tag{2.17}$$

The depth is equal to some fraction n of the maximum path length s traversed by the x-rays through the sample. Hence,

$$dV = n\,A\,ds \tag{2.18}$$

Define $(I_o)_i$ as the intensity diffracted by unit volume of pure *ith* component at an angle θ to the primary beam and under conditions of non-absorption, and f_i as the volume fraction occupied by the *ith* component. Then the intensity diffracted from element dV by component *i* of the mixture is given by

$$dI_i = n\,(I_o)_i\,f_i\,A\,e^{-\mu s}\,ds \tag{2.19}$$

Integrating between the limits s=0 and ∞, gives the total intensity of the diffracted beam from the *ith* component,

$$I_i = \frac{n(I_o)_i f_i A}{\mu} \tag{2.20}$$

Define a constant $K_i = n\,(I_o)_i\,A$, which is a function of the nature of the component *i* and the geometry of the apparatus. This gives

$$I_i = K_i\left(\frac{f_i}{\mu}\right) \tag{2.21}$$

For the purpose of quantitative analysis this can be arranged (Alexander and Klug 1948) to give

$$I_1 = \frac{K_1 x_1}{\rho_1\left[x_1\left(\mu_1^* - \mu_m^*\right) + \mu_m^*\right]} \tag{2.22}$$

where x_i, ρ_i and μ_i represent the weight fraction, density and linear attenuation coefficient, respectively, of the *ith* component.

Equation (2.22) relates the intensity of any given diffraction maximum of the component to its concentration in the sample and to the relative attenuation coefficients of each of the components.

2.9.2 Obtaining quantitative information

The case of interest in this study is trabecular bone which consists of a mixture of two components that have unequal absorbing powers. The usual technique for obtaining quantitative information in this case is by referring to a calibration curve prepared from synthetic mixtures of the two components. The theoretical form of the analysis curve is given by equation (2.22). For the pure first component

$$(I_1)_o = \frac{K_1}{\rho_1 \mu_1^*} \tag{2.23}$$

while for a mixture containing a weight fraction x_1 of the first component

$$I_1 = \frac{K_1 x_1}{\rho_1\left[x_1\left(\mu_1^* - \mu_2^*\right) + \mu_2^*\right]} \tag{2.24}$$

Division of the second equation by the first gives

$$\frac{I_1}{(I_1)_o} = \frac{x_1 \mu_1^*}{x_1(\mu_1^* - \mu_2^*) + \mu_2^*} \tag{2.25}$$

A plot of the relative intensities, $I_1 / (I_1)_o$, against the weight fraction, x_1, will give a non-linear plot, the curvature being determined by the two components of the mixture. Measurements made of unknown concentrations of these two components can then be compared to the calibration curve produced by various known concentrations in order to determine the concentration.

A difficulty with implementing this technique in the current study is that it requires the same incident intensity for all measurements because it compares absolute intensities from different measurements. The x-ray apparatus employed in this study is not sufficiently consistent for such measurements. Therefore, this technique needs to be adapted such that only relative intensities are compared.

Consider the equation describing the intensity from component 1,

$$I_1 = \frac{K_1 x_1}{\rho_1\left[x_1\left(\mu_{11}^* - \mu_{21}^*\right) + \mu_{21}^*\right]} \tag{2.26}$$

where μ_{11} is the attenuation coefficient of component 1 at the energy of the peak of component 1, and μ_{21} is that for component 2 at the energy of the peak of component 1. A similar description can be obtained for component 2. A ratio of the intensities of the two components gives

$$\frac{I_1}{I_2}=\frac{K_1 x_1}{K_2 x_2}\cdot\frac{\rho_2\left[x_2\left(\mu^*_{22}-\mu^*_{12}\right)+\mu^*_{12}\right]}{\rho_1\left[x_1\left(\mu^*_{11}-\mu^*_{21}\right)+\mu^*_{21}\right]} \tag{2.27}$$

The constant K_i has been defined as n $(I_o)_i$ A, both n and A are equivalent for both components. Also, for a two-component system $x_1 + x_2 = 1$. This produces

$$\frac{I_1}{I_2}=\frac{(I_o)_1}{(I_o)_2}\cdot\frac{x_1}{(1-x_1)}\cdot\frac{\rho_2}{\rho_1}\cdot\frac{\left[(1-x_1)\left(\mu^*_{22}-\mu^*_{12}\right)+\mu^*_{12}\right]}{\left[x_1\left(\mu^*_{11}-\mu^*_{21}\right)+\mu^*_{21}\right]} \tag{2.28}$$

The calibration curve: The shape of a typical plot of I_1/I_2 against x_1 is seen in figure 2.17. In order to find the theoretical equation describing the calibration curve (from equation 2.28) the densities of both components, the attenuation coefficient of each component at the energies of each peak and the pure diffracted intensities need to be known. Providing that both components are known, the densities and attenuation coefficients of each component will be known. In theory $(I_o)_i$ can be calculated using the values of relative interaction probabilities for the material and the differential coherent cross-section data modified by the form factor data (see § 2.1). However, accurate form factor data (as discussed in § 2.2) is not available for body tissues or any molecules or compounds (except water).

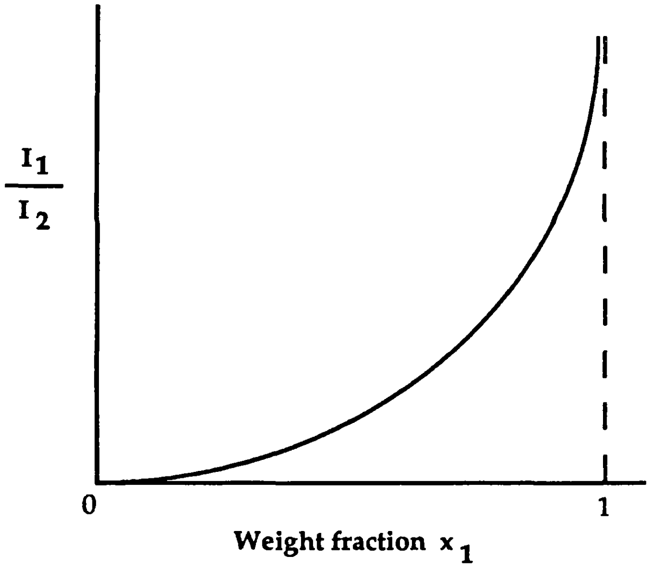

Figure 2.17 General shape of plot of ratio of intensities against the concentration of one of the components.

An alternative method exists which involves the experimental determination of the calibration curve. Measurement of the I_1/I_2 ratio of a set of prepared mixtures of known concentrations, and subsequent plotting of I_1/I_2 against concentration, will produce the calibration curve. Measurements of unknown concentrations can then be compared to this curve in order to determine the concentration. Variation of x-ray intensity between measurements will, in this case, affect only the statistical error and not the result.

- 3 -

Measurement of the Scattering Patterns

This chapter describes the final design and use of the apparatus required to measure both the energy dispersive and the angular distributed scattering patterns for *in-vitro* work, together with a design of the apparatus constructed for use in the clinical environment.

3.1 Design of the apparatus

3.1.1 Constraints of a clinical system

In this project the basic idea of x-ray diffraction at small angles has been adapted to produce a clinical system capable of the measurement of tissues *in-vivo*. Adaptation to the constraints of a clinical system requires the following considerations;

(i) Incident photon energy: The requirement of short wavelengths to penetrate the patient has been previously discussed. The copper anode x-ray tube of a conventional diffractometer emits a near monoenergetic beam at 8keV. Photons of this energy have a half value thickness in soft tissue of 0.07cm. The anatomical regions of interest in this thesis are the thigh, for femoral neck bone measurements, and the abdomen, for gallstone studies. These sites have average thicknesses of approximately 16 and 23cm respectively. Hence, an 8keV beam would be greatly attenuated. The results in this thesis have been obtained using a 70kV x-ray beam from a tungsten anode tube, which has a mean energy of 35.4keV. The half value thickness in soft tissue for this energy is 2.35cm.

Greater energies than those conventionally employed in x-ray diffraction, however, compress the diffraction pattern into a narrow angular range (0 - ~15 degrees for diagnostic energies). The same information will still be contained within the diffraction pattern but as the peaks will be narrower this requires good resolving power in the measurement apparatus. This means that fine collimation for angular diffraction and good energy resolution in the detector for energy dispersive diffraction are required.

Increased photon transmission would result from greater photon energies, however, the limiting factors are that the probability of coherent scatter decreases and the diffraction pattern is further compressed at increased photon energies.

(ii) Large diameter object: The sample size for conventional diffractometers is generally of the order of 1mm. In order to obtain very precise diffraction patterns to determine the structure smaller samples are used, the reason being that structural variations throughout the sample will result in an overlap of information, also the low energy beam will be attenuated and so some of the information will be lost. In this thesis no structural information is required, so this is not a major problem. However, the large diameter of a patient will lead to other problems, such as a great reduction in the scattered intensity thus requiring a longer measurement time, also the attenuation will cause beam hardening of the energy dispersive scatter pattern which will affect the shape.

(iii) Size of apparatus: Apparatus for measuring diffraction patterns at small scattering angles, such as the Kratky camera (Kratky 1982), is typically several metres in length. This, coupled with narrow collimation, enables excellent angular resolution. Such a size is impractical for the clinical environment, and so needs to be reduced. This will, however, compromise the angular resolution of the measurement system. The source to detector distance in the apparatus used in this thesis is 90cm.

(iv) Radiation dose: A very large source to detector distance would necessarily require a high photon intensity and a long measurement time. Reducing the distance allows both of these factors to be reduced. The radiation dose received by the patient is an important consideration which imposes a limitation on the photon intensity permissible. In most clinical radiation measurements a low dose is usually achieved at the expense of counting statistics, so a compromise is required between the two.

(v) Measurement time: The problems of patient movement restrict measurement times to a maximum of a few minutes. For the purpose of this project the ideal situation would be to have a high photon intensity for a very short time, as opposed to a low intensity for a longer time. However, this would require an industrial x-ray generator and fast counting electronics, both of which were unavailable.

3.1.2 Components of the apparatus

The basic requirements of the apparatus are that a finely collimated x-ray beam, incident upon the region of interest, is scattered and recorded by a finely collimated photon detector. The following discusses each of these components in turn.

(i) X-ray beam: For this project a diagnostic x-ray unit was employed as the photon source (the x-ray tube was a Guardian 125 tube type XF2153/01 with tungsten anode run from a Dean & Co. D44 x-ray generator). The great advantage of an x-ray source over an isotope source is the considerably greater photon flux, which will reduce statistical fluctuation and also measurement times. The probability of coherent scatter is fairly low, hence, a large incident intensity is essential. The tube had 1mm Al filtration and was operated at 70kV and generally 3mA. A kV of 70 was chosen as it produces a continuous x-ray spectrum over a large energy range, the peak energies being sufficient to pass through a patient, but it does not produce any characteristic emission from the tungsten tube (k_{abs} edge of tungsten = 69.5keV). Characteristic emission would appear as peaks on the scatter pattern, which could cause confusion. The shape of the 70kV x-ray spectrum has previously been shown (figure 2.9).

(ii) Collimation: Fine collimation of the incident beam is necessary such that all x-rays will be travelling along parallel paths to select the region of interest. If photons reached the object travelling in different directions and were then detected following scattering, the scattering angle of a given photon would be uncertain. Fine collimation of the scattered beam is required to eliminate the large number of photons which are scattered to unwanted scattering angles.

Pinhole collimation is rarely used for small angle scattering experiments due to its restriction of the intensity. Pinhole collimators are restricted for use with high intensity synchrotron sources. The probability of photons coherently scattered to the angles studied is low, therefore maximising the recorded intensity is an important consideration in the design of the apparatus. In order to increase the intensity slit collimation was used.

(iii) Photon detection: An energy dispersive detector with high energy resolution was required for measuring the energy dispersive scattering patterns. Therefore, a planar germanium detector (model no. GLP 36385/10P from EG&G ORTEC) was chosen. The detector was housed in a small liquid nitrogen dewar to allow portability. This detector has a large active diameter (36mm) thus enabling uniform detection over the height of the slit beam.

In the appropriate energy range the resolution was measured to be equal to 0.52keV at 59.5keV (Am-241) and 0.38keV at 5.9keV (Fe-55).

The intrinsic efficiency is described by the ratio of the number of pulses recorded to the number of quanta incident on the detector. The detector has a very thin (0.254mm) beryllium window for maximum transmission of the low energy range and a crystal thickness (10mm) sufficient to stop almost every photon within the energy range, thus giving great efficiency. The detector efficiency is modelled by Monte Carlo simulation in § 5.4.

The output from the detector passes to an amplifier which feeds the pulses to a multichannel analyser (MCA) or to a multichannel scalar (MCS), as required. Both MCA and MCS are interfaced to an IBM compatible PC to display the spectra. The PC enables powerful data handling such that data analysis programs can be implemented directly. The MCA, amplifier and power supply are housed within a single unit, the 92X Spectrum Master; the MCS is the 913 ACE MCS card, both are supplied by EG&G ORTEC.

3.1.3 Apparatus configuration

A diagram of the configuration of the apparatus is given in figure 3.1. The design is based upon that of the Kratky camera (Kratky 1982). The collimated x-ray beam is incident upon the site of interest. Widely separated, narrow slits, C1 and C2, provide the collimation. Further lead slits, the detector collimators D1 and D2, are positioned after the scattering site in order to restrict the photons detected to a particular scattering angle, θ. Lead shielding surrounds the detector and is positioned between both sets of collimators to prevent stray photons from being recorded, thus minimising the background count.

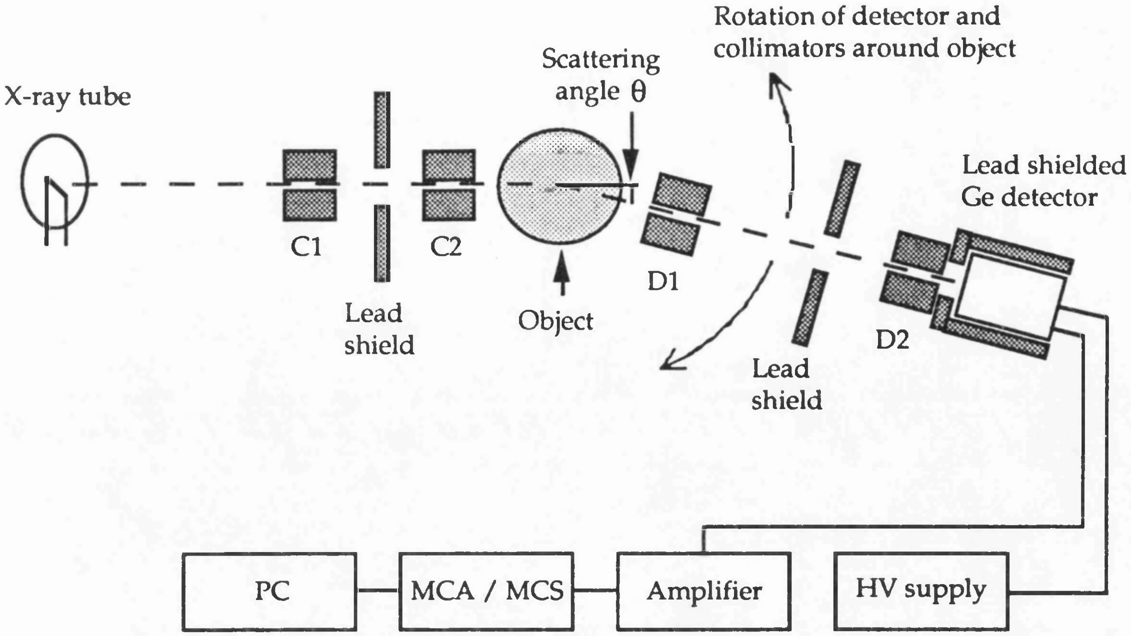

Figure 3.1 The arrangement of the apparatus.

The dimensions of the apparatus are as follows;
x-ray tube to C1 = 25cm
x-ray tube to C2 = 39cm
x-ray tube to object = 50cm
object to D1 = 11cm
object to D2 = 36cm
object to detector = 40cm
The total x-ray tube to detector distance is 90cm.
The dimensions quoted were measured from the front faces of the x-ray tube and the detector respectively, and from the centres of the object and the collimators.

The positioning of detector collimator D1 close to the object and D2 close to the detector was found to provide the best angular resolution. In this arrangement fewest photons scattered by the material in the object surrounding the region of interest were allowed through to the detector.

Both sets of collimators and the object are laser aligned, care is taken to ensure that the object is centred at the point of intersection of the directions subtended by both sets of collimators. Collimators C1 and C2 were aligned with the focal spot of the x-ray tube to ensure maximum intensity.

The detector and collimators D1 and D2 are arranged on an optical bench which is pivoted at the scattering site. The bench rests on a platform on a fine screw thread which is driven by a computer controlled stepper motor (supplied by Digiplan), causing the bench to rotate in an arc about the centre of the scattering site. This system allows accurate angular positioning. The number of steps of the stepper motor have been accurately calibrated with angle. Programs were written in GWBASIC on a PC interfaced to the stepping drive unit for controlling the stepper motor system.

Figure 3.2 shows a photograph of the apparatus.

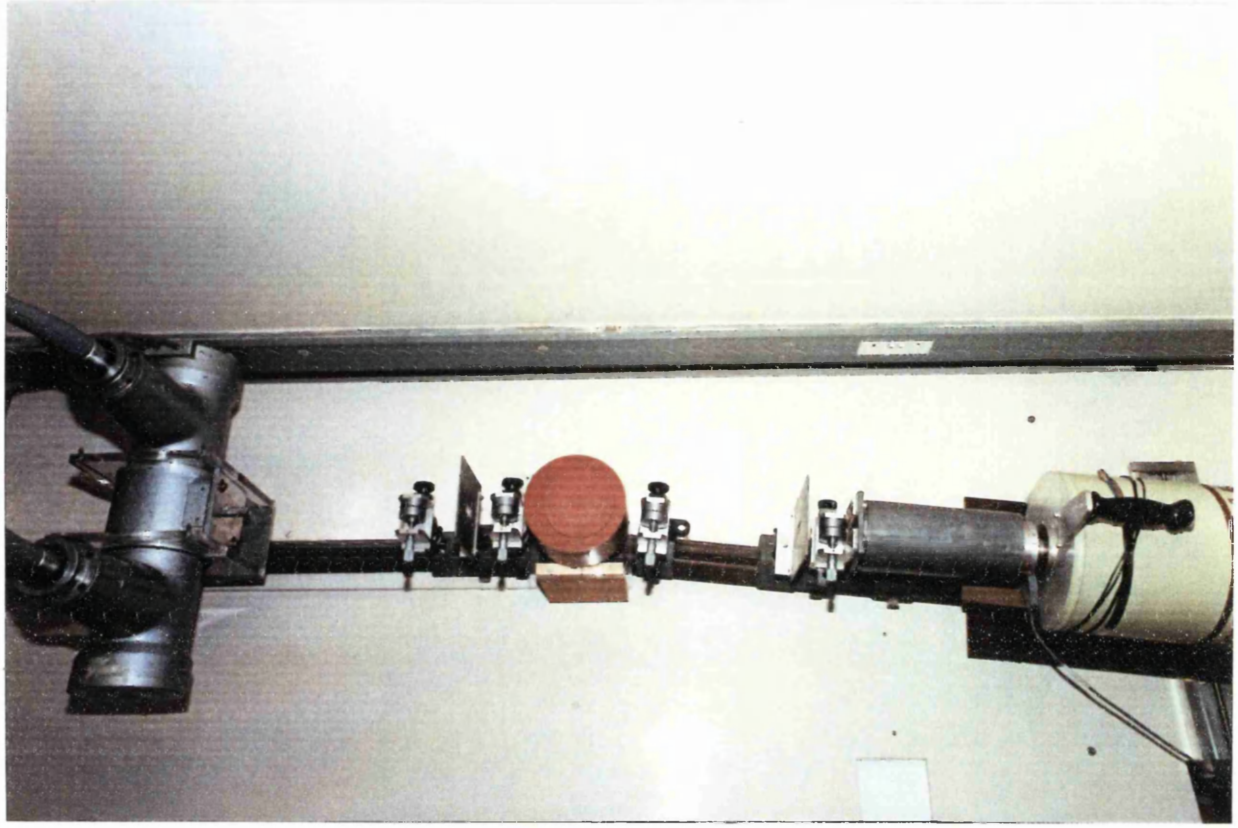

Figure 3.2 The 'bench set-up'.

3.1.4 The scattering volume

The collimator geometry selects a rhomboidal region of interest within the measurement site, as seen in figure 3.3.

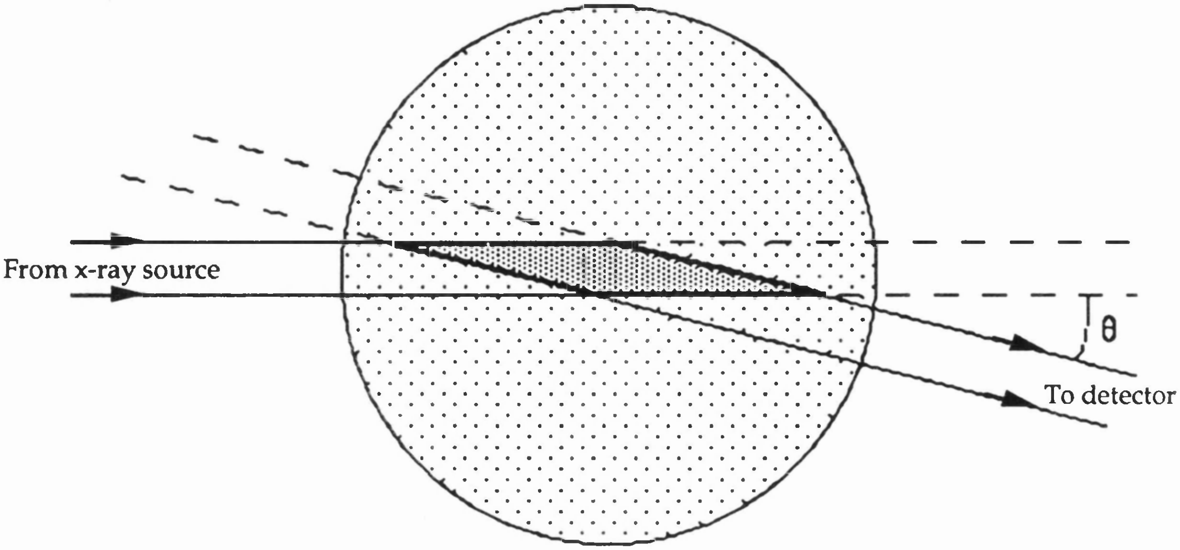

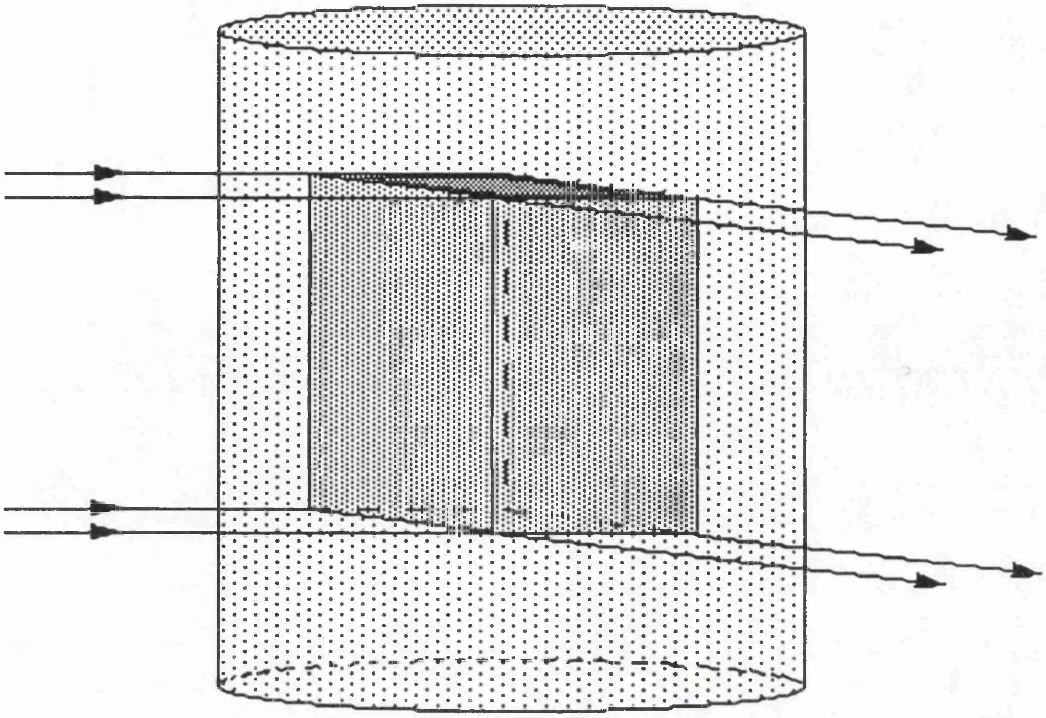

Figure 3.3 The shape of the scattering volume as subtended by the collimators.

Table 3.1 shows the dimensions of the scattering region for various slit widths and scattering angles.

D1	D2	θ	Width	Length	Area
0.5mm	0.5mm	1°	0.5mm	57.3mm	14.32mm^2
		6°	0.5mm	9.5mm	2.4mm^2
		10°	0.5mm	5.7mm	1.4mm^2
1mm	1mm	1°	1mm	114.6mm	57.3mm^2
		6°	1mm	19.1mm	9.6mm^2
		10°	1mm	11.4mm	5.8mm^2
1mm	2mm	1°	1mm	171.9mm	114.6mm^2
		6°	1mm	28.6mm	9.6mm^2
		10°	1mm	17.2mm	5.8mm^2
2mm	2mm	1°	2mm	229.2mm	229.2mm^2
		6°	2mm	38.2mm	38.3mm^2
		10°	2mm	22.9mm	23.0mm^2

Table 3.1 Dimensions of the scattering region for various collimator slit widths over the range of scattering angles.

The size of the scattering volume is determined by the slit widths of the x-ray and detector collimators, and the scattering angle. The cross-sectional area of the rhombus is given by

$$D1.D2 / \sin\theta \qquad (3.1)$$

The rhombus is long and thin. The length increases with increasing slit width and decreasing scattering angle. The scattering volume should be fully enclosed within the region of interest, otherwise the shape of the scatter pattern of the surrounding material is seen in the measured pattern. Therefore selection of the correct slit widths is an important consideration

The ability to select a particular region within an object, for example isolating the trabecular bone within the leg, is one of the main advantages of this technique.

3.1.4.1 Optimum slit dimensions

Three factors determine the optimum opening size of the collimator slits; (1) the slits need to be sufficiently narrow for the scattering volume to be entirely within the region of interest of the object (for example, the trabecular region within the thigh), (2) large slit widths do not restrict the intensity so greatly and so allow a higher recorded count, (3) narrow slit widths produce a good angular resolution for the system.

The slit widths were chosen by finding the largest slit widths which would allow the scattering volume to be fully enclosed by the scattering object. This then allows the largest possible intensity. The trabecular region of the femoral neck is approximately 25mm thick for an average person. The femoral head is approximately 35mm in diameter. For measurements of the femoral neck all slit widths were set to 1mm. At the common scattering angle of 6° the length of the scattering rhombus in this case is 19.1mm, hence the scattering volume will be contained within the trabecular region, and it also allows a few millimetres for positioning error. Slit widths of 1mm were set for most measurements, including the gallstones. For measurements of the femoral head, slit widths of 1.5mm were set. This produces a scattering rhombus of length 28.6mm at an angle of 6°, (6 degrees was selected because it is the angle at which the energy dispersive measurements are taken, see § 3.4.1).

3.1.5 Performance of the collimation

3.1.5.1 Angular spread of the primary beam

Narrow collimation and a long object-to-detector distance restrict the overlap of the primary beam with the scattered beam. However, the finite aperture of the collimators means that a contribution of the primary beam will be present at small scattering angles. In order to determine the angular spread of the primary beam, an exposure was made, with no object present, whilst the detector was slowly scanned from -3° to +3°. The counts were recorded on the multichannel scalar, and plotted as a function of angle.

Figure 3.4 shows that above 0.7° no contribution from the primary beam will be present.

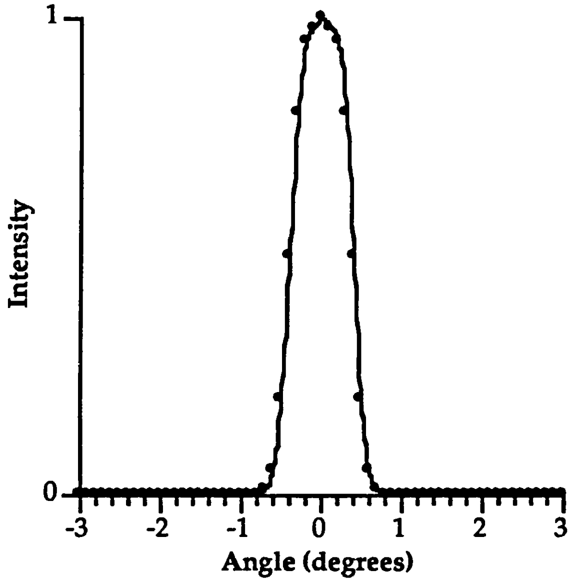

Figure 3.4 Transmitted intensity as a function of the angular position of the detector.

3.1.5.2 Intensity profiles of the slit collimators

X-ray film was placed at the object position on the apparatus and irradiated in order to observe the intensity profile through the slit collimators. The optical density was measured both along the line of the slit and across the width of the slit at the centre. Figure 3.5 shows the results. Both graphs show that the majority of photons occur at the centre of the slit in both directions. The presence of photons outside the width of the slit shows that some scatter from the collimators has occurred, but very little. The fine collimation at the detector will minimise the number of such scattered photons recorded.

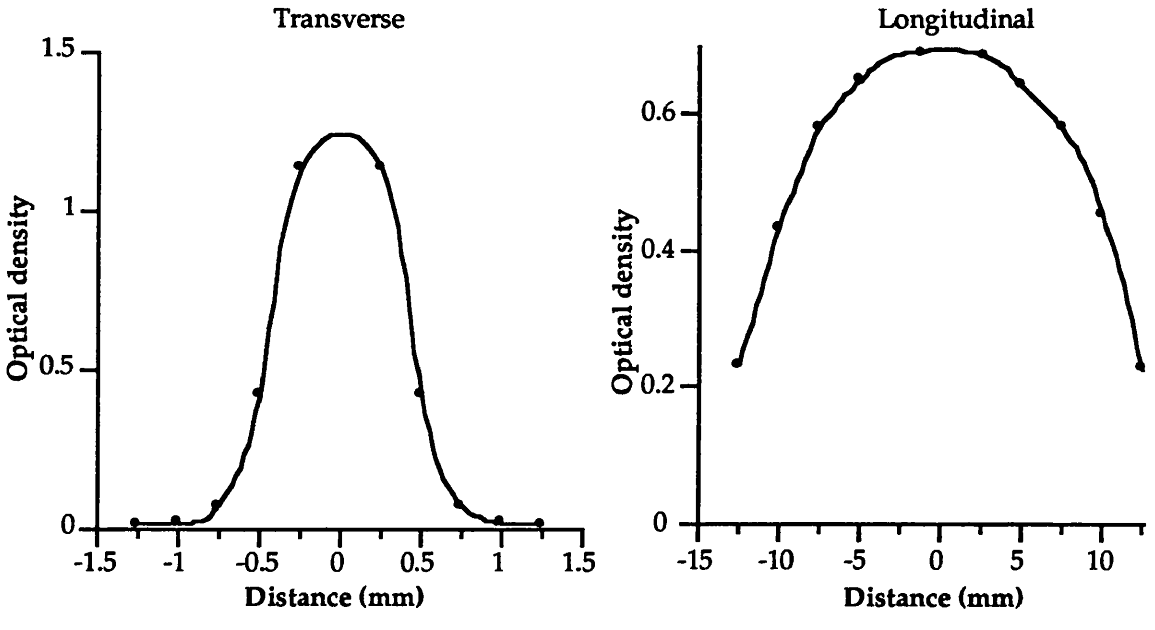

Figure 3.5 The optical density as a function of distance along both axes of the slit collimators.

In order to convert the measured optical density values to intensity it would be necessary to plot a graph of film density against log(exposure) (the Hurter-Driffield curve) for the film and processing used.

3.2 Techniques for measuring the scatter patterns

3.2.1 The angular distributive technique

The conventional approach to measuring x-ray scattering patterns is to record the scattered photon count over a range of scattering angles:-
The x-ray tube was operated in fluoroscopic mode to produce a long, continuous exposure, during which the collimated detector was slowly scanned in an arc around the measurement site from 1 - 11°. Below 1° a significant contribution of transmitted photons are detected, and above 11° the interference effects are reduced and the level of Compton scatter becomes significant.

The signals are passed to the multichannel scalar, which records the total number of photons in the energy range 15 to 70keV usually over a dwell time of 20 seconds. The total time for a measurement was generally approximately 10 minutes. A low energy threshold of 15keV was implemented to avoid including the large fluctuations in detector efficiency around the germanium k-edge (11.10keV).

Angular calibration was performed by relating the number of steps on the stepper motor to the distance moved by the platform on the screw thread. Then knowledge of the scanning speed of the detector enabled the scattering angle of each channel to be determined.

Angular distribution technique with a monoenergetic beam

The angular distributive technique for recording diffraction patterns is conventionally performed with a monoenergetic beam due to the loss of information caused by source polychromaticity (discussed in § 3.3.1.2). Possible methods for achieving a near-monoenergetic beam would be the use of an isotope source, such as Am-241 (59.5keV), filtration of the tungsten target x-ray beam to produce a harder beam, or the excitation of characteristic emission from a suitable target. The major problem with each of these techniques is that it is difficult to achieve a sufficiently high photon intensity. Trial measurements performed with a 200mCi Am-241 isotope source resulted in a very poor count rate, and measurements would have taken several hours. Probably the highest count rate would be achieved by exciting characteristic emission (metals in the 58-70 atomic number range emit photons of suitable energies, 40-60keV), however the maximum output achievable from the x-ray tube available would not cause a sufficient characteristic intensity. So in order to minimise the counting time, which is an important consideration of this project, the polychromatic tungsten target x-ray tube was used.

3.2.2 The energy dispersive technique

Giessen and Gordon (1968) developed a technique for obtaining x-ray diffraction patterns by irradiating the sample with continuous, polychromatic radiation from an x-ray tube and recording the energy spectrum of x-rays scattered to a given angle with an energy dispersive, semiconductor detector. This technique was found to produce the same signal-to-noise ratio in a much shorter time (generally two or three orders of magnitude shorter).

A greatly shortened measurement time is a major advantage in the clinical environment. Bordas *et al* (1976) have used the energy dispersive approach together with a synchrotron radiation source to study muscle tissue within a rat tail. A recognisable scatter pattern was achieved within 1 second of data accumulation, and extremely precise patterns were obtained in 200 seconds. This suggested that the technique would be capable of measuring a temporal process, such as muscle contraction.

In this thesis energy dispersive measurements were made by positioning the detector at the appropriate scattering angle (see following section). The object was irradiated with the x-ray tube in fluoroscopic mode and the pulses detected were passed to the multichannel analyser which recorded the scattered energy spectrum.

Energy calibration of the channels on the MCA was performed using the 18 and 59.5keV lines of a 10μCi Am-241 calibration source.

3.2.3 Effect of scatter angle on energy dispersive measurements

The angle of scatter to which the detector is set in energy dispersive scatter measurements is an important factor. Interference effects occur within objects only at certain momentum transfer values. Due to the requirements of clinical work the energy range (and therefore the range of wavelengths) is limited. Hence, the only way of selecting the momentum transfer range (a function of wavelength and scatter angle) that is to be investigated is by varying the scatter angle.

For a particular substance variation of the scatter angle will range from a scatter pattern showing no interference effects to one which shows the maximum amount of diffraction information (see figure 3.6). The angle of the latter needs to be found. Figure 3.6 shows energy dispersive scatter patterns of the trabecular region within a dry, human femoral neck. In each case a 70kV incident x-ray beam was used, the angle was varied to alter the momentum transfer region investigated.

At 2 and 4 degrees there is no evidence of diffraction, the scattered spectra are very similar in shape to the incident x-ray spectrum. A peak is starting to show at 5 degrees, and then at 6 to 14 degrees diffraction peaks can clearly be seen. At 14 degrees the peaks are less prominent than at the previous angles; the pattern is returning to the shape of the incident spectrum. At greater angles the peaks disappear completely and the shape is the same as the incident spectrum.

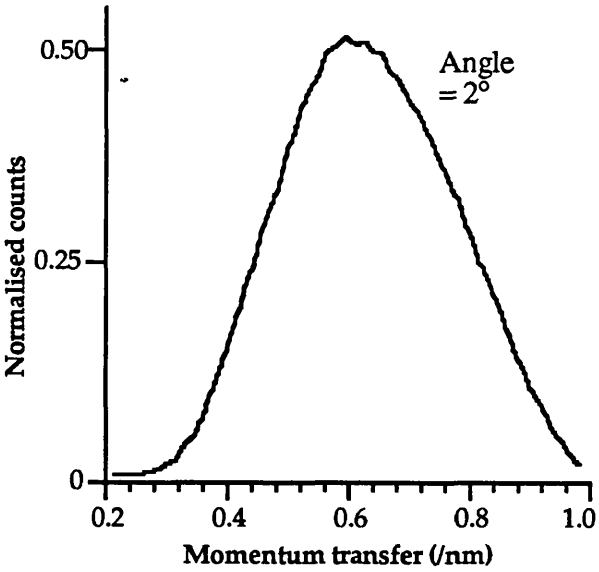
0.50
0.25
0
Normalised counts
0.2
0.4
0.6
0.8
1.0
Momentum transfer (/nm)
Angle = 2°

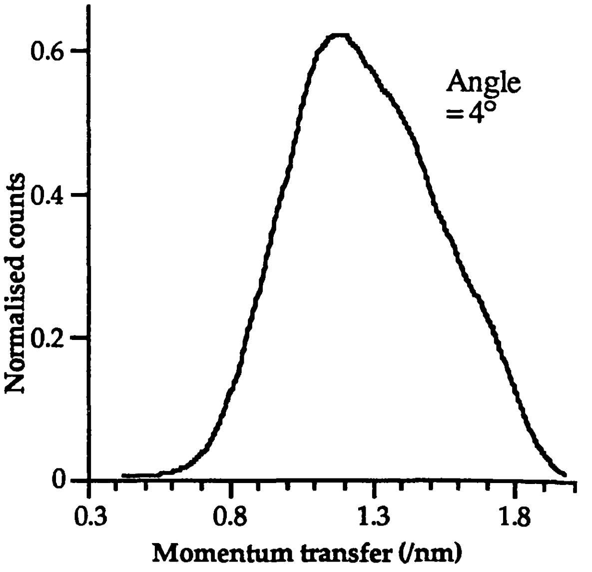
0.6
0.4
0.2
0
Normalised counts
0.3
0.8
1.3
1.8
Momentum transfer (/nm)
Angle = 4°

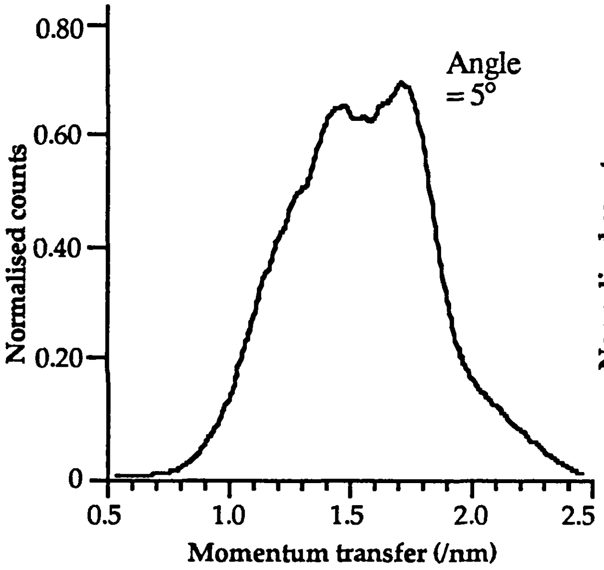
0.80
0.60
0.40
0.20
0
Normalised counts
0.5
1.0
1.5
2.0
2.5
Momentum transfer (/nm)
Angle = 5°

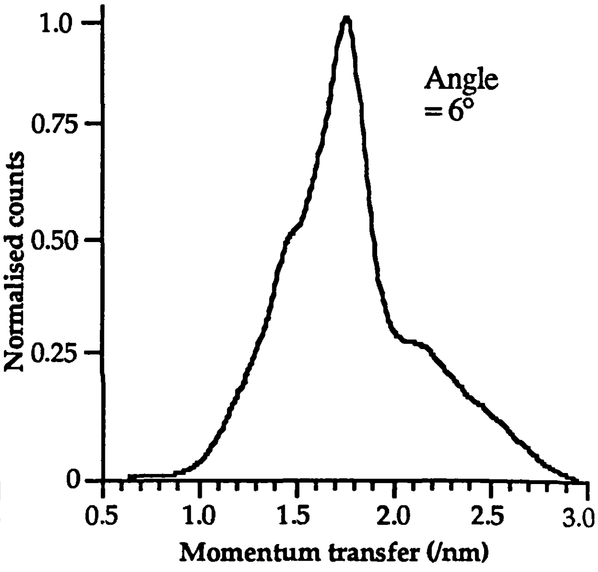
1.0
0.75
0.50
0.25
0
Normalised counts
0.5
1.0
1.5
2.0
2.5
3.0
Momentum transfer (/nm)
Angle = 6°

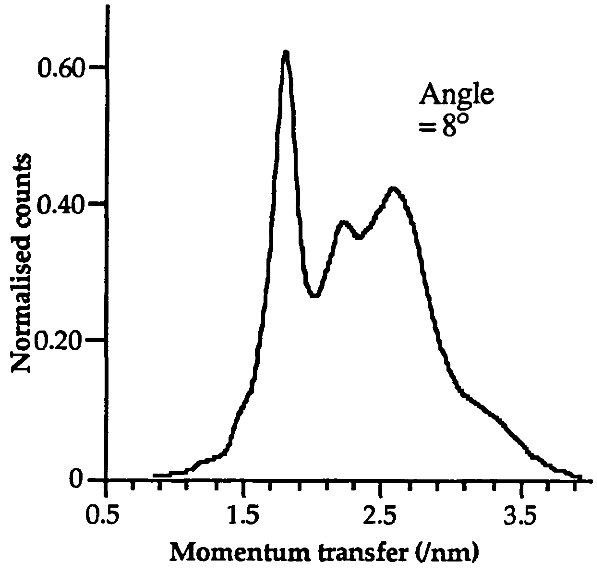
0.60
0.40
0.20
0
Normalised counts
0.5
1.5
2.5
3.5
Momentum transfer (/nm)
Angle = 8°

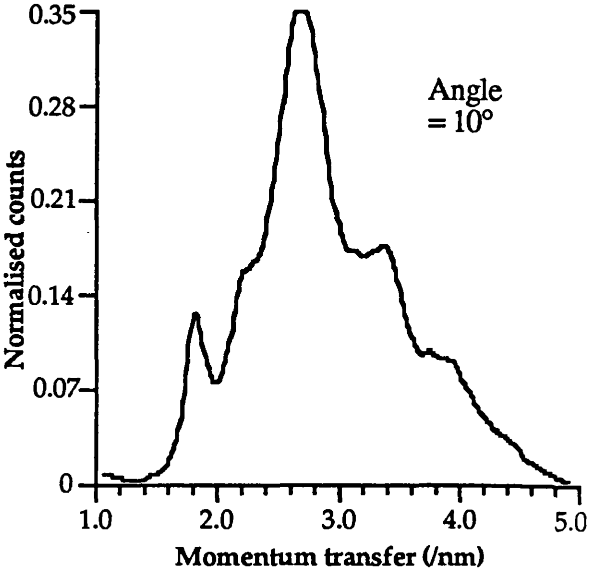
0.35
0.28
0.21
0.14
0.07
0
Normalised counts
1.0
2.0
3.0
4.0
5.0
Momentum transfer (/nm)
Angle = 10°

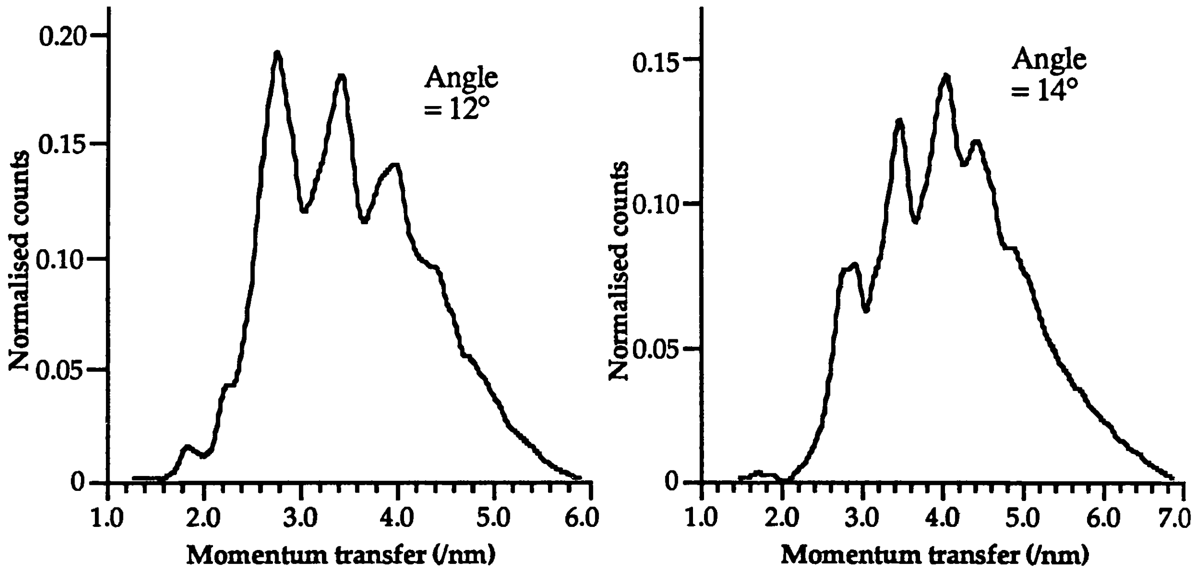

Figure 3.6 Energy dispersive scatter patterns of a dry femoral neck at various scatter angles. The heights of the patterns are normalised relative to the highest peak in the most intense of the eight patterns in order to show the relative intensities.

Figure 3.7 shows the effect of small angular changes on the resulting pattern. At 5.5° and 6° there is a principle peak in the pattern at ~1.7nm^{-1}, and the peak is fairly central. Increasing the scattering angle shows that the peak is still at a momentum transfer value of ~1.7nm^{-1} but its relative position within the pattern has shifted to a lower energy due to the change in angle. At 7° another peak is seen at ~2.2nm^{-1}; the change in angle has brought this momentum transfer region into an energy range that contains a large proportion of incident photons. Hence, the scatter angle can be varied in order for the most intense wavelengths of the incident spectrum to study the required momentum transfer range of the diffraction pattern.

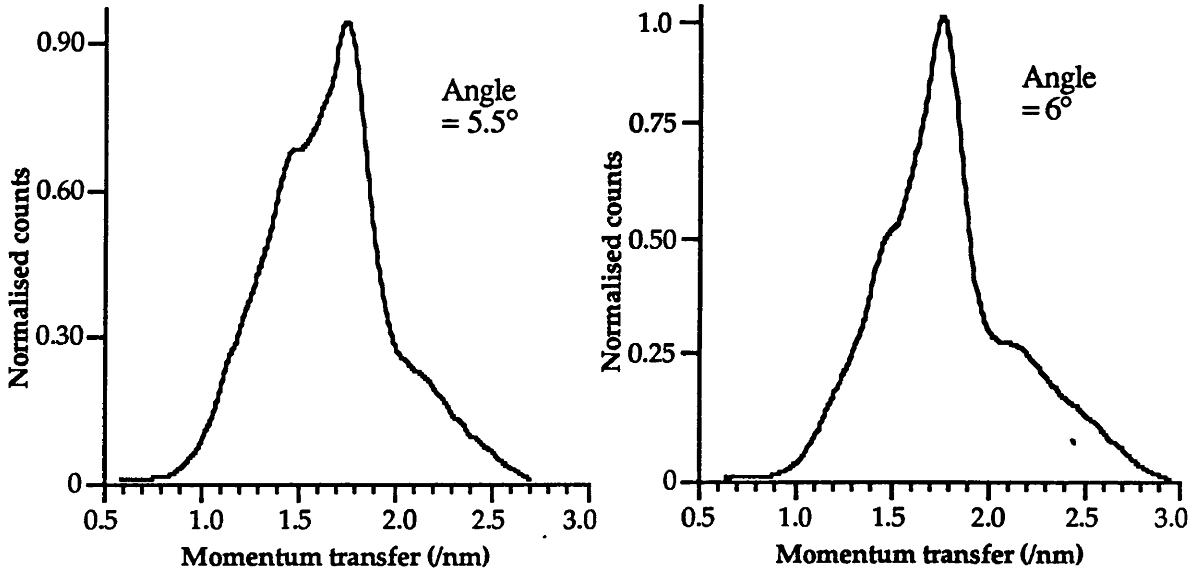

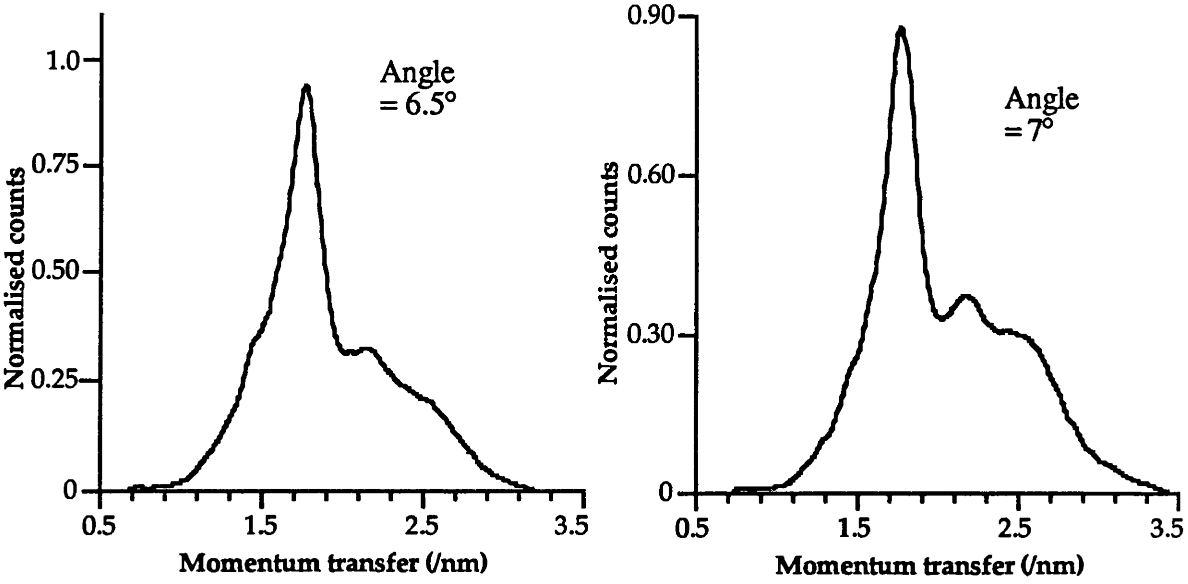

Figure 3.7 The effect of a small change in scatter angle on the relative position of the diffraction peak within the scatter pattern. The heights of the patterns are normalised relative to the highest peak in the most intense of the four patterns in order to show the relative intensities.

Figure 3.8 shows the magnitude of the peak shift in the energy dispersive pattern for small changes in angle. A change in the scattering angle of 0.3° was calculated to shift the scatter pattern along by 1keV.

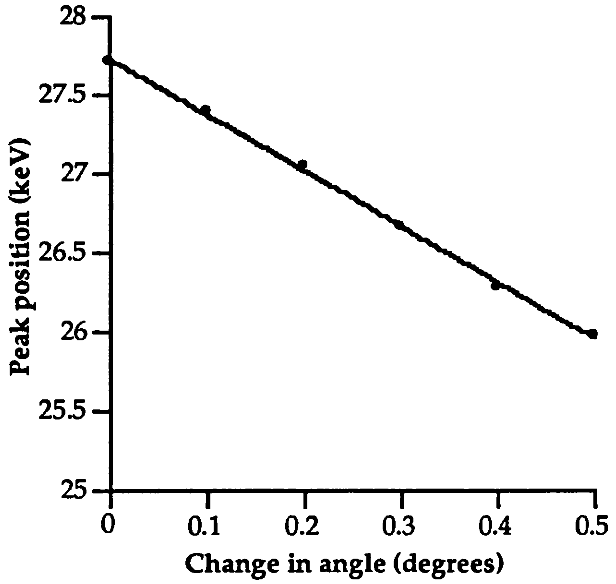

Figure 3.8 Variation of position of peak in energy dispersive patterns for small angular variations.

This section has emphasised the importance of the measured scattering angle on recording energy dispersive scatter patterns. An incorrect angle can limit the information or sensitivity present in the pattern, it can also reduce the intensity that is potentially achievable. The variation of the position of the scatter peaks with angle highlight the necessity of maintaining exactly the same scattering angle over a series of comparative measurements.

3.2.4 Determination of the optimum scatter angle

Three factors need to be considered when deciding upon the optimum scatter angle for energy dispersive scatter measurements;

(1) The angle selected should focus on the required part of the diffraction pattern, (as discussed in the previous section).

(2) The wavelengths of the diffraction peaks should correspond to wavelengths near the peak of the incident spectrum in order to maximise the scattered intensity.

(3) Angles providing the greatest scattered intensity are preferable.

The first point is obviously the most important as this determines the quality of the result, whilst the effect of points (2) and (3) is to improve the counting statistics and shorten the measurement time.

3.2.4.1 Calculation of the optimum scatter angle

Plots of diffraction spectra of various body tissues over a large momentum transfer range, measured with a standard powder diffractometer, are shown in Kosanetzky *et al* (1987). These patterns show that the most significant peaks for all common body tissues lie within the momentum transfer range 0.7 - 3.0nm^{-1}. For compact bone, adipose and muscle tissue the most significant peaks lie in the range 0.9 - 2.2nm^{-1}. Therefore the angle needs to be calculated at which this momentum transfer range lies within the energies of the incident spectrum (10 - 70keV). Considering point (2) it would be better if the highest and lowest energies were not used as these are of low intensity in the x-ray spectrum. It was decided to select the angle such that the required pattern lay in the 20 - 60keV energy range. Using the equation $x = (1 / \lambda) \sin(\theta / 2)$ it was found that when $\theta=6°$ the energy range 20 - 60keV corresponds to a momentum transfer range of 0.84 - 2.41nm^{-1}. Hence the range of interest of the momentum transfer will be within the measured range at an angle of 6°.

3.2.4.2 Scattered intensity

Figure 3.9 shows a plot of the number of scattered photons within the 20 - 60keV energy range as a function of angle for fresh bone tissue.

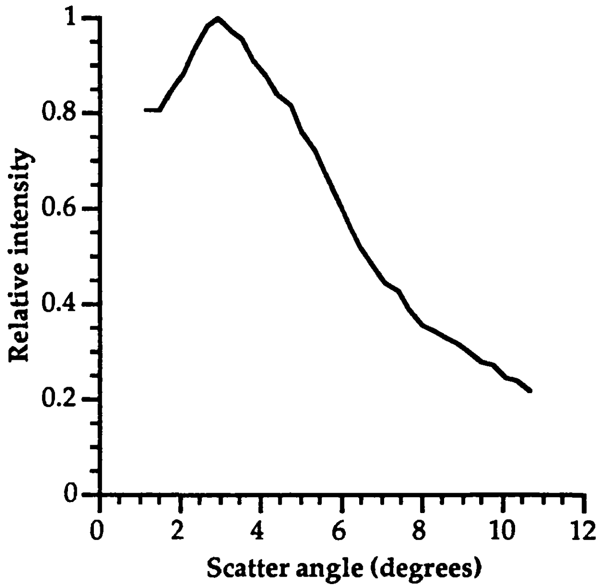

Figure 3.9 Plot of scattered intensity of bone tissue (in the 20 - 60keV energy range) as a function of angle.

This plot was produced by measuring the bone using the angular distributive technique and allowing all photons in the 20-60keV range to be recorded. The number of coherent scattered photons in the energy range of interest is seen to peak at ~3°. Therefore for energy dispersive scatter measurements of bone tissue a scatter angle of ~3° would be ideal in terms of maximising the count rate, however figure 3.6 showed that very little useful information was observed at this angle. So in order to optimise the intensity of photons elastically scattered by fresh bone tissue a scattering angle which is closest to 3° and still gives useful information should be chosen.

3.2.4.3 Application to bone measurement

Analysis of the two components of bone tissue (bone and marrow) can be simplified by selecting a scatter angle at which each component produced a peak at a separate location rather than having overlapping peaks. Figure 3.10 shows plots, at different scattering angles, comparing the energy dispersive scatter patterns of a fresh femoral head (recently excised from a patient complete with marrow tissue) and a dry femoral head (marrow tissue removed).

The large peak common to both patterns is due to the bone tissue (identified previously in § 2.7). The region where the two patterns differ shows the peak due to the marrow tissue. At small angles (below ~5°) the bone and marrow peaks occur at similar momentum transfer values. The lowest scattering angle (and therefore the largest degree of coherent scatter) at which the positions of the bone and marrow peaks are at acceptably different momentum transfer values is ~6°. At larger angles the positions of the two peaks separate further and become more distinct but the scattered intensity is less (see figure 3.9).

Summary: Calculation of the optimum angle, based upon conventional x-ray diffraction measurements, identified 6° (or an angle very close to 6°) to be the optimum angle for the energy dispersive measurements in this thesis. This conclusion was supported by experimental measurements of bone tissue. The evidence of interference within the scatter patterns of fresh bone tissue was observed at a range of scattering angles from ~3 - 14° (an example is shown in figure 3.6), however a significant difference between patterns of fresh and dry bone was seen at angles of ~6° and above. Hence, 6° was selected as the scattered intensity will be greatest at this angle. It is not essential to set an angle of exactly 6° but it is essential to maintain the same angle through all comparative measurements due to the variation of the diffraction peak position with change in the scatter angle.

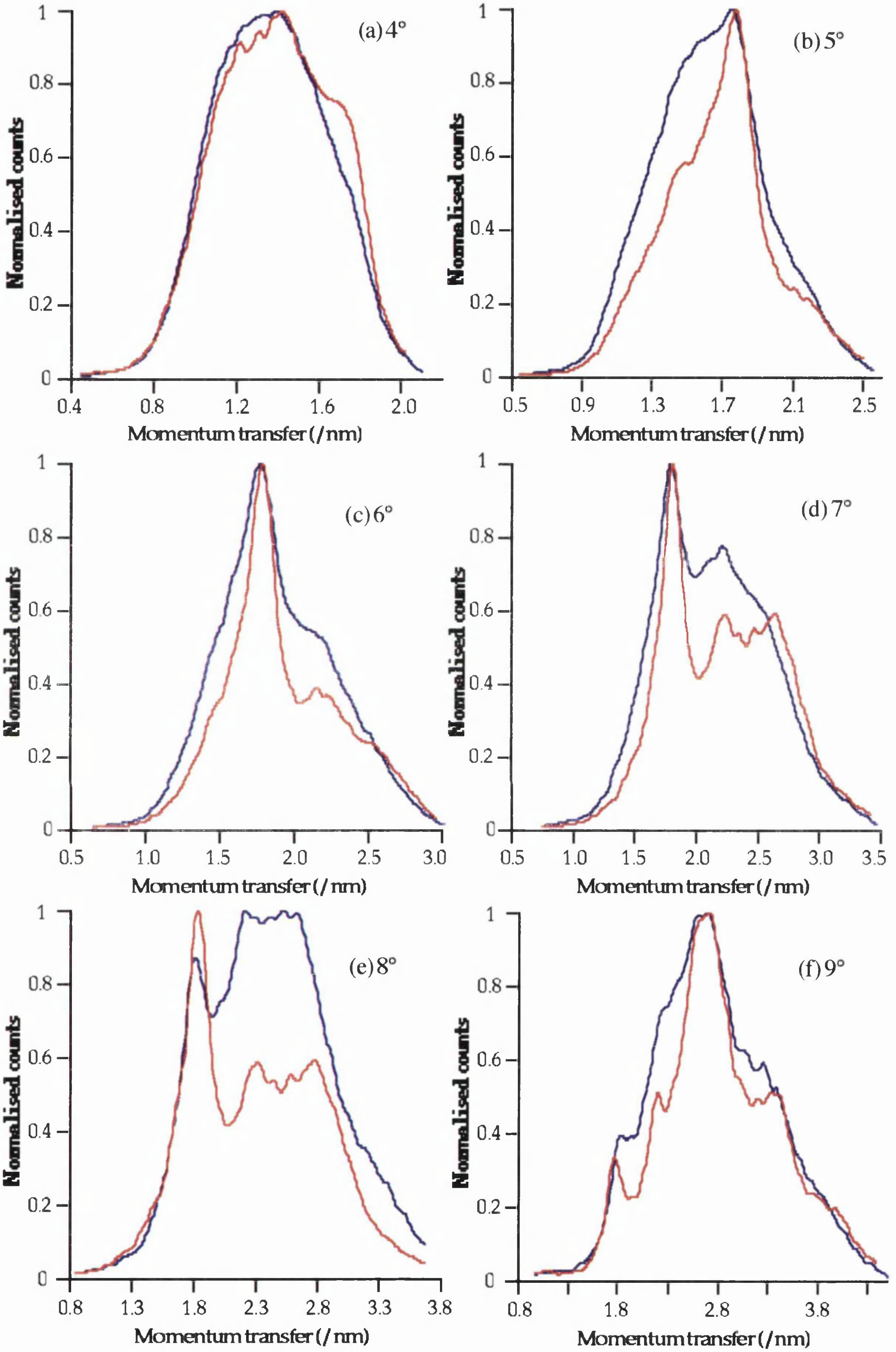

Figure 3.10 Comparison of energy dispersive scatter patterns of fresh bone (bone and marrow) with dry bone (bone only) at various scatter angles. The fresh bone pattern is the blue line and the dry bone is the red line. Both patterns are normalised to unity for comparison of the shapes.

3.3 Performance of the apparatus

3.3.1 Resolution of the momentum transfer

An ideal measurement system would consist of a point source, a point object and a point detector. In this case all detected photons would be scattered by the same angle. However in practice this cannot be attained. The actual measurement system employed is imperfect; the components have finite size and the detector does not record the exact energy of every photon. These factors convolve with the infinitely narrow line data of the true spectrum to produce the observed measured spectrum, (figure 2.10 compared the shapes of the true and the measured spectra). The peaks of the measured spectra are broader than the true spectra. The degree of peak broadening is determined by the resolution of the momentum transfer. Excellent momentum resolution leads to very well defined patterns, with the system capable of resolving closely adjacent peaks, whereas poor momentum resolution leads to less well defined patterns with broader peaks.

The factors which degrade the momentum resolution of the system depend upon which measurement technique is employed. The following discusses each in turn.

3.3.1.1 The energy dispersive technique

The factors which contribute to the momentum transfer resolution of the energy dispersive technique are the following:

(i) The energy resolution of the detector,

(ii) The angular resolution.

Energy resolution

These scatter patterns are recorded as a function of energy of the scattered photons,

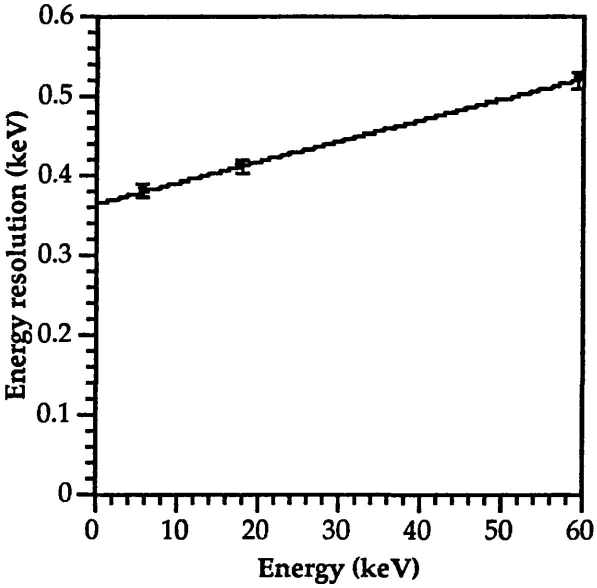

Figure 3.11 The measured energy resolution as a function of energy over the energy range of interest. The equation of the line is f(x)=0.00261x+0.3646. The values are at FWHM.

hence poor energy resolution in the detection apparatus will be convolved with the patterns resulting in broader peaks. The germanium detector used in the experiments has excellent energy resolution which does not significantly widen the peaks in the measured patterns. Figure 3.11 shows the measured energy resolution as a function of energy.

The error in the momentum transfer due to the energy resolution is given by equation (3.2).

$$x + \Delta x = \frac{1}{\lambda + \Delta\lambda} . \sin\left(\frac{\theta}{2}\right) \tag{3.2}$$

The relationship between λ in Angstroms and energy E in keV is λ=12.39842/E (by putting the values into λ=hc/Ee), so substituting into (3.2) gives

$$x + \Delta x = \frac{E + \Delta E}{12.39842} . \sin\left(\frac{\theta}{2}\right) \tag{3.3}$$

At 35 keV and 6°, for example, $\Delta x = 0.019\text{nm}^{-1}$ where Δx is the peak width at FWHM.

Angular resolution

The finite width of the slits imposes an error on the scatter angle at which the measurement is made. Energy dispersive measurements require a well defined scatter angle due to the variation in the shape of the scatter pattern with angle (seen in figure 3.6). The energy of each of the peaks is angle dependent. Varying the angle causes the positions of the peaks in the energy spectrum to change, therefore, a spread of angles will widen the peaks.

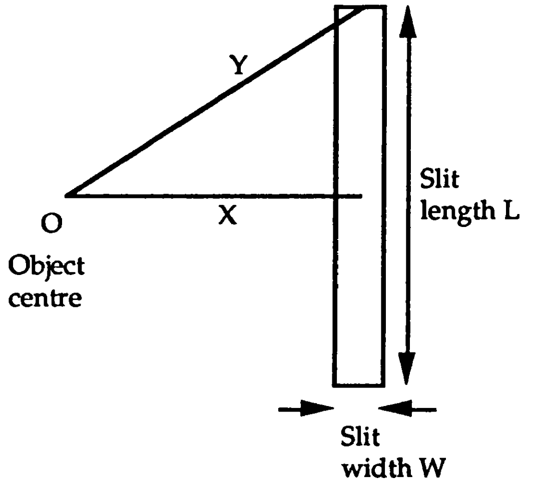

Figure 3.12 Angular error due to the slit. The incident photons pass through O perpendicular to the page. They are scattered into the page towards the slit. The dimensions X and Y are the components in the plane of the paper, perpendicular to the incident beam.

The angular resolution is determined by the slit width and the slit length of the detector collimators and the object-to-collimator distance. The effect of the finite slit dimensions is to cause a broadening of the scatter peaks due to the range of angles allowed through to the detector. The thin slit widths (generally 1mm) and large object to detector collimator (D2) distance (36cm) produce an error in the detected scattering angle perpendicular to the slit length of only ±0.16°. Hence very small changes in scattering angle can be made. The slit is 2cm in length. The length of the slit reduces the overall angular resolution of the apparatus but is necessary due to the low intensity permitted by pinhole collimation. Figure 3.12 demonstrates the effect of the slit on the angular resolution of the apparatus.

The angular range of the scattered photons allowed through the slit lies between the following values (calculated geometrically from figure 3.12)

$$\theta_{min} = \theta - \tan^{-1} {}^{W}/_{36} \tag{3.4}$$

$$\theta_{max} = \tan^{-1} \frac{\sqrt{36^2 \tan^2\theta + \left({}^{L}/_{2}\right)}}{36} \tag{3.5}$$

(36 is the distance in centimetres from the object to detector collimator D2)

The graphs showing the intensity profiles of the collimators along the width and length (figure 3.5) represent the collimator response in these directions. From these plots the values of the collimator response at FWHM for the width and length was 0.9mm and 2.1mm. If the centre of the slit is at a scattering angle of 6° then the angular range passing through the slit is 5.86 - 6.21°.

The error in the momentum transfer due to the angular resolution is given by

$$x + \Delta x = \frac{1}{\lambda}.\sin\left(\frac{\theta + \Delta\theta}{2}\right) \tag{3.6}$$

Again, substituting for λ=12.39842/E gives

$$x + \Delta x = \frac{E}{12.39842}.\sin\left(\frac{\theta + \Delta\theta}{2}\right) \tag{3.7}$$

At 35keV and 6°, for example, Δx=0.088nm^{-1} at FWHM. This value is much greater than the error due to the energy resolution of the detector.

Estimated value

The total error in the momentum transfer at FWHM (Δx_T) due to both the energy and angular resolution is given by

$$\left(\frac{\Delta x_T}{x}\right)^2 = \left(\frac{\Delta x_E}{x}\right)^2 + \left(\frac{\Delta x_\theta}{x}\right)^2 \tag{3.8}$$

The values calculated in equations 3.3 and 3.7 can be put into this equation in order to find the total error. The previous examples quoted have been at 35keV and 6°, the total error at these values is 0.09nm^{-1} at FWHM. One standard deviation of this error is 0.04nm^{-1} (given by FWHM=2.3548σ), due primarily to the angular resolution.

3.3.1.2 The angular distributive technique

The main factors which degrade the momentum resolution of the angular distributive technique are the following:

(i) The polychromaticity of the x-ray source,

(ii) The angular resolution of the apparatus.

X-ray source polychromaticity

Ideally the angular distributive diffraction patterns should be produced using a strictly monoenergetic beam. The precise angles at which interference occurs depend upon the wavelength of the x-rays and the separation of the scattering sites. In a given object the latter will be constant, so a spread of incident wavelengths will lead to a spread of scatter angles at which interference occurs. This will lead to a broadening of peaks in the diffraction pattern: the larger the wavelength spread the broader the diffraction peaks.

Section 3.2.1 discussed the use of near monoenergetic sources for the angular distributive source and found them to be inadequate due to the photon intensity. Measurements have therefore been made with the polychromatic beam from a tungsten target tube. Such a large degree of polychromaticity leads to a significant smearing of the measured pattern.

Angular resolution

The values calculated for angular resolution in the previous section (3.3.1.1) apply to this situation also. The broadening effect of the angular resolution is significantly less in this case than that caused by the source polychromaticity.

Estimated value

A value cannot be quoted for the momentum transfer resolution for this technique due to the problems of estimating the smearing effect from such a polychromatic beam. The measured patterns show it to be significant and much greater than that for the energy dispersive technique (see figure 6.1 for a comparison of the two techniques).

3.3.2 The stability of the x-ray tube operating parameters

3.3.2.1 Effect of the tube kV on the scatter pattern

The shape of the recorded energy dispersive scatter pattern has some dependence upon the shape of the incident spectrum. Energies of high photon intensity will obviously cause an elevated region of the scatter pattern than energies of a lower intensity. Hence, variation of the overall kV between measurements leads to a shifting of the incident spectrum, and hence, a variation in the relative heights of the resultant scattered spectrum.

Repeat measurements were performed with the x-ray tube operating at a different kV in each case on a thoroughly mixed powder sample of 40% calcium carbonate and 60% polyethylene (which produces a scatter pattern with two distinct peaks, see figure 2.15). Figure 3.13 shows a plot of the ratio of the calcium carbonate peak to the polyethylene peak as a function of tube kV. The scatter pattern retains the same overall shape at

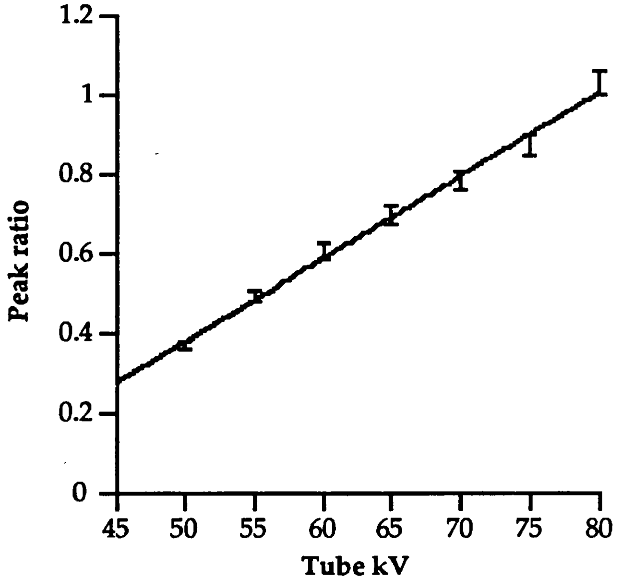

Figure 3.13 Variation of the ratio of the peak heights of the 40% $CaCO_3$ sample with tube kV. The error bars plotted were determined from the measured precision of ~2.5% for these measurements (see § 6.5.1). The equation of the straight line passing through all error bars is; f(x) = 0.02081731x - 0.6620601.

different kVs but the relative heights of different parts of the pattern differ. This is expected because of the variation of the incident x-ray spectrum with kV: at 50kV the incident x-ray spectrum peaks at 29keV whereas at 80kV the peak is at 33keV. Therefore the relative intensities of incident photons at given energies varies with tube kV, and this will distort the scatter pattern.

Significant variations in the x-ray tube kV between measurements will lead to errors. For example, an overall increase in kV from 70 to 71kV throughout the measurement will increase the measured peak ratio by 2.5%. During the measurements in this thesis, however, long exposures are made using a fully 'warmed-up' tube so such large fluctuations are unlikely. Repeat measurements of the incident spectrum using the germanium detector with very fine pinhole collimation have shown the kV to remain constant between exposures. Problems due to kV fluctuations may become significant in the case of very short exposures of high intensity. This problem can be overcome, however, using a kV meter to monitor the kV of the tube output during a measurement.

Angular distributive measurements are not significantly affected by kV variations but are affected by intensity changes. Conversely, intensity fluctuations do not affect the energy dispersive measurements.

3.3.2.2 The stability of the x-ray flux

For the purpose of measuring angular distributive scattering patterns a constant intensity x-ray tube output is necessary for the duration of a continuous scan of several minutes in order to produce a perfect diffraction pattern. Variation in the x-ray intensity incident on the object will distort the shape of the resultant diffraction pattern due to the scan time corresponding to particular scattering angles. Therefore, significant fluctuations in the x-ray beam intensity will require normalisation.

The output of the x-ray tube was monitored over long, continuous exposures to investigate time variations. Repeat exposures were compared in order to see whether the intensity levels varied between scans. The HPGe detector was used to record the x-rays; pinhole collimation reduced the photon flux to a measurable level. The MCS program sampled the total number of photons reaching the detector within the 20 - 60keV energy range every second and plotted the result.

It was observed that a more stable output was achieved if the x-ray generator had been on for at least 30 minutes and the x-ray tube had been fully 'warmed-up', i.e. several exposures had previously been made. Figure 3.14 shows the output as a function of time for this situation. The output is seen to be constant within the statistical levels for the entire duration, so normalisation of the incident intensity is not required.

A closer inspection of the beginning of the exposure is seen in figure 3.15. This plot indicates that all measurements should be started after the tube had been exposing for at least 10 seconds in order for the tube voltage to stabilise.

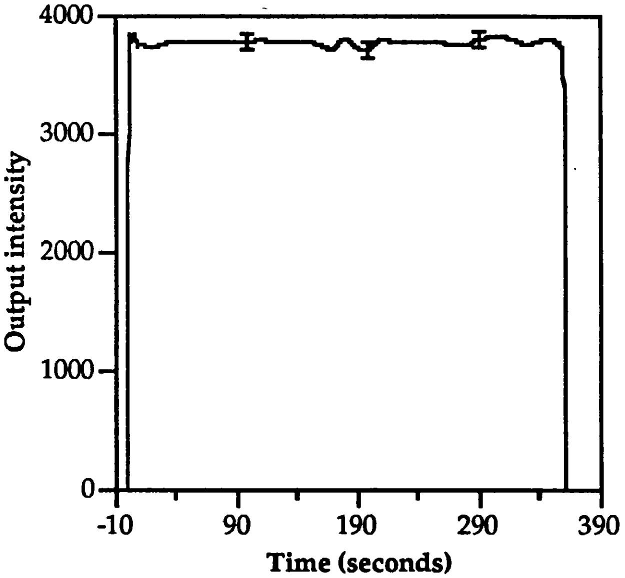

Figure 3.14 Plot to demonstrate the stability of the x-ray tube output. The size of the error bars are shown.

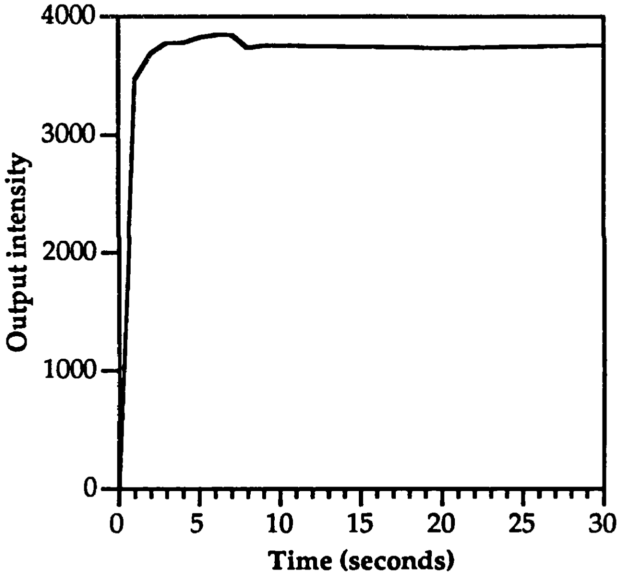

Figure 3.15 X-ray tube output during the first 30 seconds of the exposure.

3.4 Test phantoms for scatter measurements

3.4.1 Tissue substitute materials

The materials used to construct some of the test phantoms are epoxy resin based tissue substitute materials (White *et al* 1977). The material consists of an epoxy resin base (namely Araldite with a suitable hardener) into which particulate fillers, such as polyethylene, calcium carbonate, PVC, phenolic microspheres, etc., are added to produce the density and attenuation values of the required tissue. The quantities of the components to produce a particular tissue are described by White *et al* (1977). Following careful weighing they are mixed under vacuum for 1 hour and then poured into a mould and left to cure for 24 hours. The last three hours of curing are at 80°C. When cured the materials are sufficiently hard to be machined and so can be cut to any shape.

The density and attenuation properties of the substitutes provide a close approximation to the tissue simulated. Hardie-Brown *et al* (1987) conducted scatter measurements on these tissue substitute materials and found them to be adequate for scatter measurements, they reported, however, that they behaved like slightly lower effective atomic number materials (0.5 - 1 lower) than the actual tissues for coherent scatter at the energy and scattering angle used.

3.4.2 Two-component structured bone substitute materials

Trabecular bone is a two-component tissue consisting of interconnected regions of bone and marrow. The tissue substitute materials discussed in the previous section and the phantoms they were used to construct were designed to simulate the photon attenuation and physical density of the bulk tissue material, and so are ideal for densitometers which measure this parameter. A set of realistic anthropomorphic phantoms which simulate varying degrees of osteoporosis were designed and built. These are for use as test phantoms for densitometers and are briefly described in appendix 2. Further details are given in Royle and Speller (1992).

However, the technique proposed in this project is able to separate the measurement of the bone from that of the marrow tissue within a single measurement of the trabecular region. Therefore, two component bone substitute materials are required to produce phantoms for this technique. They may also be required for other methods which contain more information in the measurement than just the bulk density, such as high resolution NMR or CT.

The following subsections describe the phantom materials which have been developed that simulate both bone and marrow in the trabecular region.

3.4.2.1 Perfusing dry, human bone with marrow tissue substitute

Two previously dried, human mandibles were obtained from the University College hospital school of dentistry. The intention was to fill the spaces in the bone network with a marrow tissue substitute. Then the bone could be sliced into thin sections and bits of the bone chipped away and replaced by marrow substitute, thus simulating osteoporotic bone loss. Further details are given in Benn and Royle (1990).

The epoxy resin based adipose substitute AP6 of White *et al* (1977) was used to simulate the fatty marrow tissue. Fatty marrow consists of ~96% adipose tissue and so has very similar properties. The epoxy resin based substitutes, when in their liquid state prior to hardening, are fairly viscous. Hence, to ensure complete perfusion of the liquid throughout the network of minute spaces within the bone it was necessary to attach a long tube to the bone down which the liquid could be poured. A 50cm height of the liquid created sufficient pressure to force it into all the spaces.

The marrow perfused through all the spaces, and the bone did not crumble on sectioning. The bone was sectioned using a thin diamond cutting blade to prevent much bone from being lost. The technique was successful, however, it was a difficult and time consuming process. The mandible was chosen because the marrow spaces in it are fairly large. Bones such as vertebrae and the femoral neck have much smaller marrow spaces which will increase the difficulty of the process, so it was decided to find a simpler approach.

3.4.2.2 Powder suspension materials

In order to construct a series of two component bone phantoms in which the relative quantities of the bone and the marrow substitute could be varied it was decided to simulate a simplified bone structure by suspending particles of bone substitute within a marrow substitute.

A non-particulate two phase system, such as trabecular bone, consists of a large number of randomly oriented scattering sites, each contributing to the overall scattering process. In this sense it behaves very much like a powder (Porod 1982). Hence, for diffraction purposes trabecular bone is similar to a powder suspension of bone tissue in marrow.

A set of two component phantom materials have been developed which employ suitable powders in suspension in a marrow substitute to simulate trabecular bone. In order to achieve a useful phantom the following physical properties need to be simulated;-

(i) Scattering properties: The coherent scatter necessary for diffraction is dependent upon the atomic number of the medium. Hence, simulation of the effective atomic number (Z_{eff}) is required.

(ii) Ratio of bone to marrow: The degree of osteoporosis that the phantom is simulating depends upon the quantity of bone present. Varying the quantity of bone substitute alters the osteoporotic state of the phantom.

(iii) Geometrical properties: A simplified simulation of the structure of trabecular bone can be achieved by using bone substitute powder of similar size to the thickness of bone found in human trabecular tissue.

The trabecular structure, as previously mentioned, shows a honeycomb network of hard bone, typically 100-200μm thick, enclosing marrow spaces, typically 600-1000μm across. The hard bone has an average effective atomic number over the energy range employed of 13.41. This can be approximated by aluminium powder (Z=13) of ~200μm diameter in the correct density of suspension (i.e. to achieve the required trabecular spacing) in a material that simulates marrow tissue. The adipose substitute AP6 (of

White *et al* 1977) was used to simulate the fatty marrow.

The description of trabecular structure given would indicate that a trabecular substitute would be better achieved by suspending powdered marrow substitute within bone substitute rather than vice versa. However, the measurements of the scatter patterns obtained in this project are dependent on the relative quantities of the bone and the marrow. Therefore, it makes no difference in terms of the results which one is used as the powder. The bone substitute (aluminium) was used in powdered form because, as the quantity of it determines the degree of osteoporosis, it was easier to regulate the quantity of powder used in the manufacture of the material.

The effective atomic numbers of the body tissues were calculated from the elemental compositions of the tissues (Woodard and White 1986) using the method of Yang *et al* (1987), details of this and tabulations of the atomic numbers of body tissues are given in appendix 3.

The correct proportions of Al powder and AP6 to simulate trabecular bone can be determined by calculating the fraction of each necessary to produce the same value of Z_{eff} as trabecular bone. A mixture of 38% by weight of aluminium and 62% AP6 produced a value for Z_{eff} of 9.91 compared to 10.01 for trabecular bone. Closer approximation could be achieved by increasing the Al contribution but this would increase the density further. Table 3.2 shows the densities of each of the materials made.

The phantoms were cylindrical in shape with a diameter of 3.0cm, thus approximating the neck of the femur.

Material No.	% weight of AP6	% weight of Al powder	Al powder size	Density g/cm ^{3}
1	62%	38%	125μm	1.293 ± 0.004
2	70%	30%	125μm	1.208 ± 0.004
3	80%	20%	125μm	1.120 ± 0.004
4	98.84%	1.16%	125μm	0.983 ± 0.004
5	100%	0	-	0.978 ± 0.004

Table 3.2 Aluminium powder bone substitutes.

3.4.2.3 Encasing femoral heads

Several femoral heads were obtained from the Royal National Orthopaedic hospital following hip replacement operations. Five of these were encased within a cylinder of muscle tissue substitute MS11. The encasing muscle resin prevents the bone from decaying. The phantom was built such that the bone was in the centre of the cylinder, away from the edges. A surrounding cylinder consisting of a layer of muscle within a ring of adipose was made, within which the cylinders containing the bone would fit. This produced a very realistic phantom of the upper thigh. Figure 3.16 shows the dimensions of the phantom.

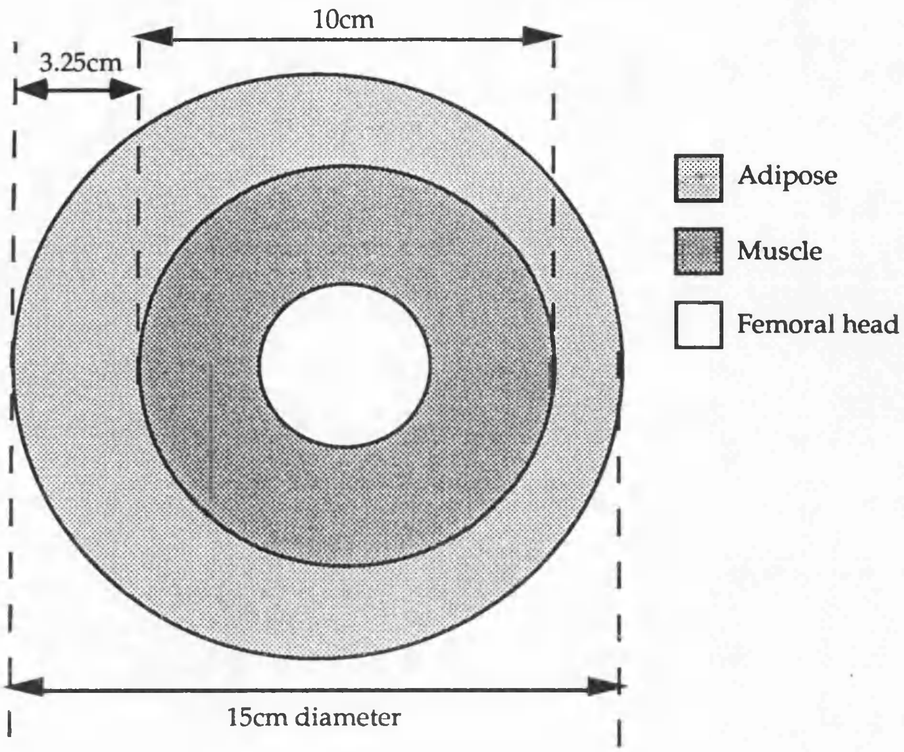

Figure 3.16 Phantom of the upper thigh containing the human femoral head. The height of the phantom is 9cm.

In this thesis the powder suspension phantoms are employed to test the performance of the apparatus, and the encased femoral head phantoms are used to assess the capabilities of the technique for the diagnosis of osteoporosis. The results are given in chapter 6. Prior to this attention needs to be paid to the factors which degrade and distort the measured pattern. Firstly a computer simulation of the technique is employed to quantify the level of non-elastically scattered photons within the measured patterns, and secondly procedures are considered to obtain a purer signal from the observed signal.

- 4 -

Computer simulation of the experiment

A realistic simulation of the experimental situation is useful for understanding the interactions taking place. Information on the exact nature and position of each photon interaction cannot be known in this experiment. Ideally the experimentally obtained scatter pattern would result purely from single coherent scatter within the region of interest, however, in the true case the pattern is degraded by Compton scattered photons, multiple scatter and photons scattered from outside the region of interest. A significant contribution of any of these factors to the final diffraction pattern would require correction for that factor in the data analysis. A computer simulation in which the path of each photon is traced through the object can provide the required information and so identify the correction required.

4.1 The Monte Carlo simulation

The most accurate and effective method for studying a photon history is using Monte Carlo techniques (Raeside 1976, Chan and Doi 1983). This method applies random numbers to known probability distributions in order to simulate a particular physical process. By generating a random number r^* ($0 < r^* < 1$) it is possible to produce a random sample x^* from the distribution F(x). If the function is the cumulative probability given by F(x) = Probability (X<x) where X is the variable, then the variable X will be randomly selected; the selection being weighted according to the particular probability distribution. For example, consider the selection of a photon from an x-ray spectrum. At each energy, x, the cumulative probability is given by the ratio of the total number of photons emitted between 0 and x to the total number of photons emitted (see figure 4.1). The probability distribution will

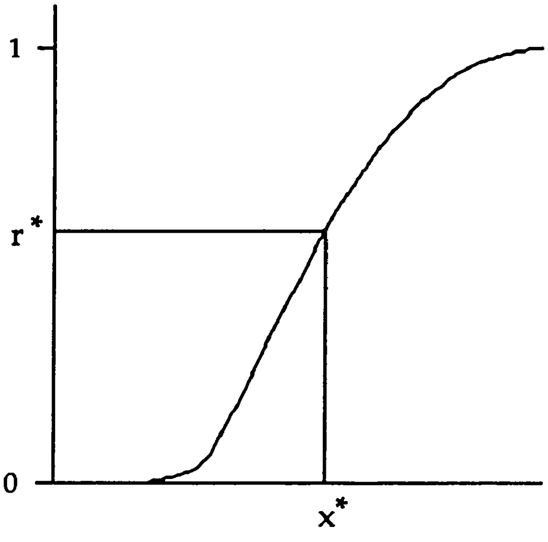

Figure 4.1 Random selection of a value from a weighted probability distribution.

have values between 0 and 1.

Generation of a random number r* between 0 and 1 will equate to a probability value and, hence, a value of energy x^*.

Monte Carlo methods are commonly used for studying photon or electron histories and have many applications in medical physics, for example, absorbed dose calculations, determination of the efficiencies of gamma-ray detectors, etc., (see Andreo 1991).

For many years Monte Carlo simulation of coherent scatter was mainly disregarded in medical physics due to the low frequency of its occurrence and the fact that it was considered to be heavily forward peaked and so indistinguishable form the transmitted primary beam. However there has been interest in recent years to study the degree of scatter at small angles, often for the purpose of studying the effectiveness of anti-scatter grids for radiographic imaging (Neitzel *et al* 1985). Models to simulate coherent scatter have been proposed (Persliden and Carlsson 1986, Williamson and Morin 1983) in order to do this.

4.2 The Monte Carlo photon transport code

The code used for this work was adapted from the basic Monte Carlo code of Koligliatis (1990). Various alterations and improvements were made to the code, in particular to the coherent scatter routine, to give greater accuracy and efficiency. Moreover the required code was adapted to simulate the experimental situation in this project, and so the following alterations were necessary;-

(i) The geometry is very relevant to the experiment and so slit collimation along with the correct intensity profile was required at both the object and detector, together with the appropriate apparatus and phantom dimensions.

(ii) The experiment focuses on the trabecular region of bone and identifies the two separate components (bone and marrow) within that region, hence the phantom modelled must simulate both components.

(iii) The requirement of information on the types and nature of the interactions occurring warrants that the relative proportions of single coherent scatter, single Compton scatter and multiple scatter from the object in energy steps of 1keV over the whole range and in angular steps of 0.5° from 0-10° are known.

A flow chart of the code used is shown in figure 4.2. The program was written in FORTRAN 77 and all computing performed on Sun workstations. The random number generator employed was a tried and tested routine from the Sun library.

More details on the points listed and other important parts of the code are discussed in the following subsections.

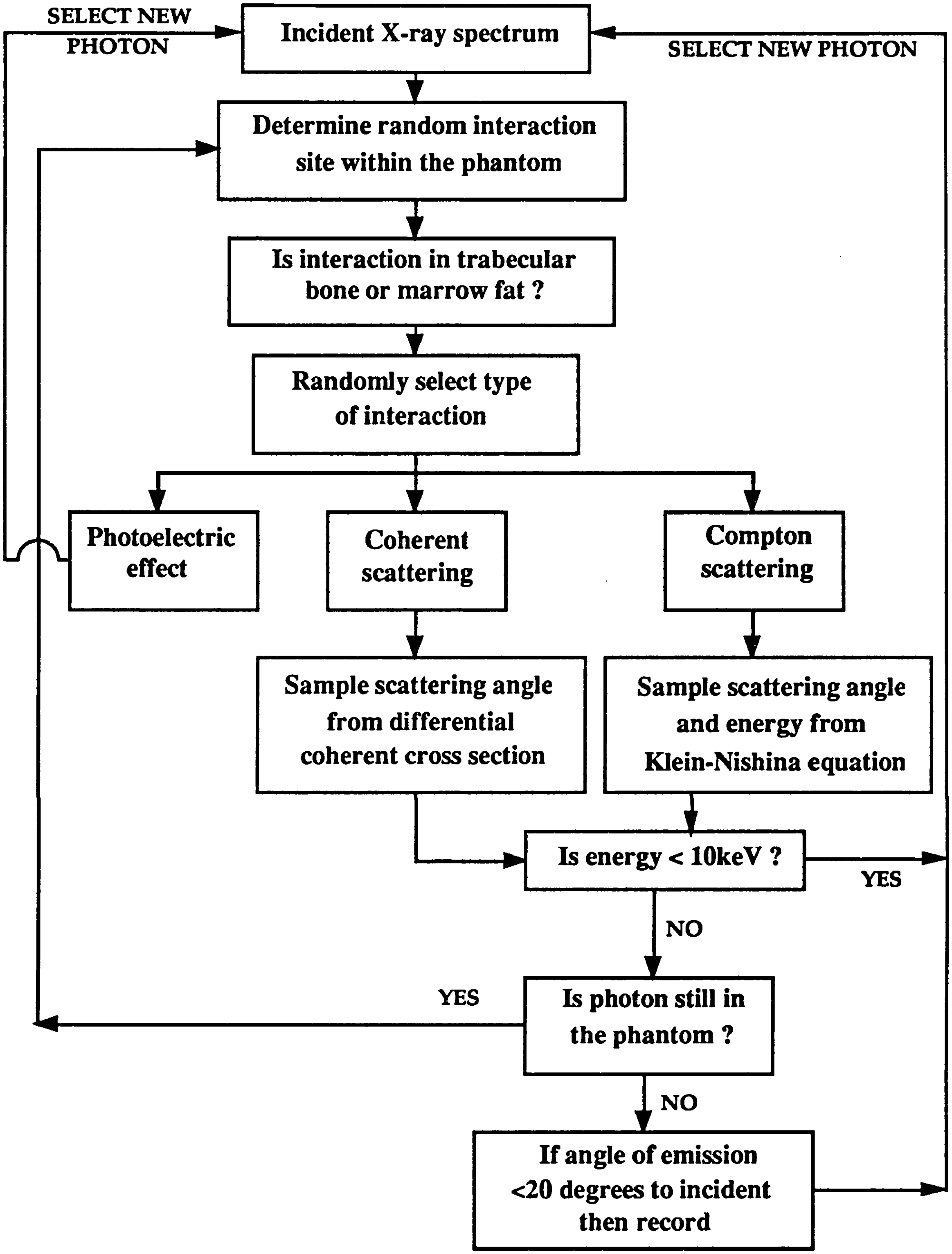

Figure 4.2 Algorithm flow chart for simulation of photon transport through the phantom by Monte Carlo methods.

4.2.1 Incident x-ray spectrum

The experimental incident x-ray spectrum was generated by a tungsten anode x-ray tube operating at 70kV with 1mm Al filtration (described in § 3.1). For the computer model the relative photon output for a spectrum at the same conditions was taken from the data of Birch *et al* (1979) to simulate the incident spectrum. The cumulated probabilities of the spectral data were calculated in 1keV intervals such that random selection of the photon energy would produce the correct energy distribution.

4.2.2 Input data

The elemental attenuation coefficients used in this program were taken from the data of Storm and Israel (1970). The coefficients for molecules were calculated using the mixture rule,

$$\mu = \sum_i \sigma_i(Z_i, E_i) n_i \qquad (4.1)$$

where n_i is the percentage composition by weight of element i and μ_i is its attenuation coefficient. The elemental composition of the body tissues was taken from the data of Woodard and White (1986).

Interpolation to smaller energy intervals than given in the data was achieved using a spline fitting routine on the Sun graph plotting package GRTOOL.

The attenuation data was also used to calculate the relative interaction probabilities for each material and at each energy using the relationship μ_{int} / μ_{tot}, where μ_{int} is the attenuation coefficient due to the interaction type (i.e. coherent, Compton or photoelectric) and μ_{tot} is the total attenuation coefficient.

The other input file was for the coherent scatter form factors, these are of particular interest and are discussed in detail in § 4.3.

4.2.3 Apparatus and phantom geometry

The geometry of the model was designed to simulate the experimental arrangement (described in chapter 3). In the model the x-rays emanate from a point source at a distance of 50cm from the centre of the object (the same as experiment). For each x-ray a coordinate is selected by Monte Carlo methods on the surface of the phantom within a region simulating the shape of the x-ray collimator. The region is a vertical slit 1mm in width and 20mm in height. The intensity profile of the x-rays across the slit is shown in figure 4.3.

A profile similar in shape was modelled also along the length of the slit. These profiles simulate the intensity profiles for the collimators in experiment (see figure 3.5). This profile was achieved by generating a random position within the boundaries of the slit and then taking the inverse sine of this value to be the position of the photon.

Slit collimation at the detector was achieved by grouping the scattered photons into angular bins of the appropriate width and height.

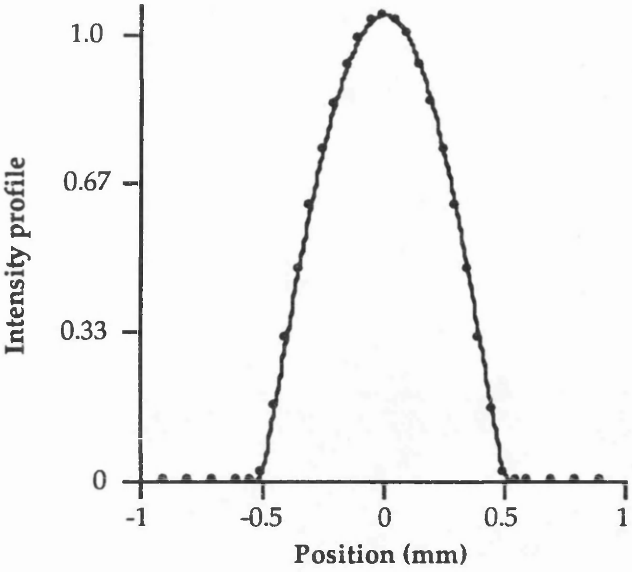

Figure 4.3 Incident x-ray intensity profile across the width of the slit.

The phantom is described by a set of ellipsoids. The a and b parameters of each ellipse can be varied as can the central coordinates of each ellipse. The height of each ellipse is much greater than the height of the x-ray beam, any photon which is scattered in a vertical direction is not followed. The number of ellipses and the material they represent is dependent on the object being modelled. Patient studies of the femur, for example, involve four concentric cylinders centred on the origin as shown in figure 4.4

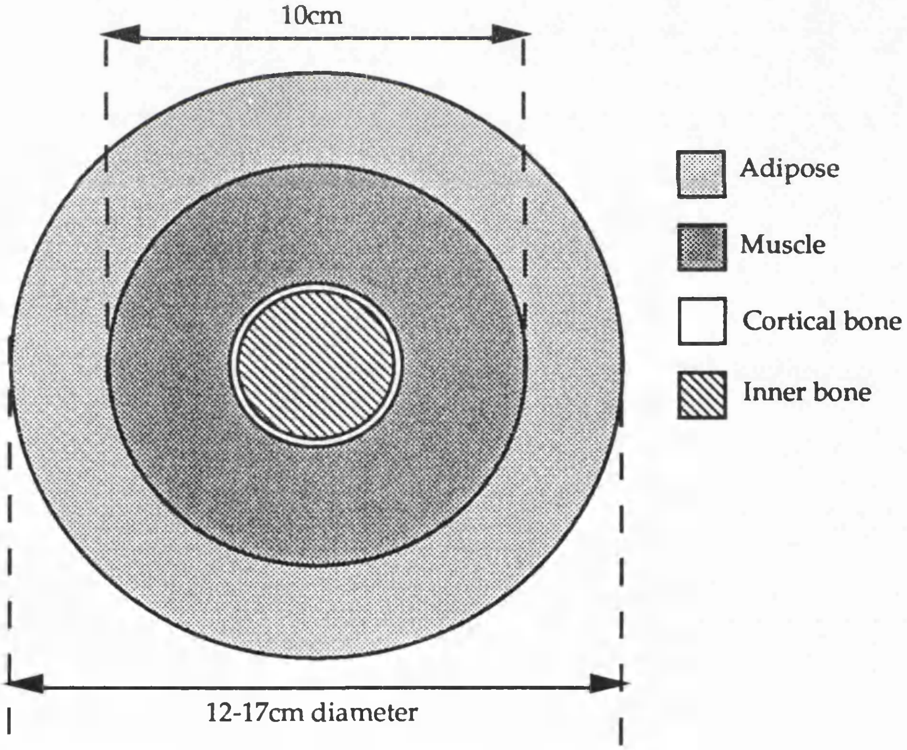

Figure 4.4 The femoral neck phantom modelled in the simulation. The diameter of the inner bone is 3cm. The surrounding layer of cortical bone is 1mm. All are circles centred on the origin.

The dimensions of the muscle tissue, hard bone and inner bone were kept constant. The diameter of the adipose tissue was varied between 12 and 17cm to investigate the effect of overlying tissue thickness on the scatter contribution.

4.2.4 Simulation of two-component trabecular bone

As described previously (§ 1.4) trabecular bone contains both marrow and hard bone, the relative percentages of each of these components vary during osteoporosis, thus causing a density change. For this project it is necessary to study the individual components within the trabecular bone, rather than the properties of the bone as a whole. To simulate the two components of bone in the model when the photon interacts within the trabecular region a decision is made as to whether the interaction takes place in the marrow or the bone. This is done by initially entering a value (between 0 and 1) for the volume fraction of bone in the trabecular region, then when an interaction occurs in the trabecular region a number is randomly generated between 0 and 1, if this number lies below the value of the percentage volume of bone then the photon is considered to have interacted in bone and the properties of bone are then used to describe the interaction. Otherwise the interaction is in marrow. The density of the total trabecular region can be calculated from the percentage volumes of each component.

4.2.5 Monte Carlo simulation of the photon interactions

The photon interactions in the diagnostic energy range, namely coherent scatter, Compton scatter and the photoelectric effect, have been fully described in § 2.1 and appendix 1. When tracing a ray through a material the probabilities of each of these interactions must be considered. The relative frequencies of the three interactions depend upon the object and the energy. In the model the interaction type is selected by Monte Carlo means using the relative interaction probability data for the object at the particular energy. Having selected the interaction type, routines are required for deciding the effect of that interaction upon the photon. The following section discusses how these processes are simulated.

4.2.5.1 Compton scatter

The Compton scatter effect was modelled using the rejection technique described by Khan (1956). This technique employs the Klein-Nishina description of Compton scatter in order to select the energy deposited and, hence, the resulting direction of the Compton scattered photon. This method has been found to provide good agreement between theoretical and experimental results. It was implemented into the code by Horrocks (1988) and later Koligliatis (1990). During the course of this project this routine has been checked but not altered.

4.2.5.2 Photoelectric effect

A photon undergoing a photoelectric interaction imparts all of its energy to the atom. In biological tissues the resulting characteristic radiation has a very low energy (<5keV) and so will be locally absorbed. Therefore, the photoelectric effect can be effectively modelled for this experiment by stopping the photon.

4.2.5.3 Coherent scatter

The coherent scatter effect was modelled using a technique for inversion-rejection sampling (Williamson and Morin 1983), as follows;-

A random number r_n is generated and substituted into equation 4.2 in order to define X*, the momentum transfer,

$$r_n = \frac{\int_0^{X^*} F^2 \, dx}{\int_0^{X_{max}} F^2 \, dx} \tag{4.2}$$

where $X_{max} = \alpha k \sqrt{2}$, $\alpha = h\nu_o/mc^2$ and k is a constant with a value of 29.1445. Integration is performed in the computer model using the trapezoidal rule. The value chosen for momentum transfer is then used to select the scattering angle, θ, from equation 4.3,

$$(\cos\theta) = 1 - \left(\frac{X^*}{\alpha k}\right)^2 \tag{4.3}$$

Accept cosθ if it satisfies the condition

$$r_{n+1} \le \frac{(1+(\cos^2\theta)}{2} \tag{4.4}$$

where r_{n+1} is a separately generated random number. If condition (4.4) is satisfied the value for cosθ is rejected and the three steps are repeated using a different set of random numbers.

The angles selected by this technique are energy and material dependent, thus simulating the true case. Therefore, providing the correct input data is used for the coherent form factors, F(x), a computer generated coherent distribution will mimic experiment.

4.2.6 Photon detection

In order to simulate the experiment the photons need to pass through two slit collimators before they can be recorded. This was achieved in the following manner; consider two larger, concentric cylinders surrounding the cylindrical object, one cylinder being larger than the other (see figure 4.5). The coordinates at which the photon crosses each of these cylinders are determined. If the angle between the incident beam and the line from the origin to the first crossing point is equal, within an acceptance angle, to the angle between the incident beam and the line from the origin to the second crossing point, then the photon is recorded.

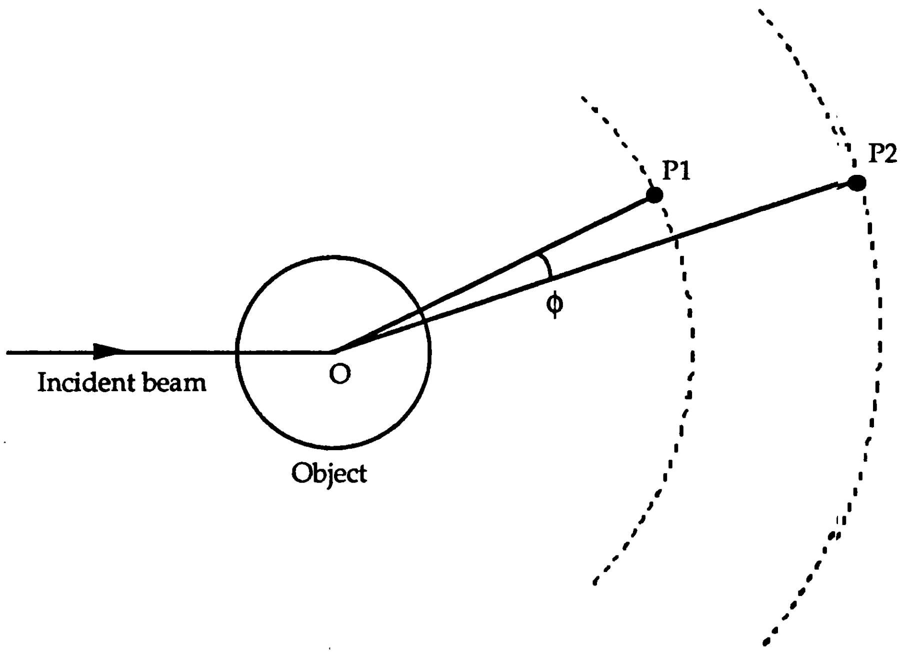

Figure 4.5 Simulating the acceptance angle of the detector collimation.

The geometry of the slit collimators was set in order to produce an acceptance angle in the horizontal plane of ±0.11° (the same as the experimental value). This eliminates all those photons which are scattered by a region of the phantom outside of the scattering volume. Photons scattered in the vertical direction which hit the detector cylinder more than 1cm above or below the height of the origin are stopped and not recorded as they lie outside the length of the detector slit.

The photons which passed through both collimators were recorded in energy intervals of 1keV and angular intervals of 0.5°. This produced the scattered energy spectrum between 10 and 70keV at each angular step over the 0 - 10° range. It was obtained for single coherently scattered photons, single Compton and multiple scatter.

In order to limit the computing time photons whose final angle of scatter was greater than 20° were stopped as they would not yield useful information.

4.3 Coherent form factors

The importance of the correct coherent form factors in mathematically modelling coherent scatter at small angles was discussed previously (§ 2.2). The form factors currently available provide a close simulation at regions where no interference exists, and so cannot be used for this work. The conclusion reached was that the form factors can only be used to investigate scattering at small angles if they are derived from experimental diffraction data. The only tabulated data of this type currently available is for water (Morin 1982). This problem limits the usefulness of coherent scatter results obtained by modelling, and so the program was confined to calculating the contribution of Compton and multiple scatter to the patterns. More use could be made of this simulation when the correct data is available.

Form factors were determined for this work which provide a reasonable simulation to the experimental case. The experimental form factors of water (Morin 1982) were used to model adipose, muscle and marrow tissue. Muscle contains a high proportion of water (74%) and so this is a valid approximation. Adipose and yellow marrow (both very similar in content) contain a smaller proportion of water (21%). However, comparison of the computing results obtained with experimental results showed this to be a good approximation (§ 4.4.2).

Form factors for bone tissue were achieved in the following way; the mixture rule was used to determine the sum of the form factors of the individual elements (Hubbel *et al* 1977) within bone weighted according to the percentage composition. This is known to be incorrect at small angles so modifications were made to the data such that the computing results approximated the shape of the experimental results (see § 4.4.2 for the comparison).

4.4 Verification of the computer model

4.4.1 Coherent scatter routine

The coherent scatter routine used in the computer model was tested by comparing the result for single coherent scatter within a cylinder of water with experimental diffraction data for water reported by Morin (1982). This is shown in figure 4.6.

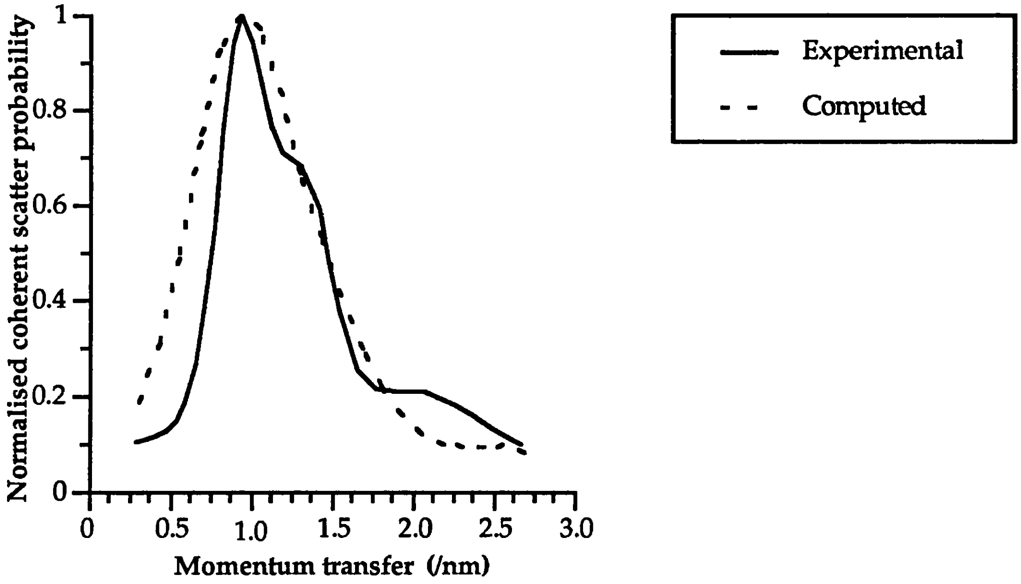

Figure 4.6 Comparison of the probabilities of coherent scatter to various scatter angles in water for the Monte Carlo program and the experimental diffraction data of Morin (1982). The curves were normalised to unity.

The simulated incident source was a 40keV photon beam emitted from a point source.

10^8 photon histories were followed. The scatter object was a cylinder of water 3cm in diameter and infinite in height.

The shapes of the curves are seen to be similar which indicates that the coherent scatter routine in the Monte Carlo model provides an adequate simulation of coherent scatter.

4.4.2 Coherent scatter form factors

In order to test the quality of simulation of the form factor data employed in the Monte Carlo model the results were compared with experiment. Figure 4.7 compares the experimental energy dispersive scatter measurement of adipose tissue with the result from the computer model.

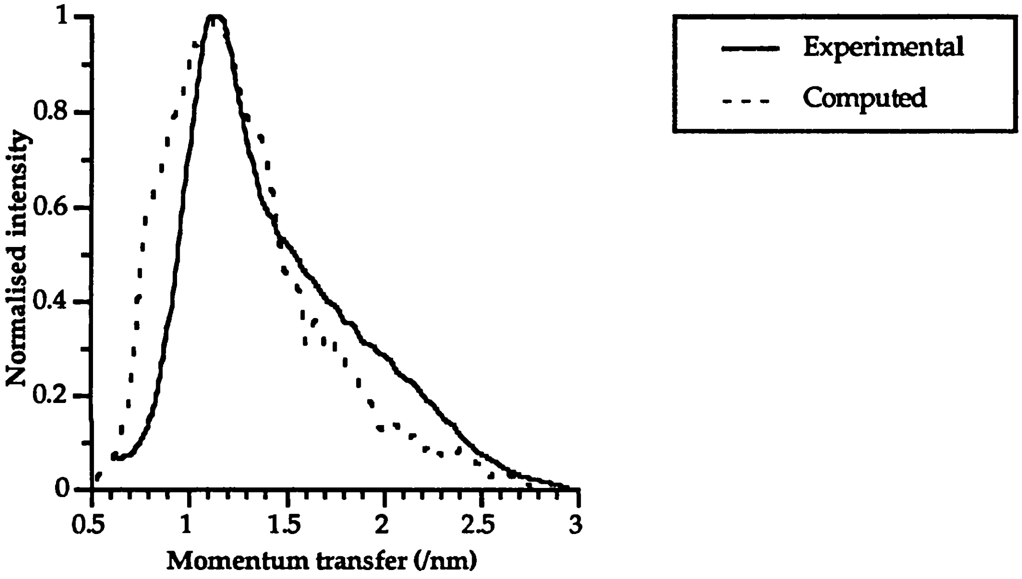

Figure 4.7 Comparison of experimental and computed results for the energy dispersive scatter patterns at 6° for adipose tissue.

The Monte Carlo results plotted are the sum of the single coherent, single Compton and multiple scattered photons, as these are all present in the experimental results.

The experimental arrangement was modelled, as described in § 4.2. A 70kV incident x-ray source was used in both cases, and the computer model recorded the scattered photons in 0.5° intervals and 1keV steps. 10^8 photon histories were traced. The experimental and simulated objects were both 3.0cm in diameter. The background spectrum was removed from the experimental data.

Figure 4.8 shows a similar comparison for bone tissue. Both plots show that the computed results provide a reasonable simulation with the experimental results, which is sufficient for the purposes of this thesis.

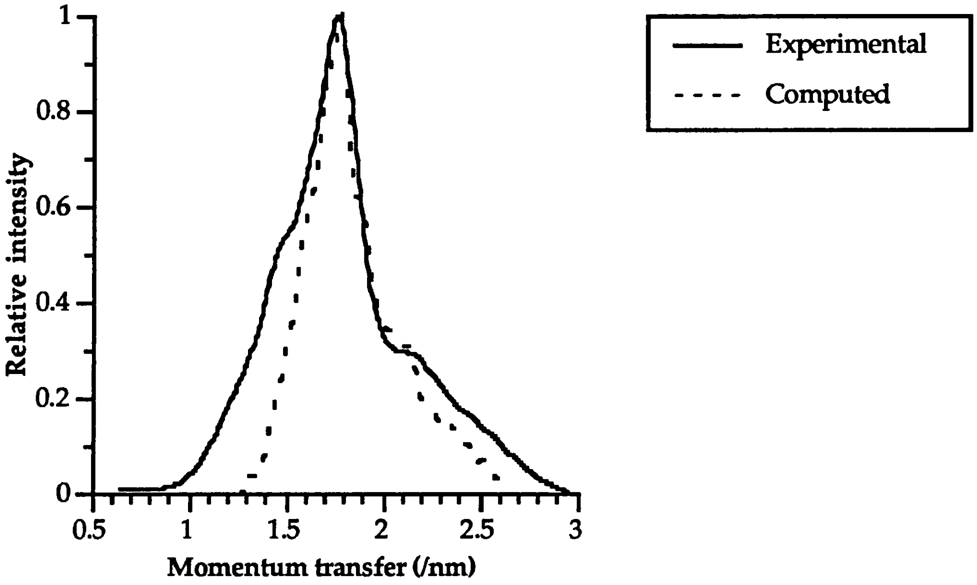

Figure 4.8 Comparison of experimental and computed results for the energy dispersive scatter patterns at 6° for dry bone tissue.

4.5 Results of the computer model

4.5.1 Contribution of Compton and multiple scatter to the scatter patterns

The relative probability of coherent scatter increases with the wavelength of the incident x-rays and the atomic number of the scattering object and decreases with the angle of scatter. The effective atomic number of most biological tissues is low (Z= 7.5 for muscle and 6.4 for adipose), however the abundance of calcium in osseous tissue leads to a value of 13.5, thus elevating its coherent scatter production above that of the surrounding tissue. Figure 4.9 shows the relative interaction probabilities for bone tissue.

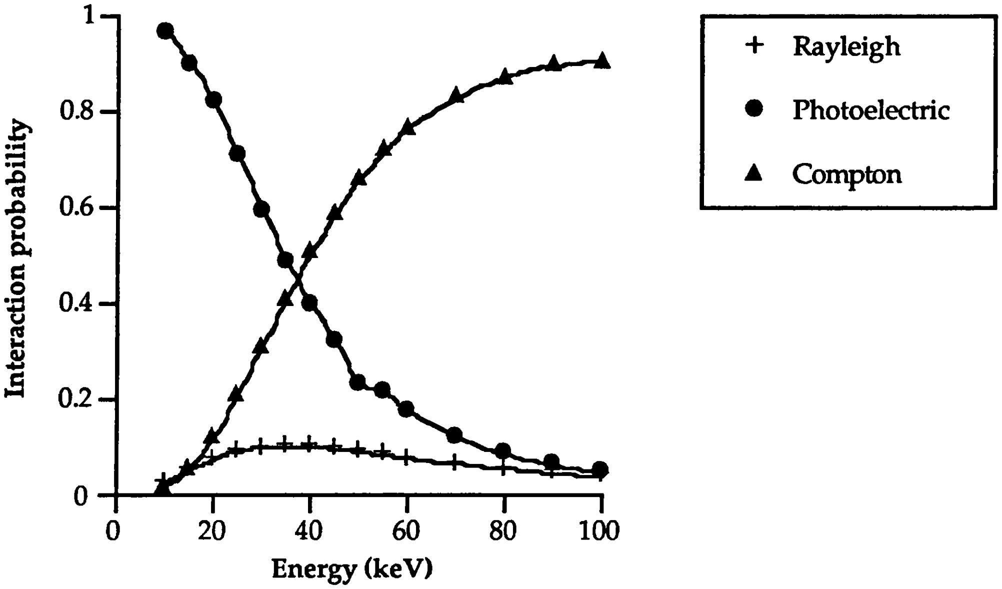

Figure 4.9 Relative interaction probabilities within trabecular bone over 0-100keV.

The total number of coherent events occurring in a material are greatly overshadowed by the number of Compton events. At small angles, however, coherent scattering predominates. Figure 4.10 shows the relative quantities of single coherent, single Compton and multiple scattered photons from a 70kV incident x-ray beam which leave water and trabecular bone at scattering angles below 10°. Both objects were 3cm in diameter.

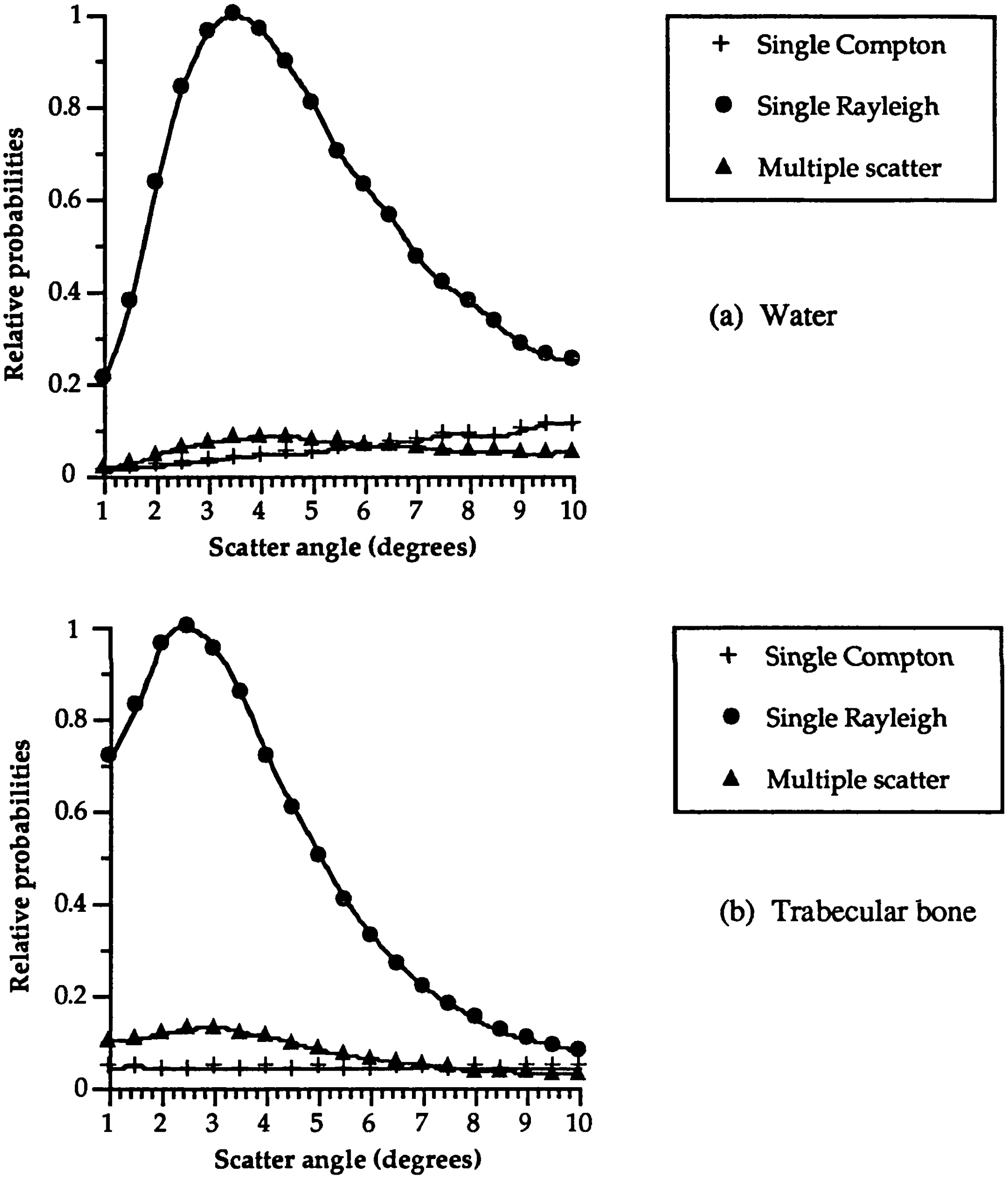

Figure 4.10 Relative scatter probabilities as a function of angle of single coherent, single Compton and multiple scattered photons leaving a 3cm diameter cylinder of (a) water and (b) trabecular bone. 10^8 photons were traced for both simulations.

The contribution of Compton and multiple scattered photons to the energy dispersive scatter patterns (at a scattering angle of 6 degrees) are shown in figure 4.11.

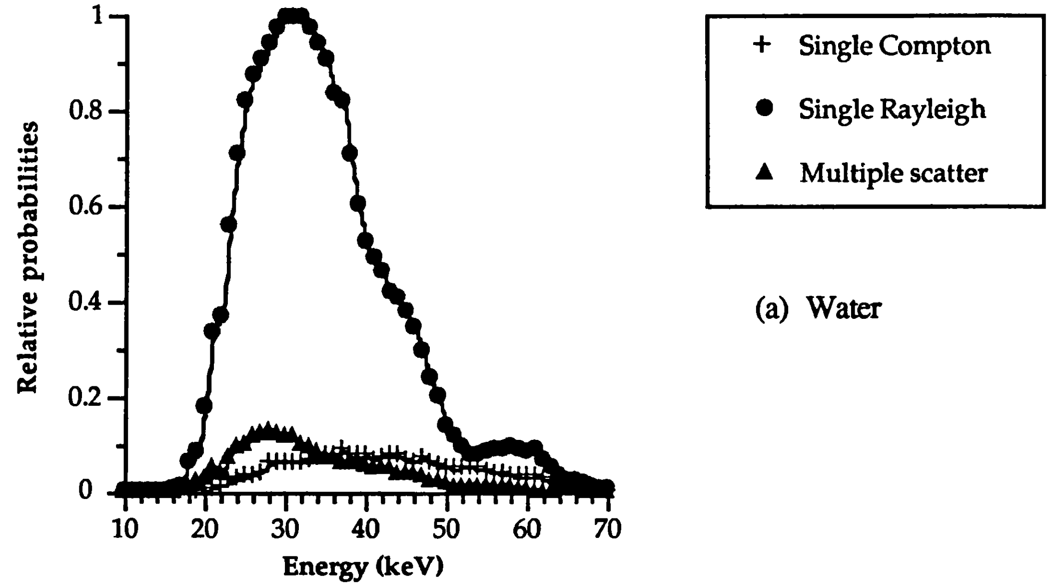

(a) Water

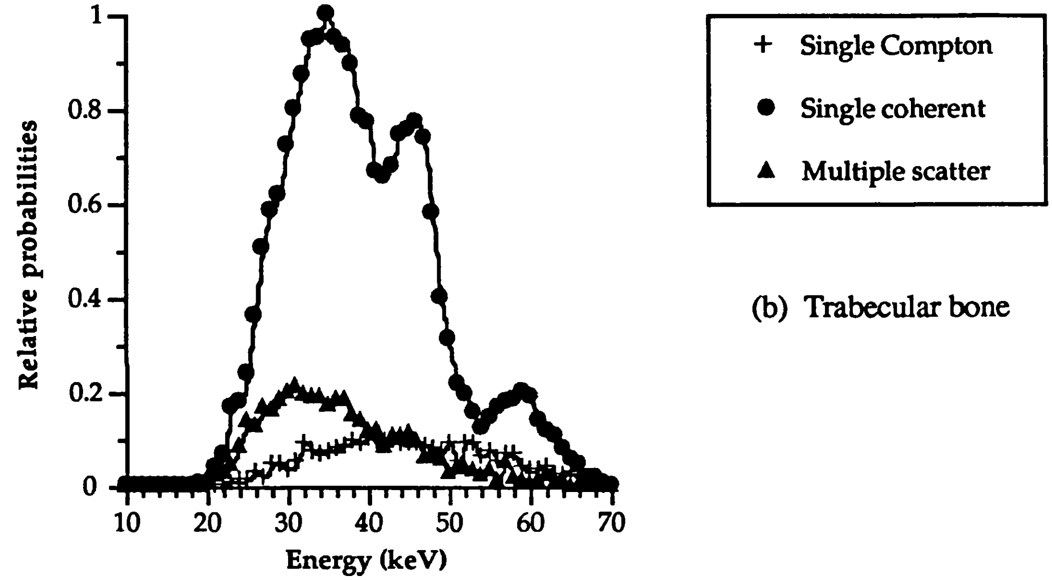

(b) Trabecular bone

Figure 4.11 Relative scatter probabilities as a function of energy of single coherent, single Compton and multiple scattered photons leaving a 3cm diameter cylinder of (a) water and (b) trabecular bone.

These results demonstrate that scattering to the low angle range from a diagnostic x-ray source incident on biological tissues is predominantly coherent, but a small proportion of Compton and multiple scattered photons are present.

It can be seen that the magnitude and variation of the Compton and multiple scatter contribution over the angle and energy range of interest are not such that they will significantly distort the shape of the measured scatter patterns, and so correction will not be required for simply observing the presence of scatter peaks, for example in material characterisation. However the fact that the level of unwanted scatter varies with energy and angle means that ratios of peak intensities will be distorted in quantitative work. This will not cause a problem if the level of unwanted scatter remains constant between the materials being compared, however, if the level varies between comparative measurements then correction will be necessary.

4.5.2 Effect of the decrease in bone-marrow ratio during osteoporosis on the level of unwanted scatter

In this thesis the only quantitative measurements made are to determine the bone-to-marrow ratios in the trabecular region. Bone and marrow tissue have differing effective atomic numbers (13.5 and 6.4 respectively) and so each will scatter differently. The program has been used to investigate whether the osteoporotic change in the quantities of bone and marrow in the trabecular region affects the levels of Compton and multiple scatter produced. This was performed by running the program for various volumes of bone in the scattering region. The bone volumes used in the program were calculated from the densities of the tissues. Hard bone and marrow have specific gravities of 1.92 and 0.92 respectively and the average specific gravity of inner bone is 1.18, (the density values are taken from Woodard and White 1986). The percentage volume of bone required to give this total density is 26%.

Figure 4.12 compares the relative fractions of single Compton, single Rayleigh and multiple scatter in the small angle range (1-10°) as a function of bone volume in the trabecular region. The fractional volumes of bone shown on the graph are 0.26, 0.142 and 0.024 respectively. These values correspond to the density of normal bone and a 10% and a 20% density drop.

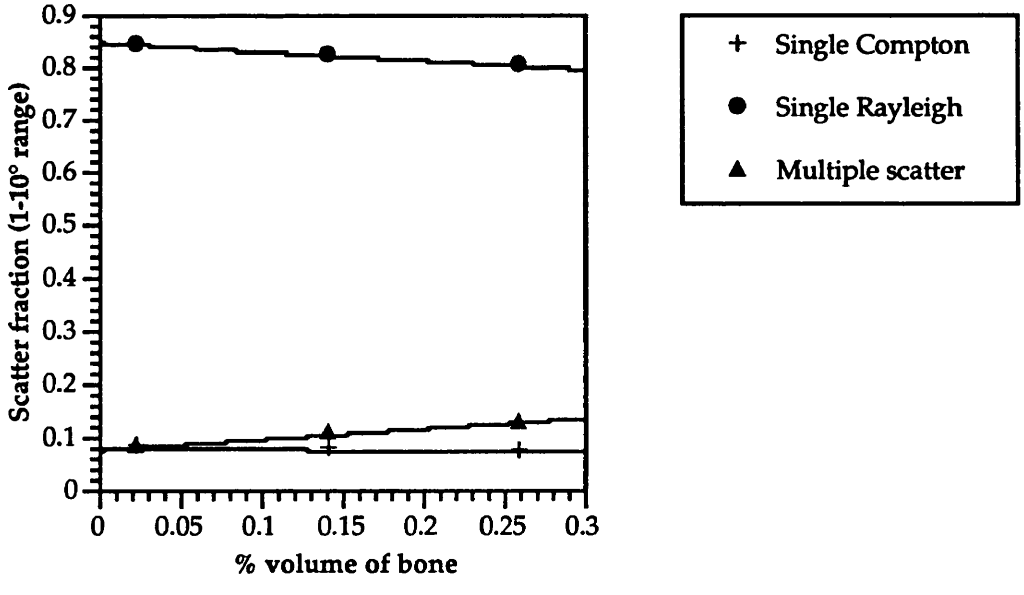

Figure 4.12 The relative quantities of the three forms of scatter which occur in the 1-10° angular range from a 70kV incident x-ray source as a function of bone volume, calculated by Monte Carlo. The scatter fraction is taken to be the total amount of each type of scatter divided by the total amount of scatter in the 1-10° range. Error bars were plotted on the graph but they are too small to show.

A similar graph was plotted (figure 4.13) for the scatter fraction at 6° as a function of the bone volume (for the energy dispersive bone measurements). This plot shows very similar trends.

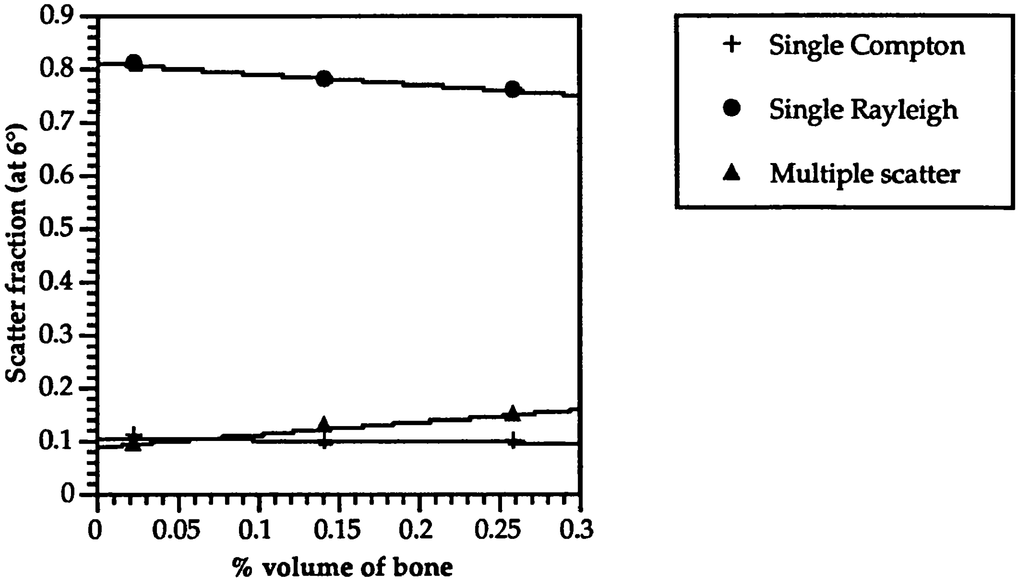

Figure 4.13 The relative quantities of the three forms of scatter which occur at 6° (the angle for energy dispersive measurements) from a 70kV incident x-ray source as a function of bone volume.

These graphs show that as the volume of bone within the trabecular region decreases (as occurs during osteoporosis) the relative quantities of coherent, Compton and multiple scattered photons leaving the bone vary. A decrease in bone causes a linear increase in the coherent and Compton scattered photons leaving the bone and a linear decrease in the multiple scatter. In order to assess the effect of this variation on the measured scatter pattern it is necessary to know the way in which the level of unwanted scatter varies relative to the coherent scatter. This is shown for the fixed angle of 6° in figure 4.14.

Quantitative bone measurements are performed serially with comparison made approximately every six months in order to determine the loss rate. Based upon an average bone loss of 1.2% per year in the trabecular region, the likely decrease in bone between serial measurements will be only 0.6%. Referring to the slopes of figure 4.14 such a loss in bone will cause a 0.27% decrease in multiple scatter and no significant change in the level of Compton scatter. Even a 2% loss of bone will produce only a 0.9% decrease in the relative level of multiple scatter and only a negligible increase in Compton scatter. Such small changes in the level of unwanted scatter between bone measurements will be overshadowed by the statistical fluctuation of the count rate, and so correction is not necessary.

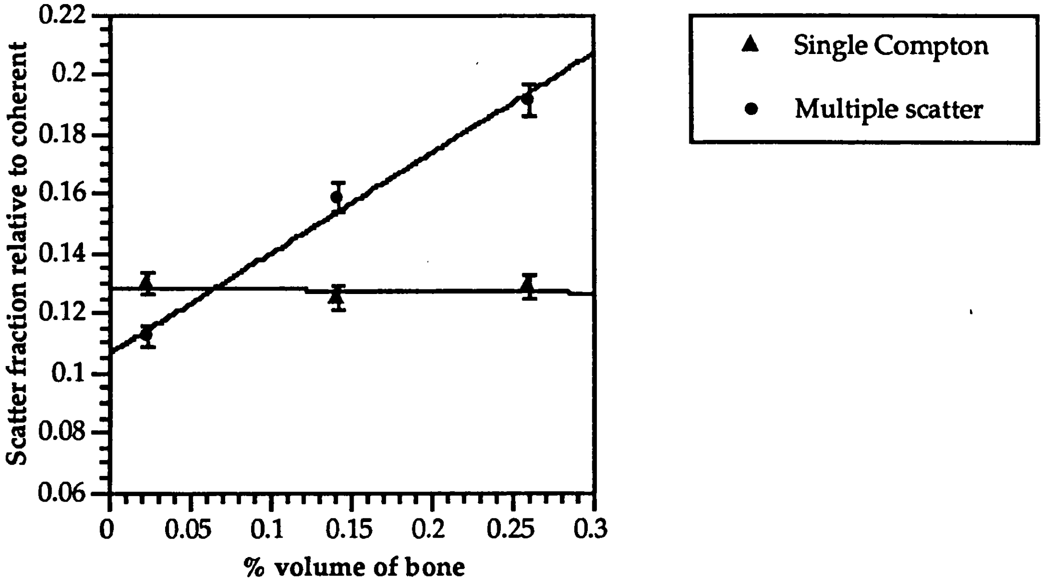

Figure 4.14 Variation of single Compton and multiple scatter relative to coherent scatter as a function of bone volume. The equations of the lines are; f(x)=-0.005484x+0.12833 for single Compton scatter, and f(x)=0.33576x+0.10637 for multiple scatter.

4.5.3 Variation of scatter contribution with phantom size

An increase in the size of the phantom causes the probability of a photon being scattered in the material surrounding the scattering volume to increase. Ideal collimation would eliminate the detection of these scattered photons and so a change in the phantom size would just lead to attenuation of the beam, for which correction can be made (discussed later in § 5.3).

The Monte Carlo program was used to investigate the effect of variation in phantom (or patient) thickness on the relative scatter levels that will be detected using the apparatus geometry of this project. The simulation of the patient's leg (shown in figure 4.4) was taken as the object. The program was run for various outer diameters of the adipose cylinder between 12 and 17cm; the diameters of all other tissues were kept the same.

For each phantom thickness the total amounts of single Compton, single Rayleigh and multiple scattered photons in the 1 - 10° angular range were determined (summed over the 10 - 70keV energy range), and the ratio of each scatter type to the total scatter in the angular range was calculated. Figure 4.15 shows the variation of the various scatter fractions with phantom thickness. For each run 2 x 10^8 photons were traced, this produced an error of <2% in the scatter fractions.

The total level of scattered photons leaving the phantoms decreases as the phantom diameter increases due to the greater attenuation.

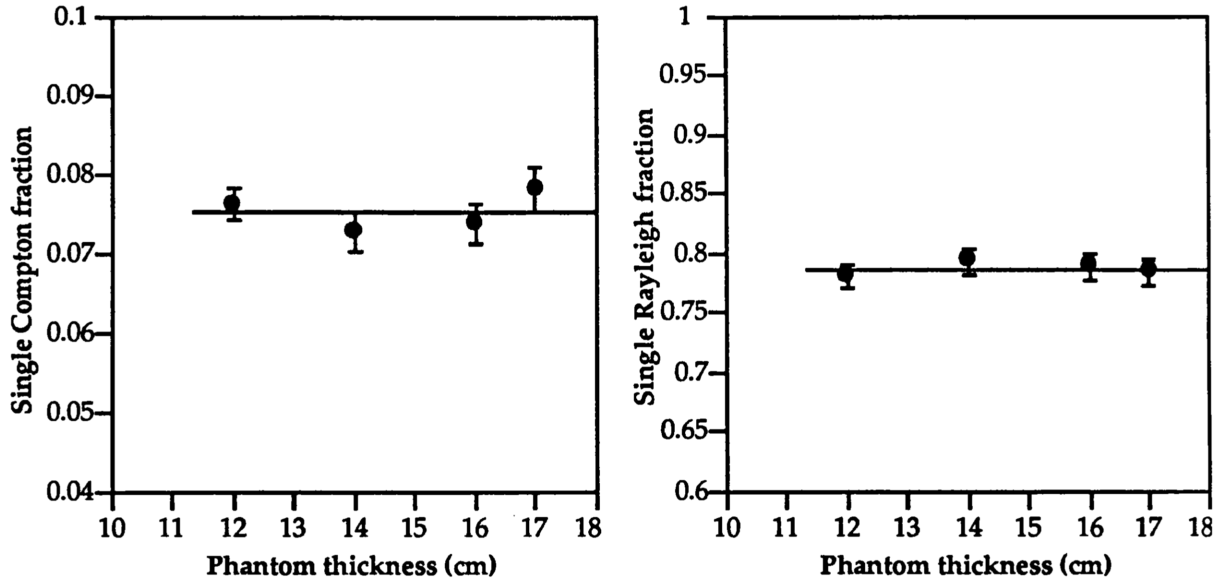

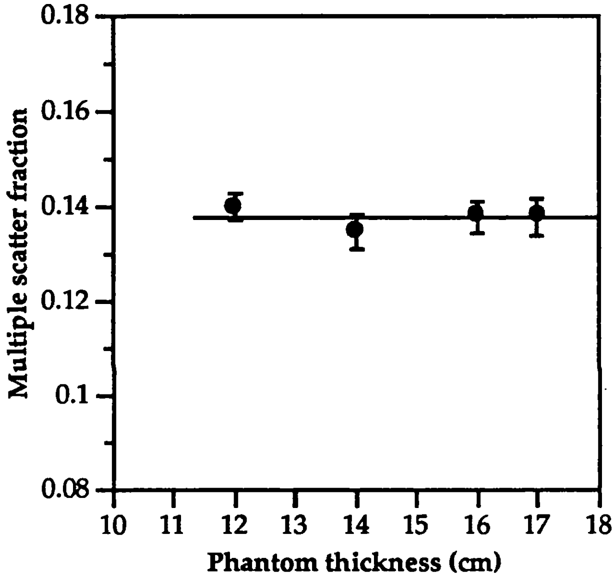

Figure 4.15 Variation of the fraction of each scatter type with phantom thickness.

The three plots demonstrate that for an increase in phantom thickness there is no significant trend in the relative amounts of scatter recorded; they remain constant within the error levels. This indicates that the size and arrangement of the collimation in the apparatus successfully prevents photons scattered in the extra layer of adipose from being recorded.

4.6 Future computing work

More use could be made of the program with the availability of the correct form factor data for biological tissues. The program could then provide an accurate simulation of the experiment. A possible use of the program would be to produce calibration curves for various mixtures of substances. The program could be run for a large number of concentrations of the two substances (for example, bone tissue and marrow) and, from the scatter pattern produced, the peak ratios can be obtained. A calibration curve produced in this way would be more accurate than that produced by experiment as it eliminates experimental error. A large number of points could be obtained to produce the curve, the only limiting factor would be the availability of computer time.

- 5 -

Data correction procedures

This chapter considers factors which degrade the scatter patterns and the procedures which can correct for them. Generally in experimental measurement the aim is to measure some underlying, pure signal, however the measurement process is imperfect and the result is a corrupted signal. The scattered patterns recorded are distorted by several factors; correction is often necessary to extract the pure pattern (or at least a purer pattern) from the raw data.

In this thesis factors which distort the patterns can be grouped into two classes; (1) those which require correction for comparative measurements, and (2) those which only require correction for absolute measurement. Class (1) describes factors which differ between measurements, and if a quantitative comparison of data is required these will require correction. The following factors fall into this category;

(a) Reduction of the statistical noise inherent in radiation data,

(b) Removal of the contribution of Compton or multiple scattered photons from the pattern,

(c) Correction for beam hardening effects in surrounding tissue. This is necessary only if the thickness of surrounding tissue varies between measurements producing a different degree of attenuation,

(d) Subtraction of the background radiation.

Class (2) describes effects which remain constant between measurements. For example, with the division of the scatter pattern by a particular function if that function is always the same then it would be unnecessary to divide all patterns by the same function if those patterns are to be compared. The division would only be necessary if absolute values or the true shape of the pattern is required. Factors which fall into this category are the following;

(a) Elimination of the effect of the solid state detector employed to record the data; this involves removal of the effect caused by the non-uniform degree of photoelectric absorption with energy variation,

(b) Elimination of the shape of the incident x-ray spectrum (for energy-dispersive patterns),

The data can be normalised such that the peak is at unity to allow direct comparison of the pattern shapes.

The following sections discuss the implementation of these corrections.

5.1 Statistical noise reduction

Radiation measurements involve an inherent degree of randomness. The number of photons collected from a particular source over a fixed time interval will vary slightly over successive measurements. Spectral measurements at fairly low count rates have a *noisy* appearance due to the statistical error of each data point in the spectrum. The noisy fluctuation distorts the shape of the true signal. The most effective method for reducing the signal to noise ratio is to collect a large number of photons, by increasing either the count rate or the measurement time. However for clinical measurements this is impractical because it would also increase the dose to the patient. Hence a compromise needs to be reached between patient dose levels and statistical error.

Several mathematical techniques exist for reducing statistical noise. One commonly used is binomial smoothing. Applied to a noisy set of data a binomial smoothing routine takes each point in turn and calculates the weighted mean of this point and the four points either side. This removes the noisy appearance of the data but it also removes some of the information present. Small, narrow peaks, when averaged with surrounding points, will be flattened and lost. Thus the shape of the true spectrum will be altered.

A far better approach is to filter out the noise by Fourier techniques to obtain the true, uncorrupted signal. Fourier transformation of discretely sampled data and the requirements of sampling are described in appendix 4.

5.1.1 Optimal (Wiener) filtering

Noise can be removed from a corrupted signal by finding the optimal filter $\phi(t)$ which when applied to the measured signal produces a signal as close as possible to the uncorrupted signal. The optimal filter is given by

$$\Phi(f) = \frac{|S(f)|^2}{|S(f)|^2 + |N(f)|^2} \qquad (5.1)$$

where $\Phi(f)$, $S(f)$ and $N(f)$ are the Fourier transforms of $\phi(t)$, $s(t)$ and $n(t)$ respectively. $s(t)$ is the pure, noiseless signal and $n(t)$ is the noise component, such that the measured signal $c(t)=s(t)+n(t)$.

$S(f)$ and $N(f)$ are not known separately so the optimal filter needs to be determined by plotting the power spectrum of the sampled data $c(x)$. The power spectrum is the square of the modulus of the Fourier transform and is proportional to the sum $|S|^2 + |N|^2$ which gives

$$|S(f)|^2 + |N(f)|^2 = |C(f)|^2 \qquad (5.2)$$

A typical power spectrum of the measured data is shown in figure 5.1,

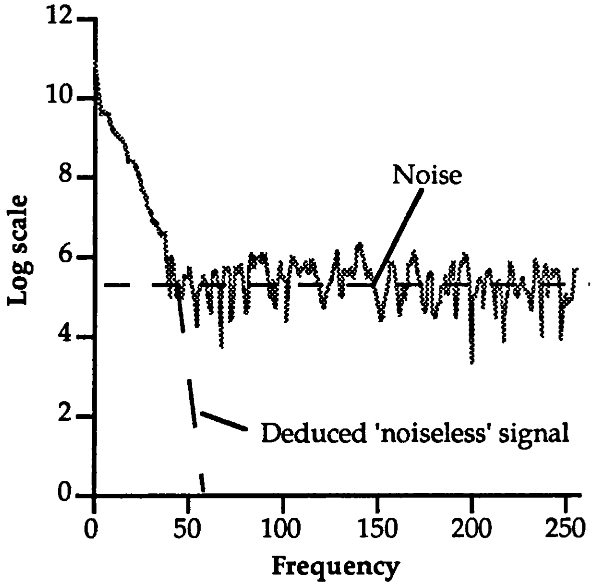

Figure 5.1 Optimal (Wiener) filtering. The power spectrum of signal plus noise shows a signal peak added to a noise tail. The power spectrum is of a typical energy dispersive scatter pattern.

A smooth curve is drawn through the measured signal (signal plus noise). The curve through the noise part of the spectrum is extrapolated back into the signal region to show the noise contribution. Subtracting the noise curve from the measured signal curve presents a smooth 'model' of the signal power spectrum. The optimal filter $\Phi(f)$, therefore, is the quotient of the signal power model to the signal plus noise power spectrum (from equation 5.1). $\Phi(f)$ is close to zero where the noise is negligible, and close to one where noise dominates.

Multiplication of the Fourier transform of the measured data with the optimal filter, and subsequent inverse transformation of the produce eliminates the noise component. An advantage of this technique is that good quality noise reduction does not require a precisely determined filter.

A program for calculating Fourier transforms was written, based on an algorithm described by Press *et al* (1986) for performing a fast Fourier transform on a set of real-valued data points. The same routine was used to calculate the power spectrum and the inverse Fourier transform. The programs were written in Microsoft FORTRAN on a 286 PC and took only a few seconds to compute 512 data points. A few known functions were used to test the quality of the routine and showed it to be satisfactory. The program for filtering the measured data was adapted from these routines.

5.2 Removing the contribution of unwanted scattered photons

Section 4.5 discussed the contribution of unwanted scattered photons to the scatter pattern. The conclusions drawn were;

(1) for characterising materials by the shapes of the patterns the contribution of the unwanted scatter is not sufficient to alter the shape of the pattern significantly,

(2) for quantitative serial bone measurements the level of unwanted scatter does not alter sufficiently between successive measurements for the bone to marrow ratios to be affected.

Therefore, correction is not required for unwanted scatter in this thesis.

5.3 The attenuating effects of surrounding material

The passing of an x-ray beam through an object results in the preferential attenuation of the lower energy photons of the spectrum. This results in an increase in the average photon energy, producing a harder beam.

Considering the measurement of bone tissue in this thesis, the incident x-ray spectrum is hardened as it passes through the surrounding tissue to the scattering volume. The scattered beam is also hardened by the tissue thickness as it exits the patient. This effect would not be a problem if the tissue thickness was constant for all patients, however the overlying soft tissue thickness can vary greatly among patients and can also change in an individual patient during the interval between repeat measurements. The effect of the soft tissue thickness changing between successive measurements is highlighted in figure 5.2.

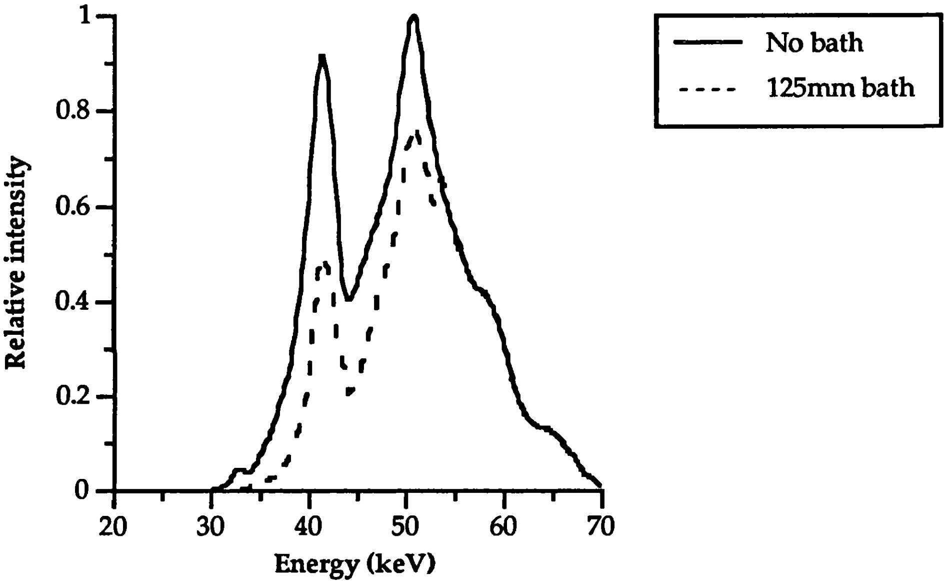

Figure 5.2 Energy dispersive scatter patterns of an aluminium - calcium carbonate powder mixture in air and centred in a 125mm diameter water bath. The scatter pattern in air is normalised to peak at unity and the pattern in water is adjusted accordingly.

The ratio of bone to marrow within a subject is determined in this project by the ratio of the heights of their respective scatter peaks within the energy dispersive scatter pattern (further details are given in § 6.6). The same quantities of bone and marrow may be present but an increase in beam hardening caused by the patient putting on weight will indicate a reduction in the bone component relative to the marrow, thus giving a false diagnosis. Hence, correction will be required.

5.3.1 Beam hardening correction

A possible method for correcting for this effect is to use the equation for the exponential law of attenuation, which states

$$I = I_0.\exp(-\mu x) \qquad (5.3)$$

where the incident intensity I_0 is attenuated to the measured intensity I by a thickness x of the material with attenuation coefficient $\mu(E)$.

The diameter of the leg (or phantom) at the region through which the x-ray beam passes is measured, and, knowing the average thickness of the bone, the total thickness of soft tissue can be estimated. Hence, using the values for the linear attenuation coefficient at each energy for soft tissue (can be determined using the mixture rule and the attenuation data of Storm and Israel (1970)), the true intensity at each energy (as opposed to the measured intensity) can be calculated. The following section discusses applying this correction procedure to account for the change in the ratios of the peaks due to attenuation.

5.3.2 Attenuation correction of the scatter peak ratio

Energy dispersive scatter patterns were measured for a phantom in air and in four different diameter water baths. The phantom consisted of a thoroughly mixed powder sample of pure aluminium powder and calcium carbonate powder. The mixture was in the ratio 30% by weight aluminium to 70% calcium carbonate. Figure 5.2 shows the scatter pattern of the sample (both in air and in a 125mm diameter water bath). This combination of powders was selected because (1) each produces one large diffraction peak in its scatter pattern and (2) the energies at which these peaks occur are very similar to those of bone and marrow tissue in trabecular bone (see figure 6.19 for bone pattern; the $CaCO_3$ and Al peaks occur at 41.45 and 50.80keV respectively, and the bone and marrow peaks occur at 41.55 and 49.02keV respectively). Therefore the attenuation of the two peaks in the powder sample by the surrounding tissue will be similar to the situation of bone tissue.

Water was used to simulate surrounding soft tissue as it has very similar density and attenuation properties (the water was distilled and at room temperature). The water baths were thin-walled (1.3mm) plastic cylinders of the following diameters; 77mm, 94mm, 125mm and 164mm. The powder sample was contained in a thin-walled plastic pot of diameter 39.2mm. This diameter was greater than the length of the scattering volume (19.1mm) to ensure that only the powder sample was included in the scattering volume. The sample was carefully positioned at the centre of each water bath for measurement. The thickness of the water was calculated in each case from the diameters of the cylinders. The sample was also measured in air, this was performed with the sample at the centre of an empty water bath, such that the x-ray beam passed through the same thickness of plastic as in each of the other measurements. Figure 5.3 shows a plot of the ratios of the heights of the Al peak to the $CaCO_3$ peak for each of the water thicknesses.

The only correction applied to the measured values was smoothing using the Wiener filter. A comparison is shown with the theoretical values. The measured peak ratios are seen to be significantly lower than the theoretical ratios. The true curve was obtained using the equation $\exp(-\mu_{Al}x)/\exp(-\mu_{Ca}x)$ where μ_{Al} and μ_{Ca} are the attenuation coefficients of water at the energy of the Al peak (41.45keV) and of the $CaCO_3$ peak (50.80keV) respectively, and x is the thickness of water. This equation describes the way in which the ratios of the heights of the peaks should change for each water thickness due to the change in attenuation.

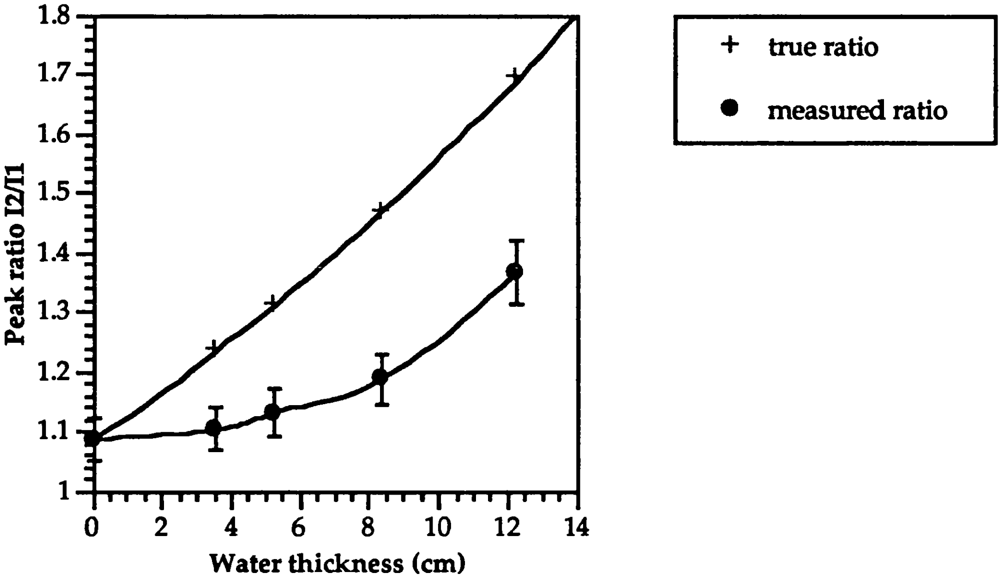

Figure 5.3 Comparison of the measured and theoretical ratios of the heights of the Al peak to the $CaCO_3$ peak at various water thicknesses.

The background spectrum for each thickness was obtained by repeating each measurement with the plastic container empty instead of filled with the powder sample. Each background spectrum was then subtracted from the respective total spectrum and the peak ratios calculated (a typical background spectrum is shown in figure 5.9). Figure 5.4 shows that the peak ratios with background subtracted are equal to the true ratios within the experimental errors.

The measured value was slightly greater in each case than the theoretical value. This was thought to be due to the fact that photons scattered by surrounding water or apparatus which pass through the sample container will be attenuated when the sample is present but not for the background count. This causes a background measurement slightly greater than is the case in the experiment, and so subtraction of the background from the sample spectrum will cause the $CaCO_3$ peak to be reduced by a greater extent than the Al peak (due to the fact that the background spectrum is more intense at the energy of the $CaCO_3$ peak).

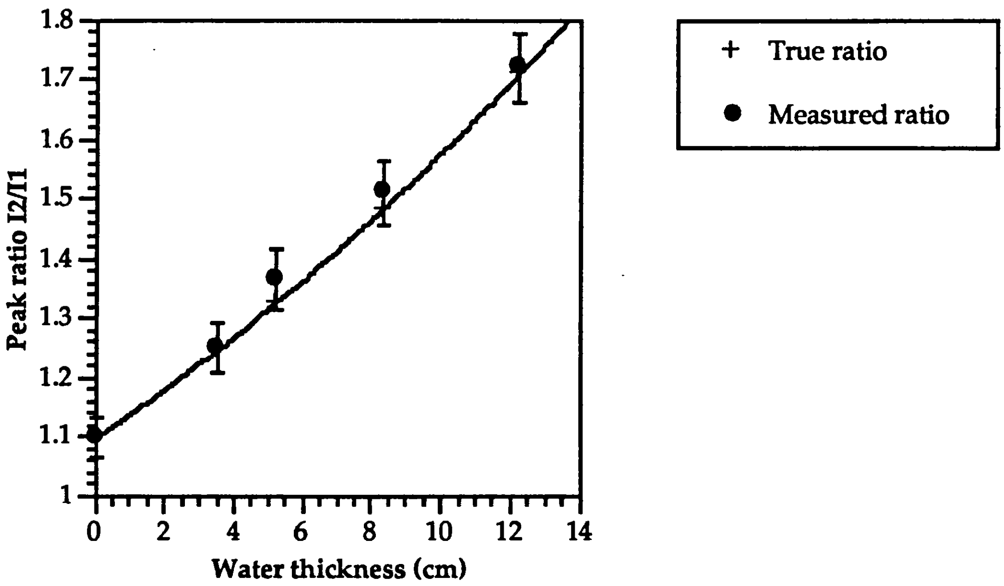

Figure 5.4 Comparison of the theoretical ratios with the background subtracted measured ratios of the Al peak height to the $CaCO_3$ peak height, for various water thicknesses. The line is drawn through the true ratio points.

This section has shown that the exponential law of attenuation can fully account for the change in the peak ratio due to the thickness of surrounding material.

5.3.3 Effect of surrounding material on the pattern shape

An experiment was designed to test whether the water surrounding the phantom affected the shape of the scatter pattern in terms of the positions and widths of the maxima, etc. The scatter pattern of the powder sample was measured (a) in the water bath, and (b) in air but with the same thickness of water attenuating the x-ray beam. Measurement (a) was performed by placing the powder sample, centred in the 125mm diameter water bath, at the scattering volume. Measurement (b) was carried out by placing the 125mm water bath in the x-ray beam between the x-ray source and the first collimator, and placing the powder sample (not in a water bath) at the scattering volume. Such that the same thicknesses of material (both water and plastic) were achieved in both measurements an empty plastic cylinder (identical to the one containing the powder sample) was centred in the water bath for measurement (b), and the same empty cylinder was positioned in the beam between the x-ray source and the first collimator for measurement (a). Figure 5.5 compares the patterns obtained. The shapes of the patterns, in terms of the positions and widths of peaks, and their relative intensities, are very similar for both cases. This indicates that the surrounding material does not significantly affect the shape of the pattern.

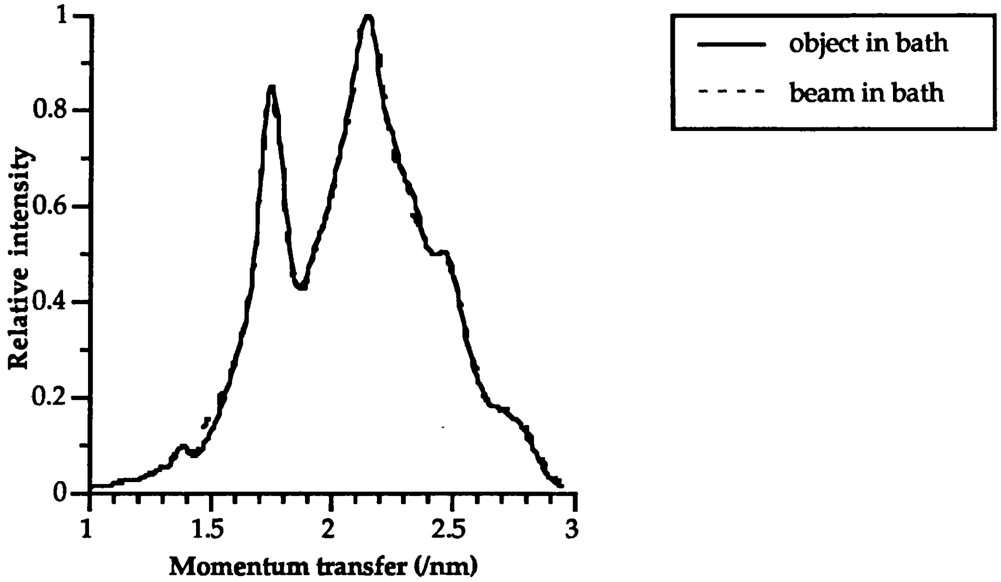

Figure 5.5 Comparison of the energy dispersive scatter patterns for a phantom in a 125mm diameter water bath and the same phantom in air but with the water bath attenuating the beam. The heights are normalised to unity for comparison of the patterns.

These results have shown that the exponential law of attenuation can account for the variation in thickness of the surrounding water and that the surrounding water does not affect the shape of the pattern. Both of these results are consistent with the result from the Monte Carlo program (§ 4.5.3) which demonstrated that the relative proportions of the elastic and the unwanted (Compton and multiple) scattered photons recorded remain constant with variation of the surrounding tissue thickness. An increase in detection of Compton or multiple scatter from the surrounding water would widen the peaks in the scatter pattern and would prevent the exponential attenuation law from fully correcting for the water thickness. The elimination of photons scattered by surrounding material was achieved by careful positioning of the fine collimation.

5.4 The energy dependent efficiency of the detector

5.4.1 Monte Carlo modelling of the germanium crystal

Correct photon detection with an energy sensitive detector requires full energy deposition in a single interaction of every incident photon. This means that each photon must be photoelectrically absorbed on the first interaction within the detector. If the crystal is too thin then it will not stop every photon, this will distort the resulting energy spectrum because the number of photons passing through the crystal will increase with photon energy. Also Compton scattered photons within the detector material cause only partial energy deposition, which gives the effect that a greater number of lower energy photons are present than is the case.

In order to determine whether correction is required for the germanium crystal of the detector, a germanium cylinder with the same dimensions as the detector employed in the experiment (diameter 36mm and depth 10mm) was modelled using the Monte Carlo simulation of chapter 4. The number of photons at each energy which were photoelectrically absorbed on the first interaction in the germanium were recorded. A 70kV x-ray spectrum from a tungsten target (the same spectrum that is used in the experiment) was incident perpendicular to the centre of the germanium. 5 x 10^7 photon histories were traced. The percentage of incident photons which undergo each type of interaction, calculated by computer simulation, are given in table 5.1.

Interaction type	**Percentage of photons undergoing interaction type**
Transmitted through detector	5 x 10^{-4} %
First-time photoelectric interaction	94 %
Single Compton scatter	0.25 %
Scattered then absorbed	5%

Table 5.1 Results from the Monte Carlo simulation describing the relative interaction probabilities within the germanium detector.

Very few photons pass through the detector indicating it to be sufficiently thick for the energy range. Over 99% of incident photons undergo a full energy deposition within the germanium detector (either first-time photoelectric absorption or scatter and then absorption). This shows the detector to be very efficient and so no correction for detector efficiency is required.

A sharp fluctuation in the efficiency of a germanium detector occurs at energies close to 11.103keV, the Ge *k* edge (Fewell and Shuping 1977). This fluctuation was avoided by selecting photons of energies greater than 15keV.

5.5 Background subtraction

The apparatus is very well collimated and the detector is well shielded with lead which prevents the majority of photons which have not been scattered by the object at the correct angle from being recorded. However, a small number of stray photons are still recorded. These are probably due to scatter from the apparatus or surroundings, and, due to the very large number of incident photons, a small proportion will penetrate the lead shielding. The background photon distribution was measured using the same operating conditions as for experiment but with no scattering object present. The distribution for both the energy dispersive and angular distributive techniques are shown in figure 5.6. They have been smoothed using the optimal filter.

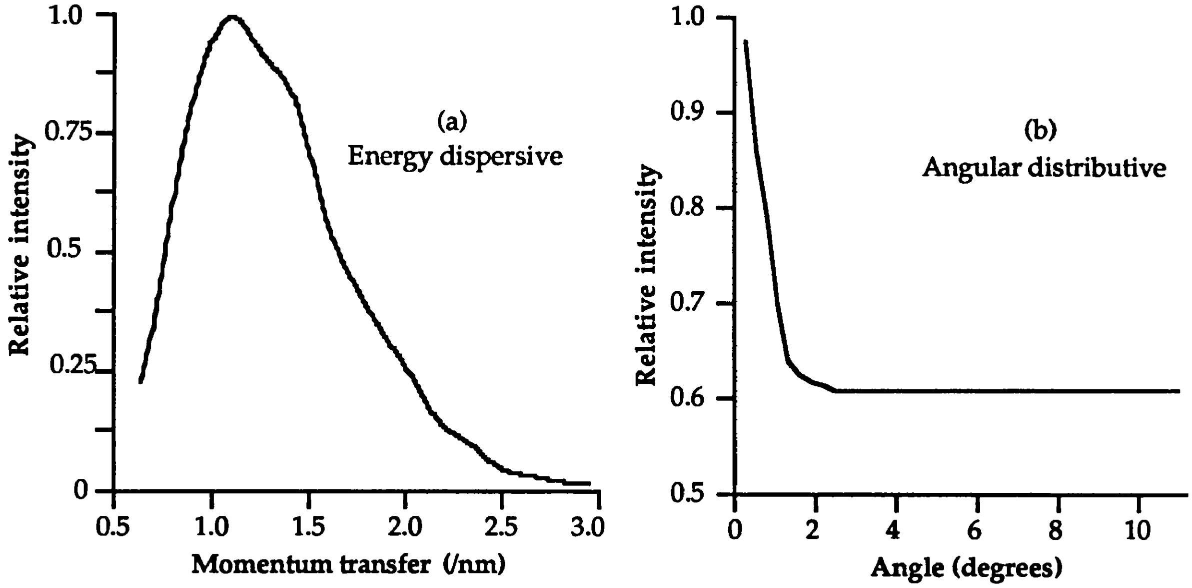

Figure 5.6 Typical background spectra for (a) the energy dispersive technique at a scattering angle of 6° (measurement time was 300 seconds), and (b) the angular distributive technique (the detector was moving at a speed of 1° per minute).

The background spectrum is recorded for each situation and subtracted from each scattering pattern.

5.6 Eliminating the shape of the incident spectrum

The incident x-ray spectrum varies with energy, peaking at ~35keV. The shape of this spectrum (which has previously been shown in figure 2.9) will distort the shape of the resulting energy dispersive scatter pattern. Division of the scatter pattern by the incident spectrum removes this effect. This correction will also be required in comparative measurements if they are performed at different tube kVs or if the tube kV is known to have altered slightly. Division by the incident spectrum will then allow comparison.

- 6 -

Results and discussion

This chapter demonstrates the type of results that are obtained using the technique of elastic photon scattering described in this thesis. The overall purpose is to demonstrate the usefulness of this technique and its application to clinical measurements, in particular the assessment of bone tissue in diseased states.

6.1 Comparison of angular distribution and energy dispersive patterns

The main points at which differences occur between the two measurement techniques are listed in the following. Each point is discussed in terms of the advantages and disadvantages of each technique to a clinical system.

(i) Measurement time and radiation dose: the energy dispersive technique requires less time to make a useful measurement than the angular approach. This reduces the problem of patient movement and, as the intensity of the x-ray beam was the same for both methods, it also reduces the radiation dose absorbed by the patient.

(ii) Size of scattering volume: The cross-sectional area of the scattering volume was shown to be $D1D2 / \sin\theta$ (§ 3.1.4). The scattering volume becomes smaller as the scattering angle increases. In the energy dispersive method the volume remains a constant size, whereas in the angular distributive technique the size of the volume changes throughout the measurement. During a scan from 1° to 11° the length of the rhomboidal region is reduced from 114.6mm to 11.4mm. This means that different parts of the object produce the scattering pattern as the measurement progresses. This is a distinct disadvantage. One of the main advantages of the small angle scattering technique is its ability to select a particular region within an object, however it becomes difficult to isolate a particular region if the scattering volume varies in size. Furthermore, an angular distributive pattern of the trabecular region of bone will result from a fairly small region of the bone at ~11° but at ~1° will result from a large volume of trabecular bone together with some cortical bone and some muscle tissue. Hence, on this basis, the energy dispersive technique has a clear advantage.

(iii) Ease of adapting to clinical system: The absence of any mechanically moving parts of apparatus in the fixed angle-energy dispersive method make it a relatively simple piece of apparatus to design and construct.

(iv) Sensitivity: In order to investigate the sensitivity of these two alternatives the same samples of two component bone materials (described in § 3.4.2.2) have been measured with both forms of investigation. The patterns recorded for each of the materials using both techniques are shown in figure 6.1

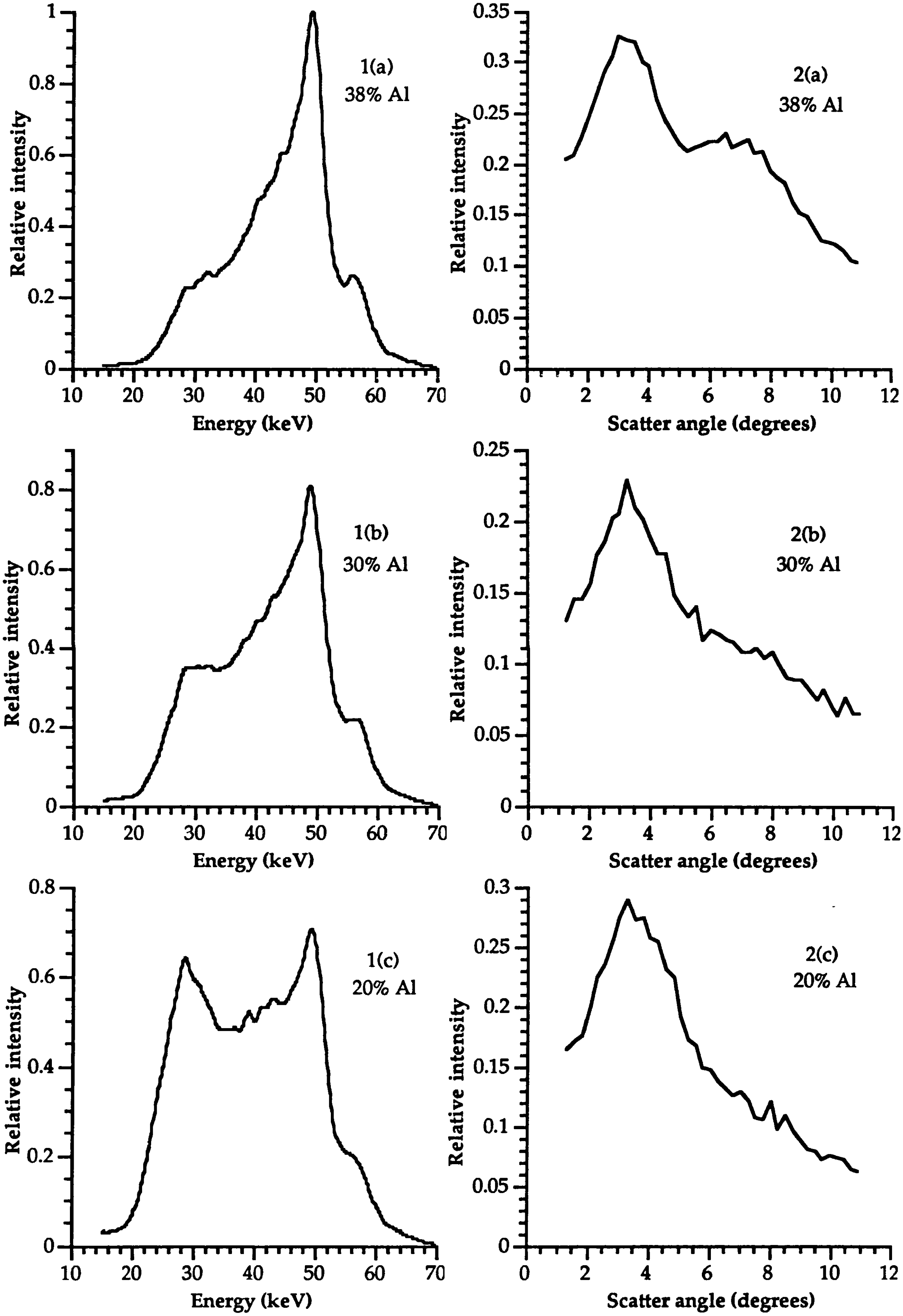

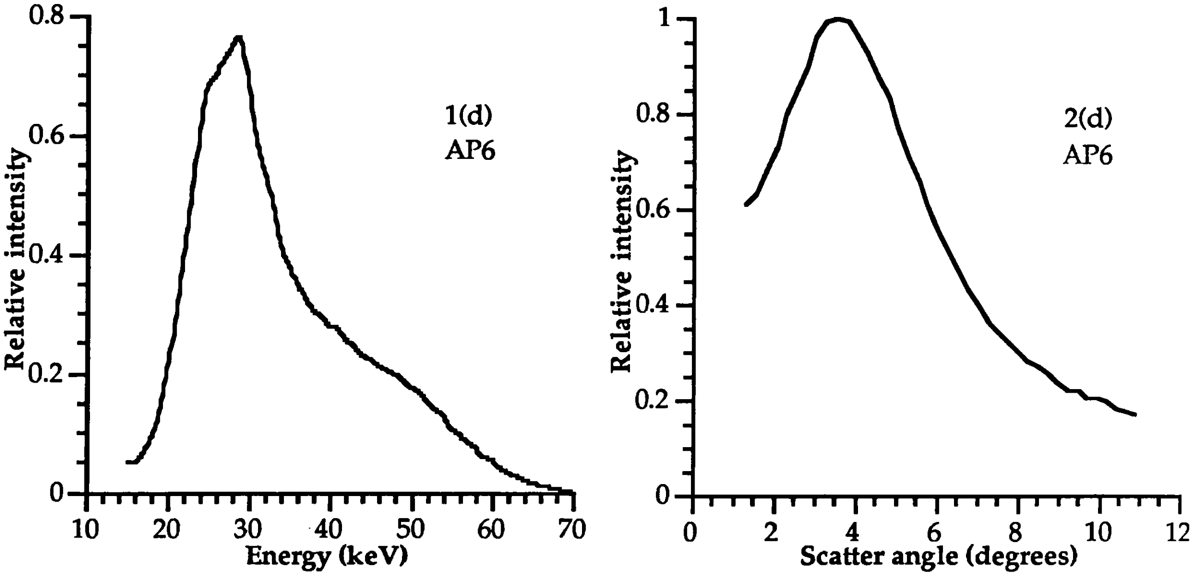

Figure 6.1 Display of (1) the energy dispersive and (2) the angular distributive patterns for the phantom materials a - d. The proportion of bone substitute (Al powder) decreases from a to d. Material d consists solely of marrow substitute AP6. The heights of the four patterns in each set are normalised relative to the highest peak in the most intense of the four patterns in that set in order to show the relative intensities.

The variation of the energy spectrum from 1 to 4 identifies two distinct components. One component is due to the bone substitute (the Al powder) and produces a peak in the energy distribution at ~48keV, the other component is due to the marrow substitute and produces a peak at ~28keV. A decrease in the proportion of the bone substitute within the phantom (i.e. from 1 to 4) causes the intensity due to the bone component to decrease relative to the marrow component. Figure 6.2 shows a comparison of the shapes of the angular distributive patterns to demonstrate the variation more clearly.

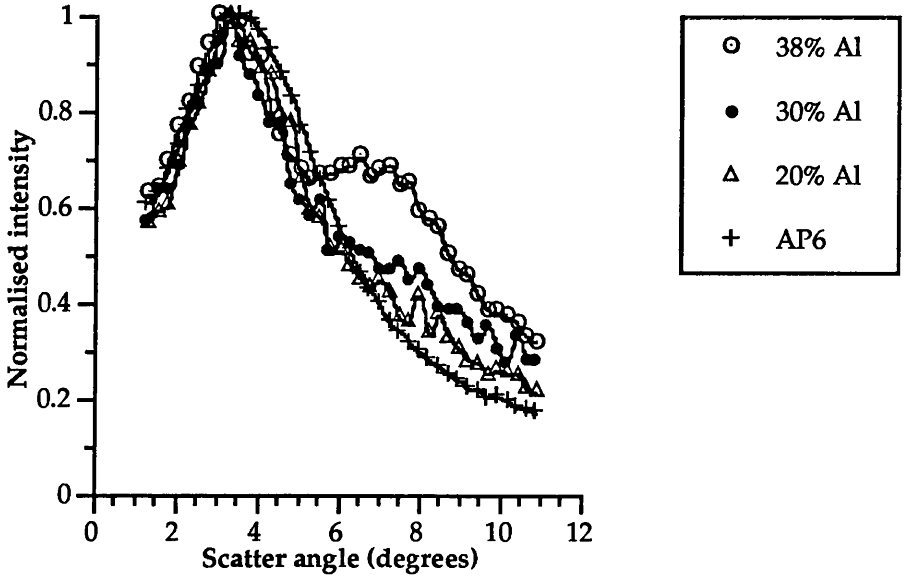

Figure 6.2 Comparison of the shapes of the angular distributive scatter patterns of the aluminium phantoms. The patterns are normalised to the same heights.

The variation of the angular intensity distribution shows similar changes with the proportion of the bone substitute, however not as clearly. A component due to the marrow substitute is seen as a peak at ~3.5° and the bone component is seen as a peak at ~7°.

Conclusion: It can be seen that both measurement techniques indicate changes due to the bone substitute concentration, however the changes are more apparent with the energy dispersive technique. The information that can potentially be obtained is identical for both techniques as they are both observing the sane diffraction effects. However the sensitivity of the measurement apparatus differs. The momentum transfer resolution of the apparatus is far better with the energy dispersive technique than the angular distribution, due to the source polychromaticity in the latter.

The various factors discussed indicate that the energy dispersive technique is the one most suited for adaptation to clinical work. All the results shown in the remainder of this chapter were obtained with the energy dispersive technique as it provides the results which are closest to the true patterns.

6.2 Material characterisation

Energy dispersive elastic photon scattering patterns are shown for various materials (figure 6.3) in order to demonstrate the capability of the technique in distinguishing between different materials. All measurements were made at a scattering angle of 6° and with tube settings of 70kV and 3mA. The counting time was 240 seconds. Recognisable patterns could be seen within 10 seconds of measurement, but counting was continued to improve statistics in order to demonstrate the shape of the patterns.

The materials shown are all white powders, similar in appearance, contained in identical cylindrical pots (2.3cm diameter). A background measurement was made of an empty pot and subtracted from each of the patterns to remove the pattern caused by the plastic.

The patterns shown indicate the type of results obtained; many other materials also produce patterns of differing shapes. It is the fact that each molecule/compound has a unique set of internal spacings that gives the technique the capability of material discrimination. Materials can be characterised by the shape of the pattern, i.e. positions and relative heights and widths of maxima. This capability, standard to x-ray diffraction techniques, has proved a useful tool in the identification of unknown substances. The diffraction pattern of a substance can be compared with a library of patterns in order to identify the substance.

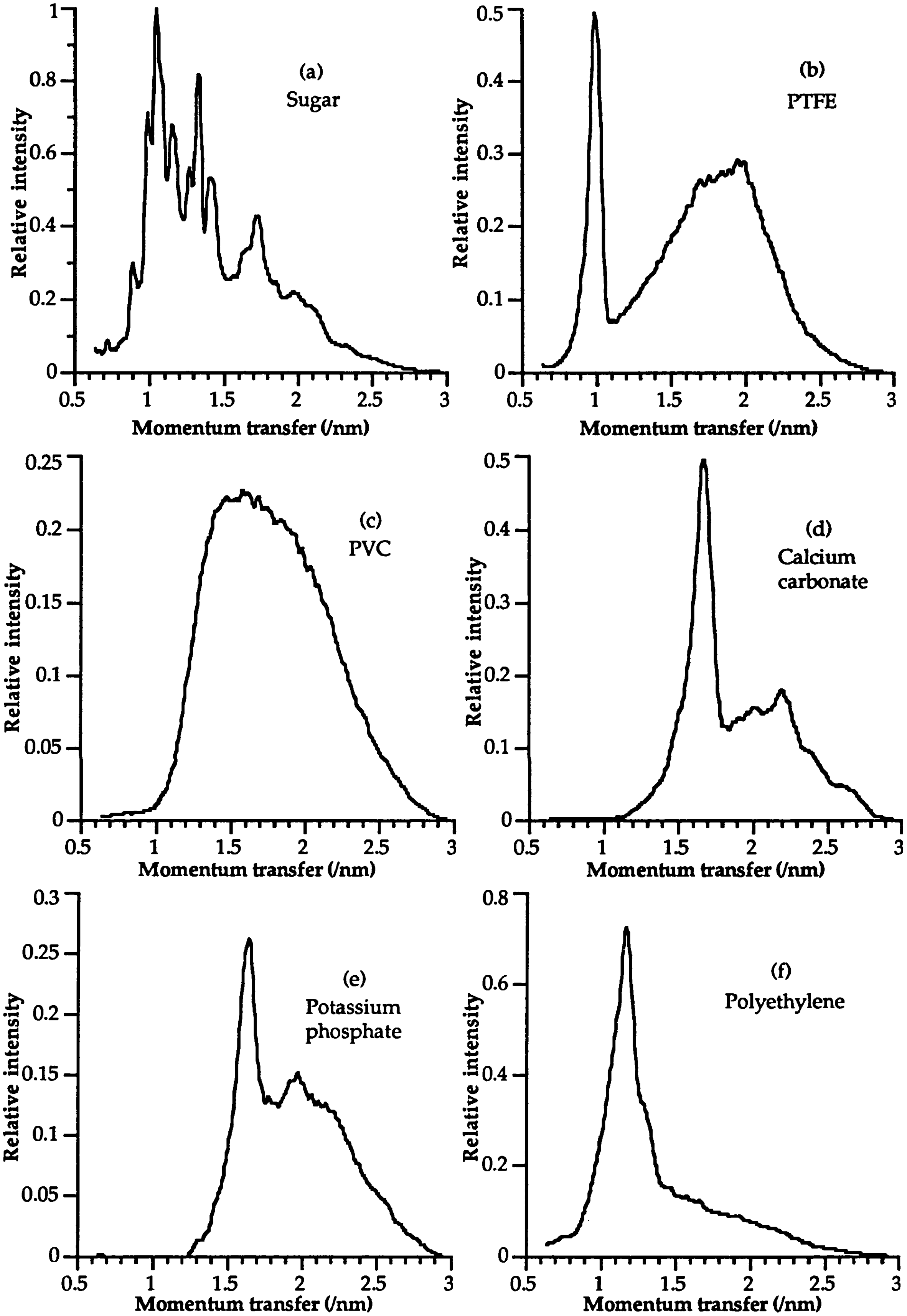

Figure 6.3 Energy dispersive scattering patterns for six powder samples. The materials were (a) white sugar, (b) PTFE, (c) PVC (polyvinyl chloride), (d) calcium carbonate ($CaCO_3$), (e) potassium phosphate (K_2HPO_4), (f) polyethylene. The heights of the patterns are normalised relative to the highest peak in the most intense of the six patterns in order to show the relative intensities.

6.3 Application to tissue characterisation

The purpose of this project has been to adapt this process to the clinical environment, and hence, tissue measurement. Scattering patterns are shown for various tissues (figure 6.4) to demonstrate the ability of this technique to distinguish between different tissues. The bone tissue measured was a dry, human femoral neck. The gallstone was a typical stone removed from a patient. The other tissues (fat, kidney, liver and muscle) were fresh tissues (all pig) obtained from the butchers. Each of these samples were ~3cm in diameter. Tube settings, scattering angle and measurement time are the same as for the material characterisation (§ 6.2). The patterns of the containers were removed from the results obtained.

A clear distinction is seen between the bone, the gallstone, the fat and the muscle tissue showing that this technique can be used to distinguish between these tissue types.

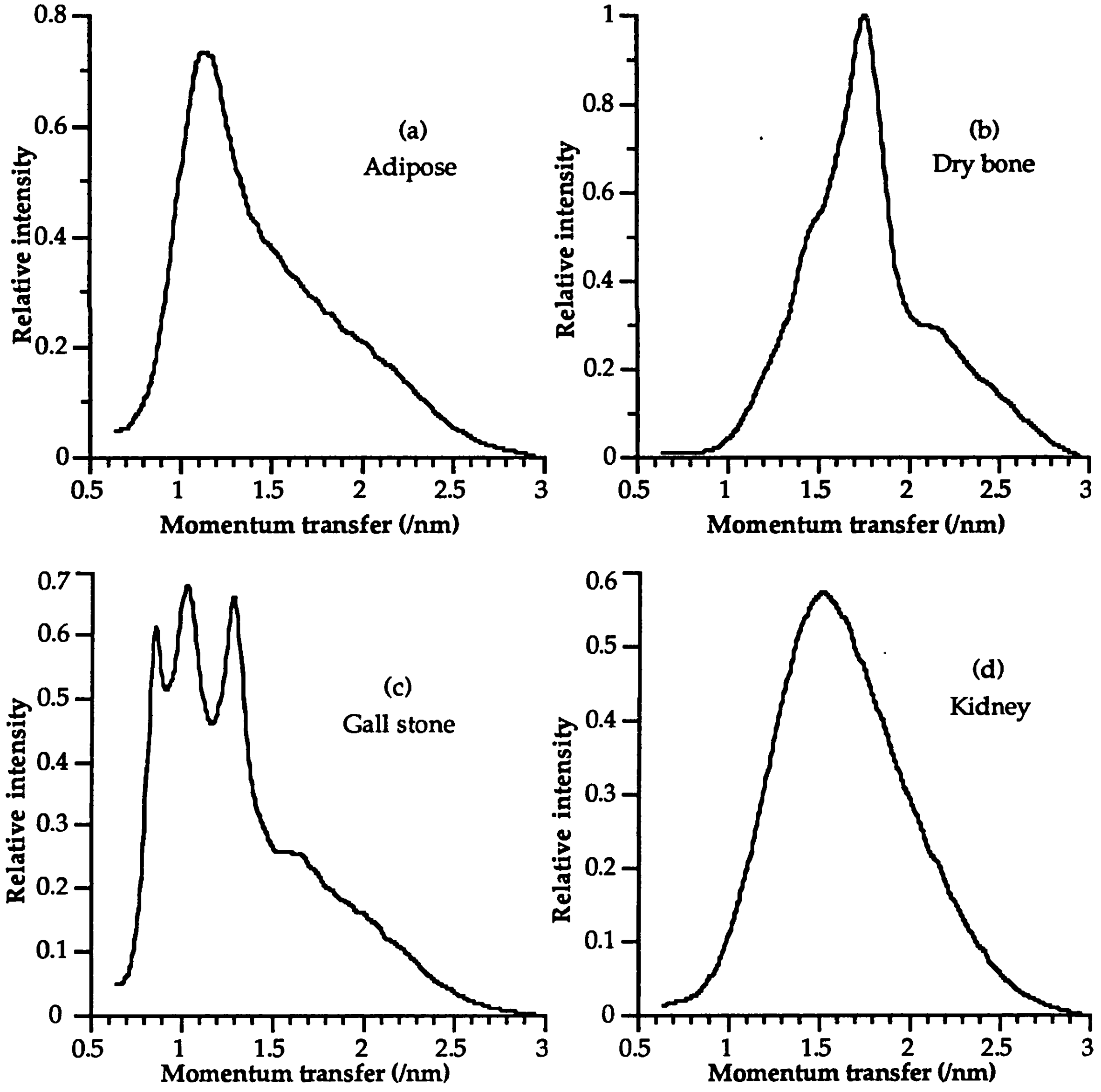

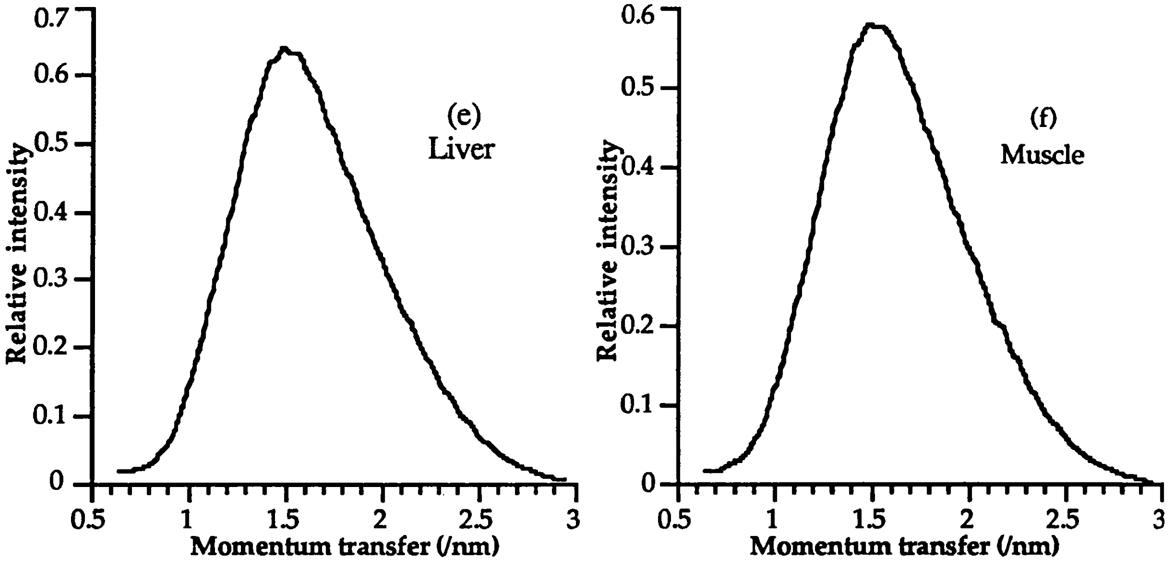

Figure 6.4 Energy dispersive scattering patterns for various tissues. The materials were (a) adipose, (b) dry bone, (c) gall stone, (d) kidney, (e) liver, (f) muscle. The most intense peak over each pattern is normalised to unity and the rest of the patterns are adjusted accordingly.

The ability to distinguish between fat and muscle could prove useful in the study of bone tissue. Yellow marrow is very similar to fat in composition (~96% fat), and red marrow is very similar to muscle tissue. The relative proportions of red and yellow marrow at a skeletal site vary with age (see § 1.2) creating a problem in most bone measurement techniques, in particular computerised tomography, as the densities of these two tissues differ. This variation should not pose a problem in this technique.

The measurements of muscle, liver and kidney are all very similar, with no obvious diffraction effects. The reason being that they are all soft tissues with very similar composition (White *et al* 1987). Table 6.1 shows the water content of each of these tissues and compares it with adipose (fat).

Body tissue	**Water content (%)**
Muscle	74.1
Liver	74.5
Kidney	76.6
Adipose	21.2

Table 6.1 Water content (percentage weight) of various tissues, taken from White *et al* (1987).

The water content is high in muscle, liver and kidney. A comparison of these tissues with the pattern from water (figure 6.5) shows little difference due to the similar composition.

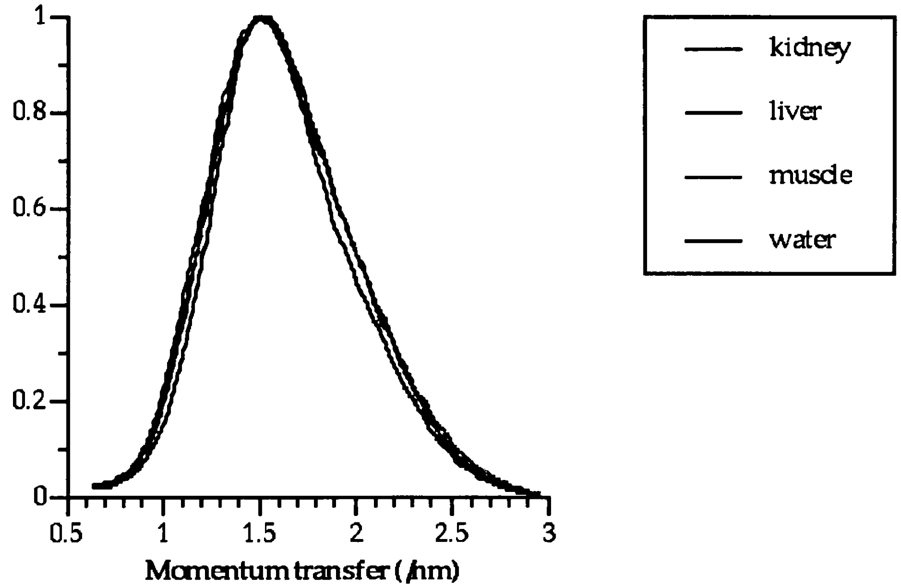

Figure 6.5 Comparison of energy dispersive patterns of soft tissues (muscle, liver and kidney) with water, all obtained at 6 degrees. Double distilled water at room temperature was used for the measurement.

Variation of the scattering angle, i.e. investigating other momentum transfer regions, does not identify any regions at which the patterns from the four tissues differ. Figure 6.6 shows the energy dispersive scattering patterns of water at a few sample scattering angles.

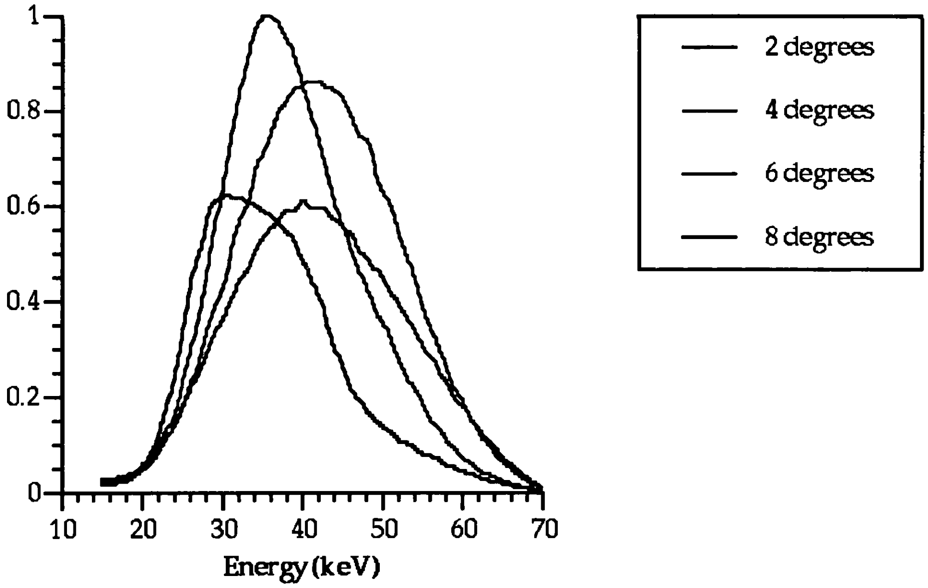

Figure 6.6 Energy dispersive scattering patterns of water at various scattering angles. These graphs are plotted as a function of energy to allow direct comparison of the pattern shapes.

The pattern shape varies with scattering angle showing that interference effects are occurring, however no prominent peaks or structure are seen in the patterns. The patterns for the soft tissues with a high water content (muscle, liver and kidney) were found to be structure in the resulting pattern. This was discussed in § 2.5 and is due to the internal atomic/molecular arrangement. The alignment of relatively large planes in a crystal causes intense diffraction peaks at particular momentum transfer values, whereas the random arrangement of molecules within water, for example, causes a general scattering to a range of momentum transfer values rather than to precisely defined values. An example which demonstrates the fact that crystalline substances produce a more structured diffraction pattern is given in figure 6.7. The pattern obtained for ice shows a number of sharp peaks, whereas the pattern obtained for cold water (at a temperature of 10°C) shows a much smoother pattern.

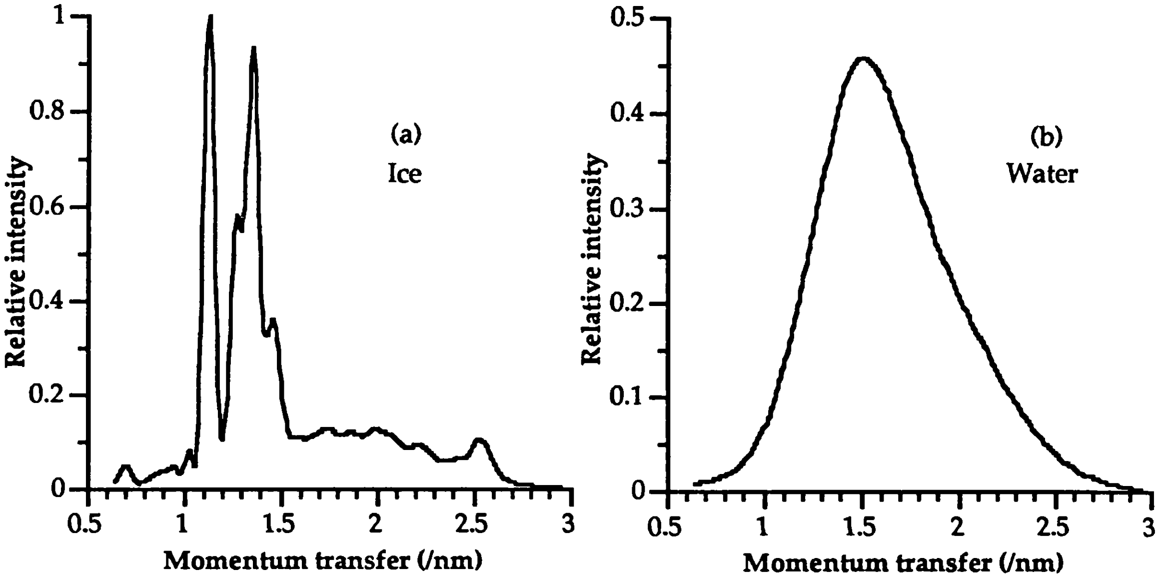

Figure 6.7 Energy dispersive scattering pattern of (a) ice and (b) water at a scattering angle of 6 degrees. Distilled water was used.

Conclusions: This technique can differentiate between bone, gallstone, adipose and muscle tissue (demonstrated in figure 6.4). The similarity of the patterns of water, muscle, liver and kidney indicates that this technique can only successfully distinguish between substances in which the crystalline structure or the percentage composition of crystalline components is significantly different. Diffraction techniques, such as this, are most useful in studying materials with a predominantly crystalline nature. Amorphous materials, such as water, produce less structured diffraction spectra.

6.4 Use of standard tissue substitute materials in scatter measurements

Comparisons were made of the energy dispersive scattering patterns of various tissues with their respective tissue substitutes. The substitute materials measured are those which provide a good simulation in radiographic measurements.

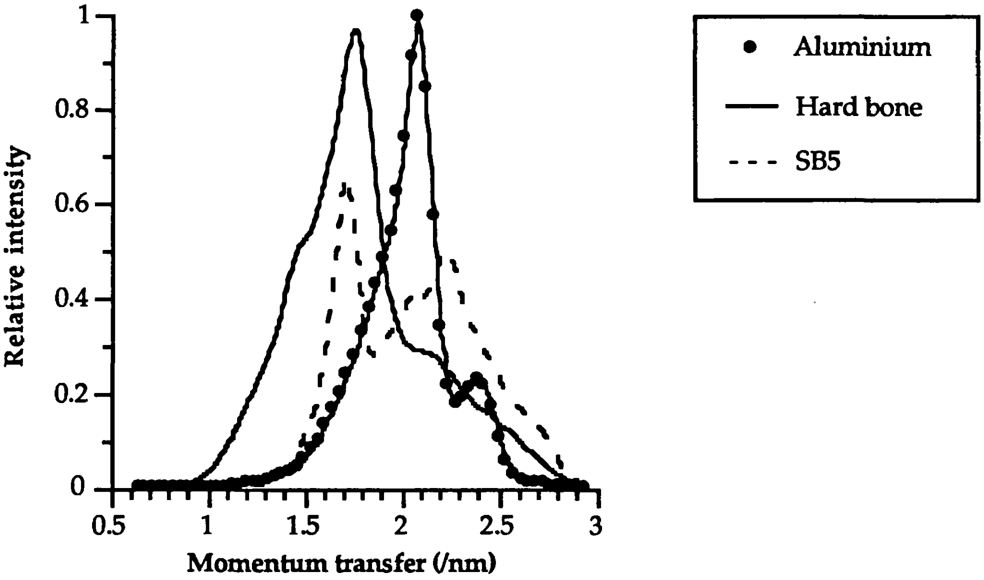

Figure 6.8 Comparison of energy dispersive spectra of hard bone tissue, the hard bone substitute SB5 of White *et al* (1977) and pure aluminium. The aluminium was in powdered form, with powder size of 125 microns and with a purity of 99.99%.

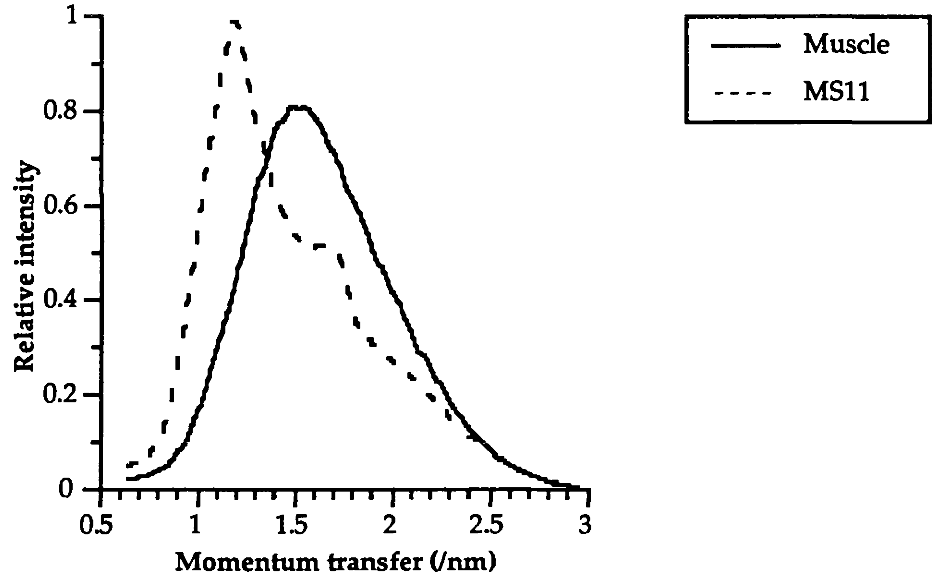

Figure 6.9 Comparison of fresh muscle tissue (pig) with the MS11 muscle substitute of White *et al* (1977).

The comparisons shown indicate that the common tissue substitutes which accurately simulate the density and attenuation properties do not simulate the diffraction properties of the tissue. This is to be expected because the internal compositions of the substitutes are different from those of the tissues. An exception to this has been found to be the adipose substitute AP6 of White *et al* (1977) (figure 6.10). The two patterns are seen to be similar.

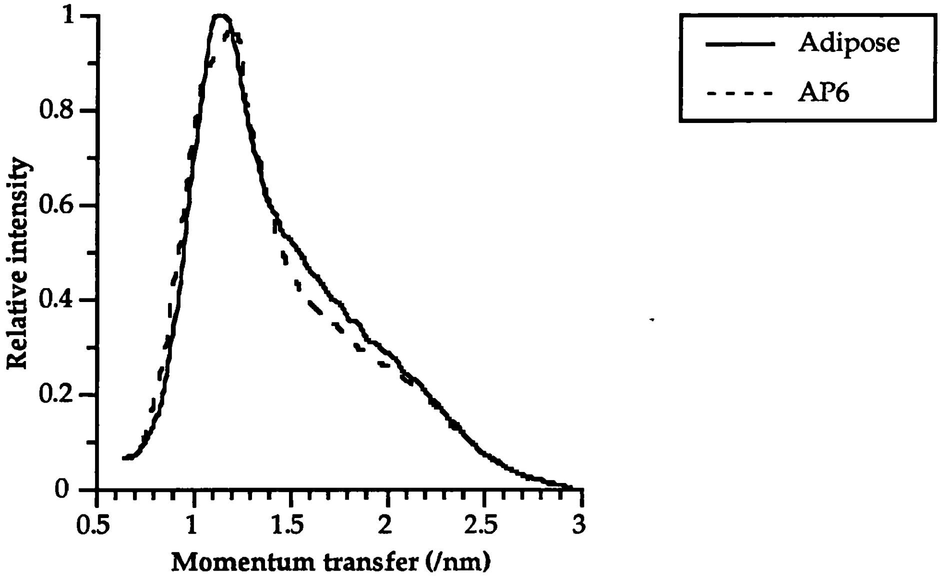

Figure 6.10 Comparison of adipose tissue (pig) with the adipose tissue substitute AP6 of White *et al* (1977).

A further example of the differing scatter properties of substitute materials is shown in figure 6.11. This graph shows the total scattered intensity (within the 15-70keV energy range) at various scatter angles for three materials which have similar radiographic properties; water, perspex and MS11 (a muscle tissue substitute of White *et al* 1977). Each of these materials can be used to simulate soft tissue in radiographic measurements due to their density and linear attenuation properties. The scattered intensities, however, peak at different scattering angles.

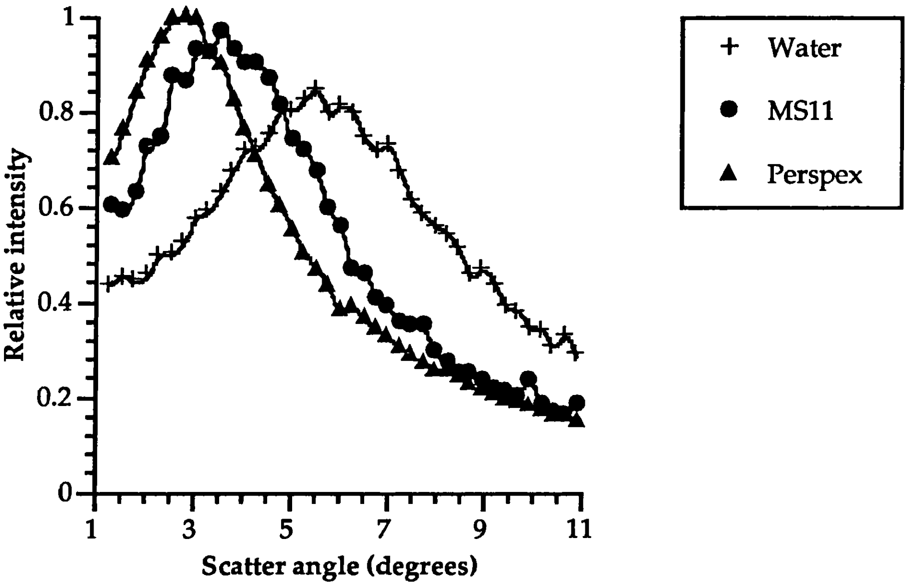

Figure 6.11 Angular distributive scatter patterns of water, perspex and MS11. The materials were each cylinders of 3.0cm diameter.

In general the substitutes designed for radiographic studies do not make good substitutes for scatter measurements of this nature. Substitutes which are required to exactly simulate the tissues for these measurements would need to be composed of the same chemical constituents in approximately the same proportions.

The two component bone substitutes used in this thesis are designed to simulate the changing nature of the bone during osteoporosis rather than provide an exact simulation of bone tissue. The two components, aluminium and AP6, were chosen because they have similar atomic numbers to the tissues they represent and therefore the degree of elastic scattering is similar. These two components produce scattering peaks which, although at slightly different momentum transfer values to the actual tissues, are in approximately the same height ratio. Hence, variation of the quantities of each component will simulate the change in the ratio of the heights of the peaks that occurs in the bone tissue.

6.5 Quantitative analysis of two-component mixtures: a determination of accuracy and precision

Section 2.9 of the theory chapter showed that direct quantitative analysis of a two-component mixture in which the components have unequal absorbing powers is possible by means of a calibration curve. The method employed was to produce a calibration curve from experimental measurements of the ratio of the intensities of the diffraction peaks from each component (I_1/I_2) at various concentrations of one of the components.

In order to assess the accuracy of the elastic photon scatter technique a mixture of two materials in various concentrations were measured. Two powders were chosen which produced a large diffraction peak at different wavelengths within the range studied. Powders were used due to the fact that they can be accurately weighed and mixed thoroughly. The patterns for the two powders chosen, calcium carbonate and polyethylene, are shown in figure 6.12. The scatter patterns of various concentrations of these powders were previously shown in figure 2.15. A further reason for choosing these particular powders was that their attenuation and density properties differ significantly because the theory employed applies to two components of unequal absorbing power.

Thirteen different concentration mixtures of the two powders were prepared. The following lists the relative concentrations of each of the samples, the values given are the percentage weights of the $CaCO_3$ component, polyethylene forms the remaining percentage; 20, 30, 35, 40, 44, 48, 50, 53, 59, 60, 70 and 80%. To produce a sample the appropriate amount of each component was weighed to ±0.01g using a precision balance. At least 20g of each of the samples was prepared. The powders were thoroughly mixed to ensure the correct concentration throughout and then each sample was poured into identical, thin-walled, plastic containers of 2.2cm diameter.

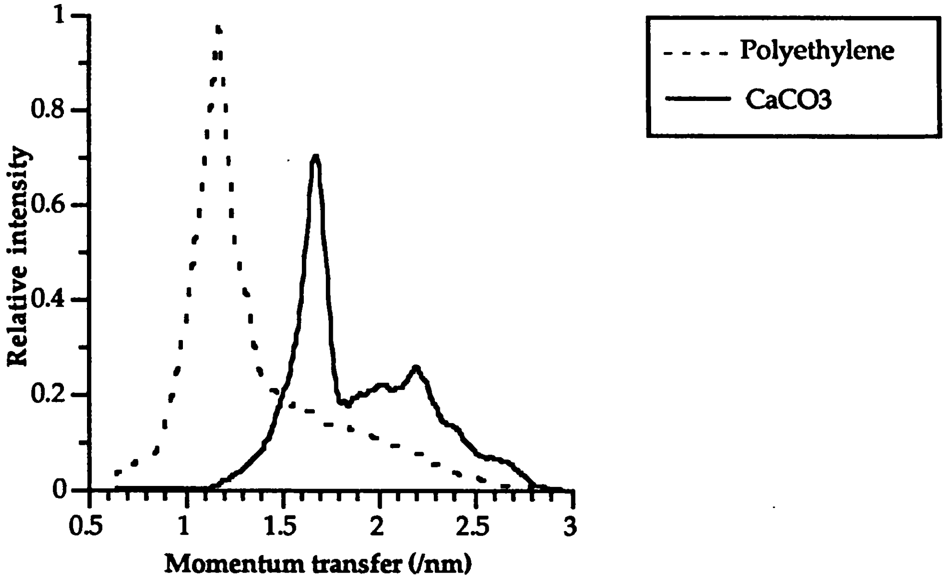

Figure 6.12 Energy dispersive scatter patterns at 6 degrees for calcium carbonate and polyethylene.

Measuring the peak ratio I_1/I_2: Assuming the highest point in the peak of the ith component to be the value for I_i will be inaccurate due to statistical errors in the count rate. These errors have been greatly reduced but not completely eliminated by the optimal filtering technique. Greater accuracy was obtained by taking I_i to be the average of the five peak points, i.e. the peak value together with the two points on each side. The ratio of the values obtained for the two peaks is then calculated.

The positions of the peaks alter slightly between the samples, this is because the attenuation of the mixture increases with the percentage composition of $CaCO_3$ (which is more attenuating than polyethylene) thus causing a greater degree of beam hardening. In this experiment the values were measured at a constant momentum transfer value, this was not necessarily the peak in every case but it was in the majority of cases. It would be equally correct to always choose the values at the peak as opposed to a constant momentum transfer value, the important factor being that consistency should be maintained over all measurements.

6.5.1 Factors which determine the precision

Five separate repeat scatter measurements were performed on four different samples in order to determine the factors which contribute to the precision of the technique. The same sample was not measured twice in succession but was removed and then later replaced for measurement such that any repositioning error will also be included in the value. Furthermore, these measurements were performed at various intervals over a period of three days. Table 6.2 lists the results. The average value of the ratio of the peaks I_1 / I_2 was calculated from the five separate measurements. The error value given in each case is the maximum deviation over all measurements from the average value of the ratio.

Sample	Average ratio and deviation	Percentage deviation
35% $CaCO_3$	0.659 ± 0.0137	2.08%
40% $CaCO_3$	0.809 ± 0.0184	2.27%
44% $CaCO_3$	1.039 ± 0.0228	2.19%
50% $CaCO_3$	1.366 ± 0.0233	1.71%

Table 6.2 Maximum percentage deviation of the peak ratio.

These results indicate that this method has a high degree of reproducibility. The deviation from the average ratio shown in the table is the maximum value, most of the results were much closer to the average ratio. The following factors contribute to this error;

(1) The statistical counting error - this has been reduced by the optimal filter routine,

(2) Non-uniformity of the sample - rotation of the sample could mean that successive measurements will irradiate slightly different percentage compositions,

(3) Sample repositioning error - displacement of the sample could lead to different contributions to the pattern from the plastic container.

The contribution from the two latter factors can be eliminated by performing repeat measurements on a single sample without moving the sample between measurements, this will demonstrate the contribution due to the statistical counting error. The 44% $CaCO_3$ sample was measured five times, the following result was obtained;- 1.017 ± 0.0094. The error in this case is 0.92%. This would indicate that an error of less than 1% would be possible on a uniform sample providing it is repositioned correctly each time and the count rate is sufficiently high. This error is entirely due to the statistical count rate and could be further improved with a higher photon intensity.

The magnitude of the statistical error is dependent upon the total number of counts recorded at the two peaks. The error in the ratio of I_1/I_2 can be calculated from equation 6.1,

$$\sigma_R = \frac{I_1}{I_2}\left(\left(\frac{\sigma_{I_1}}{I_1}\right)^2 + \left(\frac{\sigma_{I_2}}{I_2}\right)^2\right)^{1/2} \tag{6.1}$$

where σ_{I_1} is the statistical error of I_1, (taken to be the square root of I_1).

The large number of counts in the peaks of the measured powder sample produce an error of 0.9%, whereas less intense peaks will require a greater incident flux to achieve this level.

The values of precision estimated for the measurements of peak ratio in this thesis were calculated using equation 6.1 and allowing 1% for repositioning error. The measurements of the bone-to-marrow peak ratio of the bone phantoms was typically ~3.5%. Significant improvement would be possible with a greater count rate but at the expense of increased patient dose.

6.5.2 The calibration curve and determination of accuracy

The calibration curve measured for the two powders is shown in figure 6.13; the ratio of the calcium carbonate peak to the polyethylene peak is plotted against the $CaCO_3$ concentration. The shape of the curve and the fact that a smooth curve is obtained is consistent with the theory given in § 2.9. The line through the points was produced using a spline curve fitting routine in GRTOOL on the Sun workstation.

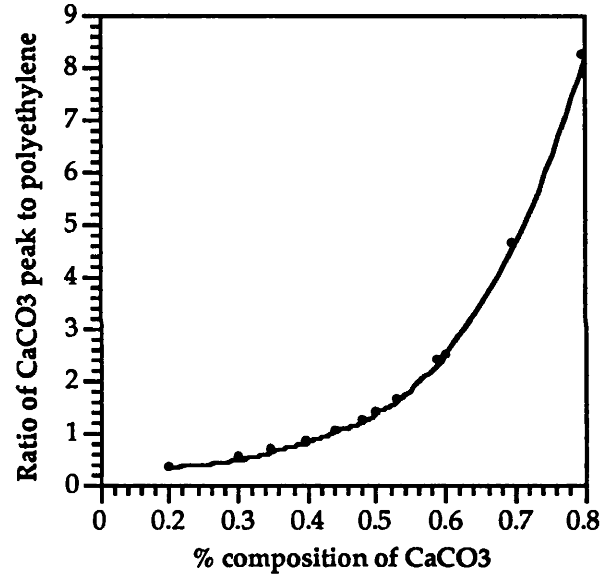

Figure 6.13 The calibration curve for calcium carbonate and polyethylene. Thirteen points were used to plot the data. The error bars calculated for the precision (~2%) shown in table 6.3 are too small to show on the graph.

With a precision of 2% it was calculated from the slope of the calibration curve that a change in the $CaCO_3$ concentration of only 0.4% can be detected using this technique. These results indicate that this technique could prove useful in measuring changes in concentration, for example the change in the bone-to-marrow ratio during osteoporosis.

The accuracy of this technique has been determined by plotting the calibration curve using the results from only some of the samples and then measuring how closely the remaining samples fit the curve. The calibration curve was plotted using all points except one. The difference was then calculated between that one value and the predicted value from the calibration curve. A comparison of the measured peak ratios with the expected values from the calibration curve is given in table 6.3.

Sample	Measured peak ratio	Expected peak ratio	% difference
44% $CaCO_3$	1.016 ±0.04	1.020	0.4
48% $CaCO_3$	1.204 ±0.04	1.212	0.66
50% $CaCO_3$	1.361 ±0.04	1.369	0.59
53% $CaCO_3$	1.588 ±0.04	1.599	0.69

Table 6.3 Comparison of the peak ratios measured by experiment with those obtained from the calibration curve.

The error quoted for the measured peak ratio includes the precision determined earlier and an estimated 0.5% error in the supposed percentage concentration of the sample within the scattering volume.

The maximum percentage difference was found to be 0.69%. All the estimated values lie well within the error level. This is expected because the technique directly compares a measured value with a calibration value. The accuracy is limited by the number of points forming the calibration curve. The greater the number of points used to plot the calibration curve the better the curve will be. Furthermore, the curve drawn through the points will be a more accurate representation of the true case in the middle of the points than at the end. So a suggested protocol for obtaining calibration curves would be to estimate the approximate percentage concentrations that will be investigated and focus most of the calibration points around that value, this combined with a large number of calibration points will produce the highest achievable accuracy. In theory if the true shape of the curve was known then the only error would be due to the precision. As the precision is limited only by the count rate, providing repositioning errors can be overcome, then both accuracy and precision are potentially very good.

6.6 Bone analysis for osteoporotic assessment

6.6.1 *In-vitro* measurements of thin samples

A 5mm thick slice of fresh trabecular bone tissue (containing both bone and marrow) was cut from a recently excised femoral head. The scatter pattern measured for this tissue is shown in figure 6.14. Also shown for comparison are the scatter patterns of a 5mm thick slice of dry bone tissue (cut from the trabecular region of a femoral head) and of a 5mm thick slice of adipose tissue (equivalent to fatty marrow).

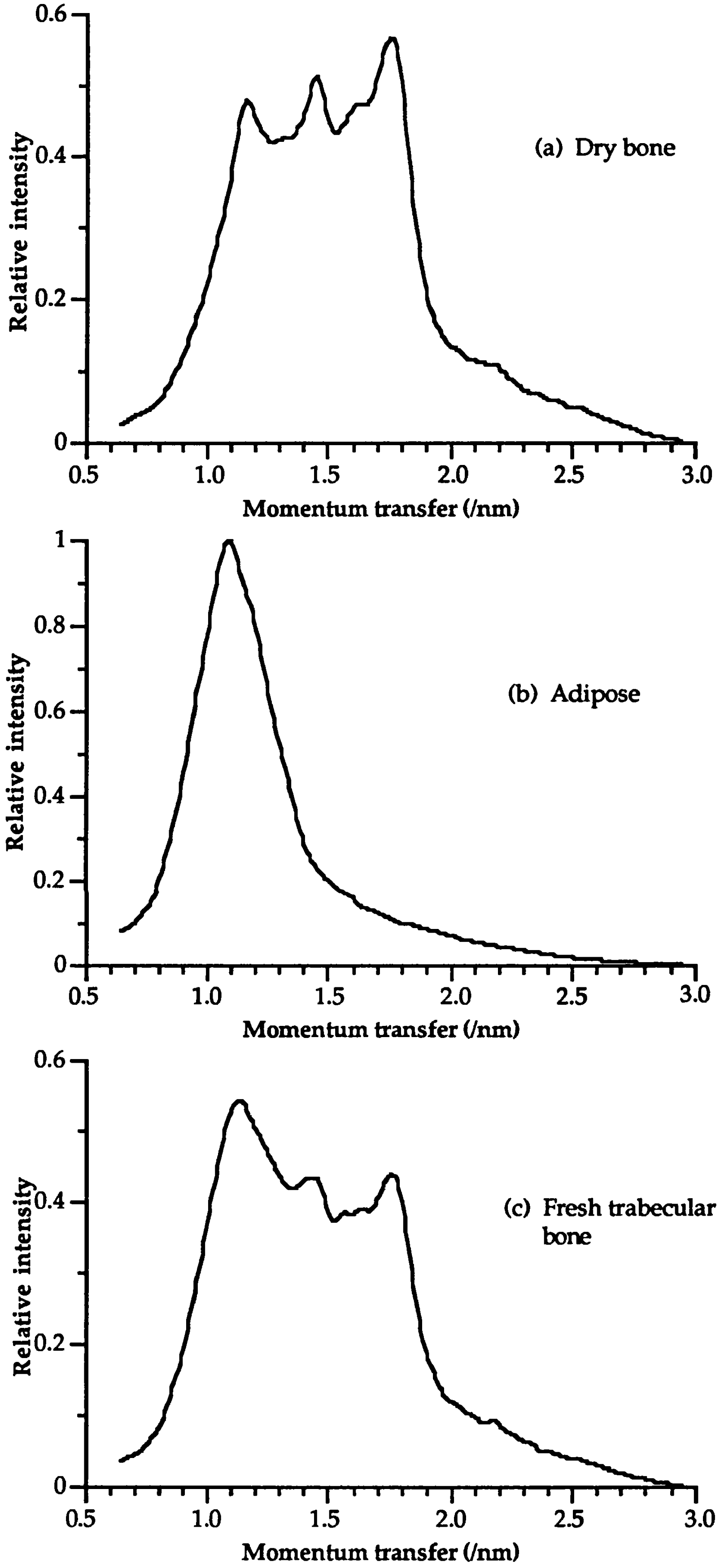

Figure 6.14 Energy dispersive scatter patterns at 6° of 5mm thick slices of (a) trabecular bone with the marrow removed, (b) adipose (marrow) tissue, (c) recently excised trabecular bone containing marrow.

patterns of the individual components, bone and marrow. The large adipose peak at ~1.1nm^{-1} together with the bone peaks at ~1.4 and ~1.7nm^{-1} are both seen in the fresh trabecular bone pattern. As in the case of the powder mixtures (discussed in § 2.8) the relative proportions of bone and marrow will determine the relative heights of the peaks of each component in the scatter pattern of trabecular bone. This is demonstrated in figure 6.15. The scatter patterns are shown for the 5mm thick slice of dry bone coupled with varying thicknesses of adipose tissue. The slices of bone and adipose were positioned adjacent for the measurement. These samples do not represent a perfect simulation of bone tissue because the bone and marrow are not thoroughly mixed as in the true state. However the samples adequately represent varying percentage compositions of bone and marrow in order to demonstrate the change in the pattern shape.

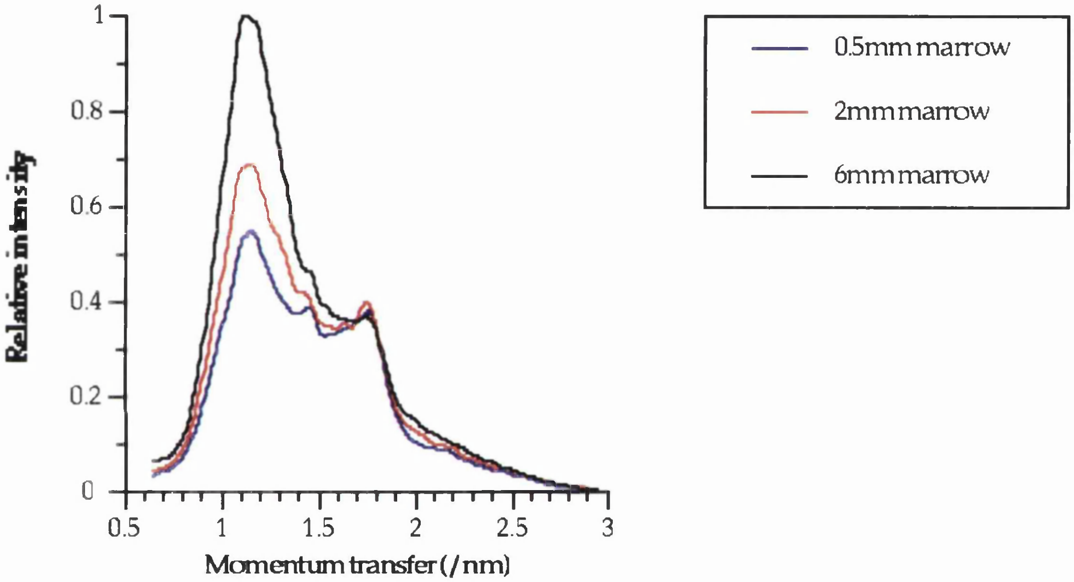

Figure 6.15 Comparison of the scatter patterns of 5mm of bone tissue with varying thicknesses of adipose tissue.

The ratio of the bone peak (at ~1.7nm^{-1}) to the marrow peak (at ~1.1nm^{-1}) decreases as the relative bone to marrow ratio decreases. This result demonstrates that the elastic photon scatter technique is sensitive to a change in the ratio of the bone to marrow volumes, and would therefore detect osteoporotic change in trabecular bone.

6.6.2 *In-vitro* measurements of larger bone samples

Increasing the size of the measured sample will cause greater attenuation of the beam, which will lead to beam hardening in the resultant scatter pattern. The effect of the thickness of the dry bone sample on the shape of the scatter pattern is demonstrated in figure 6.16. A dry femoral head was sectioned into 5mm thick slices and scatter patterns were recorded for an increasing number of slices until the complete thickness of the femoral head was reached.

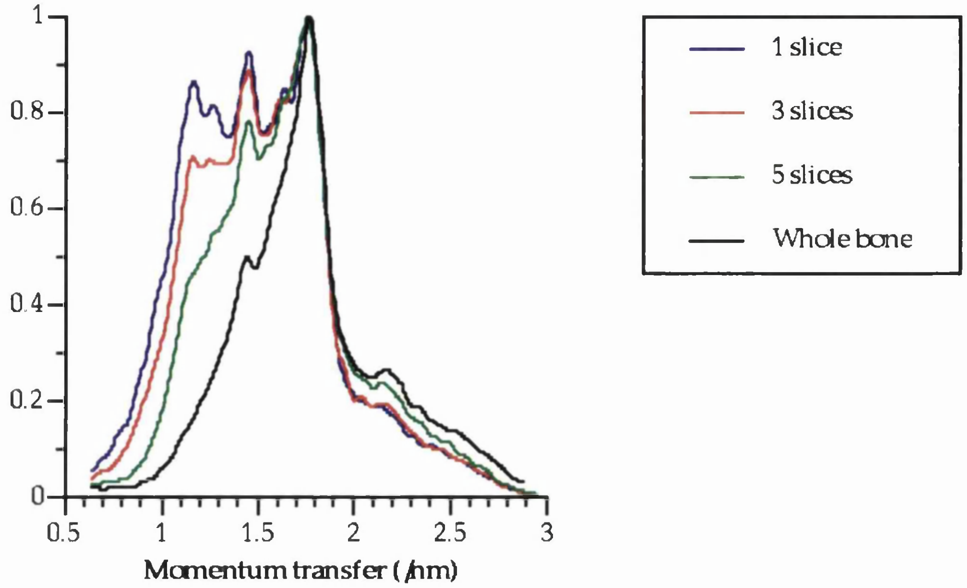

Figure 6.16 Comparison of the scatter patterns of various thicknesses of bone tissue. The height of each pattern was normalised to unity for comparison of the shapes.

Attenuation of the scattered beam causes two of the peaks to be virtually removed from the scatter pattern, such that the only remaining peak in the pattern of the whole femoral head is the one at ~1.7nm^{-1}.

The scatter pattern of a freshly excised femoral head (bone and marrow present) is compared with that of a dry femoral head (just bone) in figure 6.17. The fresh bone pattern is less intense than the dry bone pattern because of the additional attenuation of the marrow in fresh bone.

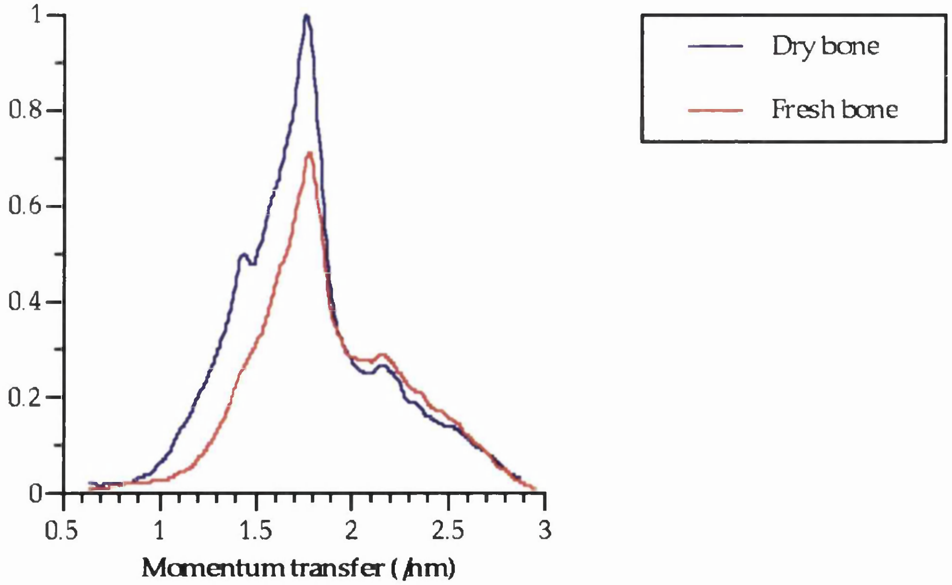

Figure 6.17 Comparison of the scatter patterns of dry bone and fresh bone.

The shapes of the scatter patterns from the fresh and dry bone tissue can be seen to differ.

In particular the ratio of the large peak at ~1.7nm^{-1} to the lesser peak at ~2.2nm^{-1} is much greater in the dry bone pattern than the fresh bone pattern. This will be accentuated by the beam hardening effect caused by the greater attenuating properties of the fresh bone (due to the presence of the marrow tissue) than the dry bone. So in order to compare the shapes of the patterns the dry bone pattern was attenuated mathematically by the appropriate thickness of marrow tissue using the exponential law of attenuation. A 2.88cm thickness of marrow tissue was estimated to be present in the fresh bone based on a 4.7cm diameter bone (the thickness of the fresh femoral head) and 64% volume of marrow (White *et al* 1987), (fatty marrow does not greatly attenuate the beam and so an error in the estimated thickness will not produce a significant error in this result). Figure 6.18 shows a comparison of the patterns of the attenuated dry bone and the fresh bone. The patterns are both normalised to unity to demonstrate the relative shapes of the patterns.

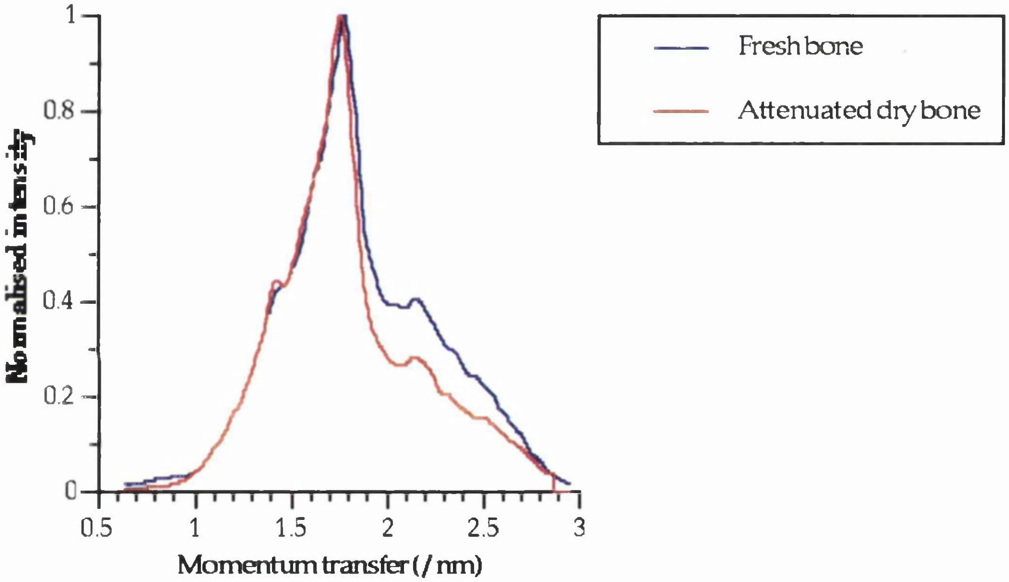

Figure 6.18 Comparison of the scatter patterns of fresh bone and dry bone tissue. The latter has been attenuated by the estimated thickness of marrow in the fresh femoral head for comparison of the shapes.

A clear difference can be seen in the shapes of the fresh and dry bone scatter patterns over the 1.8 - 2.7nm^{-1} momentum transfer region. The ratio of the two peaks is still much greater in the dry bone pattern. This difference between the two patterns must result from the presence of the marrow tissue in the fresh bone. Figure 6.19 shows the result of subtracting the dry bone pattern from the fresh bone pattern.

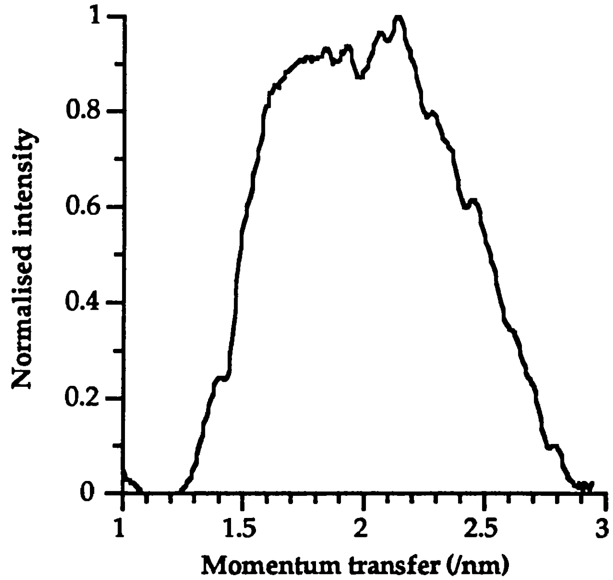

Figure 6.19 The contribution due to the marrow. The result of subtracting the dry bone scatter pattern from the fresh bone pattern.

In order to demonstrate that this pattern is due to the marrow tissue the elastic scatter pattern of a sample of adipose tissue has been attenuated by the estimated thickness of bone tissue (shown in figure 6.20). The femoral heads measured in this thesis have an average diameter of ~4.7cm. Osseous tissue is reported to occupy 54% by mass of the femoral head (including the cortical bone) while yellow marrow occupies the remaining 46% (White *et al* 1987). This means that an x-ray beam traversing a femoral head will pass through ~1.69cm of bone tissue.

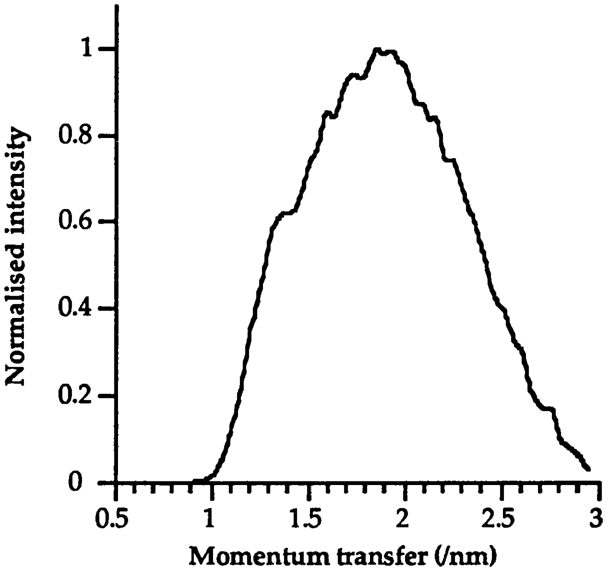

Figure 6.20 Attenuation of the adipose scatter pattern by 1.69cm of bone tissue. The linear attenuation data for bone was calculated using the mixture rule, the elemental attenuation data of Storm and Israel (1970) and the elemental composition of adipose (Woodard and White 1986). The exponential law of attenuation was used to apply the data.

The shape of this pattern is very similar to the shape of the marrow contribution shown in figure 6.19.

These findings demonstrate that the scatter pattern of fresh bone tissue results from the combination of the individual scatter patterns of bone and marrow for a large thickness of bone (i.e. the whole femoral head) as well as for the thin slices discussed previously. The bone tissue forms a narrow peak at ~1.7nm^{-1} (§ 2.7 showed this peak to be due to calcium hydroxyapatite). The marrow tissue peak however is much broader, due to it being a more amorphous substance than the crystalline bone tissue. The position of the marrow peak was taken to be at 2.2nm^{-1} for the purpose of determining the height of the marrow peak for comparison with that of the bone peak. This value is sufficiently far from the position of the bone peak to avoid any overlap. The ratio of the heights of the bone peak to the marrow peak in the scatter pattern is proportional to the ratio (by mass or volume) of bone to marrow within the region being studied, the latter ratio determining to some extent the osteoporotic nature of the trabecular bone tissue. This thesis proposes this technique as a means for providing information on the osteoporotic nature of trabecular bone tissue.

6.7 Effect of variation of position and rotation: object repositioning error

Section 6.5 identified a cause of error in the results to be due to incorrect positioning of the object for each measurement. Centring the scattering volume at exactly the same position in the object for all measurements is very difficult to achieve in practice. This section considers the effect on the scatter pattern of an object caused by (1) rotating the object, and (2) off-centring the scattering volume within the object.

6.7.1 Rotation error

Consider the case of the scattering volume centred on a cylindrical object. If the object consists of a uniform, powdered sample then rotation of the object between measurements will have no effect on the result. This is due to two reasons;

(1) The uniformity of the sample means that the scattering volume

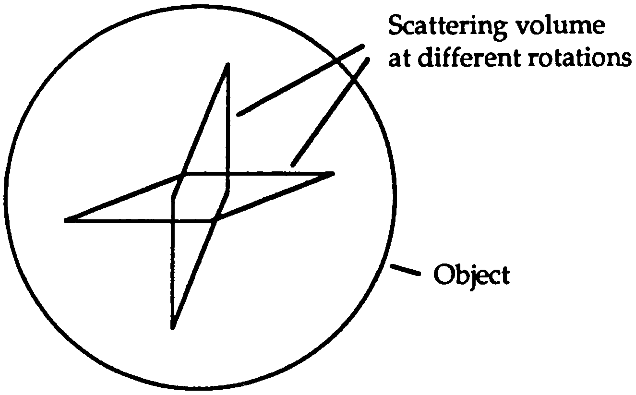

Figure 6.21 The change in the region enclosed by the scattering volume due to rotation of the object.

still encloses the same proportions of components, despite the fact that the region studied has changed (see figure 6.21).

(2) A powdered sample consists of a random arrangement of the molecules without any preferential orientation, thus the same level of scatter will result from any rotation. This differs from the case of the regular atomic arrangement within a single crystal in which the orientation determines whether diffraction peaks are observed.

This is the case for all of the objects considered in this thesis. The biological tissues have the same diffraction properties as a powder because the molecules are randomly oriented. Even the crystalline network of bone tissue consists of a random arrangement of minute crystals.

The energy dispersive scatter pattern of a freshly excised femoral head was measured for four different orientations of the bone; 0, 90, 180 and 270°. The femoral head was not enclosed by surrounding tissue. Table 6.4 lists the ratios of the bone to marrow peaks for each of these patterns. The values are equal within the measurement error thus demonstrating that rotation of the bone (or other uniform, cylindrical object) has no effect on the pattern.

Object rotation	0°	90°	180°	270°
Bone to marrow ratio	1.91 ±0.04	1.95 ±0.04	1.93 ±0.04	1.93 ±0.04

Table 6.4 Measured values of the ratio of the height of the bone peak to that of the marrow peak for four different orientations of a fresh femoral head. The femoral head approximates a circle in cross section.

Rotation of the object will affect the pattern if the object or any surrounding material is not cylindrical, see figure 6.22.

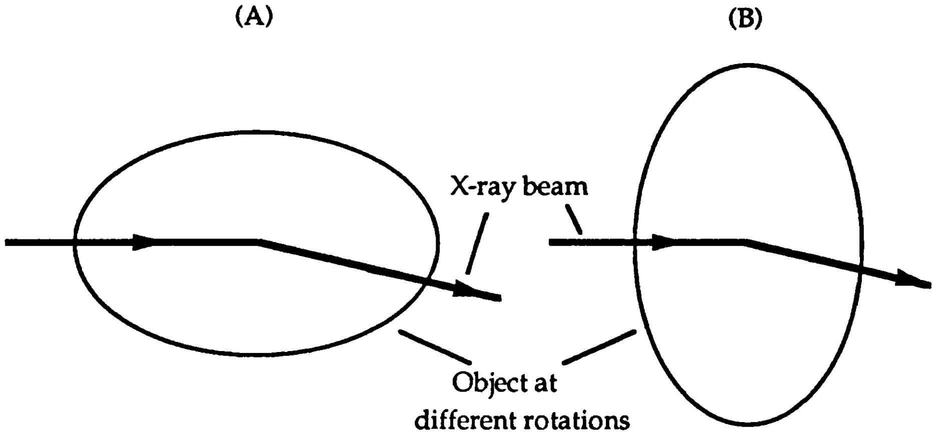

Figure 6.22 The effect of rotation of a non-cylindrical object. A different degree of attenuation is caused by the x-ray beam passing through different thicknesses of the material.

The x-ray beam passes through less material in (A) than in (B) and so the level of beam hardening in the resultant pattern will be greater. Correction will have to be made for this difference in material thickness because it will affect the relative intensities of the scatter peaks.

6.7.2 Off-centred scattering volume

The magnitude of the error due to off-centring the scattering volume depends upon the position of the volume with respect to the object, this is shown in figure 6.23.

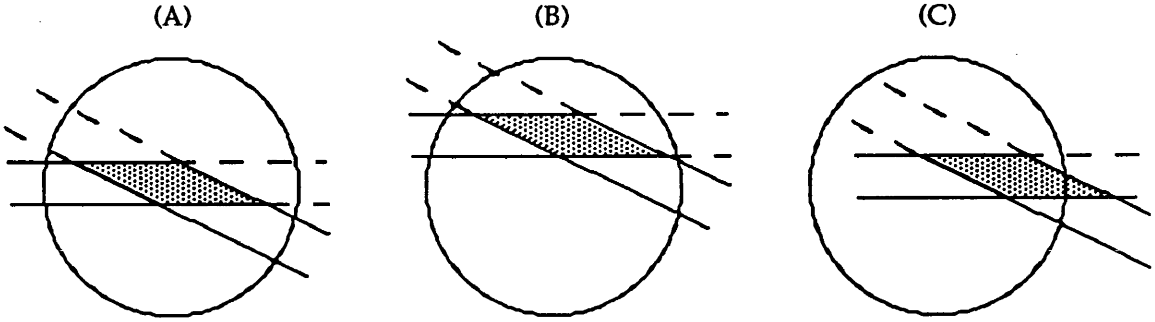

Figure 6.23 Various positions of the scattering volume (the shaded area) with respect to the object (the circle).

Three situations could be encountered; (A) the scattering volume is centred within the object, (B) the scattering volume is off-centred but is still fully enclosed within the object, and (C) the scattering volume is off-centred and is not fully enclosed within the object.

The shapes of the patterns for (A) and (B) will be the same because the same molecular components which cause the shape are present in both in the same quantities. A slight difference will arise in the relative intensities of the peaks, however, due to the fact that the x-ray beam in (B) has passed through a smaller thickness of surrounding material than in (A), and so less beam hardening will have occurred. The magnitude of this effect depends upon the amount of displacement of the volume from the centre of the object compared with the radius of the object (this determines the difference in thickness of material traversed) and the attenuating properties of the surrounding material. In the case of (C) the same applies as for (B) unless their is a different material surrounding the object of interest. For example, if trabecular bone is studied and the scattering volume overlaps the edge of the trabecular region then the surrounding cortical bone, and perhaps some soft tissue, will be included within the scattering volume. Hence, the resultant scatter pattern will consist of a combination of the patterns of trabecular bone, cortical bone and soft tissue.

Energy dispersive scatter patterns were measured for a freshly excised femoral head with the scattering volume off-set by various amounts. The centre of the bone was found by measuring the diameter and this was carefully positioned at the centre of the scattering volume for measurement. For subsequent measurements the bone was moved a given distance either parallel or perpendicular to the direction of the incident beam. Figure 6.24 shows plots of the bone to marrow peak ratio as a function of displacement perpendicular and parallel to the incident beam respectively.

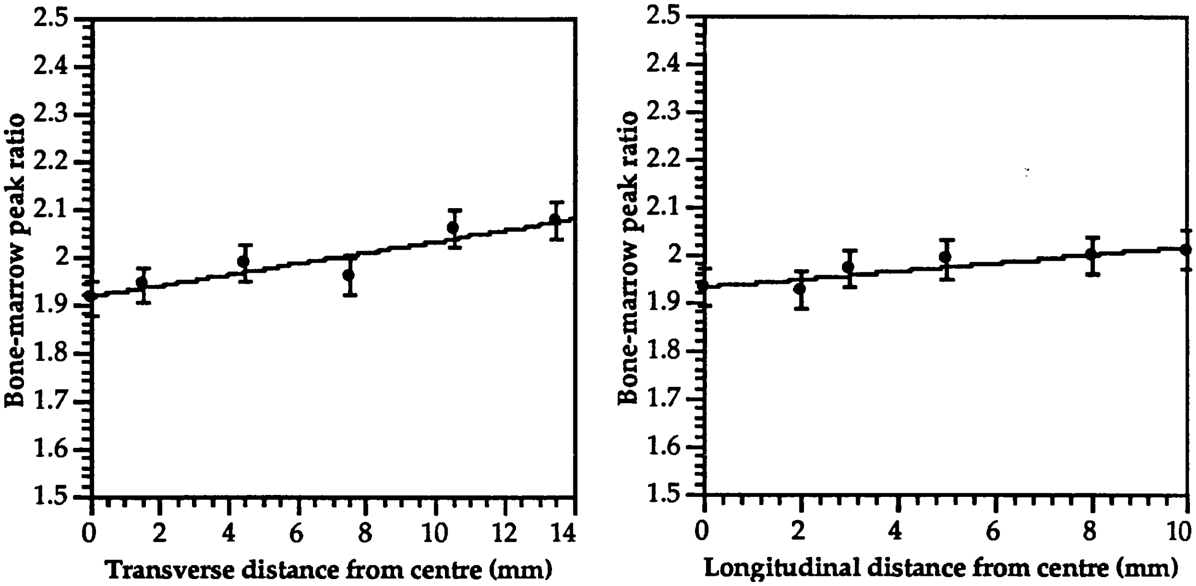

Figure 6.24 Plot of bone-marrow peak ratio for a femoral head moved (A) perpendicularly to the direction of the incident beam and (B) parallel to the incident beam. The equation of line (A) is given by $f(x)=1.165e\text{-}2x+1.916$, and that of the line (B) is given by $f(x)=8.67e\text{-}3x+1.931$.

The bone-marrow peak ratio is seen to increase the further from the centre the scattering volume is centred. This is because more of the surrounding cortical bone falls within the scattering volume and so increases the relative height of the bone peak. The gradient of increase is very small in both cases, for movement perpendicular to the beam a distance of 3.3mm from the centre is required for the peak ratio to increase beyond the 2% error level (the estimated precision for these measurements), whereas a distance of 4.5mm parallel to the beam from the centre will increase the peak ratio beyond the error level. This demonstrates that an error in the positioning of the bone less than 3mm will not significantly affect the results. It is important to note that the distance quoted applies for this particular combination of object size and scattering volume. A larger scattering volume and a smaller object will be much more susceptible to positioning error.

6.8 Measurement of anthropomorphic bone phantoms

The bone-marrow peak ratio of the five encased femoral head phantoms (described in § 3.4.2.3) were measured. Prior to measurement each phantom was radiographed at two perpendicular views. The rotation of the phantom when it was radiographed was marked on each phantom. An anti-scatter grid and a screenless film cassette were used to produce sharp radiographic images. This allowed the position of the bone within the phantom to be carefully measured, the required incident position of the x-ray beam for scatter measurements was then marked on the phantom. For the scatter measurements each phantom in turn was positioned at the scattering site such that the narrow-slit x-ray beam was incident on a slice through the bone first 1.5cm and then 2.0cm from the top-most part of the femoral head (see figure 6.25). The mark on the phantom was aligned with the slit collimators. The perpendicular radiographic view of the phantom allowed the bone to be positioned such that the scattering volume was fully enclosed within it. The positioning error was estimated to be ±2mm. Slices were measured at a particular position because CT images of thin slices of the femoral heads (seen later in § 6.9.1.1) showed the bone-marrow ratio to vary with distance from the top of the head. The slice measured was 1.5cm from the top of the femoral head, this point was reasonably central along the length of the bone.

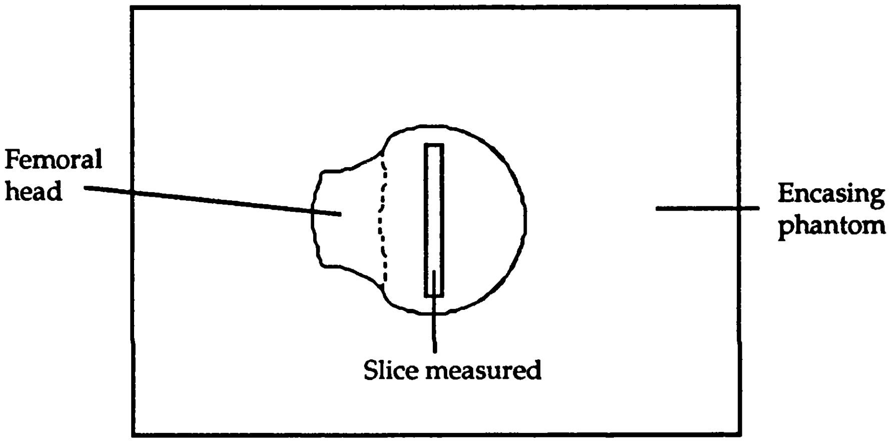

Figure 6.25 Measurement of bone slice in the encased femoral head phantoms.

The bone-to-marrow peak ratios from the scatter patterns of the five phantoms are listed in table 6.5.

Phantom number	1	2	3	4	5
Bone-marrow peak ratio	2.20 ±0.06	2.02 ±0.06	2.05 ±0.06	1.98 ±0.06	2.07 ±0.06

Table 6.5 Bone-to-marrow peak ratios of the five bone phantoms.

The error values quoted are based upon the estimated statistical precision (from § 6.5)

6.9 Comparison with bone density measurement techniques

In order to assess the validity of the bone measurements obtained with the elastic photon scatter technique the same bone phantoms need to be measured by established bone measurement techniques. Quantitative computerised tomography (QCT) and Compton scatter densitometry (CSD) were used as these are the only methods for bone measurement currently available which can isolate the response of pure trabecular bone from the surrounding tissue.

6.9.1 Quantitative computerised tomography

A CT image is produced in the following way; a conventional x-ray tube is rotated around the object to be imaged, x-ray profiles are then recorded at various orientations around the patient using scintillation detectors and suitable counting equipment. Using this information reconstruction algorithms can compute and display the cross-sectional image of a slice through the patient by considering which tissues must be present in order to produce the x-ray profiles. A CT number, based upon the linear attenuation coefficient (which due to the predominance of Compton interactions is in turn dependent upon physical density), is then assigned to each pixel of the image displayed. Quantitative CT measurements of bone have been found to be very precise (<1%, Cann 1988). Further details on this technique can be found in Speller *et al* (1989).

6.9.1.1 QCT bone measurement

CT images of the five bone phantoms were obtained using a Philips Tomoscan 350 CT scanner at University College Hospital. Operating parameters of 120kVp and 200mA, with 0.5mm copper filtration, were employed. A scanogram was performed in which the phantom was quickly scanned to enable the correct region of the femoral head to be accurately located and then seven 1.5mm thick slices, at 3mm separations, were imaged. The reason for the thin slices spaced along the femoral head was such that the slice width would be comparable to that measured using the quantitative diffraction technique (1.5mm was the thinnest slice available and so the closest to the 1mm slice quantitative diffraction measurements) and also to investigate the change in density at various positions. Density calibration was performed by attaching four solutions of K_2HPO_4 (with densities 1.05, 1.13, 1.21 and 1.30gcm^{-3}) to the surface of the phantom during the scan.

The image data was stored on tape and then transferred to a Sun workstation for analysis with image analysing software (Dispimage). A circular region of interest (ROI) was centred on each of the calibration solutions and the mean CT number noted for each, such that the relationship between physical density and CT number could be determined (the relationship was found to be linear). A large, circular ROI (of area 320mm^2) was centred on the trabecular bone region in each of the slices and the mean CT number displayed could then be transformed into a density value using the measured linear relationship.

The typical variation of physical density with slice position in the femoral heads is shown in figure 6.26.

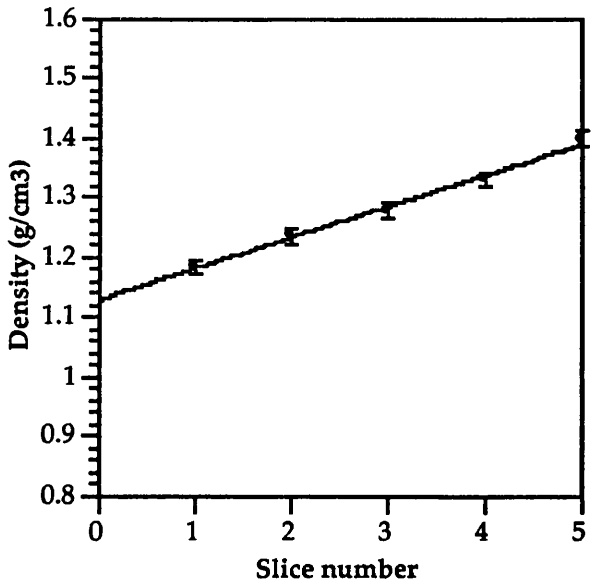

Figure 6.26 Variation of physical density with slice position in the femoral head. The slice number increases towards the top of the head.

The bone density was observed to increase towards the top of the femoral head due to the greater concentration of trabeculae. This result indicates that for an accurate comparison of the elastic photon scatter results with CT measurements both measurements need to be performed at the same position of the femoral heads, i.e. a slice 1.5cm from the top of the head. Table 6.6 lists the bone densities of the five phantoms measured from CT slices at the required position.

Phantom number	1	2	3	4	5
QCT bone density (g/cm^3)	1.38 ±0.02	1.22 ±0.02	1.27 ±0.02	1.27 ±0.02	1.38 ±0.02

Table 6.6 Bone densities of the five femoral head phantoms measured using quantitative CT. A 1.5mm slice was measured at a distance of both 1.5 and 2.0cm from the top of the femoral head.

6.9.1.2 Correlation of bone-marrow peak ratio with QCT bone density

A comparison of the results of the bone-marrow peak ratios and the QCT bone density measurements for the five femoral head phantoms is shown in figure 6.27. A similar trend can be seen over the five phantoms with the measurements of both techniques.

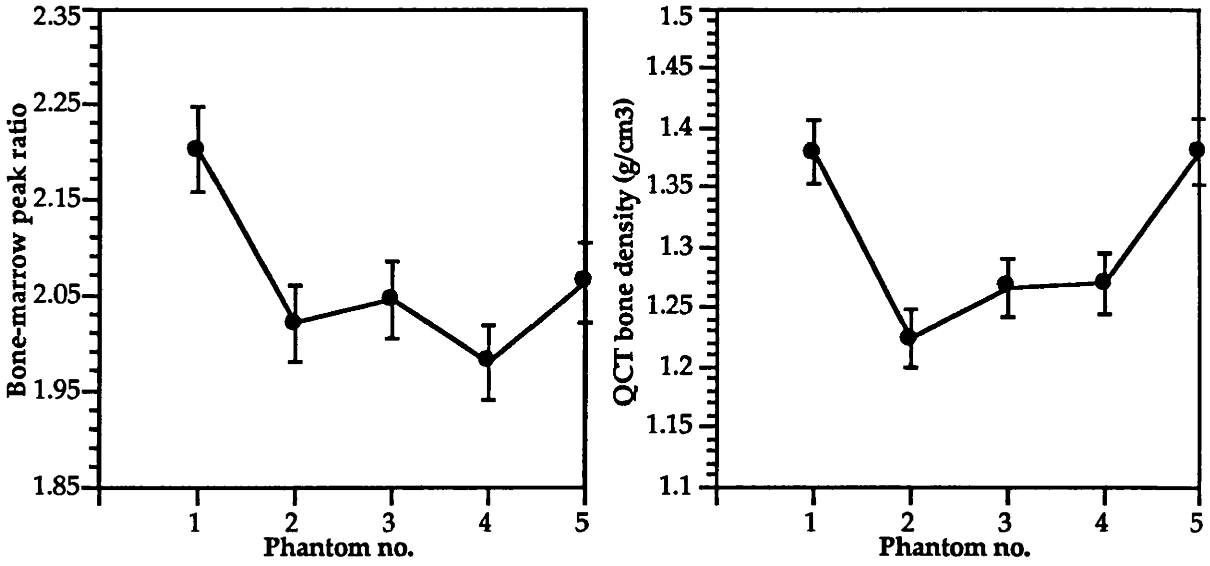

Figure 6.27 Comparison of the bone-marrow peak ratio and QCT bone density measurement for the five bone phantoms.

Plotting one set of measurements against the other gives a clearer indication of the correlation between the techniques (figure 6.28). Moderate correlation is observed (r=0.72). Correlation with an established bone measurement technique indicates that the bone-marrow peak ratio measured using the quantitative diffraction technique is sensitive to differences in the levels of bone within the trabecular region.

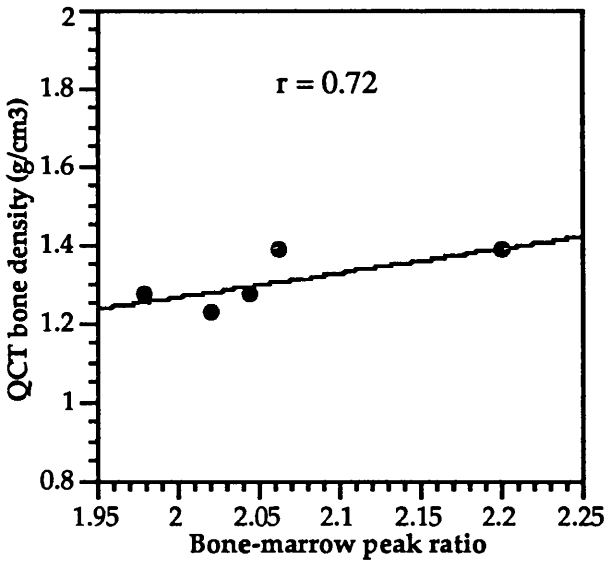

Figure 6.28 Correlation of the QCT bone density value with the bone-marrow peak ratio.

6.9.2 Compton scatter densitometry

In this technique the object is irradiated by a finely collimated x-ray beam and the Compton scattered photons produced are recorded by a collimated, energy sensitive detector positioned at a given angle such that only photons of a known degraded energy are detected. The scattered intensity is proportional to the density of the tissue that lies within the overlap of the two cone beams formed by the collimators on the source and detector. The attenuation of the scattered intensity by the surrounding tissue can be overcome either by using a dual scattering path or by recording the coherent scattered intensity. Further details can be found in Speller *et al* (1989).

6.9.2.1 CSD bone measurement

The bone densities of the five bone phantoms were measured on a dual x-ray path Compton scatter densitometer at University College London. Operating parameters of 120kV and 2mA were used during a 30 second measurement. The correct region of the phantom was located by scanning across the phantom in two dimensions. The scattering volume isolated a 0.64cm^3 region at the centre of the femoral head. The bone density values, reported by Mooney (1992), are given in table 6.7.

Phantom number	1	2	3	4	5
CSD bone density (g/cm^3)	1.21 ±0.02	1.06 ±0.02	1.07 ±0.02	1.02 ±0.02	1.16 ±0.02

Table 6.7 Bone density values of the five bone phantoms measured by Compton scatter densitometry.

6.9.2.2 Correlation of bone-marrow peak ratio with CSD bone density

The results of the bone-marrow peak ratios and the Compton scatter density measurements for the five femoral head phantoms are compared in figure 6.29.

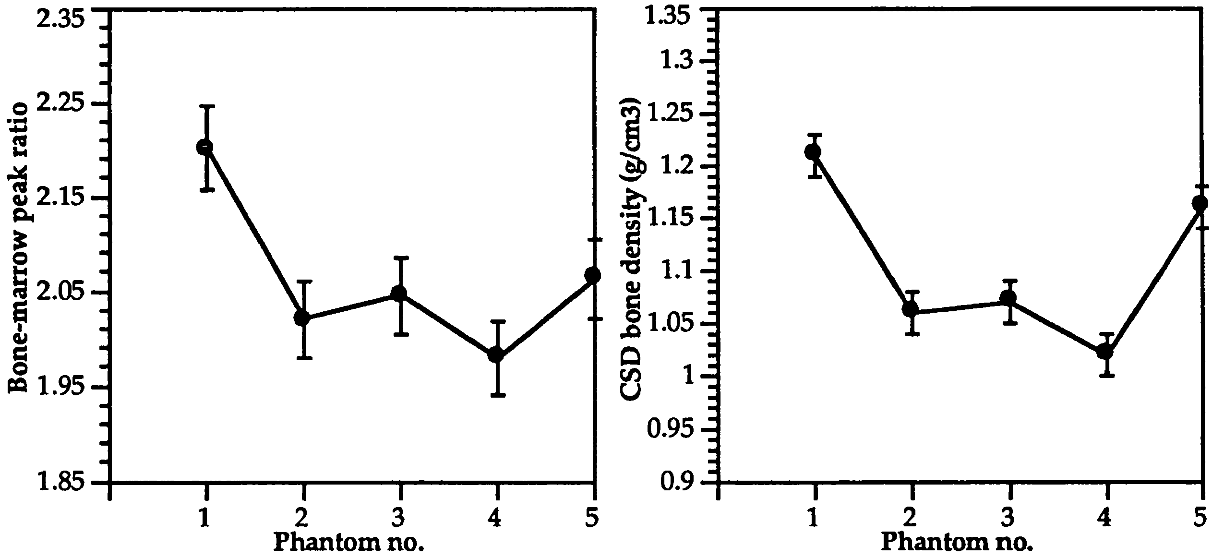

Figure 6.29 Comparison of the bone-marrow peak ratio and Compton scatter density measurement for the five bone phantoms.

As in the comparison with QCT both sets of measurements show a similar trend over the five phantoms.

The correlation between the two forms of measurement is shown in figure 6.30. Good correlation is observed (r=0.92). This result confirms that the quantitative diffraction technique is capable of quantifying changes in trabecular bone.

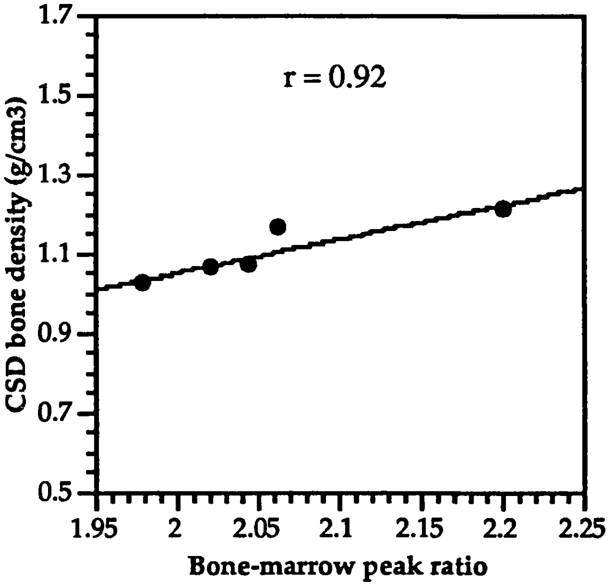

Figure 6.30 Correlation of the Compton scatter density value with the bone-marrow peak ratio.

6.9.3 Discussion

The correlation of the bone-marrow peak ratio with bone density values from established techniques has verified the sensitivity of the quantitative diffraction technique to changes in the quantity of bone tissue within the trabecular region. This technique measures the ratio of the volume of bone tissue to the volume of marrow tissue within the trabecular region. This is not the same as the bone density but, due to the relationship between volume and density, is obviously related. Therefore the values of the ratio would be expected to correlate with bone density values.

The closer correlation of the diffraction technique with Compton scatter densitometry than with QCT could be explained by the fact that they both measure the intensity of photons exiting the patient which have been scattered within the bone. Therefore attenuation of the photon beam by bits of bone or tissue in the path will be similar for each. This situation will produce a different effect on the CT numbers of the trabecular region (which leads to the QCT bone density value).

The volume ratio has possible advantages as the measured parameter over the bone density. One advantage is that the bone volume provides a better indication of the quantity of bone tissue present (which is the main factor in determining the bone strength). The reason being that the densities of tissues vary slightly among individuals and so dense osseous tissue in the trabecular region will elevate the average density of that region making the quantity of osseous tissue present appear greater. Another advantage could be the ability of the diffraction technique to differentiate between red and yellow marrow (discussed in § 6.3). Further work needs to be done to decide how to extract information on the relative quantities of red and yellow marrow but this could help solve the problem in bone density measurements caused by unknown concentrations of the different density marrow types

6.10 Determination of bone volume

6.10.1 Trabecular bone calibration curve

The theoretical description in § 2.9 together with the experimental results in § 6.5.2 demonstrated that it is possible to get quantitative information on the percentage mass or volume of a two component system from the peak ratios by means of a calibration curve. Section 6.4 explained that substitute materials required to truly simulate the material in terms of its diffraction properties must be composed of the same components as the material, therefore calibration materials for trabecular bone must be composed of mixtures of actual bone and adipose tissue.

The calibration materials were prepared by carefully weighing (to ±0.01g) powdered bone tissue and soft adipose tissue, thoroughly mixing to ensure uniformity throughout and then tightly packing into thin-walled, plastic containers (of 3.0cm diameter). The powdered bone tissue was prepared by crushing a dry bone using a vice and then grinding to a powder using a pestle and mortar. Soft animal fat was used as the adipose tissue. The study of the accuracy achieved with the calibration curve for the two powder samples (discussed § 6.5.2) demonstrated that greater accuracy will result if the majority of calibration samples are produced over the range of concentrations likely to be studied. The typical concentration of bone tissue (by percentage volume) estimated to be found in the trabecular bone studied is approximately 25 - 45% (found from computed tomography images of the trabecular slices (§ 6.9.1); the calculation is described later in § 6.10.2) so the calibration samples were prepared to cover this range. The following calibration materials were prepared (expressed as the percentage weight of bone tissue); 60, 50, 45, 40, 35, 30, 25 and 20%. These materials were placed in thin-walled plastic containers 4.0cm in diameter. This is a similar size to the trabecular bone within the region of the femoral head studied. A thin layer of cortical bone was also placed in the path of the beam to simulate the attenuation by the cortical shell surrounding the femoral heads.

The bone-to-marrow ratio as a function of the bone concentration forms the trabecular bone calibration curve (figure 6.31). Using this curve the measured bone-marrow peak ratios can be converted to an absolute value of percentage bone volume.

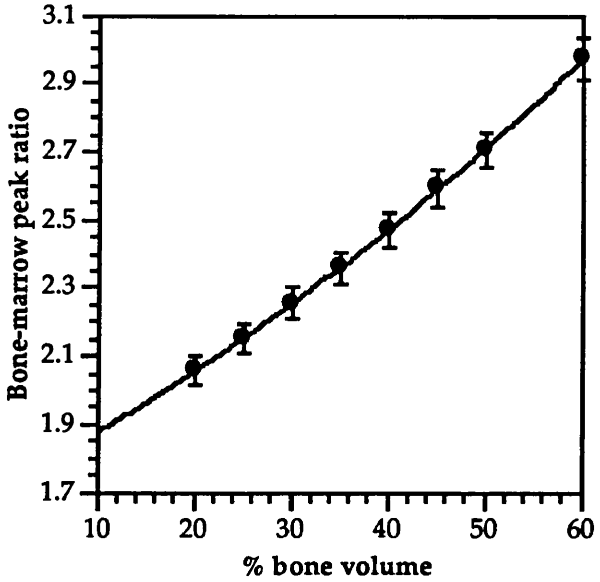

Figure 6.31 The trabecular bone calibration curve. The curve through the points is an exponential with the equation f(x)=1.712.exp(9.189e-3.x).

6.10.2 Calculating and testing the measured bone volume data

In order to make a direct comparison between the measurements of bone-marrow peak ratio for the femoral head phantoms and for the phantoms for the calibration curve correction needs to be made for the differences in attenuation between the two. Radiographs of the bone phantoms were taken in order to measure the thicknesses of the femoral head and of the surrounding muscle substitute at the position of the measured slice. The exponential law of attenuation was used to correct for the differences in tissue thickness between the phantoms and the calibration materials.

The values of percentage bone volume for the five femoral head phantoms, calculated using the equation of the calibration curve following attenuation correction, are shown in table 6.8. Also shown in order to test the diffraction bone volume data, are values of percentage bone volume for the five phantoms calculated from the QCT bone density data (the QCT bone density values were given in table 6.6). The percentage bone volumes were calculated from the bone density using the relationship between volume and density; the total trabecular mass is given by

$$V_T.\rho_T = V_B.\rho_B + V_M.\rho_M \qquad (6.2)$$

and the total volume is given by

$$V_T = V_B + V_M = 1 \qquad (6.3)$$

where V_T, V_B and V_M are the percentage volumes of the total, the bone and the marrow respectively, and ρ_T, ρ_B and ρ_M are the respective densities of the total, the bone and the marrow. The densities of bone and marrow are 1.92gcm^{-3} and 0.98gcm^{-3} (Woodard and White 1986), and the density of the total trabecular bone is given by the QCT data.

Solving equations 6.2 and 6.3 gives the percentage bone volume. These are shown in table 6.8.

Phantom number	**Diffraction % bone volume**	**QCT % bone volume**
1	41 ±3	42 ±2
2	31 ±3	26 ±2
3	32 ±3	30 ±2
4	28 ±3	31 ±2
5	34 ±3	43 ±2

Table 6.8 Percentage bone volumes for the five femoral head phantoms.

Good agreement is seen between the two sets of bone volume measurements with all but phantom 5 being equal within the estimated error levels. This result demonstrates that absolute measurements of the percentage bone volume within the trabecular bone are possible with the quantitative diffraction technique.

6.11 Estimation of radiation dose received in standard procedure

The radiation exposure at the surface of the phantom was measured using an ion chamber and radiation monitor (model 2025 from Radial Corporation). The radiation exposure time and level required to provide the signal-to-noise ratio obtained for the bone phantoms in this thesis produced an exposure of $0.996 \mathrm{Ckg}^{-1}$ at the surface. This corresponds to a dose equivalent in air of 9.96mSv. These values represent the skin surface dose. This value is reasonably high and is comparable with the surface dose of ~10mSv from computerised tomography. However, in this experiment the skin dose is very localised with only a very small region of the body irradiated (the size of the slit collimator), furthermore the region of the body irradiated (the femoral neck) is relatively non-radiosensitive. A better indication of the risk to the patient from the radiation dose is given by the *effective dose equivalent* (EDE). It represents the total radiation dose to a number of organs weighted according to a risk estimate for each organ concerned (ICRP 1977). The EDE is calculated as follows:

$$\mathrm{EDE} = \sum_{T} W_T \cdot H_T \qquad (6.4)$$

where W_T is the relative radiation sensitivity, and H_T is the mean dose equivalent.

The tissues likely to be irradiated during a femoral neck measurement have radiation sensitivity values of 0.03 for bone, 0.12 for marrow and 0.3 for general soft tissues (ICRP 1977).

The mean dose equivalent is described as follows:

$$H_T = D_T \cdot Q \cdot N \qquad (6.5)$$

where D_T is the mean absorbed dose, Q is the quality factor (1 for photons) and N is a modifying factor based on the ratio of tissue irradiated to the total tissue mass.

The EDE estimated for a femoral neck examination with this technique, based upon a 10mSv surface dose, is given as follows:

$$\mathrm{EDE} = 6.24\times\frac{1.5}{70}\times 0.3 + 6.24\times\frac{0.028}{4}\times 0.03 + 6.24\times\frac{0.042}{1.498}\times 0.12 = 0.062\mathrm{mSv}$$

A mean absorbed dose of 6.24mSv was estimated from the 10mSv surface dose based upon dosimetric measurements of Pye *et al* (1990).

The mass of each tissue irradiated was calculated by assuming that all of the tissue type within a 2cm length of the leg will be irradiated; only a narrow slit region (1mm width and 2cm length) will be irradiated by incident x-rays but photons will be scattered and absorbed within a larger region of the tissue. The leg was assumed to be 16cm in diameter and the femoral head was 3cm in diameter. The marrow was assumed to occupy 74% by volume of the trabecular region within the skeleton. The values of total organ mass for soft tissue, cortical bone and marrow were 70kg, 4kg and 1.498kg respectively (ICRP 1974).

The estimated EDE value of 62μSv compares with 30.3μSv for a femoral neck study using Compton scatter densitometry (Mooney 1992), 6.4μSv for the same study using dual x-ray absorptiometry (Pye *et al* 1990) and 60μSv for a chest x-ray (Pye *et al* 1990).

- 7 -

Application to gallstone identification

The technique proposed in this thesis is not limited to the study of bone tissue, it can also be applied to other crystalline tissues. Results have shown (figure 6.4) that gallstones produce a structured scatter pattern which can be distinguished from the patterns of other tissues. This chapter considers the various types of gallstone that exist and investigates the ability of this technique to characterise the stone types for clinical applications.

7.1 Gallstone disease

The formation of stones in the gall-bladder, generally termed gallstone disease, is a common problem, affecting approximately 10% of the adult population. Of these about a quarter will develop symptoms at some time in their lives, making it the most frequent cause of abdominal surgery. The symptoms are generally a disruption of the digestive system accompanied by anything from mild irritation to severe pain. In certain cases stones can block the fluid ducts to the liver, which can result in serious illness.

7.1.1 Cause and pathogenesis

The gall bladder is a small conical sac approximately four inches in length and one inch in breadth situated on the under side of the right lobe of the liver (figure 7.1).

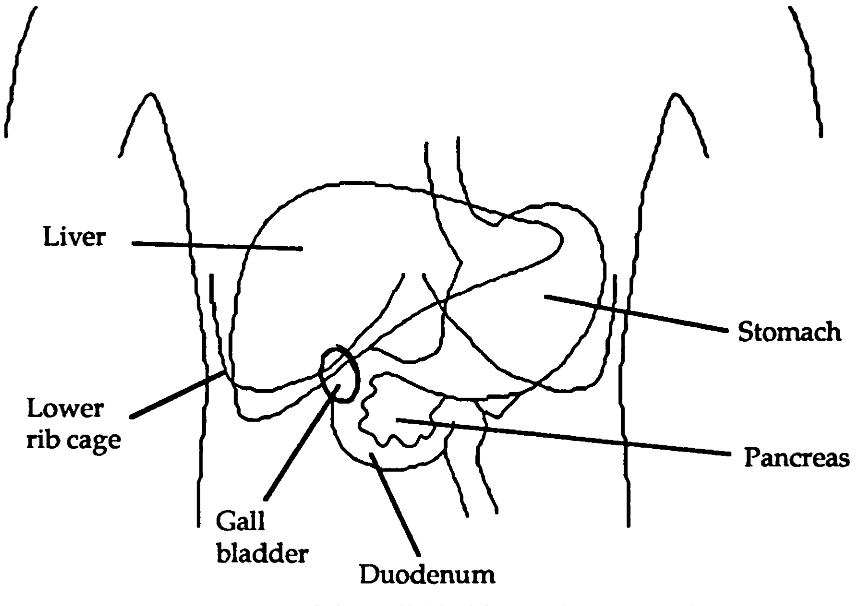

Figure 7.1 Location of the gall-bladder within the abdomen.

It serves the liver as a reservoir for the bile fluid, aiding the digestion process. Gallstones are formed from the constituents of the bile fluid, such as cholesterol, bile pigments, calcium salts and various organic substances. The proportions of each of these components in the stone differ depending on the method of formation. The cause of stone formation is generally a change in the composition of the bile (usually an increase in cholesterol concentration); other factors such as biological changes in the gall bladder or biliary tract infection can also contribute. The exact formation mechanism however is unclear, as is the cause of the change in bile composition.

7.2 Types of gallstone

Different types of gallstone exist. Variation in the proportions of the constituents produces a variety of stone types, each type having different properties. Different classifications have been proposed based on appearance or other characteristics, for example cholesterol stones and black and brown pigment stones, but for diffraction purposes they are best classified in terms of the composition of the crystalline constituents. The crystalline components of gallstones can be grouped into cholesterols and calcium salts. Some gallstones contain bile pigments and so have been classified as pigment stones, however, this is an amorphous substance which does produce diffraction peaks (Sutor and Wooley 1973) and so cannot be used for classification with diffraction studies. The principal crystalline compounds are the following; three forms of cholesterol, three forms of calcium carbonate (aragonite, calcite and vaterite) and calcium phosphate. Sutor and Wooley (1973) have suggested three categories for the purpose of x-ray diffraction under which gallstones can be classified; cholesterol stones, calcium stones and a combination of the two. Sub-categories also exist within the main headings, for example, cholesterol stones occur in either the *mixed* or the *pure* state. Biological differences can also cause small differences among the same stone type. A survey of 481 gallstones (Sutor and Wooley 1973) found the percentage of incidence of the three main stone types to be 59.9%, 13.1% and 27.0% respectively.

7.2.1 Cholesterol stones

Mixed or laminated: The most common gallstones are the cholesterol stones, the result of a high cholesterol, low fibre diet. The most common type of cholesterol stones are the mixed (laminated) stones. These are formed as a group of stones, irregular in shape, and anything up to 1cm diameter in size. A section through the stone displays a laminated structure; dark brown layers of mainly cholesterol alternate with pale layers of bile pigment. The outer colour of the stone varies greatly, being either white, pink, brown or black according to the composition of the outer layer.

Pure: Pure cholesterol stones are usually solitary, they are oval in shape, have a low density and can be fairly large (>3cm in length). A section through the stone displays sheaves of cholesterol crystals radiating outwards, with no trace of lamination. They are usually pale yellow or white, and some are almost transparent. Some of these stones (termed *combination* or *compound* stones) are found to have a laminated cortex caused by a secondary deposit of cholesterol, which occurs when the wall of the gall-bladder becomes inflamed by bacterial infection.

7.2.2 Calcium stones

Calcium stones are entirely composed of calcium salts, and are the rarest form of stones. They are small, hard stones, generally black, black-brown or red-brown in colour with white or yellow deposits often seen on the surface. These stones usually occur in groups.

7.2.3 Mixture stones

The remaining stones contain both cholesterol and calcium salts in varying proportions. Such a large number of possible combinations of the various constituents exist that no one description can adequately cover all of the stones.

7.3 The need for identification

If the symptoms of gallstone disease persist, as is likely, then treatment is necessary. The conventional method of treatment is surgery to remove the stones. This operation is a safe and effective method. However, surgery is undesirable; it can be traumatic, lead to post-operative complications, particularly in the elderly, and requires the discomfort and expense of hospitalisation. Non-surgical methods of removal are preferred. These include chemical dissolution, laser fragmentation and lithotripsy.

Chemical techniques employ particular acids to dissolve the stone. The course of treatment can last several months. Calcified stones do not, however, respond to this treatment.

The application of short, repetitive, high-powered laser pulses to the stone can safely cause fragmentation. This treatment is not suitable for cholesterol stones.

Lithotripsy employs acoustic shock waves to fragment the stone. As the acoustic impedance of the stone differs from that of the surrounding tissue the energy is reflected when the shock waves hit the stone causing a compressive wave to propagate into the stone. Following disintegration chemical treatment is necessary to flush the fragments from the body. This treatment is not suitable for stones with a high calcium content such as calcium stones or mixture stones with a large percentage of calcium salts.

This section has shown that the stone type determines the optimum method of treatment. Hence, knowledge of the stone type prior to treatment would be very useful.

A summary of the gallstone types and their properties is shown in table 7.1.

Stone type	**Nature**	**Relative occurrence**	**Response to treatment**
Cholesterol stone	Either of the following: Large, low density solitary stones, usually pale or white. A group of irregular shape stones, with a laminated interior	Most common ~60%	Responds to lithotripsy or chemical dissolution
Calcium stone	Usually occur as a group of small, hard, black, black-brown or red-brown stones	Least common ~13%	Require surgery - do not respond to chemical dissolution or lithotripsy
Mixture stone	No typical appearance	~1 in 4	If calcium content is high then surgery is needed

Table 7.1 A summary of the types of gallstones and their properties.

This section has shown that the stone type determines the optimum method of treatment. Hence, knowledge of the stone type prior to treatment would be very useful.

7.3.1 Methods for *in-vivo* identification of gallstones

Several techniques exist for identifying the stone type *in-vitro*. The most accurate ones are x-ray diffraction (Sutor and Wooley 1969) and infra-red spectroscopy (Trotman *et al* 1977), both of which can determine the chemical composition of the stone. Other, less sensitive techniques include chemical analysis, taking radiographs and morphological inspection. However, *in-vivo* identification is a much more difficult problem. Radiography can usually detect the presence of a gallstone (commonly requiring contrast media) and those with a high calcium content can often be identified, but no distinction can be made between other stone types. Techniques such as computerised tomography and ultrasound can also be used to detect the presence of a stone with reasonable sensitivity, but their ability to distinguish stone types is very limited. Dual energy techniques employing a two-detector probe which is positioned behind the patient during a fluoroscopic procedure have been shown (Baba-Hamed 1990) to be capable of distinguishing between cholesterol and pigment stones. However, at present no technique has been commonly adopted for *in-vivo* identification of stone types.

7.4 Characterising gallstones *in-vitro* using elastic photon scatter

Energy dispersive scatter patterns were measured for gallstones from 23 separate patients. Each gallstone was suspended by very fine wire at the scattering region for measurement to prevent the inclusion in the pattern of other materials. The standard x-ray tube settings of 70kV and 3mA were used and all measurements were performed at a scattering angle of 6 degrees. The irradiation time was 240 seconds, however the general shape of the pattern could be identified in less than 10 seconds.

7.4.1 Cholesterol stones

The stone type was identified prior to measurement by morphologic investigation. Almost all of the stones were cholesterol stones. Figure 7.2 shows the shapes of the pure and the laminated cholesterol stones. Only five patterns of each type are shown to simplify the graphs. The patterns of these stones were normalised and plotted on the same axes in order to demonstrate the general shape.

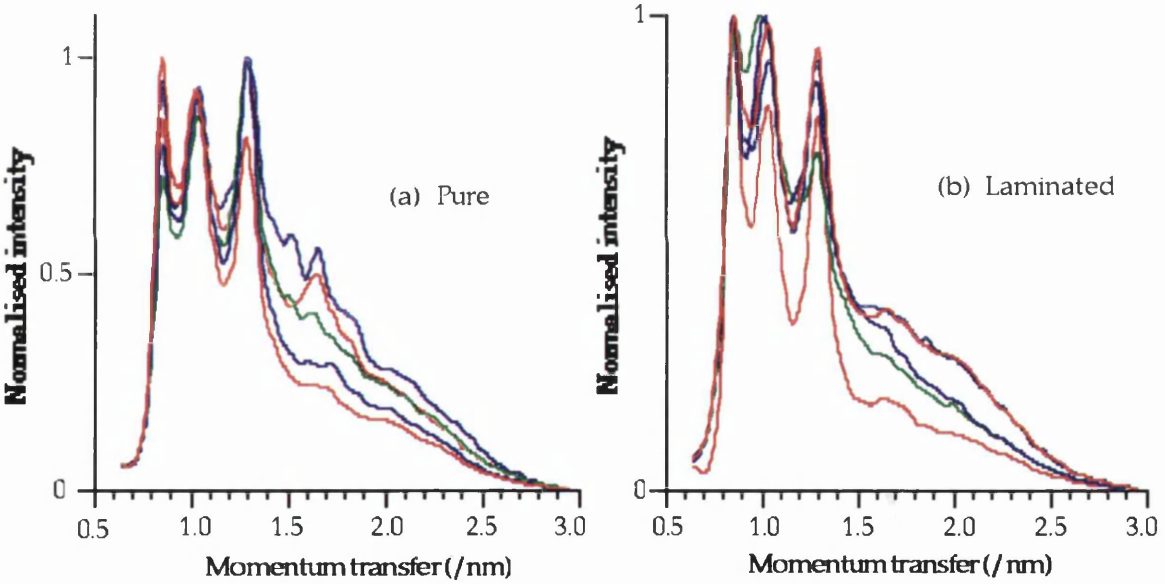

Figure 7.2 Energy dispersive scatter patterns at 6 degrees of (a) pure cholesterol stones from five separate patients and (b) laminated cholesterol stones from five separate patients.

No obvious differences can be seen between the scatter patterns of the pure and the laminated cholesterol stones. This is expected as both are principally composed of cholesterol. The lack of difference between the two forms is not significant as both respond similarly to treatment.

The typical scatter pattern of a cholesterol stone is shown in figure 7.3 for clarity (one of the scatter patterns shown in figure 7.2 was selected). The three peaks, which occur at momentum transfer values of 0.84 ± 0.04, 1.0 ± 0.04 and 1.3 ± 0.04nm^{-1}, were found to be present in the scatter patterns of all the cholesterol stones.

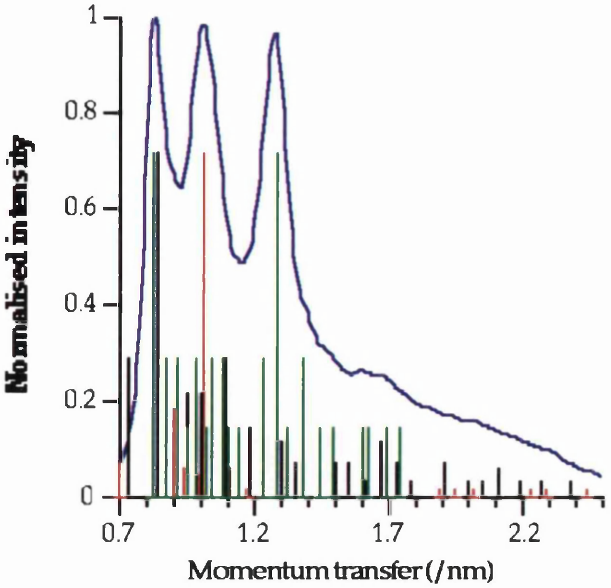

Figure 7.3 The blue curve shows the measured energy dispersive scatter pattern of a typical cholesterol stone. The red, green and black line spectra are the true spectra for the three forms of cholesterol.

The interatomic separations within the cholesterol molecule are tabulated in the Powder Diffraction File (JCPDS 1961). These separations were converted to their respective momentum transfer values at 6° (the calculation was described in § 2.7). Figure 7.3 compares the measured cholesterol stone scatter pattern with the spectra of the three different forms of cholesterol, calculated from their interatomic separations. The measured scatter pattern clearly follows the combined shape of the three sets of line spectra with the positions of the measured peaks corresponding with the positions of the true spectra. This shows the three peaks to be due to the cholesterol molecule. Therefore if these three peaks are dominant in the measured scatter pattern of a gallstone it must be a cholesterol stone. As the peaks are due to different forms of the cholesterol molecule the relative intensities of each of the peaks will differ depending on the quantity of that particular form within the gallstone. This explains why the relative heights of the three peaks vary in the measured cholesterol spectra (figure 7.2).

7.4.2 Calcium stones

Figure 7.4 shows the scatter pattern of a calcium gallstone. The peak occurs at 1.7nm^{-1}. This is at the same position as the peak in the calcium carbonate scatter pattern (figure 6.3). This pattern differs clearly from the patterns of the cholesterol stones, indicating that this technique can be used for identification.

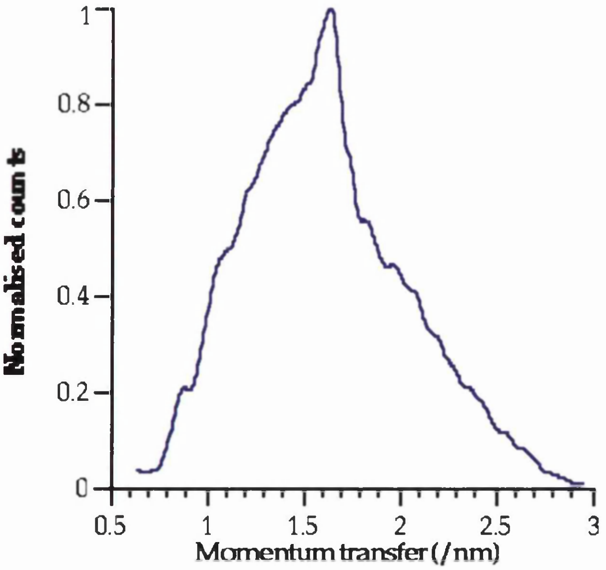

Figure 7.4 Energy dispersive scatter pattern of a calcium gallstone. Due to the rarity only one stone was available.

7.4.3 Mixture stones

Figure 7.5 shows a pattern of a gallstone which contains both calcium carbonate and cholesterol. The three characteristic cholesterol peaks can be seen within the pattern. indicating the presence of cholesterol, a peak is also seen at 1.7nm^{-1} indicating the presence of calcium carbonate. This stone can therefore be classified as a mixture stone. The relative intensities of the cholesterol and calcium peaks depend upon the relative concentrations of the two components. Further work is required to obtain quantitative information on the relative proportions of cholesterol and calcium within the stone. This would involve producing a calibration curve by making up varying concentration mixtures of cholesterol and calcium carbonate, the heights of the peaks can then be related to the percentage composition (described in § 2.9). A threshold value for calcium content must then be found above which surgery is required to remove the stone.

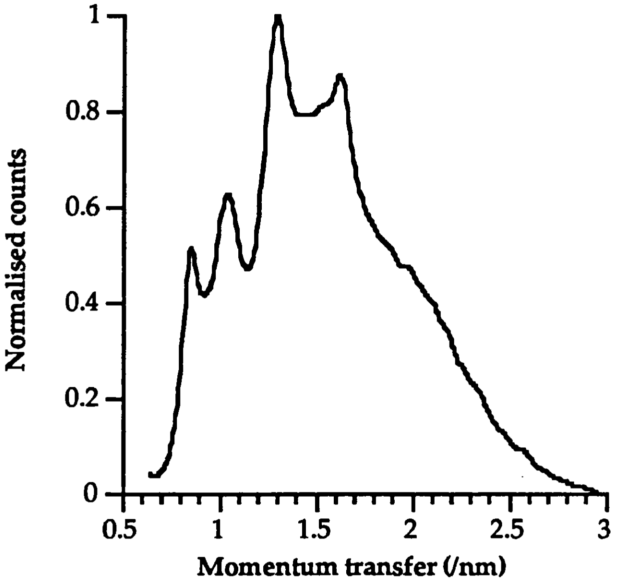

Figure 7.5 Energy dispersive scatter pattern of a mixed stone with cholesterol and calcium content.

7.5 Conclusions

Table 7.2 summarises the positions of the peaks in the patterns of each stone type.

Cholesterol stone	Calcium stone
0.84 ± 0.04nm^{-1} 1.02 ± 0.04nm^{-1} 1.29 ± 0.04nm^{-1}	1.7 ± 0.04nm^{-1}

Table 7.2 Momentum transfer values of the principal gallstone peaks. The errors quoted for these values are one standard deviation of the momentum transfer resolution of the measurement apparatus. The variation in the peak positions were found to always lie well within the resolution value quoted.

This technique has proved capable of characterising gallstones *in-vitro*. An advantage of this technique over most other methods for *in-vitro* analysis is that it does not require destroying the stone. The pattern of the cholesterol stone is quite distinctive. If an unknown stone is measured and three dominant peaks are observed at the correct momentum transfer values then the stone must be a cholesterol stone. This means that surgery is not necessary and lithotripsy or chemical means can remove the stone. If these peaks are not seen or are relatively very small than the stone contains only a small proportion of cholesterol at best, meaning that it will not be so easy to destroy. If a large peak is seen at a momentum transfer value of 1.7nm^{-1} then the stone is classified a calcium stone. Such a stone is very hard and requires surgery for removal.

7.6 Future gallstone work

Work needs to be done to assess the capability of this technique for *in-vivo* stone characterisation. The two problems with *in-vivo* measurement are; (i) locating the stone within the abdomen, and (ii) the attenuation of the surrounding tissue.

The stone will need to be located by taking a radiograph of the gall bladder region. Inclusion of the surrounding tissue within the scattering volume, and hence the scatter pattern, should not cause a major problem providing the gallstone fills the majority of the scattering volume. The surrounding tissue will have similar composition to muscle and so produce a smooth scatter pattern. The characteristic cholesterol or calcium peaks should still be evident on the background of the surrounding tissue pattern.

The beam will be heavily attenuated by the thickness of tissue in the abdomen. This will harden the beam and increase the measurement time. The measurement time can be minimised by stopping the irradiation as soon as the positions of the peaks can be identified; good counting statistics will not be necessary for pattern recognition. If the lower end of the spectrum (the region in which the cholesterol peaks are situated) is too attenuated to identify the peaks then the scatter angle at which measurement is made can be decreased. This will shift the cholesterol peaks to a higher and so less attenuated energy (see § 3.2.3).

- 8 -

Conclusions and future work

The aim of this work was to identify whether useful information on the osteoporotic state of bone tissue would result from elastically scattered photons in a clinical adaptation of x-ray diffraction. The design of a standard diffractometer was adapted and constructed for this work. The constraints of *in-vivo* measurement in the clinical environment require shorter wavelengths for penetration of the patient, a restricted photon flux for low dose, a short measurement time and reasonably compact apparatus. The attenuation effects in an object of patient dimensions are also considered. Two formats for measuring the diffraction pattern are possible; the scanning detector, angular distributive approach and the fixed detector, energy dispersive technique. The scatter angle of the detector in the latter is optimised to focus on the desired interference effects. The energy dispersive technique was found to be the best suited to clinical work as it has superior resolution, was easier to construct and could produce a result in less time.

The measured scatter pattern of trabecular bone was shown to be a combination of the individual patterns of the constituents; bone and marrow. Diffraction peaks were identified due to each component. The peaks due to each component are more evident with thin slices of bone (due to the absence of beam hardening) but can also be observed within the pattern of a full size bone. Quantitative analysis related the relative intensities of the diffraction peaks from each component to the relative proportion of that component within the scattering region. The ratio of the intensity of the bone peak to that of the marrow peak was shown to quantify the level of bone tissue present, and so was proposed as the parameter to assess the osteoporotic state of the trabecular tissue. Measured bone-marrow peak ratios of anthropomorphic phantoms containing excised femoral heads correlated with the established bone density measurement techniques of quantitative computerised tomography (r=0.72) and Compton scatter densitometry (r=0.92). This demonstrated that the quantitative diffraction technique is sensitive to differences in the quantity of bone in the trabecular region.

A trabecular bone calibration curve consisting of a plot of the bone-marrow peak ratios for varying percentage volumes of bone was produced from synthetic bone-marrow mixtures. Values of percentage bone volume within the measured slice of the anthropomorphic phantoms, calculated using the measured peak ratios and the calibration curve, approximated the expected values, thus demonstrating that the technique is capable of absolute measurement.

The principal advantages of this method to bone measurement are the ability to isolate the more indicative trabecular region of the bone during an *in-vivo* procedure, and the fact that separate signals from the bone and the marrow result from a single measurement.

The precision of the technique was found to depend upon the statistical counting error and the repositioning of the scattering volume within the measurement site. If a high photon intensity and a high detection efficiency could be achieved the precision would be very good (possibly as low as 1%). The accuracy of the technique in determining the percentage composition of a substance is also potentially very good as a direct comparison is made with calibration materials. The accuracy is limited by the number of points that define the calibration curve.

Monte Carlo simulation of the experiment, for the purpose of identifying necessary correction procedures, found the following;

(1) Coherent scatter is dominant in the 0-10° scatter range at diagnostic energies.

(2) The relative proportions of coherently scattered, Compton scattered and multiply scattered photons recorded by the detector vary slightly as a function of the percentage volume of bone tissue irradiated, but it is not significant to affect the results.

(3) The collimator geometry successfully prevented significant amounts of scatter in the material surrounding the scattering volume from reaching the detector.

Experiment has also shown that variation in the thickness of the surrounding material, caused for example by a patient putting on or losing weight, can be corrected by mathematically attenuating the diffraction peaks by the required amount.

The technique has also proved useful in the characterisation of tissues. The elastically scattered photons interfere to produce a diffraction spectrum that is dependent upon the internal atomic/molecular arrangement of the substance. This arrangement is unique to a given substance. The technique can distinguish between bone, gallstone, adipose and soft tissue. It cannot easily distinguish between the different types of soft tissue however because they each have a similar content, consisting primarily of water. Also, like all x-ray diffraction techniques it is particularly suited to substances with a crystalline nature.

The ability of characterisation was applied to gallstone identification. Gallstones can be classified into three main categories according to their crystalline constituents, each stone type requiring different patient treatment. A clear distinction between the three types was demonstrated with this method.

8.1 Future work

8.1.1 Clinical work

In order to progress further with this technique clinical trials on patients must be undertaken to investigate the performance of the technique in the clinical environment. This would involve comparative measurements between this technique and QCT and

CSD for a large number of subjects, together with serial and absolute measurements on groups of healthy and recognised osteoporotic subjects.

The apparatus described previously was a bench set-up for *in-vitro* work It was used to test the feasibility and capabilities of the method and to develop the idea. Realistic anthropomorphic phantoms can be measured with this system but there is no room for a whole patient, so apparatus was designed and built which is capable of *in-vivo* measurement. Figure 8.1 shows a diagram of the clinical apparatus.

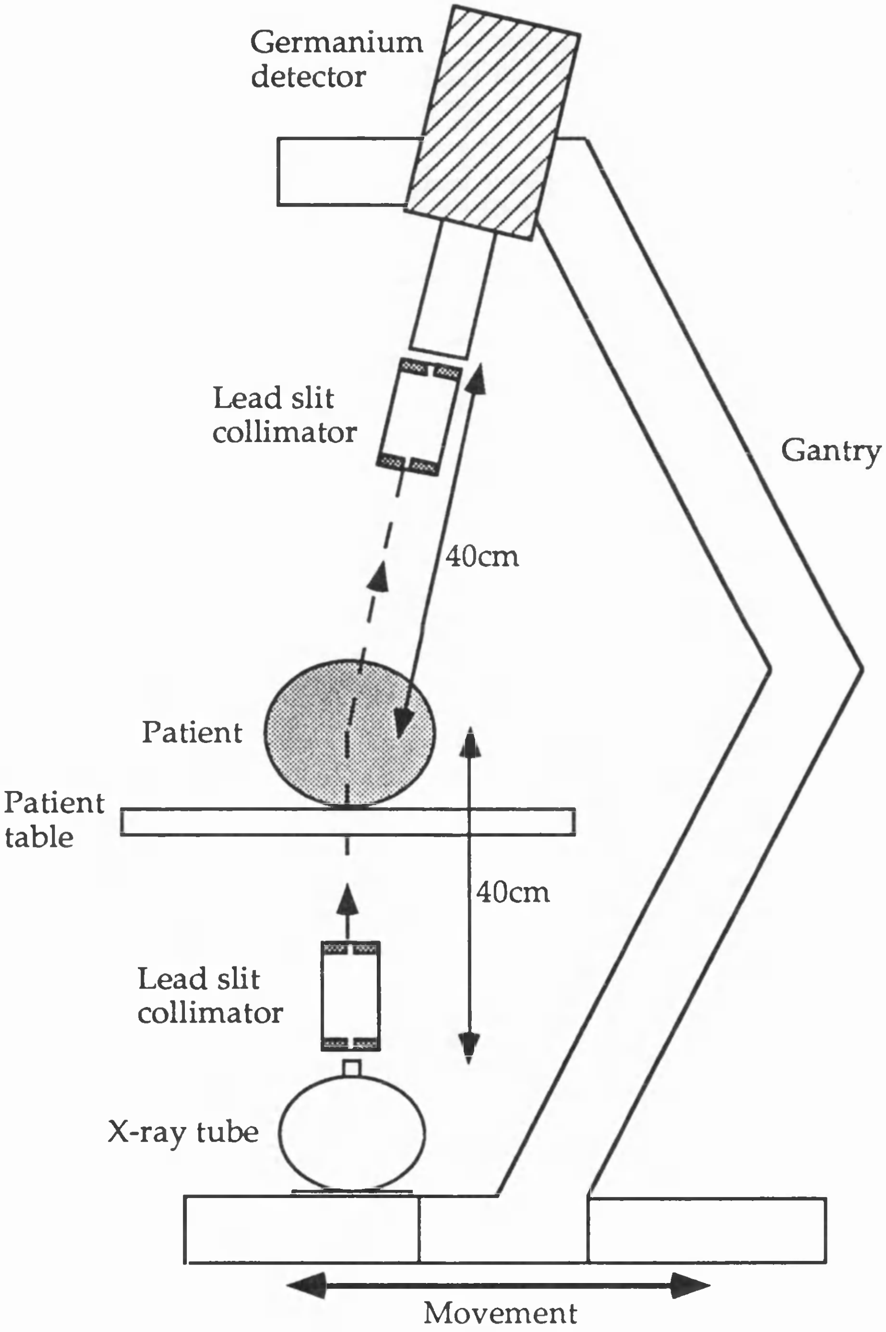

Figure 8.1 Design of the apparatus for the clinical environment.

Square, steel tubing (4cm in cross-section) was used to construct the frame to support the apparatus. The base was made sufficiently large (~80cm square) for the frame to be stable. The whole apparatus was rigidly mounted upon a screw thread platform attached to a stepping unit. This will enable the patient to be scanned in search of the correct region of interest.

The x-ray tube was mounted on the base of the frame, this was for two reasons,
(1) the apparatus was more stable with this weight on the base,
(2) the underside of the patient bed can be lined with lead to minimise the total body dose.

The detector was bolted to the frame at a fixed angle of 6° to the incident x-ray beam. A large plate bolted to the apparatus, to which the detector was attached, allows the detector to be fixed at other scattering angles if necessary.

Collimation for both the x-ray tube and the detector consists of a dural cylinder 23cm in length and 6.5cm in diameter with a lead slit collimator at each end (a diagram is shown in figure 8.2). The lead was 3mm thick and could slide along a mounting to allow the width of the slit to be varied. Rigid brackets were constructed to attach the collimators to the x-ray tube and the detector. Careful laser alignment was necessary such that all four slits were parallel and in line, and such that the slits they subtended overlapped to form the scattering rhombus at a suitable position at which the patient could be placed.

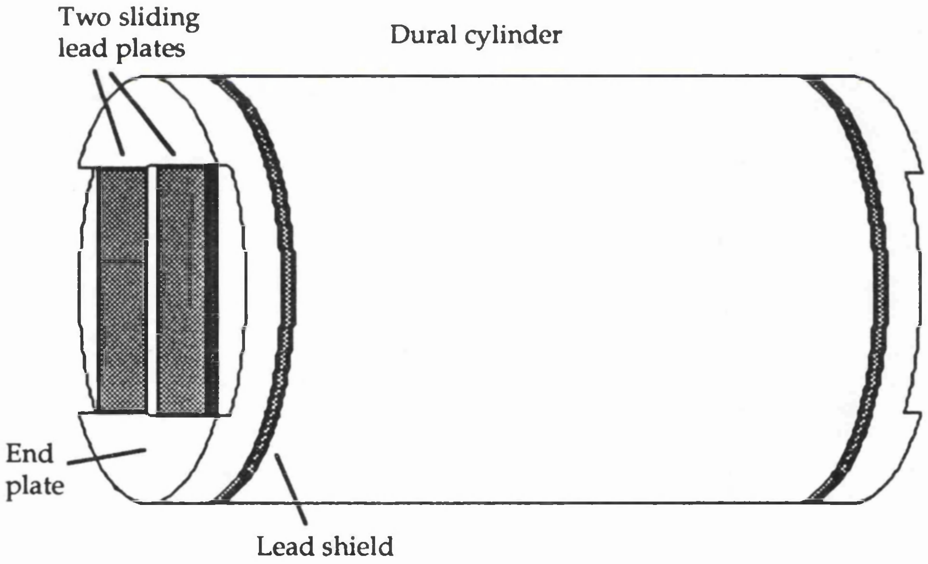

Figure 8.2 Collimators for the clinical system. Two lead plates are used to form the slit collimator. They can be slid along their mount to vary the width of the slit. An end plate at each end of the cylinder forms a base for the lead slits. Behind the end plate is a lead disc with a central hole to provide extra shielding. The end plates can each be independently rotated to align the slits.

In order to test the clinical system comparative measurements were performed on both the bench set-up and the clinical apparatus. The arrangement of the detector and collimators were adjusted until the clinical apparatus reproduced the shapes and relative intensities of diffraction peaks in the patterns of test phantoms previously measured on the bench set-up. This required a great deal of careful alignment to set the exact scatter angle and find the position of the scattering volume.

8.1.2 Modifications to the apparatus

The problem of poor count rate needs to be addressed with this technique. The precision is dependent to a large extent on the counting statistics, furthermore the problems of patient movement require the count level to be reached in the shortest possible time. The obvious way of increasing the scattered intensity is by increasing the incident intensity. This will however require an x-ray generator capable of a high continuous output (>10mA) and fast counting electronics, both of which are expensive. A possible way of increasing the counting efficiency is to adapt the apparatus to use two sodium iodide (NaI) scintillation counters rather than the solid state detector. The arrangement is shown in figure 8.3.

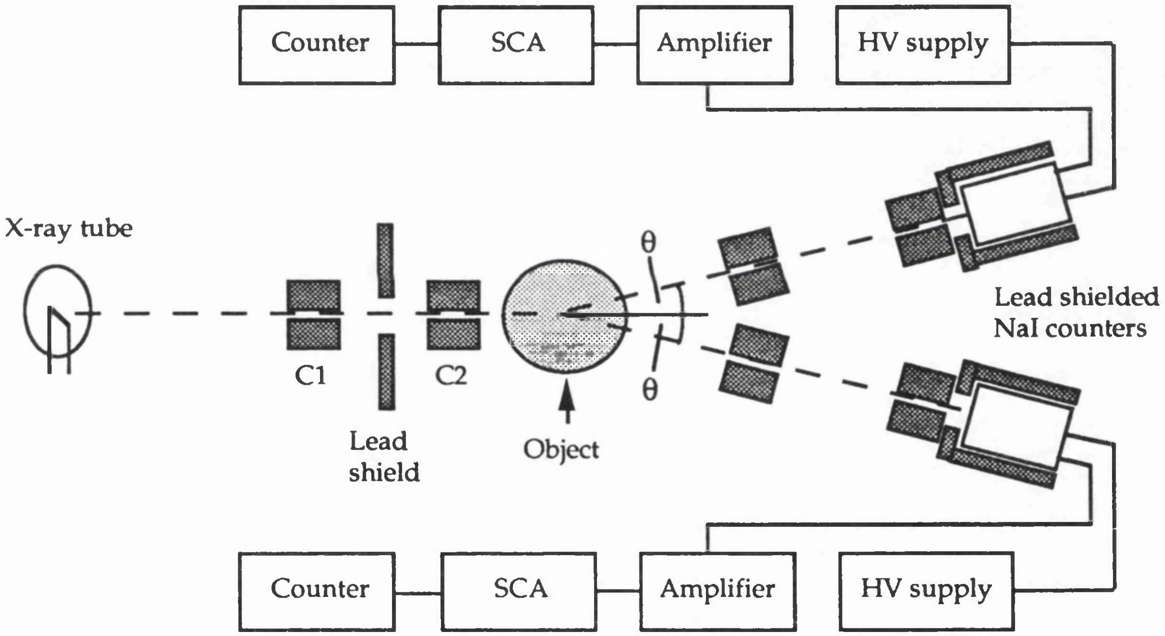

Figure 8.3 Suggested arrangement of apparatus for future work.

Both scintillation counters are finely collimated and positioned at scattering angles of 6° to the incident beam (one on each side). The intention is for one NaI counter to record the intensity of the bone peak and the other counter to record the marrow peak intensity. From these results the bone-marrow peak ratio can be found. Single channel analysers (SCA) are used to select narrow energy windows around each peak and counters record the intensity.

The excellent efficiency of NaI counters could improve statistics and decrease the measurement time. Also the cost of two scintillation counters and SCAs will be considerably lower than the cost of a large area solid state detector and multichannel analyser.

The eventual aim of this technique is to attach the apparatus to an existing bone measurement device, such as a dual photon absorptiometer, so that twice the information can be obtained from a single measurement. This would allow the bone-marrow ratio in the trabecular region to be found from the scatter measurement plus the bone mineral density of the total bone to be determined by the absorptiometer. The measurement of two parameters could help to reduce the overlap currently seen between measurements of normal and osteoporotic groups. This idea needs to be considered further together with the technical details involved.

Appendices

Appendix 1 - The interaction of x-rays with matter

1.1 Compton scatter

Compton scatter is the inelastic, incoherent scatter of photons by the outer electrons of atoms. It is assumed that the photon energy is sufficiently large compared to the atomic binding energies that the electrons may be considered as free electrons.

The differential atomic scattering cross section of a photon with energy hν' to be observed at an angle θ per unit solid angle per atom, when the incident photon energy is hν, is given by the Klein-Nishina formula,

$$\frac{d\sigma_C}{d\Omega} = \frac{e^4 Z}{2m_o^2 c^4} \left(\frac{h\nu'}{h\nu}\right)^2 \left(\frac{h\nu}{h\nu'} + \frac{h\nu'}{h\nu} - \sin^2\theta\right) \tag{1.1A}$$

The atomic cross section is seen to be directly proportional to Z.
The error introduced by neglecting the atomic binding of the electrons is generally less than 5%.

At very low energies the angular distribution of Compton scattered photons is symmetrical about 90°, and as the photon energy increases the scattered energy tends more towards the forward direction. In the diagnostic energy range the majority of photons will be scattered >50°, only a very small proportion will be emitted in the angular range of interest in this project (i.e. <10°).

1.2 Photoelectric effect

In this process all of the energy of the incident photon is imparted to an orbital electron, which is then ejected from the atom. The vacancy left by the ejected photoelectron is then filled by an electron falling from an outer orbit. The potential energy emitted by this electron due to the difference in orbital energies sometimes appears in the form of characteristic radiation. For the case of low atomic number materials, such as biological tissues, the characteristic radiation has energy <5keV, thus any characteristic photons produced will be absorbed locally by the tissue. Therefore for this experiment we can assume that any photon undergoing the photoelectric effect is totally absorbed.

1.3 Photon attenuation

The probabilities of occurrence of each of the photon interactions with an atom are described by their respective atomic interaction cross sections. The total probability of a photon interacting with a material by any of the three mechanisms is given by the sum of the interaction cross section values;

$$\sigma_{tot} = \sigma_{phot} + \sigma_{incoh} + \sigma_{coh} \qquad (1.2A)$$

Clearly, the interaction of a photon within the beam with the material it is traversing causes that photon to be removed from the primary beam, either by absorption or by scattering to a secondary direction. Thus, attenuation occurs.

The *linear attenuation coefficient* represents the degree of attenuation at a particular energy by a material of unit thickness, it is described by the following expression:

$$\mu_i = \sigma_i n_i \qquad (1.3A)$$

where n_i is the number of atoms per unit volume. If σ_i is the total cross section then μ_i represents that total linear attenuation coefficient.

From a statistical consideration of the numbers of photons removed from the beam due to interaction, the exponential law of attenuation can be derived:

$$I = I_0 . \exp(-\mu . x) \qquad (1.4A)$$

where I is the photon intensity after traversing a medium of thickness x, I_0 is the incident intensity and μ is the linear attenuation coefficient. The intensity of the beam is the number of photons passing through a cross section of the beam of unit area per second. The exponential attenuation law only applies to ideally collimated, narrow beam geometry because this eliminates the chance of photons being scattered back into the beam.

Appendix 2 - Anthropomorphic phantoms for bone density measurement

A set of anthropomorphic phantoms, intended for use as test tools in bone densitometry, has been designed and constructed for the most common measurement sites, namely, the lower forearm, the upper thigh, and the abdomen (further details of each of these phantoms are given in Royle and Speller 1992). The dimensions of the various tissues closely approximate the corresponding tissues within a healthy, adult subject of average size. One condition included within the design of the phantoms was for the shapes of the various tissues to be simplified for ease in construction and to avoid complicating the use of the phantoms. Symmetrical shapes, in particular those with circular symmetry, are used where possible to minimise errors in the repositioning of the phantoms in the machine.

The anthropomorphic phantoms can be used to simulate a patient at various stages of osteoporosis. To allow the evaluation of the precision of bone densitometers, the phantoms were designed such that the bone models could be removed and replaced by bone inserts of the same dimensions but with different density simulating various degrees of osteoporosis. In this way the ability of a densitometer to distinguish between small differences in bone mineral content can be tested by performing measurements on the phantom over a range of densities of bone inserts.

2.1 The lower forearm phantom

The lower forearm, in particular the radius at mid and distal positions, is the site commonly measured in single photon absorptiometry. The important factors which should be incorporated within the design of the forearm phantom are (i) the inclusion of the distal and mid-radius positions, at which measurements are usually made, (ii) the correct separation of the radius and ulna bone models throughout their lengths, this is because the densitometer searches for a particular separation of the bones for repositioning, and (iii) the relative proportions of inner and outer bone at each site.

The design of the lower forearm phantom is shown in figure 2.1A. The dimensions of the bones were found from a survey of radius and ulna sizes at University College and Middlesex school of medicine anatomy department. The outer dimensions of the surrounding muscle substitute were taken from the mean values of 20 female wrists. The radius and ulna are fabricated as removable inserts consisting of an outer cortical shell containing inner bone (a homogeneous tissue with the average properties of trabeculae filled with marrow). The variation that has been observed in these two bone components have been incorporated in a set of inserts to simulate changes that occur over the space of ~2-4 years for a normal postmenopausal woman. The density changes are;

(i) insert one - normal density values of inner and outer bone,
(ii) insert two - 2.5% reduction in cortical density, 3% reduction in inner bone,
(iii) insert three - 4% reduction in cortical density, 4.8% reduction in inner bone.

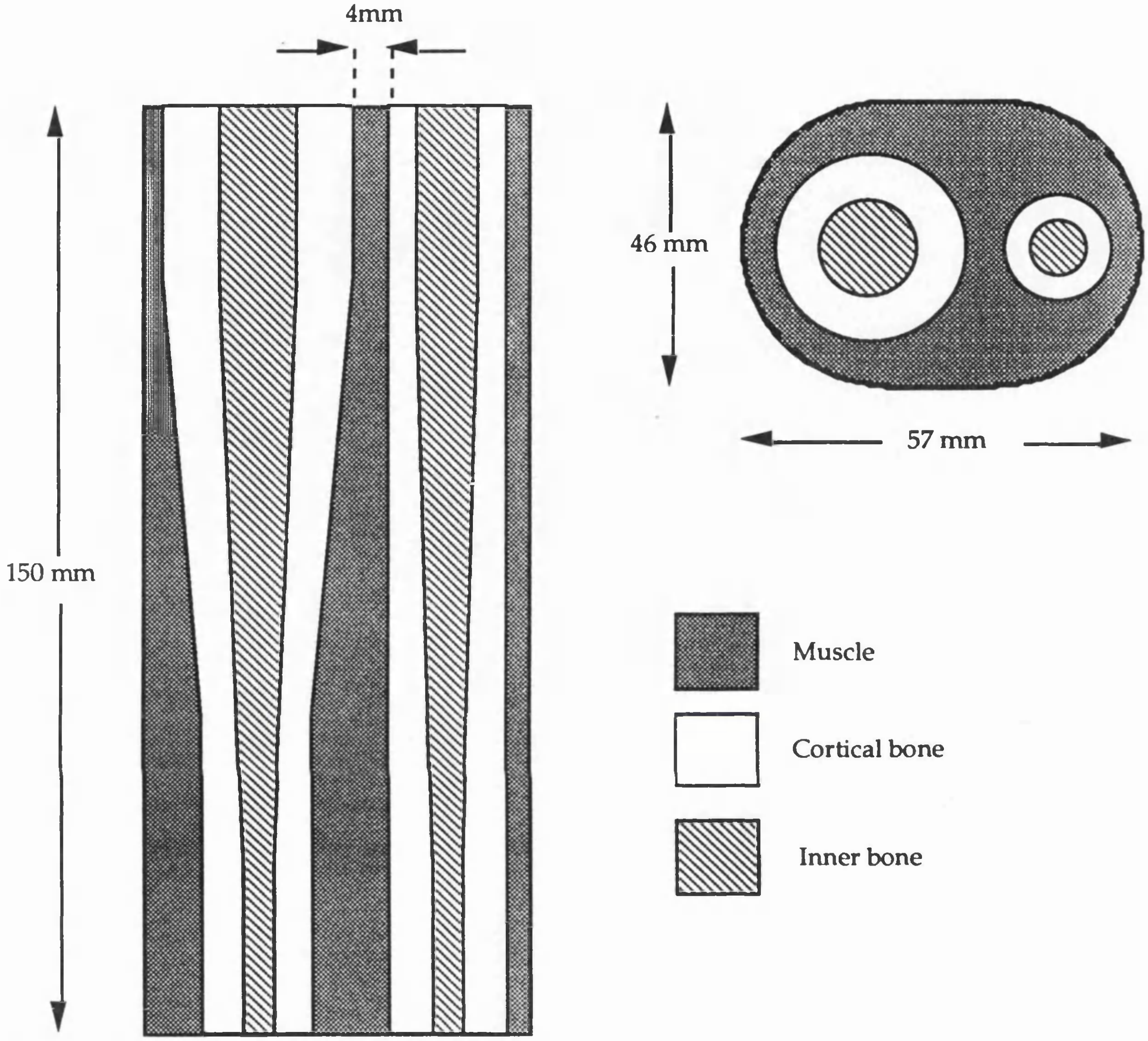

Figure 2.1A Top view and cross-section of the lower forearm phantom. The radius is to the left and the ulna to the right.

2.2 The upper thigh phantom

Bone densitometers which are able to account for an overlying thickness of soft tissue measure the clinically relevant areas, which are the lower spine or the femoral neck. The phantom of the upper thigh, which contains the femoral neck, is shown in figure 2.2A.

The cortical and trabecular bone models were taken from the work of Woodard and White (1982). The femoral neck is comprised of mainly trabecular bone filled with marrow and therefore it is this section that is made replaceable. The variation in the cortical shell was assumed to not represent a significant effect due to the proportion of the bone it occupies. A set of inner bone models of varying densities was developed to provide changes in bone mineral content from a normal value to a 10.5% decrease.

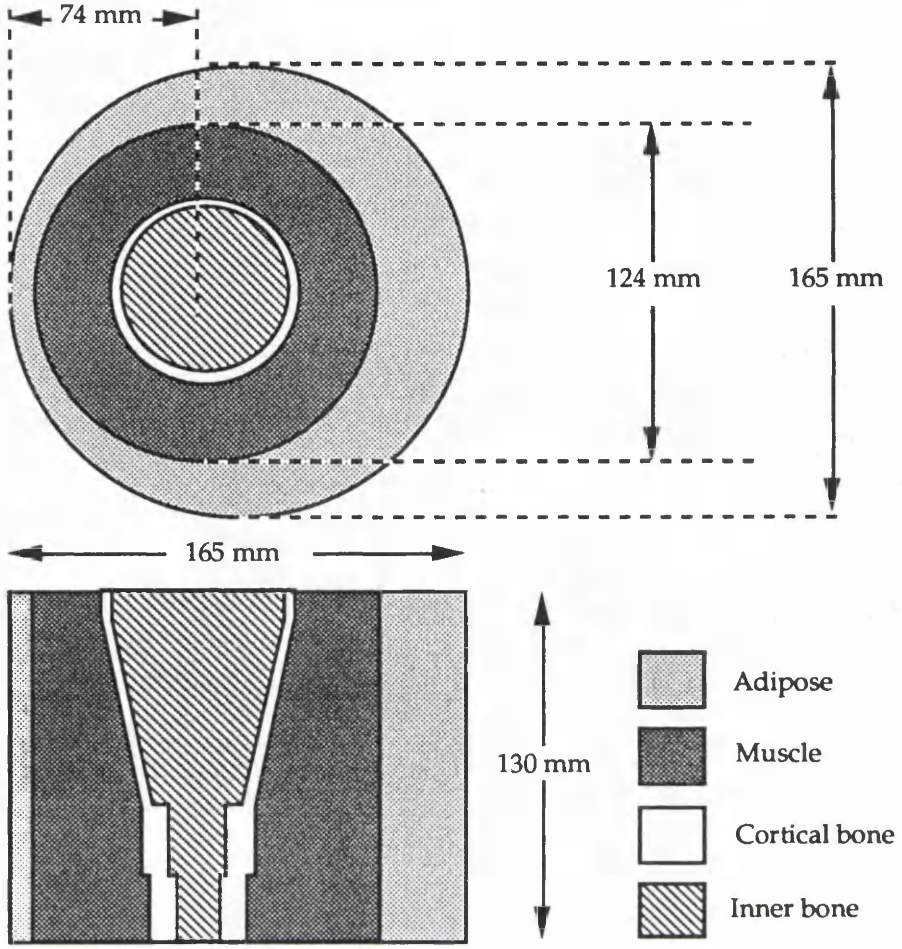

Figure 2.2A The phantom of the upper thigh containing the femoral neck.

2.3 The abdomen phantom

The lumbar vertebrae from L1 - L3 enclosed within the abdomen is a region of great clinical interest within the study of bone disease. Similarly to the measurement of the femoral neck the spine is measured by techniques which can account for the overlying soft tissue thickness.

The abdomen is a very complex region of the body encompassing a large range of tissues of intricate shapes, thus presenting problems in the design of a realistic body phantom. However, a study of the properties of the tissues in this region showed that some tissues have similar density and attenuation and so can be grouped together as one tissue for the purposes of building the phantom. This greatly reduces the number of tissues types that need to be simulated. The substitute materials eventually made were muscle, adipose, cortical and trabecular bone, liver, kidney, gut, pancreas and a blood/fat mixture used to simulate the central group of arteries. Furthermore, slight simplification of the shapes of each of the tissues made the phantom easier to construct and reduced the effect of repositioning errors.

Due to the extreme difficulties of building a three dimensional phantom of this region four thin layers have been used to create a solid structure. Each layer representing the anatomical dimensions at a particular location as imaged with a CT type investigation within an average, adult subject. Correct positioning of the four slices provides a '3-D' simulation. When used care must be taken to ensure that slab interfaces are inclined to the radiation beam at small angles to avoid the effects of the slice edges. The completed phantom that consists of four 2.5cm thick slices to form a total 10cm thick abdominal section. The anatomical shapes and dimensions at each of these layers were given by Koritke and Sick (1983). Different degrees of osteoporosis are simulated by replacing the rod of inner bone passing down the vertebral column. The rod represents the inner bone section and was designed to allow changes from normal values to a 10% decrease.

2.4 Density of bone substitutes

The formula used for normal density inner bone is taken from White *et al* (1977). The density of this material was reduced to produce the osteoporotic inner bone substitute by adding specific quantities of phenolic microspheres, PMS, to the mixture. PMS is a powder made of hollow, gas filled spheres having a low density of ~0.2 g/cm^3. A small quantity of this material when added to the mixture can reduce the density by the required amount.

Table 2.1A shows the percentage weights of the chemical constituents required to produce the substitutes to simulate both healthy and osteoporotic bone. The density of each of the tissue substitutes was calculated by measuring the mass and volume of an accurately machined block of the material.

Tissue	Percentage weights of constiuents	Density (g/cm^3)
Inner bone 1	CB1 (75.17); P.V.C. (24.83)	1.18 (Healthy)
Inner bone 2	CB1 (74.61); P.V.C. (24.83); PMS (0.56)	1.15 (~2% drop)
Inner bone 3	CB1 (74.05); P.V.C. (24.83); PMS (1.12)	1.13 (~4% drop)
Inner bone 4	CB1 (73.42); P.V.C. (24.83); PMS (1.75)	1.11 (~6% drop)
Inner bone 5	CB1 (72.90); P.V.C. (24.83); PMS (2.27)	1.09 (~8% drop)
Inner bone 6	CB1 (72.12); P.V.C. (24.83); PMS (3.05)	1.06 (~10% drop)

Table 2.1A The percentage weights of the constituents for both healthy and low density bone substitute materials.

Appendix 3 - Effective atomic number

The interaction of low energy x-rays with matter involves photoelectric absorption or scattering (elastic or inelastic), and each of these mechanisms depend on the photon energy and on the atomic number of the medium. Hence, the atomic number is an important factor.

For non-elemental materials, such as molecules, compounds, mixtures, etc., an *effective* atomic number exists. The effective atomic number, Z_{eff}, of a substance is defined as the number Z of such an element in which, the measurement conditions being kept the same, the attenuation of an x-ray beam of a given energy is the same as for the substance.

Yang *et al* (1987) have described an accurate technique (within 4%) for calculating the effective atomic numbers in human tissues over the diagnostic energy range. The total photon interaction cross sections per electron of the tissues are used to define the values of Z_{eff}.

$(\sigma_e)_{Tissue}$ is equal to the ratio of the total photon interaction cross section per gram to the total number of electrons per gram of the tissue. This is calculated as follows:

$$(\sigma_e)_{Tissue} = \sum_i W_i \frac{N_A}{A_i} Z_i \sigma_{ei} \Big/ \sum_i W_i \frac{N_A}{A_i} Z_i \qquad (3.1A)$$

where W_i is the fractional chemical composition, Z_i the atomic number, A_i the atomic weight, N_A is Avogadro's number (=6.0222 x 10^{23} mole^{-1}), and σ_{ei} is the total photon interaction cross section per electron of the individual element in the tissue.

Yang *et al* (1987) explain that $(\sigma_e)_{Tissue}$ can be interpolated by a cubic spline method on the known relation between σ_{ei} and Z_i, for each energy, in order to obtain an equivalent atomic number. This number is taken to be Z_{eff}. Values of Z_{eff} for the tissues relevant to this project have been calculated using the method of Yang *et al* (1987) and based upon the latest available data of tissue chemical composition (the data of Woodard and White 1986).

The values of $(\sigma_e)_{Tissue}$ at the energies 10, 15, 20, 30, 40, 50, 60 and 80keV were calculated for each of these tissues. The values of the total photon interaction cross section per electron (σ_e) for each of the elements were taken from the data of Storm and Israel (1970).

A cubic spline fitting routine in GRTOOL on a Sun workstation was employed to determine values of Z_{eff} at these energies for each of the materials. Table 3.1A lists these values:

Energy (keV)	Effective atomic number					
	Muscle	Adipose	Inner bone	Cortical bone	Yellow marrow	Red marrow
10	7.54	6.42	9.67	13.01	6.31	7.05
15	7.55	6.43	9.92	13.28	6.32	7.08
20	7.57	6.44	10.04	13.37	6.33	7.11
30	7.56	6.43	10.08	13.44	6.32	7.11
40	7.56	6.41	10.16	13.53	6.30	7.10
50	7.53	6.39	10.16	13.54	6.28	7.08
60	7.53	6.33	10.09	13.51	6.22	7.07
80	7.47	6.25	10.05	13.44	6.14	6.99
Mean	7.54	6.39	10.02	13.39	6.28	7.07

Table 3.1A The effective atomic numbers of human tissues calculated by the method of Yang *et al* (1987), using the elemental composition data of Woodard and White (1986).

Appendix 4 - Fourier transform of discretely sampled data

The Fourier transform is given by the following equation

$$H(f)=\int_{-\infty}^{\infty} h(t).e^{2\pi ift}\,dt \qquad (4.1A)$$

Transformation of a continuous function is a straightforward integral producing another function which contains all of the information present in the original function. However, in typical physical measurements, such as those in this project, the exact mathematical function is not known. Information is obtained on the function h(x) by sampling at evenly spaced intervals (in, for example, time, space, energy, etc.). Let Δ denote the interval between successive samples, such that the N sampled values are

$$h_n = h(n\Delta) \qquad n = 0, 1, 2, 3, \ldots, N-1$$

The reciprocal of the interval Δ is called the sampling rate.

With N numbers of input only N independent numbers of output can be produced. Estimates are obtained only at the discrete values

$$f_n \equiv n / N\Delta \qquad n = -N/2, \ldots, N/2$$

The extreme values of n correspond exactly to the upper and lower limits of the Nyquist critical frequency range.

The discrete Fourier transform of the N points h_n is described by the following summation

$$H_k = \sum_{k=0}^{N-1} h_n.e^{2\pi ik^{n}/_{N}} \qquad (4.2A)$$

N complex numbers (the h_n's) are mapped into N complex numbers (the H_k's).

4.1 Sampling

To fully represent the signal by a series of sampled values, retaining all the original information, sufficient samples and a sufficiently small interval are required. For example, a smooth function requires only a few samples, whereas a jagged function needs far more.

The maximum sampling frequency, called the Nyquist critical frequency, is given by

$$f_c = 1 / 2\Delta$$

Shannon's sampling theorem states that if a continuous function, sampled at an interval Δ happens to be band-width limited to frequencies smaller in magnitude than f_c, then the function is completely determined by its samples h_n.

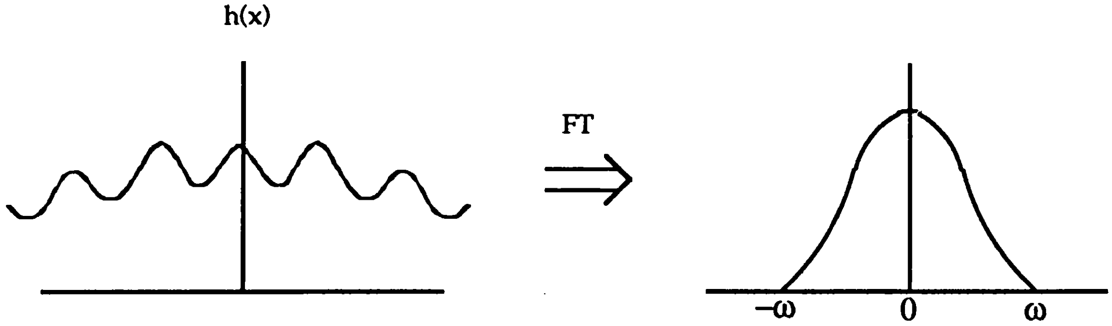

Figure 4.1A The function h(x) is band-width limited, that is, ω is finite. If ω is less than the Nyquist critical frequency f_c then the function can be fully recovered from its Fourier transform.

However, if the function is not band-width limited to less than the Nyquist critical frequency aliasing occurs. Any frequency component outside of the frequency range is aliased into that range.

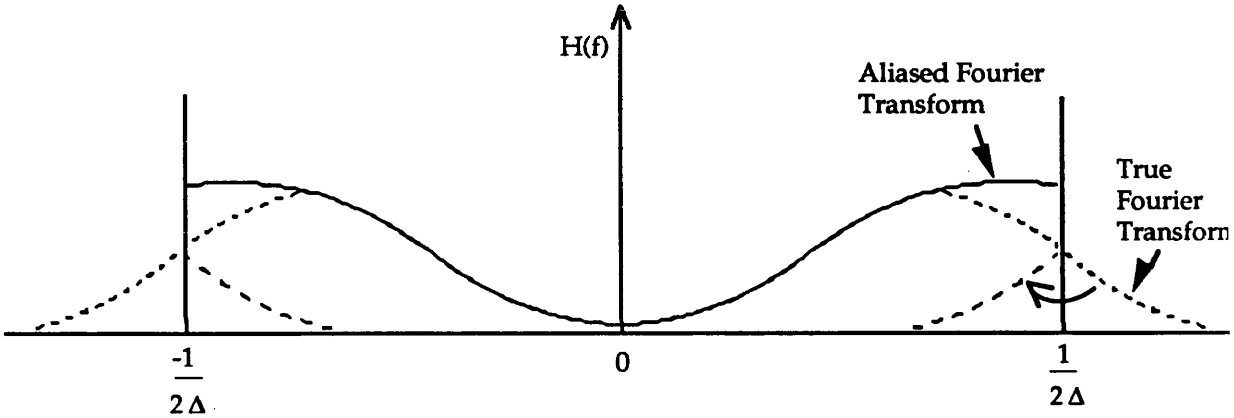

Figure 4.2A If the function h(x) is sampled with a sampling interval Δ and is not band-width limited within the Nyquist critical frequency, then power outside that range is folded over into it.

The effect of undersampling is that the aliased signal appears to have a much longer period than the actual signal has.

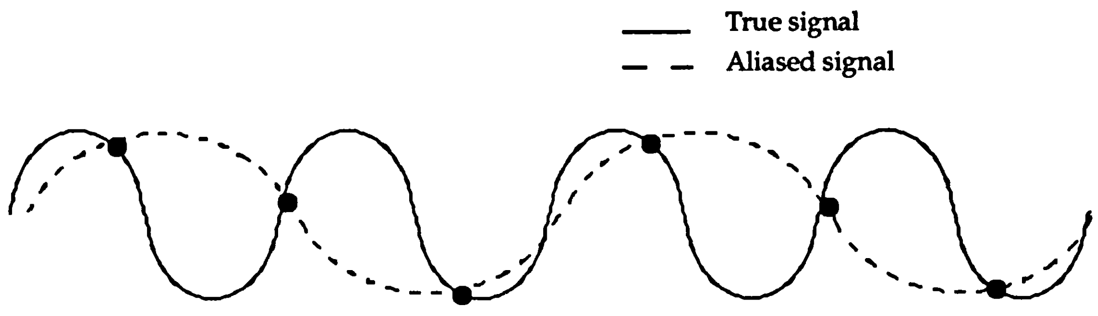

Figure 4.3A The true signal is sampled at the points shown by the black dots. The information obtained from the sampled points would indicate that the dashed curve is the sampled signal. The true signal must be sampled at least every half-cycle to avoid aliasing.

References

Alexander L and Klug H P 1948 Basic aspects of x-ray absorption *Analytical Chemistry* **20** 886

Aloia J F, Vaswani A, Ross P and Cohn S H 1990 Ageing bone loss from the femur, spine, radius and total skeleton *Metabolism* **39** 1144

Andreo P 1991 Monte Carlo techniques in medical radiation physics *Phys. Med. Biol.* **36** 861

Andresen J and Nielsen H E 1986 Amount of bone and bone remodelling in normal subjects and in patients with chronic renal failure *Acta. Radiol. Diag.* **27** 341

Baba-Hamed T 1990 Application of dual energy techniques for tissue characterisation in conventional diagnostic radiology *Ph.D Thesis, Univ. London*

Barnett E and Nordin B E C 1960 The radiological diagnosis of osteoporosis: a new approach *Clin. Radiol.* **11** 166

Benn D K and Royle G J 1990 Perfusion of dry human mandibles with radiographic equivalent soft tissue epoxy resin presented at *The British Society for Dental Research* London, UK

Birch R, Marshall M and Ardran G 1979 Catalogue of spectral data for diagnostic x-rays *HPA scientific report series - 30*

Blum L 1971 X-ray scattering from liquids with nearly spherical molecules *J. Comput. Phys.* **7** 55

Bordas J, Munro I H and Glazer A M 1976 Small angle scattering experiments on biological materials using synchrotron radiation *Nature* **262** 541

Boyd D P, Cann C E, Couch J L, Faul D D, Gould R G, Peschmann K R and Genant H K 1982 Future advanced CT technology for bone and tissue densitometry. Isotope source and electron beam scanners *J. Comput. Assist. Tomogr.* **6** 202

Bradley D A, Evans S H, Dance D R and Bateman J E 1988 The characterisation of low atomic number media by small angle x-ray scattering *Phys. Med. Biol.* **33** 182

Browne M A, Gaydecki P A, Gough R F, Grennan D M, Khalil S I and Mamtora H 1987 Radiographic image analysis in the study of bone morphology *Clin. Phys. Physiol. Meas.* **8** 105

Cameron J R, Mazess R B and Sorenson J A 1968 Precision and accuracy of bone mineral determination by direct photon absorptiometry *Invest. Radiol.* **3** 141

Cameron J R and Sorenson J 1963 Measurement of bone mineral in vivo: an improved method *Science* **142** 230

Cann C E 1988 Quantitative CT for determination of bone mineral density: A review *Radiology* **166** 509

Cann C E, Ettinger B and Genant H K 1985b Normal subjects vs. osteoporotics: no evidence using dual energy CT for disproportionate increase in vertebral fat *J. Comput. Assist. Tomogr.* **9** 617

Cann C E, Genant H K, Kolb F O and Ettinger B 1985a Quantitative computed tomography for prediction of vertebral fracture risk *Bone* **6** 1

Chan H-P and Doi K 1983 The validity of Monte Carlo simulation in studies of scattered radiation in diagnostic radiology *Phys. Med. Biol.* **28** 109

Chesnut C H 1988 Diagnostic criteria for osteoporosis, presented at *Osteoporosis and bone mineral measurement conf.* Bath, UK

Christiansen C and Rodbrø P 1977 Long term reproducibility of bone mineral content measurements *Scand. J. Clin. Lab. Invest.* **37** 321

Christiansen C, Rodbrø P and Jensen H 1975 Bone mineral content in the forearm measured by photon absorptiometry. Principles and reliability *J. Clin. Lab. Invest.* **35** 323

Cohn S H, Dombrowski C S and Fairchild R G 1970 *In-vivo* neutron activation analysis of calcium in man *Int. J. Appl. Radn. Isot.* **31** 127

Cohn S H, Shukla K K, Dombrowski C S and Fairchild R G 1972 Design and calibration of a 'broad-beam' ^{238}Pu, Be neutron source for total body neutron activation analysis *J. Nucl. Med.* **13** 487

Coupron P, Meunier P, Bressot C and Giroux J M 1976 Amount of bone in iliac crest biopsy. In: Bone Histomorphometry (edited by Meunier P J) *Armour Montagu: Paris* 39

Dalen N, Hellstrom L G and Jacobsen B 1976 Bone mineral content and mechanical strength of the femoral neck *Acta Orthop. Scand.* **47** 503

Darby A J and Meunier P J 1981 Mean wall thickness and formation periods of trabecular bone packets in idiopathic osteoporosis *Calcif. Tissue Int.* **33** 199

Dequeker J 1973 Bone and ageing. Differentiation between physiological and pathological bone loss In: Clinical aspects of metabolic bone disease (edited by Frame B, Parfitt A M and Duncan H) *Excerpta Medica*

Dickenson R P, Hutton W C and Stott J R 1981 The mechanical properties of bone in osteoporosis *J. Bone Joint Surg.* **63B** 233

Dunn W L, Wahner H W and Riggs B L 1980 Measurement of bone mineral content in human vertebrae and hip by dual photon absorptiometry *Radiology* **136** 485

Dunnil M S, Anderson J A and Whitehead R 1967 Quantitative histological studies on age changes in bone *J. Pathol. Bacteriol.* **94** 275

Durand E P and Ruegsegger P 1991 Cancellous bone structure - Analysis of high resolution CT images with the run-length method *J. Comp. Assist. Tomogr.* **15** 133

Evans S H, Bradley D A, Dance D R, Bateman J E and Jones C H 1991 Measurement of small-angle photon scattering for some breast tissues and tissue substitute materials *Phys. Med. Biol.* **36** 7

Feldkamp L A, Kleerekoper M, Kress J W, Freeling R, Mathews C H E and Parfitt A M 1983 Investigation of three-dimensional structure of trabecular bone by computed tomography of iliac biopsy samples *Calcif. Tissue Int.* **35** 669

Fewell T R and Shuping R E 1977 Photon energy distribution of some typical diagnostic x-ray beams *Med. Phys.* **4** 187

Ford J C and Wehrli F W 1991 *In-vivo* quantitative characterisation of trabecular bone by NMR interferometry and localised proton spectroscopy *Mag. Res. Med.* **17** 543

Genant H K and Boyd D 1977 Quantitative bone mineral analysis using dual-energy computed tomography *Invest. Radiol.* **12** 545

Giessen B C and Gordon G E 1968 X-ray diffraction: new high speed technique based on x-ray spectrography *Science* **159** 973

Glatter O and Kratky O 1982 In: Small angle x-ray scattering *Academic Press*

Haddaway M, Grantham M and Davie M W 1988 Contribution of cortical and trabecular bone to density in lumbar vertebrae and relationship of trabecular density to mechanical strength, presented at *Osteoporosis and bone mineral measurement conf.* Bath, UK

Hardie-Brown D, Lillicrap S C and Scott J 1987 Phantom materials for photon scattering measurements *Phys. Med. Biol.* **32** 1175

Harding G, Kosanetzky J and Neitzel U 1987 X-ray diffraction computed tomography *Med. Phys.* **14** 515

Harding G, Newton M and Kosanetzky J 1990 Energy dispersive x-ray diffraction tomography *Phys. Med. Biol.* **35** 33

Horrocks J A 1988 The application of dual energy techniques to digital ionography *Ph.D. thesis, Univ. London*

Horsman A and Simpson M 1975 The measurement of sequential changes in cortical bone geometry *Brit. J. Radiol.* **48** 471

Hosie C J, Richardson W and Gregory N L 1985 A gamma-ray computed tomography scanner for the quantitative measurement of bone density *J. Biomed. Eng.* **7** 30

Hosie C J and Smith D A 1986 Precision of measurement of bone density with a special

Hubbel J H, Veigele W J, Briggs E A, Brown R T, Cromer D T and Howerton R J 1977 Atomic form factors, incoherent scattering functions and photon scattering cross sections *J. Phys. Chem. Ref. Data* **6** 615

Huddleston A L and Bhaduri D 1978 Measurement of bone density using single-source Compton-scattering methods *Fourth International Conference on Bone Measurement* NIH Publication No. 80-1938 334

ICRP 1974 Publication 23 *Pergamon Press, Oxford*

ICRP 1977 Publication 26 *Pergamon Press, Oxford*

James R W 1948 In: The optical principles of the diffraction of x-rays *G.Bell and sons: London*

JCPDS 1961 Powder diffraction file (compiled by JCPDS: International centre for diffraction data; edited by W. F. McClune) *JCPDS: Pennsylvania, USA*

Johns P C and Yaffe M J 1983 Coherent scatter in diagnostic radiology *Med. Phys.* **10** 40

Kalender W A, Klotz E and Suess C 1987 Vertebral bone mineral analysis: An integrated approach with CT *Radiology* **164** 419

Kennedy N S, Eastell R, Ferrington C M, Simpson J D, Smith M A, Strong J A and Tothill P 1982 Total body neutron activation analysis of calcium: calibration and normalisation *Phys. Med. Biol.* **27** 697

Khan H 1956 Applications of Monte Carlo *RAND, Santa Monica, Ca.*

Kleerekoper M, Villanueva A R, Stancia J, Sudhaker Rao D and Parfitt A M 1985 The role of three-dimensional trabecular microstructure in the pathogenesis of vertebral compression fractures *Calcif. Tiss. Int.* **37** 593

Koligliatis T 1990 A scattering method for bone density measurements with polychromatic sources *Ph.D thesis, Univ. London*

Koritke J G and Sick H 1983 In: Atlas of sectional human anatomy *Urban and Schwarzenberg: Munich*

Kosanetzky J, Knoerr B, Harding G and Neitzel U 1987 X-ray diffraction measurements of some plastic materials and body tissues *Med. Phys.* **14** 526

Kratky O 1982 In: Small angle x-ray scattering (edited by Glatter O. and Kratky O.) *Academic Press: London* 53-84

Krølner B and Pors Nielsen S 1980 Measurement of bone mineral content (BMC) of the lumbar spine, I. Theory and application of a new two-dimensional dual-photon attenuation method *Scand. J. Clin. Lab. Invest.* **40** 653

Langton C M, Palmer S B and Porter R W 1984 The measurement of broadband ultrasonic attenuation in cancellous bone *Eng. in Med.* **13** 89

Laval-Jeantet A M, Conn E E, Roger B and Gallant P 1984 A postprocessing dual energy technique for vertebral CT densitometry *J. Comput. Assist. Tomogr.* **8** 1164

Leichter I, Bivas A, Giveon A, Margulies J Y and Weinreb A 1987 The relative significance of trabecular and cortical bone density as a diagnostic index for osteoporosis *Phys. Med. Biol.* **32** 1167

Lips P, Coupron P and Meunier P J 1978 Mean wall thickness of trabecular bone packets in the human iliac crest: changes with age *Calcif. Tissue Res.* **25** 13

Maclwyn-Hughes J 1964 In: Physical chemistry *Pergamon Press* 458

Mazess R B 1982 On ageing bone loss *Clin. Orthop. Rel. Res.* **165** 239

Mazess R B 1983 Errors in measuring trabecular bone by computed tomography due to marrow and bone composition *Calcif. Tiss. Int.* **35** 148

Mazess R B 1987 Bone density in diagnosis of osteoporosis: thresholds and breakpoints *Calcif. Tiss. Int.* **41** 117

Mazess R B, Barden H, Ettinger M and Schultz E 1988a Bone density of the radius, spine and proximal femur in osteoporosis *J. Bone Mineral Res.* **3** 13

Mellish R W E, Garrahan N J, Vedi S and Compston J E 1986 A new computerised method for direct measurement of mean trabecular plate thickness in human iliac crest biopsies *Bone* **7** 310

Meltzer M, Lessig H J and Siegel J A 1989 Bone mineral density and fracture in postmenopausal women *Calcif. Tissue Int.* **45** 142

Merz W A and Schenk R K 1970 Quantitative structural analysis of human cancellous bone *Acta Anat.* **75** 54

Mooney M J 1992 A study of scattered x-ray radiation in bone density measurement *Ph.D. thesis, Univ. London*

Morin L R 1982 Molecular form factors and photon coherent scattering cross sections of water *J. Phys. Chem. Ref. Data* **11** 1091

Morin L R and Berroir A 1983 Calculation of x-ray single scattering in diagnostic radiology *Phys. Med. Biol.* **28** 789

Muntz E P, Fewell T, Jennings R and Bernstein H 1983 On the significance of very small angle scattered radiation to radiographic imaging at low energies *Med. Phys.* **10** 819

Narten A H and Levy H A 1971 Liquid water: molecular correlation functions from x-ray diffraction *J. Chem. Phys.* **55** 2263

Neitzel U, Kosanetzky J and Harding G 1985 Coherent scatter in radiographic imaging: a Monte Carlo simulation study *Phys. Med. Biol.* **30** 1289

Nelp W B, Palmer H E, Murano R, Pailthorp K, Hinn G M, Rich C, Williams J L, Rudd T G and Denny J D 1970 Measurement of total body calcium (bone mass) *in-vivo* with the use of total body neutron activation analysis *J. Lab. Clin. Med.* **76** 151

Nelp W B, Denny J B, Murano R, Hinn G M, Williams J L, Rudd T G and Palmer H E 1972 Absolute measurement of total body calcium in-vivo *J. Lab. Clin. Med.* **79** 430

Newton M, Hukins D W L and Harding G 1992 Bone composition measured by x-ray scattering *Phys. Med. Biol.* **37** 1339

Nicoll J J, Tothill P, Smith M A, Reid D, Kennedy N S J and Nuki G 1987 *In-vivo* precision of total body calcium and sodium measurements by neutron activation analysis *Phys. Med. Biol.* **32** 243

Nordin B E C, Aaron J, Speed R and Crilly R G 1981 Bone formation and resorption as the determinants of trabecular bone volume in postmenopausal osteoporosis *The Lancet ii* 277

Nordin B E C 1987 The definition and diagnosis of osteoporosis *Calcif. Tiss. Int.* **40** 57

Pacifici R, Susman N, Carr P L, Birge S J and Avioli L V 1987 Single and dual energy tomographic analysis of spinal trabecular bone: A comparative study in normal and osteoporotic women *J. Clin. Endocrinol. Metabol.* **64** 209

Parfitt A M, Matthews C, Villanueva A R, Kleerekoper M, *et al* 1983 Relationships between surface, volume and thickness of iliac trabecular bone in ageing and in osteoporosis *J. Clin. Invest.* **72** 1396

Peppler W W and Mazess R B 1981 Total body bone mineral and lean body mass by dual photon absorptiometry *Calcif. Tiss. Int.* **33** 353

Persliden J and Carlsson G A 1986 Calculation of the small angle distribution of scattered photons in diagnostic radiology using a Monte Carlo collision density estimator *Med. Phys.* **13** 19

Porod G 1982 In: Small angle x-ray scattering (edited by Glatter O. and Kratky O.) *Academic Press: London* 17-52

Press W H, Flannery B P, Teukolsky S A and Vetterling W T 1986 In: Numerical recipes. The art of scientific computing *Cambridge* Chapter 12

Pugh J W, Radin E L and Rose R M 1974 Quantitative studies of human subchondral cancellous bone. Its relationship to the state of its overlying cartilage *J. Bone Joint Surg.* **56A** 313

Pye D W, Hannan W J and Hesp R 1990 Effective dose equivalent in dual x-ray absorptiometry *Br. J. Radiol.* **63** 149

Raeside D E 1976 Monte Carlo principles and applications *Phys. Med. Biol.* **21** 181

Richelson L S, Wahner H W, Melton L J and Riggs B L 1984 Relative contributions of ageing and oestrogen deficiency to postmenopausal bone loss *N. Engl. J. Med.* **311** 1273

Riggs B L, Wahner H W, Dunn W L, Mazess R B, Offord K P and Melton L J 1981 Rates of bone loss in the appendicular and axial skeletons of women *J. Clin. Invest.* **67** 328

Riggs B L, Wahner H W, Seeman E, Offord K P, Dunn W L, Mazess R B, Johnson K A and Melton L J 1982 Changes in bone mineral density of the proximal femur and spine with ageing *J. Clin. Invest.* **70** 716

Ringe J D 1982 Precision and clinical application of peripheral single photon absorptiometry In. Non-invasive Bone Measurements: Methodological Problems (edited by Dequeker J and Johnston C) *IRL Press* 47

Ross P D, Wasnich R D, Heilbrun L K and Vogel J M 1987 Definition of a spine fracture threshold based upon prospective fracture risk *Bone* **8** 271

Royle G J and Speller R D 1992 Phantoms for evaluating the performance characteristics of bone densitometers *Br. J. Radiol. (accepted for publication)*

Ruegsegger P, Anliker M and Dambacher M 1981 Quantification of trabecular bone with low dose computed tomography *J. Comput. Assist. Tomogr.* **5** 384

Ruegsegger P, Dambacher M A, Ruegsegger E, Fischer J A and Anliker M 1984 Bone loss in premenopausal and postmenopausal women *J. Bone Joint Surg.* **7** 1015

Schaadt O and Bohr H 1988 Different trends of age related diminution of bone mineral content in the lumbar spine, femoral neck and femoral shaft in women *Calcif. Tissue Int.* **42** 71

Seldin D W, Esser P D and Alderson P O 1988 Comparison of bone density measurements from different skeletal sites *J. Nucl. Med.* **29** 168

Simkin A, Ayalon J and Leichter I 1987 Increased trabecular bone density due to bone loading exercises in postmenopausal osteoporotic women *Calcif. Tissue Int.* **40** 59

Speller R D, Royle G J and Horrocks J A 1989 Instrumentation and techniques for bone density measurement *J. Phys. E: Sci. Instrum.* **22** 202

Storm E and Israel H I 1970 Photon cross sections from 1keV to 100MeV for elements Z=1 to 100 *Nuclear data tables* **A7** 565

Sutor D J and Wooley S E 1969 X-ray diffraction studies of the composition of gallstones from English and Australian patients *Gut* **10** 681

Sutor D J and Wooley S E 1973 The nature and incidence of gallstones containing calcium *Gut* **14** 215

Thomsen K, Gotfredsen A and Christiansen C 1986 Is postmenopausal bone loss an age-related phenomenon? *Calcif. Tiss. Int.* **39** 123

Tothill P, Smith M A and Sutton D 1983 Dual photon absorptiometry of the spine with a low activity source of Gadolinium-153 *Brit. J. Radiol.* **56** 829

Trotman B W, Morris T A, Sanchez H M 1977 Pigment versus cholesterol cholelithiasis: identification and quantification by infra-red spectroscopy *Gastroent.* **72** 496

Vernon-Roberts B and Pirie C J 1973 Healing trabecular microfractures in the bodies of lumbar vertebrae *Ann. Rheum. Dis.* **32** 406

Virtama P and Helela T 1969 Radiographic measurements of cortical bone. Variations in a normal population between 1 and 90 years of age *Acta Radiol.* **Suppl No 293**

Virtama P and Mahonen H 1960 Thickness of the cortical layer as an estimate of mineral content of human finger bones *Brit. J. Radiol.* **33** 60

Webber C E and Kennett T J 1976 Bone density measured by photon scattering. I. A system for clinical use *Phys. Med. Biol.* **21** 760

Weinstein R S and Hutson M S 1987 Decreased trabecular width and increased trabecular spacing contribute to bone loss with ageing *Bone* **8** 137

Wehrli F W, Ford J C, Attie M, Kressel H Y and Kaplan F S 1991 Trabecular structure -

preliminary application of MR-interferometry *Radiol.* **179** 615

White D R, Martin R J and Darlison R 1977 Epoxy resin based tissue substitutes *Br. J. Radiol.* **50** 814

White D R, Woodard H Q and Hammond S M 1987 Average soft tissue and bone models for use in radiation dosimetry *Br. J. Radiol.* **60** 907

Whitehouse W J and Dyson E D 1974 Scanning electron microscope studies of trabecular bone in the proximal end of the human femur *J. Anat.* **118** 417

Williamson J F and Morin R L 1983 An efficient method of randomly sampling the coherent angular scatter distribution *Phys. Med. Biol.* **28** 57

Wilson C R 1977 Bone mineral content of the femoral neck and spine versus the radius or ulna *J. Bone Joint Surg.* **59A** 665

Woodard H Q 1964 The composition of human cortical bone. II. Effect of age and of some abnormalities *Clin. Orthop.* **37** 187

Woodard H Q and White D R 1982 Bone models for use in radiotherapy dosimetry *Br. J. Radiol.* **55** 277

Woodard H Q and White D R 1986 The composition of body tissues *Br. J. Radiol.* **59** 1209

Yang N C, Leichner P K and Hawkins W G 1987 Effective atomic numbers for low-energy total photon interactions in human tissues *Med. Phys.* **14** 759